Dynamics and Structure of Halogen-Bonded Cocrystals: Synthesis, Solid-State NMR, and X-ray Diffraction

Shubha Gunaga

A thesis submitted to the University of Ottawa
in partial fulfillment of the requirements for the
Doctorate in Philosophy degree in Chemistry

Department of Chemistry and Biomolecular Sciences
Faculty of Science
University of Ottawa

Abstract

Supramolecular chemistry explores the use of intermolecular noncovalent bonds, focusing on entities formed by associating multiple chemical species to construct supramolecular assemblies. Among these bonds, the halogen bond (XB) has attracted significant interest for its role in shaping these assemblies. The presence of the σ-hole positioned opposite to a C-X covalent bond (X most commonly being I, Br, or Cl) endows the halogen bond with exceptional directional and tunable properties. This feature appeals to crystal engineers aiming for precise control in molecular assemblies. Advances in the areas of crystal engineering and crystal structure prediction have paved the pathway for innovative applications harnessing halogen bonding. These applications span diverse fields such as catalysis, liquid crystals, drug delivery, protein-ligand complexes, pharmaceutical science, functional materials, molecular gyroscopes, and dynamics involved in these different systems, showcasing the vast potential of exploiting the halogen bonding. Dynamics, with its ubiquitous presence in nature has long captivated researchers driving their pursuit to understand and decipher the intricate rate of reactions unravelling the complexities of chemical kinetics and gain insights into how reactions occur at the molecular level. Dynamic processes play a crucial role in dictating the functionality of various materials.

This thesis examines the halogen bond, its nature, its role in supramolecular assembly, and impact on molecular dynamics. We also explore synthetic methods for materials dependent on this interaction, and investigate the modulation of methyl rotational dynamics, shedding light on the influence of noncovalent halogen bonds in these dynamics. Our exploration commences with the design and synthesis of a novel series of cocrystalline architectures incorporating halogen bonds to deuterated tetramethylpyrazine (TMP) utilizing gas phase, solution, and solid state mechanochemical methods. Powder X-ray diffraction methods are used to confirm the

phase purity of these samples. We have successfully solved the single crystal X-ray structures of this novel series featuring a cocrystal involving molecular bromine as well as weak chloro halogen bond (XB) donors, which serve as strong directional structural directing elements. We have made use of static deuterium solid-state NMR experiments over a wide range of temperatures to measure T_1 time constants and then calculated the rotational barrier of methyl groups located near the halogen bond. The experimentally determined methyl rotational activation energy (E_a) for the range of halogen bonded cocrystals, when compared to the halogen bond acceptor reference molecule, reveals a significant reduction in the energy barrier upon the introduction of the halogen bond. Computational studies employing linear transit calculations have shown that electronic factors significantly influence the E_a calculated for the XB systems examined here. Furthermore, careful consideration of satellite atoms positioned around the methyl groups also impacts E_a, by acting as a steric factor. Our meticulous examination of the average number of carbon-carbon close contacts to the methyl group, a pivotal steric factor, has rationalized the observed trends in the chloro-, bromo- and iodo- XB series. This finding offers an excellent approach to potentially understanding and controlling the dynamics in molecular machines, supramolecular catalysts, and biochemical systems. By modulating the number of carbon-carbon close contacts by altering the stoichiometry of designed cocrystal synthons while maintaining the core chemical features, new opportunities to design complex geared or cascade dynamics involving larger functional groups found in e.g., metal-organic frameworks, engineered rotors, protein and enzymes are created.

The role of the halogen bond in crystal engineering was then further explored. We report another novel cocrystal of 2,3,5,6-tetramethylpyrazine and 1,3,4,5-tetrabromo-2,6-difluorobenzene showcasing type II halogen bonding. We have studied the structural features of this system using single crystal X-ray diffraction and computations. Infinite chains of approximately coplanar donor and acceptor molecules are held by Br···N halogen bonds and

bromine in positions 3 and 5 of the halogen bond donor molecule acts simultaneously as a halogen bond donor and acceptor. This results in a herringbone arrangement of the infinite chains influenced by crystal packing; halogen bond strength and pedal motion ability suggests potential for greater thermal expansion. The findings underscore the significance of developing novel aromatic-based solids specifically crafted for electronic applications.

Dedication

"Dedicated to my amma (mother, Mrs. Nirmala Gunaga), pappa (father, Mr. Shridhar Gunaga), late grandparents and to the universe where I find my solace – the eternal bonds that have nurtured my path"

Acknowledgements

In a world where unity prevails and connections bind us all, I reflect on the culmination of my academic journey with a profound belief in the timeless adage, 'The world is one family.' With this ethos guiding my endeavors, I extend my sincerest appreciation to all who have contributed, both directly and indirectly, to the completion of this thesis. Your unwavering support and invaluable assistance have been pivotal in shaping this scholarly pursuit, and for that, I am truly grateful.

I believe it was only because of Dave and his work that I was encouraged to come to Ottawa and embark on my brand-new journey called a PhD in solid-state NMR. Dave's passion for solid-state NMR, discipline in meeting deadlines and his unwavering patience towards his students in every situation are qualities I cannot stop praising. I am still striving to emulate these qualities, Dave, and they continue to inspire me. I am grateful to you, Dave, for believing in me, even as someone who began their journey in solid-state NMR without prior experience in NMR, and for having me figure out the dynamics project. These challenges have strengthened me and transformed me into a more independent researcher, a trait I carry forward into my next endeavor. Fond memories, such as my first-ever experience with snow sports - skiing and group activities like “secret Santa”, gathering at Sir John A pub, and barbeques at Dave's house, have added a memorable dimension to my PhD journey. Additionally, the conferences and workshops Dave sent me to have been invaluable in expanding my network and deepening my understanding of science. Dave, I am profoundly thankful to you for your support and mentorship throughout my journey.

Prof. Guru Row (IISc, Bengaluru), your unwavering support and encouragement ignited my passion for solid-state chemistry and opened the door to the fascinating world of crystallography. Your steadfast belief in my potential, even during my most challenging times, empowered me to pursue my dream, PhD. I am deeply grateful for your guidance, which has been invaluable to my academic journey. Thank you for being my guiding light, providing both financial and moral support, including arranging my flights to Ottawa while I was enjoying my tea at Café Prakruthi. I vividly remember your call, asking me, "Don't you want to book your tickets for Ottawa?!" I extend heartfelt appreciation to Lata Ma'am for her enduring motherly care. I am fortunate to have crossed paths with you both!

Dr. Glenn Facey, your presence has been pivotal in shaping my journey as a student of NMR. I cannot forget the day when, as a novice, I found myself in a precarious situation during a variable temperature experiment, and you rushed to my aid, when I was holding the hose filled with liquid nitrogen that was about to explode. Your swift action and guidance not only averted a potential disaster but also instilled in me a sense of security and confidence. I cherish the moments spent in your class, where you patiently taught us how to navigate NMR software from the basics, and your insightful questions challenged us to think critically. Your dedication to providing resources, including your invaluable NMR blog, coupled with your caring demeanor and occasional reprimands, have left a lasting impact on me. Above all, it is your unwavering discipline, love for the subject, and profound knowledge of NMR that continue to inspire me.

Dr. Peter Pallister, I often sought your guidance amidst numerous questions and frustrations understanding SSNMR. Your patient explanations helped us grasp the details of basic NMR experiments, pulse sequences, and experiment setups. I deeply appreciate your invaluable assistance and constant availability. Thank you for patiently listening to our doubts and concerns. I'm happy that you are still just an email away to help us clear our NMR doubts.

Dr. Patrick M. J. Szell, as our senior, you provided invaluable assistance by helping us find accommodation in this new land. I recall our Skype call before joining the group, where you generously guided me through the research conducted in the Bryce group. Although our time in graduate studies did not overlap, I received the baton of overlapping research project to carry forward. Your support in understanding the project, and later as our NMR manager at uOttawa, where you continued to aid in NMR projects, is deeply appreciated.

Dr. Jeffrey Ovens, I extend my heartfelt gratitude to you for your unwavering assistance whenever I encountered challenges with my X-ray data. You patiently reviewed my previously learned concepts and aided me in solving issues with disordered crystals and low-quality data. Your consistent availability ensured timely acquisition of crystal data and results, especially when reviewers required quick turnarounds. Thank you immensely for your invaluable support and guidance.

Tamali, we both embarked on our PhD journey together, from finding places to live to getting groceries done, attending conferences, indulging in favorite foods, and being crazy lab mates and flatmates. Since 2019, we have stood by each other through every high and low of our lives. Despite your occasional craziness, when I’m stressed you turn into a wise big bro faster than one can say "woah!"! I'm grateful for your help in teaching me to create ESP maps from scratch and for your enthusiasm in trip planning. My ultimate memory? Easy: our escapades in Banff and Niagara take the cake! But let's not forget the Irish pub in Colorado post-Rocky Mountains, where altitude changed the attitude!

Thank you Vince, the first friend we made here, for always being the go-to person whenever I needed help. Also, grateful for the first French words you taught me! Thank you, Vijith, for all the support and help throughout. Kirill and Tristan, I'm truly grateful for the opportunity to have met you in the Bryce Lab when you both joined as postdocs. Your unwavering support and assistance have been invaluable to me. Tristan, I deeply admire your perseverance and hard work; it serves as an inspiring example for all of us to follow. I extend my heartfelt thanks to Vova for his invaluable assistance as the NMR technician at uOttawa.

My sincere gratitude to all the past and present members of the Bryce Lab community. Collette, your patient interactions and unwavering support, even after graduating, have been invaluable to me. Scott, I am thankful for your prompt and detailed responses to my email inquiries. Christelle, our time together as lab mates and good friends was truly memorable. Ali, wishing you all the best for your PhD journey!

I'm delighted to have crossed paths with some amazing undergraduates here in the Bryce Lab. Theo, my dear 'baby brother,' I can't thank you enough for your technical support and I adore the unique way you address me as 'shoobidobidoo.' I wish you all the success in your journey to becoming a medical doctor. Janice, your discipline and hard work are truly commendable, and I have no doubt they will lead you to great achievements in life. Here's to wishing you both the very best. Ella, Carina, Matthew, Ezana, Sachin, Audrey-Anne, Mahee, Manon, Roberta, Grace, Elizabeth thank you all, and best of luck in your future endeavors.

I extend my heartfelt gratitude to the University of Ottawa for granting me the opportunity to pursue my doctoral studies in the Department of Chemistry and Biomolecular Science. I am grateful for the exceptional facilities, high-class research programs, diverse ambiance, and excellent teachers and core facilities provided, which have been instrumental in conducting my research. I am grateful to the chemistry office staff and graduate office staff for their efforts in making administrative processes smoother and more manageable for us students. Your support has been invaluable. I want to express my special thanks to Chloé, Annette, Victoria, and Hajjar for supporting me throughout.

I extend my sincere gratitude to my TAC members, Prof. Darrin Richeson, Prof. Natalie Goto, and Prof. Javier Giorgi, for their invaluable suggestions and comments. Their guidance has propelled me to go the extra mile in writing my manuscripts and approaching research questions with a deeper understanding. Thank you, Dr. Richeson, for always listening to my concerns and engaging in discussions. Thank you, Dr. Goto, for pushing me to be clearer in stating my research. Thank you, Dr. Giorgi, for your interesting questions during my presentation. They all have greatly helped me.

I extend my heartfelt gratitude to all my teachers, from preschool to the present day, for believing in me. Thank you.

I express my gratitude to my younger brother Shashank for remaining with our family as I pursued my education outside our hometown since the 10th standard. Additionally, I extend my thanks to my cousins Chandan and Chaitra for patiently listening to my rants. I'm grateful to Pamma, Kusumakka, and Belagavi mama for their heartfelt well-wishes. I love you all. Suman, words cannot express how much I owe you. Thank you for helping me start afresh in life. Sampada, Vibha, and Seema, you have been incredible in my life. Sandeep, I'll always be grateful for your help when I needed to join a research lab. Manjunath Sunagar Sir, thank you for being supportive throughout my research journey.

Kartik and Rekha, I cannot put into words how much I cherish both of you. You have been my rocks, standing by me when no one else did and caring for me when I felt like giving up on everything. Thank you for your unwavering support and love. Our friendship means world to me.

Pramath and Mahesh, your constant support has been my anchor through thick and thin. I'm forever grateful for our friendship. Pramath, thank you for always being there when I needed you. Maheshaa, our endless conversations and life talks are invaluable to me. Here's to our friendship!

I extend my heartfelt thanks to my entire IISc A-mess bunch. Thank you to my Ottawa family away from home: Marcin, Chanjot, Neha, Piyas, Anindya da, Aprita di. Your presence has made my time here truly special.

Ottawa, you have my heart. Thank you for your kindness and love. Canada, you have been my cherished home for 4.7 years now. I'm grateful for you!

I'm appreciative of my younger self for envisioning a career in research during my school days, despite my lack of knowledge about how to pursue it.

Oh, how could I ever forget those relatives and so-called friends who scoffed at the idea of pursuing a BSc and insisted I should have chosen a "more lucrative" field? Thank you ever so much for guiding me down this path!

“In the tunnel's end, a shimmering light,

NMR echoes, revealing insight.”

Statement of Authenticity

I hereby certify that the results presented in this dissertation are my own efforts. All ideas and references to other work are fully acknowledged using scientific references. I acknowledge my PhD supervisor Prof. David L. Bryce for his guidance in the research project as well as being invaluable in editing, revising, and in helping me write the manuscripts. Permissions have been granted by the publisher to reproduce my original work in the thesis. The following chapters of this dissertation are based on work published in peer-reviewed journals.

Chapter 4: Gunaga, S. S. and Bryce, D. L. Modulation of Rotational Dynamics in Halogen-Bonded Cocrystalline Solids, *J. Am. Chem. Soc.,* **2023***, 145,* 19005-19017.

Chapter 5: Gunaga, S. S. and Bryce, D. L. Type II Halogen-Halogen Contacts in the Single-Crystal X-ray Diffraction Structure of a 1:1 Halogen-Bonded Cocrystal of 2,3,5,6-Tetramethylpyrazine and 1,3,4,5-Tetrabromo-2,6-difluorobenzene, *J. Chem. Crystallogr.,* **2024**, *54*, 150-156.

Table of Contents

Abstract ii

Dedication v

Acknowledgements vi

Statement of Authenticity xii

Table of Contents xiii

List of Tables xix

List of Figures xxi

List of Abbreviations xxvii

List of Symbols xxx

Part 1: Objectives and Introduction 1

Objectives 1

Chapter 1 Introduction to Halogen bonding 4

- 1.1 Chemical bonding 4
  - 1.1.1 Halogen bond 7
    - 1.1.1.1 Origin of the halogen bond 8
  - 1.1.2 σ-hole interactions 11
  - 1.1.3 Definition of the halogen bond 13

1.1.4 Applications 17

1.1.4.1 Crystal Engineering 17
1.1.4.2 Biological applications 21
1.1.4.3 Functional materials 22
1.1.4.4 Solid state NMR insights into study of dynamics and halogen bonding 25

1.1 References 29

Chapter 2 General Introduction to NMR (Nuclear Magnetic Resonance) 38

2.1 The Zeeman interaction 39

2.2 Polarization 40

2.3 The basic NMR experiment 44

2.4 The Echo pulse sequences 45

2.5 NMR interactions 47

2.5.1 Magnetic Shielding (σ) and Chemical Shift Anisotropy (CSA) 47

2.5.2 Nuclear Quadrupolar Interaction 53

2.5.2.1 Deuterium 60

2.5.3 Direct Dipolar Coupling 64

2.5.4 Indirect Nuclear Spin-Spin Coupling 65

2.6 General Introduction to Relaxation in SSNMR 68

2.6.1 Spin-lattice relaxation or longitudinal relaxation (T_1) 70

2.6.1.1 Inversion Recovery Experiments: T_1 measurement 71

2.6.2 Spin-Spin Relaxation or Transverse Relaxation (T_2) 73

2.6.3 Relaxation and Rotational Dynamics 74

2.7 Mechanisms of Relaxation.. 76

2.7.1 The Dipolar Mechanism of Relaxation 77

2.7.2 Chemical Shift Anisotropy 78

2.7.3 Electric Quadrupole Relaxation.. 79

2.8 Effects of dynamics on ^{2}H line shapes and applications.. 81

2.9 References.. 84

Chapter 3 X-Ray Crystallography 91

3.1 Background on X-ray diffraction and its importance 91

3.2 Growing crystals: Methods in brief 92

3.3 Basics of X-ray crystallography... 93

3.3.1 Crystals and polycrystalline or powder samples 93

3.3.2 The unit cell and faces of a crystal 94

3.3.3 Crystal lattice, symmetry, space groups 95

3.3.4 Diffraction and Bragg's equation 97

3.4 Single crystal X-ray diffraction 99

3.5 Powder X-ray diffraction 100

3.6 Applications of X-ray diffraction data 101

3.7 References 104

Part 2: Modulation of Dynamics 108

Chapter 4 Modulation of Rotational Dynamics in Halogen-Bonded Cocrystalline Solids 108

4.1 Abstract 109

4.2 Introduction 110

4.3 Experimental 114

4.3.1 (i) Sample preparation 114

4.3.2 (ii) Single crystal X-ray diffraction 116

4.3.3 (iii) Mechanochemistry and powder X-ray diffraction 116

4.3.4 (iv) ^{2}H solid-state NMR spectroscopy 117

4.4 Results and Discussion 118

4.4.1 (i) Synthesis, X-ray diffraction, and description of crystal structures 118

4.4.2 (ii) Measurement of methyl rotational activation energies via ^{2}H NMR spectroscopy 123

4.4.3 (iii) Factors influencing methyl dynamics 130

4.5 Conclusions 139

4.6 Acknowledgements 141

4.7 References 142

Part 3: Cocrystal design and study 152

Chapter 5 Type II Halogen-Halogen Contacts in the Single-Crystal X-ray Diffraction Structure of a 1:1 Halogen-Bonded Cocrystal of 2,3,5,6-Tetramethylpyrazine and 1,3,4,5-Tetrabromo-2,6-difluorobenzene 152

5.1 Abstract 153

5.2 Graphical Abstract 154

5.3 Introduction 155

5.4 Experimental 156

5.4.1 (i) Synthesis 156

5.4.2 (ii) Single crystal X-ray diffraction 156

5.4.3 (iii) Computational details 157

5.5 Results and Discussion 157

5.6 Conclusions 167

5.7 References 168

Part 4: Final Conclusions 171

Overview 171

Challenges/limitations 173

Future directions 174

References 177

Appendices 179

Appendix 1: Chapter 4 Supporting Information 179

Appendix 2: Chapter 5 Supporting Information 229

Appendix 3: Contributions by Shubha S. Gunaga and conference presentations, participation 231

List of Tables

Table 4.1. Selected crystallographic and halogen bond geometrical parameters for the compounds studied herein. 122

Table 4.2. Experimental activation energies for methyl rotation, and computed molecular electrostatic potential maxima, in a series of halogen-bonded cocrystals of 2,3,5,6-tetramethylpyrazine (TMP) 129

Table 4.3. Void volumes. 132

Table 4.4. Average number of carbon-carbon contacts to methyl groups[a] 136

Table 5.1. Single crystal data and structure refinement for 1 (2,3,5,6-tetramethylpyrazine 1,3,4,5-tetrabromo-2,6-difluorobenzene (1:1 cocrystal)) 157

Table 5.2. Selected distances (Å) and angles (°) in cocrystal 1. 160

Table 5.3. Halogen bond distances and angles in 1. 162

Table S 1. Single crystal data and structure refinement for 1,4-dibromotetrafluorobenzene·2,3,5,6-tetramethylpyrazine (1) 179

Table S 2. Single crystal data and structure refinement for 1,3,5-tribromo-2,4,6-trifluorobenzene·2,3,5,6-tetramethylpyrazine (2). 180

Table S 3. Single crystal data and structure refinement for bromine·2,3,5,6-tetramethylpyrazine (3). 181

Table S 4. Single crystal data and structure refinement for 1,4-dichlorotetrafluorobenzene·2,3,5,6-tetramethylpyrazine (4). 182

Table S 5. Single crystal data and structure refinement for 1,3,5-trichloro-2,4,6-trifluorobenzene·2,3,5,6-tetramethylpyrazine (5). 184

Table S 6. T_1 and Effective Quadrupolar Data for Cocrystal (1) 221

Table S 7. T_1 and Effective Quadrupolar Data for Cocrystal (2) 221

Table S 8. T_1 and Effective Quadrupolar Data for Cocrystal (3) 222

Table S 9. T_1 and Effective Quadrupolar Data for Cocrystal (4) 222

Table S 10. T_1 and Effective Quadrupolar Data for Cocrystal (5) 223

Table S 11. Linear fits of lnT_1 vs 1/T data 223

Table S 12. Void volumes 223

Table S 13. DFT computed activation energies from linear transit calculations 224

Table S 14. Average effective π bond order^b 225

Table S 15. Single crystal X-ray data and structure refinement details for 1,3,4,5-tetrabromo-2,6-difluorobenzene 230

List of Figures

Figure 1.1. Pictorial depiction of orbital overlap in ethylene molecule to show sigma bond (linear overlap of atomic orbitals showed in green) and pi bond (sideways overlap of atomic orbitals showed in blue); sp^2 hybridized orbitals from each carbon overlap to form a sigma bond and unhybridized 2p orbitals (shown in light pink) of each carbon overlap to form a π bond............. 5

Figure 1.2. Molecular electrostatic potential map of Br_2 prepared using Gaussian '09 (B3LYP/3-21G; contour radius 0.001); electron depleted region is shown in blue (σ-hole) along the covalent bond and higher electron density region is shown in red orthogonal to the covalently bonded Br_2. 9

Figure 1.3. The DFT calculated electrostatic potential at the 0.001 a.u. isodensity surface of (a) trifluoroiodomethane, (b) bromotrifluoromethane, (c) chlorotrifluoromethane, (d) carbon tetrafluoride. Blue shows more electropositive region highlighting the sigma hole and red indicates more electronegative regions in the molecule. The calculations were performed using B3LYP with 3-21G basis set for (a) and 6-31G basis set for (b), (c), and (d). 12

Figure 1.4. Schematic representation halogen bond interaction. X = I, Br, Cl, F. R is electron withdrawing moiety. Y is electron rich species. 14

Figure 1.5. Single crystal structures showing the one-dimensional chain in halogen bonded systems. (a) linear homomeric chain formed by self-assembly of 4-iodo-2,3,5,6-fluorobenzonitrile (CSD ref code: ACOKIM). (b) linear heteromeric chain formed by self-assembly of 4,4'-dipyridyl-N,N'-dioxide and 1,4-diiodotetrafluorobenzene (CSD ref code: IKUHUR) (c) one dimensional stepped chain formed by self assembky of 4,4'-dipyridyl and 1,6-diiodododecafluorohexane (CSD ref code: QANRUS) (d) Infinite zig-zag infinite chains formed by bis(2-bromo)imidazoleboronium chloride.THF (CSD ref code: IKUXER) 18

Figure 1.6. Two-dimensional crystal structures: (a) two-dimensional flat network formed by Cl_2 (CSD ref code: YATKIP) (b) Honeycomb like crystal structure obtained by cocrystallizing potassium iodide and K.2.2.2 with 1,8-diodoperfluorobenzene (CSD ref code: TEHRAA). 20

Figure 2.1. Zeeman splitting for nuclei in the presence of an external magnetic field B_0........... 39

Figure 2.2. Precession of nuclei with magnetogyric ratio γ at Larmor frequency (ω_0) in the external field B_0. 41

Figure 2.3. Detection of the free induction decay in the *xy*-plane. 43

Figure 2.4. Pulse sequence for the pulse-acquire NMR experiment and evolution of the bulk magnetization M_0 during the acquisition time 44

Figure 2.5. Schematic representation of vector diagram (top) and pulse sequence for the Hahn echo. 46

Figure 2.6. Simulated ^{31}P solid-state NMR spectra of a stationary powder (without spinning at magic angle 54.74°) at 9.4 T magnetic field strength. The powder pattern is broadened due to chemical shift anisotropy. The principal values of the chemical shift tensor are illustrated along with the asymmetry parameter (skew, κ) values. 52

Figure 2.7. Illustration of quadrupolar nuclei based on distribution of electric field gradient (EFG) around the nucleus. (a) prolate shape ellipsoid (b) oblate shape ellipsoid.................................. 53

Figure 2.8. EFG tensor view as an ellipsoid surrounding a nucleus with 3 principal components along 3 major axes. 55

Figure 2.9. Simulated ^{2}H line shape illustration when $\eta = 0$, $\eta = 0.33$, $\eta = 1$. 56

Figure 2.10. Depiction the effect of 1st and 2nd order quadrupolar effects on the Zeeman energy levels in spin 3/2 quadrupolar nuclei. 59

Figure 2.11. Energy levels for an $I = 1$ nucleus. 61

Figure 2.12. ^{2}H line shape showing a powder averaged Pake doublet with $\Delta V_{XX} = \Delta V_{YY}$. The doublet pattern is due to the allowed spin transitions. 63

Figure 2.13. Pulse sequence for the inversion recovery experiment to measure the longitudinal relaxation time constant, T_1.. 71

Figure 3.1. Illustration of basic symmetry operations. 95

Figure 3.2. Depiction of 7 types of crystal systems with corresponding cell parameters to distinguish them. 96

Figure 3.3. Illustration of Bragg's law: Diffraction of X-rays from the lattice plane. 97

Figure 3.4. Depiction of array of two type of atoms in a crystal and each array separately satisfies the Bragg equation. The amplitude of the diffracted wave depends on the number of electrons in the two atoms here and the angle, θ. This produces different intensities of diffraction spots for the two atoms in consideration. 98

Figure 4.1. Key concepts explored in this work. Left: Molecular electrostatic potential surface of one of the halogen bond donors used herein, 1,3,5-tribromo-2,4,6-trifluorobenzene, with the σ-hole on bromine indicated (blue). Right: 2,3,5,6-tetramethylpyrazine, the halogen bond acceptor. The halogen bond is indicated in purple. The possible role of steric clashes (brown), both with the halogen bond donor and with atoms in the extended crystal lattice, in determining the barrier to pseudo-C3 rotation (red) of the deuterated methyl groups, is depicted. 113

Figure 4.2. Depiction of halogen bonds in the single crystal structures (this work) and molecular structures of five halogen-bonded cocrystals. Pure TMP (6) is also shown. The dashed light pink lines represent halogen bonds. Carbon: grey; fluorine: yellow; chlorine: green; nitrogen: blue; hydrogen/deuterium: white; bromine: orange. 114

Figure 4.3. Packing motifs obtained from single-crystal X-ray diffraction studies of cocrystals 1, 2, 3, 4, 5, and pure TMP (6). Halogen bonds are depicted with dashed lines. Carbon: grey; hydrogen/deuterium: white; nitrogen: blue; bromine: orange; yellow: fluorine; green: chlorine. 122

Figure 4.4. Experimental (bottom) and simulated (top) powder X-ray diffractograms of the 1,4-dibromotetrafluorobenzene·TMP cocrystal (cocrystal 1). A partially resolved peak splitting near 2θ = 16° in the simulated diffractogram appears as an unresolved asymmetric broadening in the experimental pattern.. 123

Figure 4.5. Experimental and simulated deuterium quadrupolar echo line shapes for compounds 1 to 6 at room temperature (296 ± 3 K; left) and low temperature (147 ± 3 K; right). These errors represent the small range in temperatures over which the data were acquired for different samples rather than the uncertainty in the temperature measurement. 125

Figure 4.6. Inversion-recovery ^{2}H NMR measurement of $T_1(^2H)$ for cocrystal 3 at 296.1 K. Experimental data are shown in black and the best fit is shown in red. Data were fit to I[t]=I[∞](1-2Aexp(-t/T_1)). 126

Figure 4.7. Arrhenius plot of ln$T_1(^2H)$ vs 1/T for compounds 1 to 6. 128

Figure 4.8. (a) The 1,4-diiodotetrafluorobenzene·TMP cocrystal (which has the lowest methyl rotational barrier among the compounds discussed in this work) has an average of 1.5 close contacts between the methyl carbons and any other carbons in the crystal structure. (b) The largest number of methyl-carbon contacts (marked with dashed red and turquoise lines) are noted for 1,4-dichlorotetrafluorobenzene·TMP (4), with an average of 3.75 contacts per methyl group. (c) The pure TMP molecule has an average of 3.00 contacts per methyl group. Contacts are defined here as carbon-carbon distances within the sum of the van der Waals' radii + 0.5 Å. 134

Figure 4.9. Plots of experimental methyl rotational barriers vs the average number of carbon close contacts. (a) Data for all cocrystals discussed in this work, plus TMP. $E_a = 1.3658N + 1.3634$; $R^2 = 0.5958$. (b) Data separated by the nature of the halogen bond donor: iodinated (red circles; $E_a = 0.5000N + 2.150$; $R^2 = 0.9586$); brominated (blue squares; $E_a = 0.8657N + 2.889$; $R^2 = 0.9963$); chlorinated (black triangles; $E_a = 1.665N + 0.8386$; $R^2 = 1$). 137

Figure 5.1. (a) Asymmetric unit of 1 showing the one of the halogen bonds between 2,3,5,6-tetramethylpyrazine 1,3,4,5-tetrabromo-2,6-difluorobenzene (Br1···N3); (b) Crystal packing of 1 shown along the *c* axis. 159

Figure 5.2. Halogen bond network in 1, with bromine-nitrogen and bromine-bromine distances indicated. Inset: geometry of the type II bromine-bromine contact. 162

Figure 5.3. (a) Experimental powder X-ray diffractogram acquired for the as-received product from Sigma-Aldrich. (b) Simulated PXRD data based on the cif file of 1,3,4,5-tetrabromo-2,6-

difluorobenzene (CCDC 2328690). (c) Simulated PXRD data based on the structure of 1,3,5-tribromo-2,4,6-trifluorobenzene.[29] (d) Unit cell viewed along the *b*-axis from the single-crystal X-ray structure of 1,3,4,5-tetrabromo-2,6-difluorobenzene (CCDC deposition number 2328690) determined in this work (see Supporting Information for further details on this structure). 164

Figure 5.4. (a) Computed molecular electrostatic potential surface of 1,3,4,5-tetrabromo-2,6-difluorobenzene (B3LYP/6-311+G*; 0.0004 a.u isosurface.). Areas in blue show elevated electrostatic potential while areas in yellow-orange show areas of depleted electrostatic potential. (b) Hirshfeld d_{norm} surface of 1. Areas in red depict close contacts. 165

Figure 5.5. (a) Hirshfeld fingerprint plot for 1; (b) Br-Br contacts highlighted; (c) Br-N contacts highlighted. 166

Figure S 1. Packing diagram of 1,4-dibromotetrafluorobenzene·2,3,5,6-tetramethylpyrazine (1). 185

Figure S 2. Packing diagram of 1,4-dibromotetrafluorobenzene·2,3,5,6-tetramethylpyrazine (1). 185

Figure S 3. Packing diagram of 1,3,5-tribromo-2,4,6-trifluorobenzene·2,3,5,6-tetramethylpyrazine 186

Figure S 4. Packing diagram of 1,3,5-tribromo-2,4,6-trifluorobenzene·2,3,5,6-tetramethylpyrazine (2). 186

Figure S 5. Packing diagram of Br_2·2,3,5,6-tetramethylpyrazine (3) 187

Figure S 6. Packing diagram of 1,4-dichlorotetrafluorobenzene·2,3,5,6-tetramethylpyrazine (4). 187

Figure S 7. Packing diagram of 1,4-dichlorotetrafluorobenzene·2,3,5,6-tetramethylpyrazine (4). 188

Figure S 8. Packing diagram of 1,3,5-trichloro2,4,6-trifluorobenzene·2,3,5,6-tetramethylpyrazine (5). 188

Figure S 9. Packing diagram of 1,3,5-trichloro-2,4,6-trifluorobenzene·2,3,5,6-tetramethylpyrazine (5). 189

Figure S 10. PXRD for 1,4-dibromotetrafluorobenzene·2,3,5,6-tetramethylpyrazine (1). 190

Figure S 11. PXRD of 1,3,5-tribromo-2,4,6-trifluorobenzene·2,3,5,6-tetramethylpyrazine (2). 190

Figure S 12. PXRD of 1,4-dichlorotetrafluorobenzene·2,3,5,6-tetramethylpyrazine (4). 191

Figure S 13. PXRD of 1,3,5-trichloro-2,4,6-trifluorobenzene·2,3,5,6-tetramethylpyrazine (5). 191

Figure S 14. Plot of DFT calculated vs experimental activation energies for methyl rotation in compounds 1 to 6 plus I_2.TMP. E_a(calc) = 0.3051 x E_a(expt) + 1.6924. R^2=0.6024. 224

Figure S 15. DFT-computed linear transit calculations of rotational energy barriers in compounds 1-6 plus I_2·TMP. 225

Figure S 16. Lack of correlation between experimental activation energies and π bond order.. 226

Figure S 17. Rotational activation energy does not correlate universally with the molecular electrostatic potential maximum at the σ-hole. 226

Figure S 18. Rotational activation energy does not correlate universally with the reduced distance parameter associated with the halogen bond. 227

Figure S 19. Orange Br_2·TMP cocrystals (3) obtained using a cosublimation furnace. 228

List of Abbreviations

a.u.	atomic units
ADF	Amsterdam Density functional
B3LYP	Becke-3-parameter Lee Yang Parr
CCD	charge-coupled device
CCDC	Cambridge Crystallographic Data Centre
CIF	Crystallographic Information File
CS	Chemical Shift
CSA	chemical shift anisotropy
CSD	Cambridge Structural Database
CT	central transition
DFT	density functional theory
DSO	diamagnetic spin orbital
EFG	electric field gradient
FC	fermi contact
FID	free induction decay

HB	hydrogen bond
ISXB	International Symposium on Halogen Bonding
IUCR	International Union of Crystallography
IUPAC	International Union of Pure and Applied Chemistry
LDA	local density approximation
MAS	magic angle spinning
MEP	molecular electrostatic potential
MOF	metal organic framework
NMR	nuclear magnetic resonance
ORTEP	Oak Ridge Thermal-Ellipsoid Plot Program
PAS	principal axis system
PDB	Protein Data Bank
ppm	parts per million
PRESO	polarization transfer to quadrupolar nuclei
PSO	paramagnetic spin orbital
PXRD	powder X-ray diffraction

RAM	resonant acoustic mixing
REDOR	rotational-echo double resonance
RF	radiofrequency
RT	room temperature
SAPT	symmetry-adapted perturbation theory
SSNMR	solid-state nuclear magnetic resonance
ST	satellite transition
TEDOR	transferred-rotational-echo double resonance
TZ2P	triple-zeta basis set with two polarization functions
UV	ultra-violet
VDLIT	variable delay list
XB	halogen bond

List of Symbols

$\hat{H}$	general Hamiltonian operator
$\widehat{H_Q}$	quadrupolar interaction Hamiltonian
$\widehat{H_Q^{(1)}}$	first order quadrupolar interaction Hamiltonian
$\widehat{H_Z}$	Zeeman interaction Hamiltonian
$\widehat{H_\sigma}$	magnetic shielding Hamiltonian
$\hat{I}, \widehat{I_x}, \widehat{I_y}, \widehat{I_z}$	angular momentum operator
ΔJ	anisotropy of J coupling tensor
$\Delta\delta$	chemical shift difference
$\Delta \nu$	difference in the splitting
a,b,c	unit cell dimensions
B_0	magnetic field strength
B_0	magnetic field vector
B_1	radiofrequency magnetic field strength
C_Q	quadrupolar coupling constant

D	dipolar coupling interaction
D	dipolar coupling tensor
d	perpendicular spacing between the lattice planes in the crystal
ΣdvdW	sum of van der Waals radii
d_{X---Y}	distance between halogen bond donor and acceptor
e	fundamental charge
F_0	observed structure factor amplitudes
F_c	calculated structure factor amplitudes
h	Planck's constant (6.626077 x 10^{-34}J.s)
h	reduced Planck's constant
I	spin quantum number
I	spin angular momentum
J_{11}, J_{22}, J_{33}	principal component of the *J* coupling tensor
J_{iso}	isotropic *J* coupling constant
k	Boltzmann constant (1.3806 x 10^{-23} J.K^{-1})
k	rate constant

m	magnetic angular momentum
M	bulk magnetization vector
M_x, M_y, M_z	net magnetization along x, y, z axes
N, N	Boltzmann population at lower and higher energy states
$n\lambda$	path difference
Q	nuclear quadrupolar coupling constant
Q_{11}, Q_{22}, Q_{33}	principal components of the quadrupolar tensor
Q_{xx}, Q_{yy}, Q_{zz}	Cartesian components of the quadrupolar tensor
r	internuclear distance
R	reliability index
R_{DD}	dipolar coupling constant
R_{XB}	normalized distance parameter
T_1	spin-lattice or longitudinal relaxation time constant
$T_{1\rho}$	spin-lattice relaxation in the rotating frame
T_2	spin-spin or transverse relaxation time constant
V	electric field gradient tensor

V(r)	electrostatic potential
V_{11}, V_{22}, V_{33}	principal components of the EFG tensor
$V_{\mathrm{S,\ max}}$	maximum electrostatic potential
V_{xx}, V_{yy}, V_{zz}	Cartesian components of the EFG tensor
α,β,γ	Euler angles
γ	magnetogyric ratio
$\delta_{11},,\delta_{22},\delta_{33}$	principal components of the chemical shift tensor
δ_{iso}	isotropic chemical shift
η	asymmetry parameter
θ,ϕ	polar angles
$\theta_{\mathrm{R\text{-}X\text{---}Y}}$	R-X---Y halogen bond angle
κ	chemical shift tensor skew
λ	wavelength
μ	magnetic moment
μ_0	permeability constant
ν_0	Larmor frequency in Hz

ν_{DD}	dipolar splitting constant
σ	magnetic shielding
$\sigma_{11}, \sigma_{22}, \sigma_{33}$	principal components of the magnetic field tensor
$\sigma_{xx}, \sigma_{yy}, \sigma_{zz}$	Cartesian components of the magnetic field tensor
τ_c	correlation time
Ω	chemical shift tensor span
ω_0	Larmor frequency in rad.s^{-1}

Part 1: Objectives and Introduction

Objectives

This dissertation aims to explore halogen bonding, focusing on its impact on structure and on rotational dynamics within halogen-bonded cocrystals. The overall objective entails elucidating the underlying factors contributing to rotational barriers in these cocrystals through the strategic design of novel structures via crystal engineering methodologies. The investigation utilizes solid-state NMR and X-ray crystallography for a comprehensive study.

Halogen bonds represent a class of noncovalent interactions that play pivotal roles in various research fields including crystal engineering, functional materials, molecular machines, pharmaceutical compounds, organocatalysis, and biological molecules, etc. These bonds involve the noncovalent interaction between the electrophilic region of the halogen atom and an electron donor. Known for its highly directional and tunable properties, the halogen bond finds utility across diverse research domains. Chapter 1 serves as an introductory exploration of chemical bonds, encompassing various types to provide fundamental understanding. The focus then shifts to a detailed examination of halogen bonding, thoroughly exploring its origin and applications. The chapter further elucidates this noncovalent interaction, drawing examples from relevant literature to illustrate its significance.

In Chapter 2, the thesis delves into the versatile utility of nuclear magnetic resonance (NMR) spectroscopy as a robust characterization tool applicable to both solutions and solids. The orientation dependent nature of many NMR interactions in the solid state is highlighted, offering valuable insights into the local electronic structure, particularly in halogen bonded cocrystals.

Acknowledging the ubiquitous role of dynamic processes in nature, this chapter emphasizes their diverse functionalities in biomolecules, materials and catalysis. The modulation of various systems is explored to achieve desired material properties, with numerous ongoing efforts in progress. Chapter 2 not only outlines the fundamentals of solid-state NMR but also elucidates relevant results for halogen-bonded systems within the thesis. It further addresses solid-state NMR relaxation mechanisms broadly, focussing on relaxation of quadrupolar deuterium nuclei and line shape analysis to discern structural and dynamic features in various systems, including halogen bonded cocrystals.

In Chapter 3, the thesis underscores the significance of X-ray diffraction as a complementary technique for the exploration of newly synthesized compounds, offering valuable insights into interatomic interactions. This section briefly covers the fundamentals of X-ray diffraction and traces its evolution into a robust analytical tool in the contemporary era. The chapter further scrutinizes the diverse applications of X-ray diffraction in various systems, with a specific focus on its role in the investigation of halogen-bonded cocrystals. The combination of solid state NMR (SSNMR) and X-ray diffraction studies emerges as a potent approach, providing a comprehensive tool for the investigation of dynamics and noncovalent interactions within the solid state.

Part 2 specifically presents experimental evidence showcasing the use and applicability of crystal engineering in halogen bonded cocrystals, alongside the utilization of solid-state NMR and X-ray diffraction to characterize the novel synthesized cocrystals. Meticulous structural investigation lays the foundation for designing advanced materials in molecular gyroscopes and pedal motions involving electronic applications, which are current active research topics. Chapter 4 expounds on systematic studies on the modulation of methyl dynamics in halogen bonded cocrystals. It explores the synthesis of halogen bonded cocrystals using varied techniques, measures methyl rotational barriers via variable-temperature deuterium solid-state NMR, and analyzes crystal packing and void volume. A key finding rationalizes activation energy trends using carbon-carbon close contacts and offering insights into complex system dynamics. Chapter 5 highlights a cocrystal composed of rare brominated halogen bond donor and tetramethylpyrazine acceptor, exemplifying type II halogen bonding and molecular self assembly. Single crystal X-ray diffraction and computational studies validate these observations.

Chapter 1 Introduction to Halogen bonding

1.1 Chemical bonding

Chemical bonding was first identified as an interaction of atoms; later, it was recognized that electrons play a key role in the formation of bonds. There are several observable patterns in the physical and chemical properties of elements as we descend in a group or move across a period in the periodic table. A group or family of the elements in a vertical column of the Periodic Table exhibit similar chemical behaviour. This similarity is because they have the same number and distribution of electrons in their outermost orbitals. Thus, the elements are classified into four blocks called s-block, p-block, d-block and f-block depending on the type of atomic orbitals that are being filled with electrons. The horizontal rows are called periods. The period number is assigned based on the highest principal quantum number (n) of the elements in the period. Metallic character and reactivity increase as we go down a given group, and the non-metallic character increases as one goes from left to right across the Periodic Table. The attractive force which holds various species (atoms, ions, etc.) together is called a chemical bond. It becomes important to understand these interactions to understand the structure of the molecules.

There are diverse types of bonds that are defined to explain interactions observed in chemical compounds. The complete transfer of valence electrons from one atom to the other results in an ionic bond. The transfer of electrons results in an electrostatic attraction between the two ions of opposite charge (cations and anions) and an ionic bond is formed[1] (like in $MgSO_4$, LiF, NH_4Cl). For elements with relatively high ionization energies it requires significant amount of energy to remove an electron, and elements of relatively low electron affinity cannot easily take up the electrons; rather they both share their electrons and thus acquire stability (examples include H_2,

C_2H_4, CO_2).[2] Depending on the number of electron pairs shared, the covalent bond can be stated as single (ex: alkanes), double (ex: alkenes) and triple covalent bonds (ex: alkynes). The sharing of electrons can be quantum mechanically expressed as an overlap of atomic orbitals, to create molecular orbitals. The sigma (σ) bond is formed when two x axes overlap linearly where the electron density is centred along the internuclear axis and when they overlap sideways along the *y* and *z* axes, generating pi (π) molecular orbitals having electron density on opposite sides of internuclear axis. The Figure 1.1 is the schematic depiction of atomic orbital overlap in ethylene (also known as ethene) molecule showing σ and π bond formation.

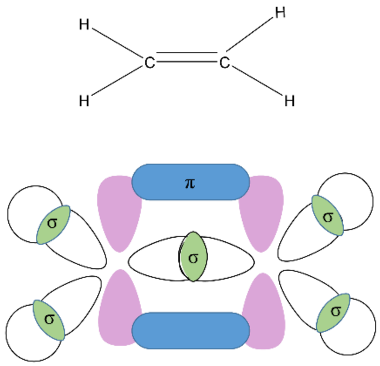

Figure 1.1. Pictorial depiction of orbital overlap in ethylene molecule to show sigma bond (linear overlap of atomic orbitals showed in green) and pi bond (sideways overlap of atomic orbitals showed in blue); sp^2 hybridized orbitals from each carbon overlap to form a sigma bond and unhybridized 2p orbitals (shown in light pink) of each carbon overlap to form a π bond.

Covalent bond strength increases with its order and hence the triple bond needs more energy to break the bond than does the double bond, and then comes the single bond. Also, as the bond order increases, the dissociation energy increases and the bond length decreases. A single C-C bond has a bond length of approximately 1.53 Å and a dissociation energy of 276 kJ/mol, the C=C double bond has a bond length of ~1.34 Å and a bond strength of 472 kJ/mol, and the triple C≡C bond has a length of ~1.20 Å and a bond dissociation energy of 628 kJ/mol.[2,3] Another type of bond which involves sharing of electron pair which is donated by the same atom is called a coordinate or dative bond.[4] Metallic bonding is the attraction between the cores of metal atoms (metal cations) and their delocalized valence electrons. The electron-sea model is a widely accepted explanation for metallic bonding. In this model, metal atoms contribute their valence electrons to form a "sea" of delocalized electrons that are free to move throughout the entire metal lattice. These delocalized electrons are not associated with any particular atom; instead, they are shared among all the metal atoms in the structure.

Chemical bonding is a huge area of study, while my thesis concentrates on intermolecular interactions. Molecules are brought together by another set of relatively weak non-covalent interactions.[5] The intermolecular forces involved in non-covalent interactions may include hydrogen bonding, dipole-dipole interactions, induced dipole interactions, and London dispersion forces. A comprehensive depiction of these interactions is important to understand the noncovalent interactions investigated in this thesis. Noncovalent interactions[5] are important for the three-dimensional secondary and tertiary structures in larger molecules such as proteins and other biomolecules. Non-covalent interactions involve attraction between two species with partial charge distributions.[6] An asymmetric electron density distribution in a molecule causes it to have partial negative charge (δ^-) on the more electronegative element and a partial positive charge (δ^+) on the less electronegative element. The attractive force between the partial positive charge on one molecule and partial negative charge on another molecule is called a dipole-dipole interaction. An ion or polar molecule may approach an atom or non-polar molecule and cause a temporary, weak, and induced dipole attraction by redistributing the arrangement of electrons in the atom or non-polar molecule. Such interactions are called ion-induced or dipole-induced forces. Dispersion forces are caused by momentary oscillations of electron charge in atoms, and hence present between atoms, ions, molecules.[7]

Hydrogen bonding[8] plays a crucial role in supramolecular chemistry as seen in the formation of hydrogels, to support the three-dimensional structure of DNA, proteins and biomolecules, and to supply stability to crystal structures. Hydrogen bonding is a special type of dipole-dipole interaction. It occurs between molecules where a hydrogen atom is bonded to a highly electronegative atom such as nitrogen, oxygen, or fluorine. The hydrogen bond definition goes as follows, "The hydrogen bond X-H---Y-Z is an attractive interaction in which an electropositive H atom intercedes between two electronegative species X and Y and brings them closer together".[9] The hydrogen bond strength can vary from 2 kJ/mol to 160 kJ/mol depending on the type of interaction.

Thus, noncovalent interactions are crucial for holding supramolecular assemblies together.[5] The study of these noncovalent interactions have led to better understanding of protein folding, drug-target interactions, as well as recent advances including their applications in materials science. One such noncovalent interaction involves halogen bonding. In our study, we have investigated halogen-bonded cocrystals and explored their applications in dynamics.

1.1.1 Halogen bond

Halogens make up the Group 17 elements in the periodic table (in Greek, *hals* meaning salt and *gennan* meaning to form, i.e., salt producers).[10] The group includes fluorine (F), chlorine (Cl), bromine (Br), iodine (I), astatine (At), and tennessine (Ts). They are not found in in their elemental forms in the nature. They can form negatively charged ions or homonuclear diatomic molecules. Fluoride and chloride are abundant in nature while bromide and iodide are less majorly found.

Fluorine[11] is 13th and chlorine[12] 21st most abundant element by weight in the earth's crust. Fluorine is mainly present in minerals in insoluble salts such as fluorspar (CaF_2), cryolite (NA_3AlF_6), and fluorapatite [$3Ca_3(PO_4)_2.CaF_2$], and small quantities are present in soil, bones. Chlorine is mainly found as NaCl salt (rock salt). Seawater has bromine and iodine salts of potassium, magnesium, sodium and calcium but is mostly NaCl (2.5% by mass). Astatine and Tennessine are radioactive elements of this group. Diatomic forms of the halogens, i.e., gases of F_2, Cl_2, are very toxic. Br_2 exists as liquid with an unpleasant choking odour, and I_2 is an intensely purple-coloured solid, which sublimes when heated. Fluorine is used in the manufacture of Teflon $(C_2F_4)_n$, which is generally inert to chemical reactions, and in freons (CCl_2F_2) which were used in refrigerators. Chlorine is used largely in chlorinated organic solvents such as chloroform ($CHCl_3$), carbon tetrachloride (CCl_4), and as a bleaching agent and germicide. Bromine finds its application in sedatives, fire retardants,[13] insecticides, etc. Iodine compounds are used in drugs,[14] dyes, and catalysts. Thus, the halogens have played a pivotal role in organic and inorganic chemistry. They can be equally utilized in non-covalent interactions to study their applications in crystal engineering, supramolecular chemistry.

1.1.1.1 Origin of the halogen bond

The electron density distribution in halogens is anisotropic by nature whenever they are bonded to other atoms.[15] When halogens are involved in a covalent bond, there is a higher electron density region corresponding to a negative electrostatic potential formed orthogonal to the covalent bond, and a lower electron density region corresponding to a positive electrostatic potential called a σ (sigma) hole. This is due to the depleted electron density that is generated from the elongation of the covalent bond. This electron-depleted region is used to interact with nucleophiles. Figure 1.2 depicts the molecular electrostatic potential map calculated at the 0.001 contour radius of Br_2 and extracted using Gaussian '09. This map highlights the electron-depleted region, indicated in blue, along the covalently bonded Br_2.

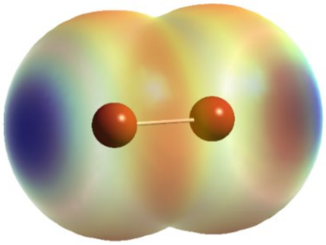

Figure 1.2. Molecular electrostatic potential map of Br_2 prepared using Gaussian ’09 (B3LYP/3-21G; contour radius 0.001); electron depleted region is shown in blue (σ-hole) along the covalent bond and higher electron density region is shown in red orthogonal to the covalently bonded Br_2.

Reports of I_2 complexed with Lewis base ammonia (NH_3) in 1814 by J.J. Colin started the story of halogen bonding[16] and this structure was identified as I_2---NH_3 by F. Guthrie in 1863 by preparing a pure sample. Bromine and iodine bonded complexes were reported in the 19th century by I. Remsen and J. F. Norris with amines.[17] 80 years later, a halogen bonded adduct of F_2 was found by isolating F_3^- in 1977.[18] More than a decade later, adducts F_2---NH_3 and F_2---OH_2 were made by Legon.[19] No halogen bonded adducts with astatine or tennessine are reported to date due to their short-lived isotopes.

The Nobel Prize in Chemistry in 1966 was won by R. Mulliken for work on the chemical bond using spectroscopic techniques and dipole moments in ground and excited states of dihalogen bonded complexes with benzene and other organics.[20,21] Hassel won the 1969 Nobel Prize[22] in part for describing the single crystal X-ray structure of the Br_2---$O(CH_2CH_2)_2O$ adduct[23] which was important in identifying intermolecular distances in halogen bonded species. The intermolecular distance found between bromine and oxygen was shorter than their respective van der Waals radii[24] and the Br---Br distance was found to be slightly elongated relative to pure Br_2 and Br-Br---O angle did not deviate much from 180°. These are distinctive features observed in a halogen bond. Similar adduct systems of Br_2 and Cl_2 in benzene were also reported by Hassel as continuous chains of benzene and dihalogen molecules.[25,26] These two structures were notably intriguing due to their demonstration of aromatic π systems functioning as electron density donors toward dihalogens and this study was also confirmed later by J. K. Kochi by studying different π-systems acting as electron density donors to the halocarbons.[27] Desiraju et al[28] confirmed the study of Bent's[29] in 1986 on the geometry of the halogen bonded system in terms of directionality as they found that interatomic distances of the halogen bond are shorter than the sum of the van der Waals radii of the two atoms involved and the angle is nearly 180˚. The halogen bond strength scales as per the halogen bond polarizability of halogen bond donor atom, i.e. I>Br>Cl>>F.[29] Fluorine only rarely acts as halogen bond donor as it is the least polarizable halogen atom. The polarizability of astatine is higher than that of iodine, and therefore exhibits halogen bonding stronger than iodine as reported in a computation study recently.[30]

There are numerous examples of halogen bonding applications in the field of supramolecular chemistry.[31,32] Halogenated derivatives act as lone pairs bearing species along with π-systems and anions to form aggregates. Halogens being the most electronegative elements in the periodic table, it was difficult for the scientific community to believe that they could act as electrophiles and form useful halogen bonds. In this regard, the contributions of Politzer and Murray[33,34] help to explain the anisotropic distribution of electron density when halogens are involved in covalent bonding, paving the way to understand the electronic reasons behind it. This work led to the concept of the σ-hole, or region of positive electrostatic potential, on the halogens.

1.1.2 σ-hole interactions

The σ (sigma) hole concept was introduced by Politzer,[35,36] who elucidated the role of halogen as an electrophile. Due to the position of halogens in the periodic table, they are considered to be electronegative elements. Consequently, covalently bonded halogens are regarded electron-withdrawing groups. When halogens are covalently bonded to an electron-withdrawing group, they experience an anisotropic distribution of charge, yielding an oblate spheroid shape.[35–37] This results a depletion of electron density on the surface of halogen, a positive electrostatic potential region opposite to the covalent bond,[38,39] named as σ (sigma hole).[35,36,39] This enables halogens to interact attractively or non-covalently with negative sites on the other molecules (σ hole bonding). The electrostatic potential at any point in the space of a molecule is given by the equation below:[36]

$$V(r) = \sum_A \frac{Z_A}{|R_A - r|} - \int \frac{\rho(r')dr'}{|r' - r|} \qquad \text{Eq. 1.1.2.1}$$

In Eq. 1.1.2.1, V(r) is the surface electrostatic potential, Z_A is the charge on the nucleus A, located at distance R_A, and $\rho(r)$ is the molecule's electron density. V(r) can be determined computationally or experimentally using diffraction techniques.[40] Examples of the σ-hole are depicted for various compounds in Figure 1.3:

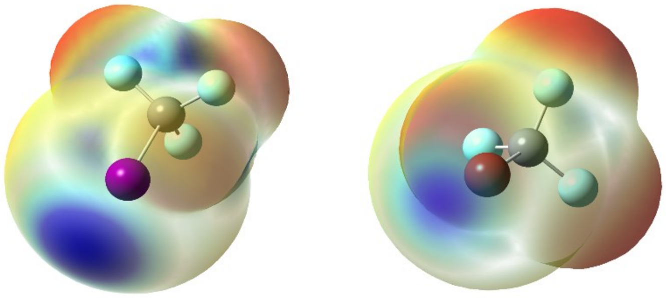

(a) CF_3I (b) CF_3Br

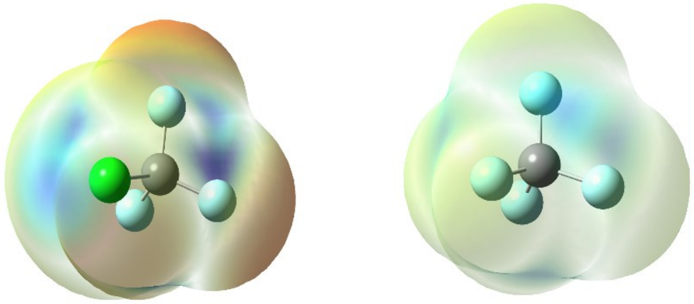

(c) CF_3Cl (d) CF_4

Figure 1.3. The DFT calculated electrostatic potential at the 0.001 a.u. isodensity surface of (a) trifluoroiodomethane, (b) bromotrifluoromethane, (c) chlorotrifluoromethane, (d) carbon tetrafluoride. Blue shows more electropositive region highlighting the sigma hole and red indicates more electronegative regions in the molecule. The calculations were performed using B3LYP with 3-21G basis set for (a) and 6-31G basis set for (b), (c), and (d).

The magnitude of the σ-hole is significantly influenced by the polarizability of electrons on the halogen. The larger halogens possess more polarizable electrons, resulting in the greatest σ –hole magnitude in the order of I>Br>Cl>>F.[36] Consequently, iodine and bromine demonstrate may possess a σ-hole. Conversely, chlorine typically exhibits a weak σ-hole, while fluorine seldom engages in halogen bonding.[41]

The engineering of the σ-hole offers several attractive features. Firstly, the addition of nearby electron withdrawing groups can amplify the magnitude of the σ-hole, thus enhancing the strength of interactions. Consequently, σ-hole based interactions can be tailored by manipulating the nearby substituents.[42] An example of this strategy involves incorporating fluorine atoms into the halogen bond donor, resulting in a fluorinated molecule that can form a robust halogen bond. Secondly, since the σ-hole is localized opposite to the covalent bond, it enables highly linear interactions with respect to the R-X bond axis.[43]

1.1.3 Definition of the halogen bond

There is a similarity between halogen bonding and hydrogen bonding with isostructural systems when the halogen/hydrogen bond acceptor involved in the interaction is the same. However, hydrogen bonds can be nonlinear, whereas halogen bonds are usually highly linear.[19,38] The IUPAC definition of the halogen bond states that a "halogen bond occurs when there is evidence of a net attractive force between an electrophilic region associated with a halogen atom in a molecular entity and a nucleophilic region in another, or the same, molecular entity".[44–46] As per this definition, a typical halogen bond is denoted as R−X···Y. R−X is the halogen bond donor where X is any halogen associated with the electron deficient R group[44,47] covalently bound to X. Y is another molecular entity with a nucleophilic site on it. R−X could be dihalogen molecules, haloalkanes, haloarenes, haloimides, etc. Y can typically be an anion, an atom with lone pair of electrons, or π systems. Figure 1.4 shows a schematic representation halogen bonding.

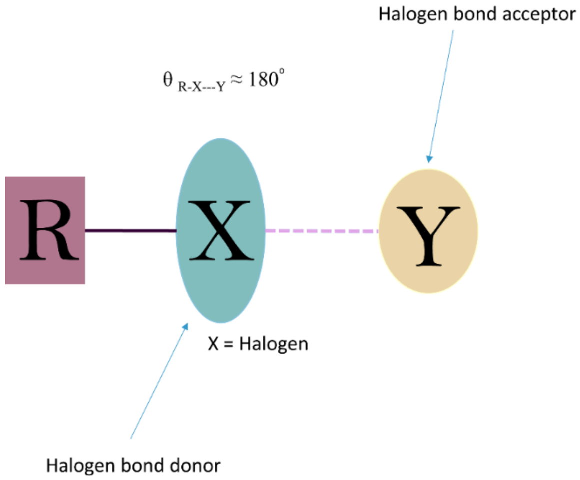

Figure 1.4. Schematic representation halogen bond interaction. X = I, Br, Cl, F. R is electron withdrawing moiety. Y is electron rich species.

Key geometric features of the halogen bond include: (1) The distance between halogen bond donor (X) and the nucleophilic atom (Y) tends to be less than the sum of the van der Waal's radii $(d_{X\cdots Y}) \leq (\sum d_{vdW})$; (2) The halogen bond angle $(\theta_{R-X\ldots Y})$ tends to approach 180°, typically between 150° to 180° favoring linearity. The halogen bond is measured quantitatively in terms of a reduced bond distance parameter, R_{XB}, defined as the ratio of the halogen bond length $(d_{X\cdots Y})$ to the sum of the van der Waals radii $(\sum d_{vdW})$ of the halogen bond donor and acceptor atoms involved in the bonding. A smaller value (less than 1) of R_{XB} therefore implies a shorter, stronger halogen bond. The equation for the reduced distance parameter is given below:

$$R_{XB} = \frac{d_{X\cdots Y}}{d_{vdW}} \qquad \text{Eq. 1.1.3.1}$$

In Eq. 1.1.3.1, R_{XB} is the reduced distance parameter, $d_{X\cdots Y}$ is the halogen bond length, and d_{vdW} is the van der Waals radii of atoms involved in halogen bonding. Although the R_{XB} values serves as a quantitative measurement, it does not necessarily reflect the strength of the halogen bond, as bond strength can be influenced by additional interactions such as stabilization by hydrogen bonding.

The σ-hole plays a pivotal role in the strength of the halogen bond and therefore, incorporating electron withdrawing groups and/or enhancing the polarizability of the halogen atom itself can strengthen the halogen bond. This was demonstrated[36,48] with a series of halomethanes which showed the positive electrostatic potential of the σ-hole increasing as $CH_3I > CH_3Br > CH_3Cl > CH_3F$. When the R group was replaced with more electronegative compounds while keeping the halogen donor same in CH_3-I vs CF_3-I vs NC-I, the positive electrostatic potential of σ-hole increased with NC-I > CF_3-I > CH_3-I. The halogen bond strength varies from 10kJ/mol (for N---Cl contacts in azoaromatic chlorides)[49] to 150kJ/mol (I_2 ---I^- adduct).[50,51] Similarly, the halogen bond acceptor can be tuned by the addition of electron donating groups aimed to enhance its negative electrostatic potential and consequently enhance the halogen bond strength. Examples of halogen bond acceptors include nitrogen containing heterocycles, amines and nitriles. In addition, other examples include halides of phosphonium or ammonium ions such as tetrabutylammonium chloride, tetraphenylphosphonium chloride etc.[52,53]

The σ-hole concept introduced by Politzer[36] effectively rationalized the behaviour of halogen atoms as electrophiles. Nonetheless, documented instances exist of halogen-bonded complexes whose properties cannot be fully elucidated solely through the σ-hole concept. For instance, there have been unexpected patterns in the strengths of halogen-bonded-adducts of CY_3I (Y=F, Cl, Br, I) with two typical Lewis bases (chloride and trimethylamine). In these adducts the halogen bond donor strength (Lewis acidity) of a compound R-X does not consistently increase with the higher electronegativity of the carbon based group R.[54] Charge transfer, dispersion, electrostatic, polarization interactions along with a repulsive component arising from the Pauli exclusion principle have all been invoked to account for the strength and directionality of halogen bonding. The electrostatic component explains the electron depleted region on halogens as we discussed previously, explained by Politzer[36] and as shown in Eq. 1.1.2.1. The amphoteric character of covalently bonded halogen atoms were revealed by the analysis of CSD (Cambridge Structural Database) showing that halogens can interact both with electrophiles and nucleophiles. The electrophile tends to interact orthogonal to the R-X bond, while nucleophiles tend to enter from the elongation of the R-X bond. This amphoteric nature of covalently bonded halogens results angles of 90° to 120° and 160°-180° ranges respectively between the covalent and noncovalent bonds at halogens. One or two iodines in I_2 act both as an electron donor and acceptor in an I_2 adduct (showing the amphoteric character) formed in the charge transfer complexes.[31,55,56] Evidence for charge transfer complexes of the halogen bond were produced by UV-vis and X-ray diffraction studies. Rosokha et al. studied bromocarbons interacting with Br^- by UV-vis and found that there is a direct correlation between the absorptive energy and the oxidative potential of halogen bond acceptor.[57] Further, X-ray diffraction confirmed the elongation of C-I and C-Br bonds in the complexes compared to the pure form suggesting a charge transfer interaction between $n \rightarrow \sigma^*$ orbitals.[27] The initial studies indicated the origin of halogen bonding was through charge transfer phenomena mainly, and this attribution may stem from the framework in which some of the earliest studies on the subject were conducted. Later studies emphasized electrostatic interactions largely with the analogy of hydrogen bonding, the halogen being the positively charged species with the σ-hole concept, and the negatively charged species. Symmetry Adapted Perturbation theory with density functional theory (DFT-SAPT) applied on series of halogen bonded systems decomposed the total interaction energy into four components: electrostatics, polarization, dispersion and exchange repulsion.[58] This method was utilized to analyze a series of halogen bonded complexes such as $X_2\cdots$benzene systems, and the set of $H_nF_{3-n}CBr\cdots NH_3$ complexes. Binding energy decomposition curves were generated which revealed that crucial contributions to stabilization come from the electrostatic and dispersion terms, with smaller role played by induction.[59] The study showed that the dispersion energy can stabilize the type II halogen···halogen interactions when larger halogens are involved, whereas the electrostatic part plays a role in tunability and directionality of halogen bonding.[59]

1.1.4 Applications

Due to the tunability and directionality of halogen bonds, their applications in various fields such as crystal engineering, functional materials, supramolecular assemblies, biological systems have been explored widely.

1.1.4.1 Crystal Engineering

Crystal engineering is a field of supramolecular chemistry focussing on the understanding of intermolecular interactions in terms of crystal packing, and the use of this knowledge to design new solids with desired properties.[60,61] As defined by Lehn in 1987, *"Just as there is a field of molecular chemistry based on the covalent bond, there is a field of supra molecular chemistry, the chemistry of molecular assemblies and of the intermolecular bond"*.[61,62] Desiraju describes supra molecular chemistry as *chemistry beyond the molecules*.[63] As halogen bonds are one such intermolecular interaction with moderate strength and high directionality and tunable properties, they have emerged as promising tools for the design of new materials with specific qualities of interest.[64] Such molecular assemblies formed by halogen bonding have found applications in supramolecular chemistry.[31,65,66]

Halogen bonding is known for its directionality and its ability to form geometries of 180° leading to several 1-D (one-dimensional) architectures with homomeric assemblies. In the homomeric assemblies, the halogen bond donor and acceptor undergo self-assembly to form halogen bonds and in case of heteromeric systems where the ditopic halogen bond donor and acceptor get self-assembled to form halogen bonding interactions.[46] These infinite 1-D chain structures are reported in the literature for homomeric systems with iodine being the strong halogen bond donor undergoing self-assembly.[67] 1D chains have been formed with heteromeric systems where one of the acceptor is an electron rich nitrogen atom.[68] Figure 1.5 shows the crystal structures of homomeric, heteromeric, stepped chain and zig-zag arrangements of halogen bonded systems. In general, 1-D chains with linear geometry tend to form when the axes of both donor and acceptor sites are parallel and coaxial. The infinite chains are formed when the binding sites are parallel but not collinear. Due to the high directionality of halogen bonding, different types of molecular assemblies are possible, such as linear, zigzag or stepped, depending on the requirement of crystal packing. By carefully choosing the synthons, the new structure can be fine-tuned by changing the donor acceptor systems, hybridization, type of halogen bond acceptor etc.

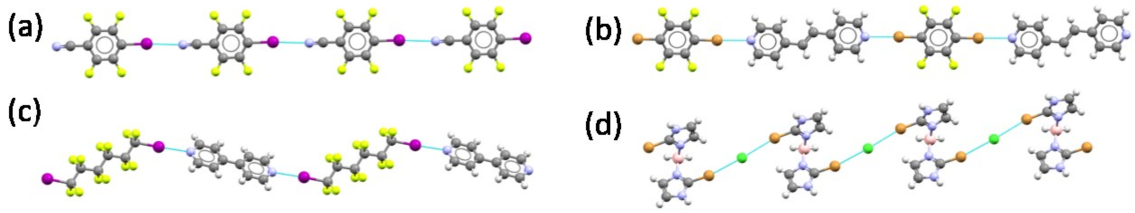

Figure 1.5. Single crystal structures showing the one-dimensional chain in halogen bonded systems. (a) linear homomeric chain formed by self-assembly of 4-iodo-2,3,5,6-fluorobenzonitrile (CSD ref code: ACOKIM). (b) linear heteromeric chain formed by self-assembly of 4,4’-dipyridyl-N,N’-dioxide and 1,4-diiodotetrafluorobenzene (CSD ref code: IKUHUR) (c) one dimensional stepped chain formed by self assembky of 4,4’-dipyridyl and 1,6-diiodododecafluorohexane (CSD

ref code: QANRUS) (d) Infinite zig-zag infinite chains formed by bis(2-bromo)imidazoleboronium chloride.THF (CSD ref code: IKUXER)

Expanding the number of XB donor and/or acceptor sites on the initial molecular modules has proven to be a widely adopted and effective strategy over the years. It involves positioning the binding sites on the molecular scaffold to achieve the desired binding profile of the interacting partners and to create the targeted network. For instance, in the pursuit of a three-dimensional structure, it is advisable to place three or four XB donor sites in a roughly orthogonal orientation to each other. Layered two-dimensional structures can be made by using simple dihalogens due the presence of two σ-holes on the extensions of halogen bonding which are two electron deficient sites acting as halogen bond donor and the two electron rich sites orthogonal to the covalent bond which act as halogen bond acceptor (Figure 1.5). Repetition of such synthons creates supramolecular assembly as 2D, flat or layered structures. A layered structure was reported for 1,3,5-tris(4-iodophenoxycarbonyl)benzene when it was crystallized from $CHCl_3$, benzene and pyridine, yielding hexagonal inclusion complexes with chloroform and channel like inclusion complexes with pyridine and benzene.[69] These structures contained bifurcated I···O and I···π interactions which lead to triangular motifs that were the basis for hexagonal honey-comb like structures with solvent molecules sitting in nanometer sized channels which showed the role of solvent molecules in the crystallization. These honeycomb-line structures are common in 2D assembly. Figure 1.6 shows the simple flat two dimensional layered structure formed Cl_2 molecules[70] due to presence of two σ-holes on the extension of covalent bonds and two XB acceptor sites orthogonal to the covalent bond. Another example is shown in Figure 1.6 (b), with the honey-comb like crystal structure formed by cocrystallizing potassium iodide and K.2.2.2 ([2.2.2] cryptand bound to K^+) with 1,8-diodoperfluorobenzene.[71]

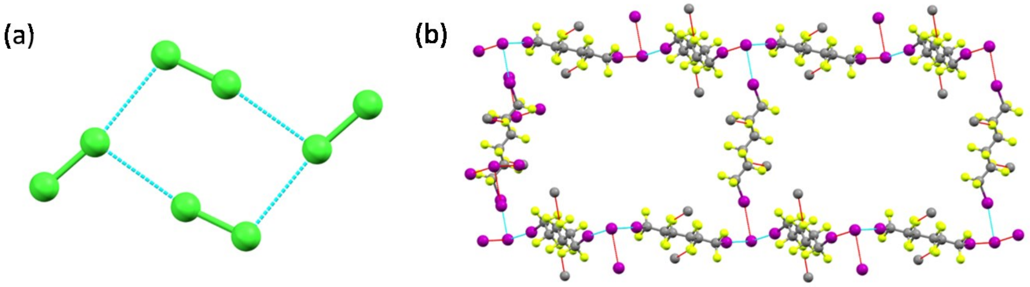

Figure 1.6. Two-dimensional crystal structures: (a) two-dimensional flat network formed by Cl_2 (CSD ref code: YATKIP) (b) Honeycomb like crystal structure obtained by cocrystallizing potassium iodide and K.2.2.2 with 1,8-diodoperfluorobenzene (CSD ref code: TEHRAA).

Bi-or tridentate and halide halogen bond donors forming rhombic and octagonal networks are also observed in the 2D topology.[72,73] Porous supramolecular assemblies have potential applications in sensory devices, catalysis as they provide a large surface area per unit volume, allowing for increased interaction with target molecules. By depositing 4,4”-dibromo-*p*-terphenyl (DBTP) on Ag (111) at 80K, porous networks were formed with the Br···Br motifs taking the vertex position. The dimension of porous structures can be scaled up by increasing the chain length and keeping the Br termination intact.[74]

Similarly, three dimensional networks are presented in the literature of crystal engineering where simple synthons with halogens show their unusual directionality and strength in maintaining the structure. Lindeman et al showed the consistent formation of diamondoid networks using tetrabromomethane and chloride anions as simple building blocks, alternating at the nodes of the network.[73] In other example, the number and position of iodine (halogen bond donor) and nitrile group (halogen bond acceptor) in iodophthalonitrile was altered to create a triple helix spiral staircase assembly.[75] Supramolecular nanowire crystals have also been obtained using halogen bond networks by R. Kato and coworkers.[76] They synthesized a aromatic tecton with an extended skeleton, 2,2′,4,4′,6,6′-hexafluoro-3,3′,5,5′-tetrakis((4-(iodoethynyl)phenyl)ethynyl)biphenyl with halide ions which formed a supramolecular assembly with pseudotetrahedral symmetry.

1.1.4.2 Biological applications

Halogen bonding has found applications in the field of pharmaceutics, medicinal chemistry, biochemistry, protein binding, drug interactions, serving as stabilizing intra- and intermolecular interactions.[77–79]

The first reports of short Br···O contacts in biological systems were identified in the 0.66 Å resolution structure of IDD594 with aldose reductase (AR)[80] and in a four-stranded Holliday junction with a bromouracyl unit.[81] The high resolution of the IDD594 structure revealed clear observation of a short contact between the bromine atom of the inhibitor and the hydroxyl oxygen of the Thr113 protein residue, with a distance of 2.97 Å and a C–Br···O(γ) angle of 152.8°. This interaction met the criteria for a halogen bond and was suggested to be crucial for IDD594's specificity for aldose reductase over aldehyde reductase. Holliday junctions are four stranded intermediates involved in genetic-recombination dependent mechanisms such as DNA repair and integration. In a study focused on nucleotide sequences stabilizing Holliday junctions, P. S. Ho and coworkers presented initial evidence highlighting the substantial impact of halogen bonding on polynucleotide structure.[81] They studied the competition between halogen bonding and hydrogen bonding in d(CCGGCGCCGG) by replacing thymine with a 5-bromouracyl unit, d(CCAGTACbr^{5}UCG). It was found that the halogen bonding was 5kJ/mol and more stable than a hydrogen bond in the system.[82] DNA Holliday junctions containing halogenated uracil bases (DNA structures where uracil bases in the junction are replaced with halogen atoms like fluorouracil, chlorouracil, bromouracil, or iodouracil) demonstrated the enthalpic stabilization of the halogen bond follows the σ-hole trend, being least for fluorine and increasing as the polarizability increases to iodine.[83] Though chlorine is considered a weak halogen bond donor, its presence in the active site of the bactericide triclosan, which inhibits enoyl reductase, has shown better potency than the other substituents having lipophilic or hydrogen bonding abilities.[84,85] In this complex, a 3.25 Å Cl···O contact is observed with Gly204, featuring a C–Cl···O angle of 162.4°. Additionally, a shorter and more linear halogen bond is observed with the Ala97 of enoyl-acyl reductase from Bacillus anthracis, with a Cl···O distance of 3.08 Å and a C–Cl···O angle of 166.2°.

A survey of the Protein database (PDB) found that 64.5% of C-X···Y contacts occur with the protein backbone rather than with the amino acid side chains, potentially due to steric hindrance and solvent entropic costs associated with forming halogen bonds with the latter.[46] The majority of these backbone halogen bonds involve the carbonyl oxygen rather than the amide nitrogen.[77,79,83,86] This phenomenon is attributed to two factors: (i) in carbonyl groups both oxygen lone pairs and the double bond can serve as electron donors, whereas nitrogen possesses only one pair of electrons, and (ii) accessing backbone nitrogen presents a steric challenge. The peptide bond also acts as a good halogen bond acceptor.[77,87]

1.1.4.3 Functional materials

Halogen bonding has been exploited in various fields such as catalysis and high value functional materials[65,88–91] ICl_3, iodine trichloride, was reported to catalyze the ring opening polymerization of L-lactides in the presence of 11-bromo-1-undecanol (11-BU). FTIR and multinuclear NMR spectroscopy showed that the L-lactide and 11-BU interact with ICl_3 via strong hydrogen and halogen bonds which catalyzes the reaction.[92] The fluoronium cation, F^+, derived from *N*-fluoropyridinium triflate, acts as an effective organocatalyst for aziridine synthesis.[93] This catalyst's electrophilic nature suggests that the F^+ cation forms robust halogen bonds with the imine component, thereby activating it for subsequent nucleophilic attack by ethyl diazoacetate. Kniep et al reported that the neutral multidentate halogen bond donors, 2,6-diiodo-3,4,5-trifluorophenyl groups catalyze the reaction of 1-chloroisochroman with ketene silyl acetals. The iodinated halogen bond donors showed conversions of 37% and 91%, after 12 hours at −78 °C, while the corresponding noniodinated species did not react. Meanwhile introduction of strong halogen bond acceptors (20 mol% tetrabutylammonium chloride) made the halogen bond inactive, confirming the XB's activation role. Meta-substituted compound and monodentate variant were also inactive, emphasizing the importance of iodine substituents' number and orientation. These were the first studies which assessed the number and orientation of iodine substituents acting as halogen bond based organocatalysts.[94] In 2014, Huber et al. demonstrated that dicationic halogen bond donors can activate the carbonyl group towards Diels-Alder reactions.[95] Halogen bonding is used in synthesis of soft materials as well. Complexes of molecular iodine with alkoxystilbazoles formed a liquid crystal with high mesophase stability, whereas this phase did not form when iodine was replaced with bromine.[96] Fluorinated imidazolium ionic liquid potentially forming halogen bonds, is used as a source of iodide ions in solvent based electrolyte in dye-sensitized solar devices which improved the efficiency of device by charge transport within the electrolyte and charge transfer dynamics at TiO_2 dye/electrolyte interface compared that of hydrogenated ionic liquids.[97] This effect is explained by the low affinity of perfluorocarbons for organic and aqueous phases, may provide a more favorable solvation environment, potentially driving the long alkyl chains of the sensitizer (Z907 in this case) into densely packed layers to minimize interactions with the fluorinated electrolyte. Additionally, the fluorinated electrolyte may lead to higher I_3^- diffusion coefficients in the bulk of the electrolyte.

Perovskite-based materials are extensively studied in solar-cell technology for their high energy conversion efficiency and cost-effectiveness. They have molecular formula $CH_3NH_3PbX_3$ where X could be I^-, Br^-, or Cl^-. Halide anions on the perovskite crystal surface act as efficient halogen bond (XB) acceptors, passivated by XB donors. Surface passivation via XB significantly enhances solar cell performance. Untreated devices show 13% efficiency, while XB passivation boosts efficiency to 15.7%. This improvement is attributed to halide anions acting as hole traps in untreated devices, causing charge accumulation at the perovskite–hole-transport-layer interface. XB-induced passivation prevents this, enhancing device performance.[98] Kiguchi et al. demonstrated an application of the gold–iodine interaction by forming single-molecule junctions of gold electrodes bound with 1,4-diiodobenzene and studied their conductance.[99] They found that the iodine site serves as an effective anchoring group for building single-molecule junctions, whereas similar junctions were not formed using dibrominated or dichlorinated benzenes, attributed to the gold–iodine halogen bond (XB). The authors used the distances required to break the single-molecule junctions as an indicator of the binding strength between the electrodes and the bridging molecules. They concluded that the $Au\cdots I$ bond is stronger than the $Au\cdots NH_2$ bond but notably weaker than the $Au\cdots SH$ bond.

Halogen bonding enhances the thermal and mechanical properties of polymer–carbon nanotube (CNT) composites in the context of carbon-based nanomaterials. Salavagione et al.[100] studied multiwalled, alkyl-modified CNT dispersions in a poly(vinyl chloride) (PVC) matrix. The PVC matrix acts as a solubilizing agent for nanotubes, resulting in composites with improved mechanical and thermal properties, influenced by polymer tacticity. The enhanced performance is partly attributed to carbon–chlorine···oxygen double bond ($C—Cl\cdots O═C$) halogen bonding, improving CNT dispersion within the matrix.

1.1.4.4 Solid state NMR insights into study of dynamics and halogen bonding

Understanding the functionality of materials, biomolecules,[101] catalysts,[102] and supramolecular assemblies[103] relies on grasping their structure and dynamics. As a complement to the valuable information available from X-ray crystallography, solid-state NMR spectroscopy (SSNMR) also yield important and novel information on halogen-bonded compounds. SSNMR allows the chemical and electronic environments of crystalline compounds to be characterized, often based on the four major NMR interactions: magnetic shielding, quadrupolar coupling, J-coupling, and dipolar coupling. Furthermore, SSNMR can be applied not only to crystalline samples, but also to amorphous samples for which diffraction techniques may not be suitable. SSNMR also offers opportunities to characterize dynamics in solids, as well as the nature of static or dynamic disorder.

Halogen bonds have emerged as potentially stabilizing interactions within biomolecular systems, exerting influence over processes such as ligand binding and molecular folding.[77] Solid-state NMR spectroscopy (SSNMR)[104] emerges as a powerful tool, complementing X-ray crystallography by offering insights into halogen-bonded compounds' chemical environments and dynamics, both in crystalline and amorphous materials. The isotropic and anisotropic components of the chemical shift tensors of nuclei involved in halogen bonds will be influenced by the molecular and electronic structure of such bonds. Most of the NMR-active nuclides of the periodic table are quadrupolar (nuclear spin $I > ½$), including the halogens $^{35/37}$Cl ($I = 3/2$), $^{79/81}$Br ($I = 3/2$), and ^{127}I ($I = 5/2$). The NMR spectra of such nuclides are affected by the interaction between their nuclear electric quadrupole moments (Q) and the electric field gradient tensor (V) at the nucleus. In the context of halogen bonding, J-couplings between nuclei involved in the $RX\cdots Y$ (Figure 1.4) moiety will be sensitive to the electronic structure of the halogen bond and to changes in geometry and the nature of the substituents. These NMR interactions are discussed in detail in the next chapter.

In recent years, there have been successful endeavors in engineering a variety of molecular machines, switches, and rotors within porous crystals and on surfaces. Hypermobile rotor of zinc based MOF containing rigid building block bicyclopentane-dicarboxylate demonstrated by Perego et al.[105] The carboxylate groups attached to the metal clusters serve as an axile, while the bicyclic unit freely rotate. The rotor's three-fold bipyramidal symmetry clashes with the four fold symmetry of the struts in the cubic crystal cell of the framework, preventing the formation of stable conformation. This allows for continuous, unidirectional, hyperfast rotation of the bicyclic units characterized by the very low barrier of 6.2 cal/mol (0.026 kJ/mol) measured by ^{1}H (T_1) ssNMR relaxation time constants.

Wei et al.[106] studied the chain motion of polyethylene with regularly placed methyl groups. A twisted motion centred at the branching of polyethylene was found using ^{2}H NMR of deuterated methyl groups and ^{13}C NMR and the dynamics of linear polymer changing upon branching affect the processability of polymers as well engineering of the polyethylene for various applications.

Shcherbakov et al.[107] studied the dynamics involved in the membrane protein EmrE, bacterial multidrug transporter from *E. coli* mediating the substrate transport. The EmrE in complex with cationic substrate, tetra(4-fluorophenyl)phosphonium (F_4-TPP$^+$) exhibits different structures at acidic and basic pH levels, indicating changes upon the binding or release of a proton from residue E_{14} (an essential glutamate in the homodimer EmrE), respectively. To gain understanding into the protein dynamics involved in substrate transport, ^{15}N rotating-frame spin lattice relaxation ($R_{1\rho}$) rates of F_4-TPP$^+$ bound S_{64}V-EmrE in lipid bilayers under magic-angle spinning (MAS) were conducted. ^{1}H detected ^{15}N $R_{1\rho}$ relaxation dispersion experiment under fast MAS suggested the occurrence of backbone motions at a rate of approximately 6000s^{-1} at 280 K for the protein at both acidic and basic pH which falls in the range of substrate binding.

^{1}H MAS, along with ^{13}C and ^{15}N CP/MAS solid-state NMR experiments, studied imidazole and morpholine-based model compounds with halogen bonding and hydrogen bonding capabilities.[108] The study was complemented by GIPAW DFT computations of relevant NMR parameters. The sensitivity of ^{15}N chemical shifts to halogen bond strengths was demonstrated by the noticeable difference in the chemical shifts of the $+NH_2$ protons of the morpholinium cation. However, attributing systematic changes in ^{13}C chemical shifts to the halogen bond environment or strength proved challenging due to difficulties in observing signals of carbon atoms directly bonded to iodine.

A detailed study of halide anions involved in strong halogen bonds[109] revealed correlations between bond geometry, electronic structure, and quadrupolar coupling tensors of $^{35/37}$Cl and $^{79/81}$Br. Using ultrahigh-field SSNMR spectroscopy, a wide range of geometries, from linear to octahedral, was characterized. In these systems, halide anions act as electron donors to multiple halogen bond acceptors. In $-C–I\cdots X^{-}\cdots I–C–$ environments, asymmetry (η), quadrupolar coupling (Q) values for $^{35/37}$Cl and $^{79/81}$Br correlated with the $I\cdots X^{-}\cdots I$ angle, and quadrupolar coupling constants correlated with halogen bond strengths.

The principles of crystal engineering[61] have been useful in assembling stators and rotators into cocrystals which results in supramolecular rotor arrays. The supramolecular synthons available in the crystal engineering toolbox[60] aid in strategizing the design of the cocrystals desired. By controlling the non-covalent interactions involving rotators and stators of these synthons, it may be possible to tune the dynamics. Hydrogen bonding, π-π stacking, metal coordination, van der Waal's interactions, halogen bonding are a few types of non-covalent interactions available to design crystal structures. The synthesis of crystalline halogen-bonded molecular rotors from fluoro-substituted iodobenzenes and DABCO leverages crystal engineering principles. This involves meticulous control over the assembly of stators and rotators within co-crystals, enabling the efficient utilization of supramolecular synthons and ensuring precise tuning of dynamic performance. Notably, halogen bonding (XB) and hydrogen bonding (HB) play crucial roles, serving as robust rotational axles that facilitate molecular motion. Characterization via variable-temperature solid-state ^{1}H NMR spectroscopy confirms efficient rotational dynamics, with pre-exponential factors comparable to rotors featuring covalent axles. This underscores the versatility of crystal engineering in designing functional materials and molecular machines, with a particular focus on the solid-state NMR analysis and dynamics study of the halogen system, revealing an activation energy (E_a) range of 10.04–20.5 kJ/mol[109] which was lower than that of pure crystalline DABCO which has an E_a of 34.3 kJ/mol.

In conclusion, halogen bonding is a versatile and impactful interaction across various scientific disciplines. Understanding halogen bonding help in utilizing them in designing and preparing the novel cocrystals produced in the thesis. These insights are helpful in studying the interactions involved based on type of halogen involved in the interaction as well the sigma hole associated with them which contribute to the energy barrier associated with these cocrystals. Moreover, solid-state NMR spectroscopy along with X-ray crystallography emerge as a crucial tool for understanding the structural dynamics of halogen-bonded compounds, providing valuable insights into molecular machines and crystal engineering. Collectively, the broad applications of halogen bonding underscore its importance in continued exploration and development across various field.

1.1 References

(1) Stauffer, E.; Dolan, J. A.; Newman, R. CHAPTER 3 - Review of Basic Organic Chemistry. In *Fire Debris Analysis*; Academic Press: Burlington, **2008**; pp 49–83.

(2) Haynes, W.M.; Lide, D.R.; Bruno, T.J. CRC Handbook of Chemistry and Physics. CRC Press, Boca Raton, **2016**.

(3) Lippert, E. *Angew. Chem.* **1960**, *72* (16), 602–602.

(4) Miessler, G.L.; Fischer, P.J.; Tarr, D.A. Inorganic Chemistry 5th, Pearson Education, Inc., Boston, **2013**.

(5) De La Roza, A.O.; Dilabio, G.A. Non-Covalent Interactions in Quantum Chemistry and Physics. Theory and Applications. Elsevier, Cambridge, **2017**.

(6) Feynman, R. P. Forces in Molecules. *Phys. Rev.* **1939**, *56* (4), 340–343.

(7) Wilcox, C. J. *J. Chem. Educ.* **1998**, *75* (10), 1301.

(8) Pauling, Linus. *J. Am. Chem. Soc.* **1931**, *53* (9), 3225–3237.

(9) Desiraju, G. R. Angewandte Chemie International Edition **2011**, 50 (1), 52–59.

(10) Berzelius, J.J.; Bache, A.D. *Am. J. Sci*. **1832**, *22*.

(11) Budisa, N.; Kubyshkin, V.; Chulze-Makuch, D. *Life*, **2014**, *4* (3), 374-385.

(12) Svensson, T.; Kylin, H.; Montelius, M.; Sandén, P.; Bastviken, D. *Environ. Sci. Pollut. R*. **2021**, 28, 7691-7709.

(13) Alaee, M.; Arias, P.; Sjödin, A.; Bergman, Å. *Environ. Int.* **2003**, *29* (6), 683–689.

(14) Goodwin, M. J.; Steed, B. W.; Yufit, D. S.; Musa, O. M.; Berry, D. J.; Steed, J. W. *Cryst. Growth Des.* **2017**, *17* (10), 5552–5558.

(15) Metrangolo, P., Resnati, G., *Halogen Bonding*; Springer Berlin Heidelberg, **2008**; Vol. 126.

(16) Colin, M. *Ann. Chim.* **1814***, 91*, 252−272.

(17) Remsen, I.; Norris, J. F. *Am. Chem. J.* **1896**, *18*, 90−95.

(18) Ault, B. S.; Andrews, Lester. *Inorg. Chem.* **1977**, *16* (8), 2024–2028.

(19) Legon, A. C. *Angew. Chem. Int. Ed. Engl*. **1999**, *38* (18), 2686–2714.

(20) Mulliken, R. S. *Science* **1967**, *157* (3784), 13–24.

(21) Mulliken, R. S. *J. Am. Chem. Soc.* **1950**, *72* (1), 600–608.

(22) Hassel, O. *Science* **1970**, *170* (3957), 497–502.

(23) Hassel, O.; Hvoslef, J. *Acta Chem. Scand.* **1954**, *8*, 873–873.

(24) Hassel, O.; Rømming, C. *Q. Rev. Chem. Soc.* **1962**, *16* (1), 1–18.

(25) Hassel, O.; Strømme, Knut O. *Acta Chem. Scand.* **1958**, *12*, 1146-1146.

(26) Hassel, O.; Strømme, Knut O. *Acta Chem. Scand.* **1959**, *13,* 1781-1786.

(27) Rosokha, S. V.; Kochi, J. K. X-Ray Structures and Electronic Spectra of the π-Halogen Complexes between Halogen Donors and Acceptors with π-Receptors. In *Halogen Bonding:*

Fundamentals and Applications; Metrangolo, P., Resnati, G., Eds.; Structure and Bonding; Springer: Berlin, Heidelberg, **2008**; pp 137–160.

(28) Desiraju, G. R.; Parthasarathy, R. *J. Am. Chem. Soc.* **1989**, *111* (23), 8725–8726.

(29) Bent, H. A. *Chem. Rev.* **1968**, *68* (5), 587–648.

(30) Schwerdtfeger, P. Atomic Static Dipole Polarizabilities. In *Atoms, Molecules and Clusters in Electric Fields*; Computational, Numerical and Mathematical Methods in Sciences and Engineering; published by Imperial College Press and distributed by World Scientific Publishing Co., **2006**; Vol. 1, pp 1–32.

(31) Metrangolo, P.; Resnati, G. Halogen Bonding: A Paradigm in Supramolecular Chemistry. *Chem. Eur. J.* **2001**, *7* (12), 2511–2519.

(32) Priimagi, A.; Cavallo, G., Metrangolo, P.; Resnati, G. *Acc. Chem. Res*. **2013**, *46* (11), 2686-2695.

(33) Brinck, T.; Murray, J. S.; Politzer, P. *Int. J. Quantum Chem.* **1992**, *44* (S19), 57–64.

(34) Brinck, T.; Murray, J. S.; Politzer, P. *Int. J. Quantum Chem.* **1993**, *48* (2), 73–88.

(35) Politzer, P.; Murray, J. S.; Clark, T. *Phys. Chem. Chem. Phys.* **2013**, *15* (27), 11178–11189.

(36) Clark, T.; Hennemann, M.; Murray, J. S.; Politzer, P. *J. Mol. Model.* **2007**, *13* (2), 291–296.

(37) Sedlak, R.; Kolar, M. H.; Hobza, P. *J. Chem. Theory Comput.* **2015**, *11* (10), 4727-4732.

(38) Nyburg, S. C. *Acta. Crystall. A-Crys.* **1979**, *35* (4), 641-645.

(39) Politzer, P., Murray, J. S. *Crystals* **2017**, 7(7), 212.

(40)) Stewart, R. F. *J. Chem. Phys.* **2003**, *57* (4), 1664–1668.

(41) Eskandari, K.; Lesani, M. *Chem. Eur. J.* **2015**, *21* (12), 4739–4746.

(42) Riley, K. E., Murray, J. S., Fanfrlík, J., Řezáč, J., Solá, R. J., Concha, M. C., Politzer, P. *J. Mol. Model.* **2013**, 19, 4651-4659.

(43) Riley, K. E., Murray, J. S., Fanfrlík, J., Řezáč, J., Solá, R. J., Concha, M. C., Politzer, P. J. Mol. Model. **2011**, 17, 3309-3318.

(44) Desiraju, G. R.; Ho, P. S.; Kloo, L.; Legon, A. C.; Marquardt, R.; Metrangolo, P.; Politzer, P.; Resnati, G.; Rissanen, K. *Pure Appl. Chem.* **2013**, *85* (8), 1711–1713.

(45) Muller, P. *Pure Appl. Chem.* **1994**, *66* (5), 1077–1184.

(46) Cavallo, G.; Metrangolo, P.; Milani, R.; Pilati, T.; Priimagi, A.; Resnati, G.; Terraneo, G. *Chem. Rev.* **2016**, *116* (4), 2478–2601.

(47) Favre, H. A.; Powell, W. H. *Nomenclature of organic chemistry:* IUPAC recommendations and preferred names **2013**. Royal Society of Chemistry.

(48) Bundhun, A.; Ramasami, P.; Murray, J. S.; Politzer, P. *J. Mol. Model.* **2013**, *19*, 2739-2746.

(49) Xu, K.; Ho, D. M.; Pascal Jr, R. A. *J. Am. Chem. Soc.* **1994**, *116* (1), 105-110.

(50) Müller, M.; Albrecht, M.; Gossen, V.; Peters, T.; Hoffmann, A.; Raabe, G.; Rissanen, K. *Chem. Eur. J.* **2010**, *16* (41), 12446-12453.

(51) Lommerse, J. P. M.; Stone, A. J.; Taylor, R.; Allen, F. H. *J. Am. Chem. Soc.* **1996**, *118* (13), 3108–3116.

(52) Cavallo, G.; Metrangolo, P.; Pilati, T.; Resnati, G.; Sansotera, M.; Terraneo, G. *Chem. Soc. Rev*. **2010**, 39(10), 3772-3783.

(53) Fourmigué, M. *Acta Crystallogr. B* **2017**, 73(2), 138-139.

(54) Huber, S. M.; Jimenez-Izal, E.; Ugalde, J. M.; Infante, I. *Chem. Commun*, **2012**, *48* (62), 7708-7710.

(55) Bailey, R. D.; Grabarczyk, M.; Hanks, T. W.; Pennington, W. T. *J. Chem. Soc. Perk. T. 2* **1997**, *0* (12), 2781–2786.

(56) Rimmer, E., Bailey, R., Pennington, W., Hanks, T. (1998). *J. Chem. Soc. Perk. T. 2* **1998**, *11*, 2557-2562.

(57) Rosokha, S. V.; Stern, C. L.; Ritzert, J. T. *Chem. Eur. J.* **2013**, *19* (27), 8774–8788.

(58) Heßelmann, A. *J Chem. Theory Comput.* **2018**, *14* (4), 1943–1959.

(59) Riley, K. E.; Hobza, P. *Phys. Chem. Chem. Phys.* **2013**, *15* (41), 17742–17751.

(60) Desiraju, G. R. *J. Am. Chem. Soc.* **2013**, *135* (27), 9952–9967.

(61) Desiraju, G. R. *Angew. Chem. Int. Edit. Eng.* **1995**, *34* (21), 2311 2327.

(62) Lehn, J.-M. Supramolecular Chemistry—Scope and Perspectives Molecules, Supermolecules, and Molecular Devices (Nobel Lecture). Angew. Chem. Int. Edit. Eng. 1988, 27 (1), 89–112.

(63) Desiraju, G. R. *Nature* **2001**, *412* (6845), 397–400.

(64) Teyssandier, J.; Mali, K. S.; De Feyter, S. *ChemistryOpen* **2020**, *9* (2), 225–241.

(65) *Supramolecular Chemistry*, 1st ed.; John Wiley & Sons, Ltd, **1995**.

(66) Gilday, L. C.; Robinson, S. W.; Barendt, T. A.; Langton, M. J., Mullaney, B. R.; Beer, P. D. *Chem. Rev.* **2015**, *115* (15), 7118-7195.

(67) Bond, A. D.; Griffiths, J.; Rawson, J. M.; Hulliger, J. *Chem. Commun.* **2001**, (23), 2488-2489.

(68) Bianchi, R.; Forni, A.; Pilati, T. *Acta Crystallogr. B* **2004**, 60(5), 559-568.

(69) Christopher Pigge, F.; R. Vangala, V.; P. Kapadia, P.; C. Swenson, D.; P. Rath, N. *Chem. Commun.* **2008**, *0* (39), 4726–4728.

(70) Boese, R.; Boese, A. D.; Bláser, D.; Antipin, M. Y.; Ellern, A.; Seppelt, K. *Angew. Chem. Int. Edit.* **1997**, *36* (13-14), 1489-1492.

(71) Liantonio, R. Metrangolo, P.; Pilati, T.; Resnati, G. *Cryst. Growth Des*. **2003**, *3* (3), 355-361.

(72) Hembree, W. I.; Baudry, J. *J. Phys. Chem. B* **2011**, *115* (26), 8575–8580.

(73) Lindeman, S. V.; Hecht, J.; Kochi, J. K. *J. Am. Chem. Soc.* **2003**, *125* (38), 11597–11606.

(74) Chung, K.-H.; Park, J.; Yeop Kim, K.; Keon Yoon, J.; Kim, H.; Han, S.; Kahng, S. J. *Chem. Commun.* **2011**, *47* (41), 11492–11494.

(75) Ateş, Ö. D.; Zorlu, Y.; Kanmazalp, S. D.; Chumakov, Y.; Gürek, A. G.; Ayhan, M. M. *CrystEngComm* **2018**, *20* (27), 3858–3867.

(76) Lieffrig, J.; Yamamoto, H. M.; Kusamoto, T.; Cui, H.; Jeannin, O.; Fourmigué, M.; Kato, R. *Cryst. Growth Des.* **2011**, *11* (10), 4267–4271.

(77) Auffinger, P.; Hays, F. A.; Westhof, E.; Ho, P. S. *P. Natl. A. Sci.* **2004**, *101* (48), 16789–16794.

(78) Hegde, B. M. Textbook of Endocrine Physiology. *Postgrad Med J* **1994**, *70* (819), 57.

(79) Xu, Z.; Yang, Z.; Liu, Y.; Lu, Y.; Chen, K.; Zhu, W. *J. Chem. Inf. Model.* **2014**, *54* (1), 69–78.

(80) Grebe, J.; Geiseler, G.; Harms, K.; Dehnicke, K.. Zeitschrift für Naturforschung B 1999, 54 (1), 77–86.

(81) Hays, F. A.; Vargason, J. M.; Ho, P. S. *Biochemistry* **2003**, *42* (32), 9586–9597.

(82) Vander Zanden, C. M.; Carter, M.; Ho, P. S. *Methods* **2013**, *64* (1), 12–18.

(83) Carter, M.; Voth, A. R.; Scholfield, M. R.; Rummel, B.; Sowers, L. C.; Ho, P. S *Biochemistry* **2013**, *52* (29), 4891–4903.

(84) Heath, R. J.; Yu, Y.-T.; Shapiro, M. A.; Olson, E.; Rock, C. O. *J. Biol. Chem.* **1998**, *273* (46), 30316–30320.

(85) Freundlich, J. S.; Anderson, J. W.; Sarantakis, D.; Shieh, H.-M.; Yu, M.; Valderramos, J.-C.; Lucumi, E.; Kuo, M.; Jacobs, W. R.; Fidock, D. A.; Schiehser, G. A.; Jacobus, D. P.; Sacchettini, J. C. *Bioorg. Med. Chem. Lett.* **2005**, *15* (23), 5247–5252.

(86) Wilcken, R.; Zimmermann, M. O.; Lange, A.; Joerger, A. C.; Boeckler, F. M. *J. Med. Chem.* **2013**, *56* (4), 1363–1388.

(87) Paulini; R., Müller; K., Diederich, F. *Angew. Chem. Int. Ed*. **2005**, *44* (12), 1788-1805.

(88) Etter, M. C. *Acc. Chem. Res.* **1990**, *23* (4), 120–126.

(89) Gholami, M. R.; Talebi, B. A. *J. Phys. Org. Chem.* **2003**, *16* (1), 79–83.

(90) Curran, D. P.; Kuo, L. H. *Tetrahedron Lett.* **1995**, *36* (37), 6647–6650.

(91) Metrangolo, P.; Pilati, T.; Terraneo, G.; Biella, S.; Resnati, G. *CrystEngComm* **2009**, *11* (7), 1187–1196.

(92) Coulembier, O.; Meyer, F.; Dubois, P. *Polym. Chem.* **2010**, *1* (4), 434–437.

(93) Bew, S. P.; Fairhurst, S. A.; Hughes, D. L.; Legentil, L.; Liddle, J.; Pesce, P.; Nigudkar, S.; Wilson, M. A. *Org. Lett.* **2009**, *11* (20), 4552–4555.

(94) Kniep, F.; Jungbauer, S. H.; Zhang, Q.; Walter, S. M.; Schindler, S.; Schnapperelle, I.; Herdtweck, E.; Huber, S. M. *Angew. Chem. Int. Ed.* **2013**, *52* (27), 7028–7032.

(95) H. Jungbauer, S.; M. Walter, S.; Schindler, S.; Rout, L.; Kniep, F.; M. Huber, S. *Chem. Commun.* **2014**, *50* (47), 6281–6284.

(96) J. McAllister, L.; Präsang, C.; P.-W. Wong, J.; J. Thatcher, R.; C. Whitwood, A.; Donnio, B.; O'Brien, P.; B. Karadakov, P.; W. Bruce, D. *Chem. Commun.* **2013**, *49* (38), 3946–3948.

(97) Abate, A.; Petrozza, A.; Roiati, V.; Guarnera, S.; Snaith, H.; Matteucci, F.; Lanzani, G.; Metrangolo, P.; Resnati, G. *Org. Electron.* **2012**, *13* (11), 2474–2478.

(98) Green, M. A.; Ho-Baillie, A.; Snaith, H. J. *Nat. Photonics* **2014**, *8* (7), 506–514.

(99) Komoto, Y.; Fujii, S.; Hara, K.; Kiguchi, M. *J. Phys. Chem. C* **2013**, *117* (46), 24277–24282.

(100) J. Salavagione, H.; Martínez, G.; Marco, C. *J. Mater. Chem.* **2012**, *22* (14), 7020–7027.

(101) Karplus, M.; Kuriyan, J. *Proc. Natl. Acad. Sci.* **2005**, *102* (19), 6679–6685.

(102) Zhang, Y.; Zhu, X.; Zhang, G.; Shi, P.; Wang, A. L. *J. Mater. Chem. A* **2021**, *9* (10), 5890–5914.

(103) Henzler-Wildman, K. A.; Lei, M.; Thai, V.; Kerns, S. J.; Karplus, M.; Kern, D. *Nature* **2007**, *450* (7171), 913–916.

(104) Bryce, D. L., Viger-Gravel, J. Solid-state NMR study of halogen-bonded adducts. Halogen Bonding I: Impact on Materials Chemistry and Life Sciences, **2015**, 183-203.

(105) Perego, J.; Bracco, S.; Negroni, M.; Bezuidenhout, C. X.; Prando, G.; Carretta, P.; Comotti, A.; Sozzani, P. *Nat. Chem.* **2020**, *12* (9), 845–851.

(106) Wei, Y.; Graf, R.; Sworen, J. C.; Cheng, C.-Y.; Bowers, C. R.; Wagener, K. B.; Spiess, H. W. *Angew. Chem.* **2009**, *121* (25), 4687–4690.

(107) Shcherbakov, A. A.; Brousseau, M.; Henzler-Wildman, K. A.; Hong, M. *J. Am. Chem. Soc.* **2023**, *145* (18), 10104-10115.

(108) Horike, S.; Matsuda, R.; Tanaka, D.; Matsubara, S.; Mizuno, M.; Endo, K.; Kitagawa, S. *Angew. Chem. Int. Edit.* **2006**, *45* (43), 7226–7230.

(109) Viger-Gravel, J., Leclerc, S., Korobkov, I., Bryce, D. L. *J. Am. Chem. Soc*. **2014**, *136* (19), 6929-6942.

Chapter 2 General Introduction to NMR (Nuclear Magnetic Resonance)

Matter is made of atoms that are composed of protons and neutrons within their nuclei, and electrons. The physical properties of atomic nuclei include mass, electric charge, magnetism, and spin. Electric charge is very important as it determines the chemical properties of each element.[1] A rotating object possesses an angular momentum and in quantum mechanics; it is quantized. Though spin is a type of angular momentum, it is not generated by a rotation of a particle; instead, spin is as an intrinsic property of the particle. The nuclear spin quantum number is generally denoted by the letter *I.* For example, the nucleus of the most commonly known isotope of hydrogen, ^{1}H, has a spin of $I = 1/2$. ^{2}H, the deuteron, another isotope of hydrogen, has a spin $I = 1$. The spin quantum number *I* leads to ($2I$+1) sublevels denoted by the magnetic quantum number *m*, which are degenerate in the absence of external fields. Some nuclei have integer values of *I i.e.*, 0, 1, 2…etc. For half integer nuclei, the *I* values are 1/2, 3/2, 5/2, 7/2, etc. NMR inactive nuclei ($I = 0$) have an even number of protons and neutrons; examples include ^{12}C, ^{32}S, ^{16}O, etc. Nuclei with an odd number of protons and neutrons are NMR active nuclei, and which covers most of periodic table and examples include ^{1}H, ^{15}N, ^{17}O, etc.

Nuclear magnetic resonance (NMR) spectroscopy[2,3] provides atomic level details regarding the local chemical environment and is used to study different types of nuclei. SSNMR has many important applications in pharmaceutics, glasses, polymer science, materials applications, and in studying protein dynamics, binding; etc.[4] An advantage of solid-state NMR with respect to solution NMR is that complete anisotropic nuclear spin interactions can be measured to gain structural insights. Solid-state NMR is useful for characterizing both crystalline and amorphous materials as well as transitions between phases when long range order is lacking and when diffraction techniques cannot be used. This chapter explores the fundamentals of NMR and concludes with a comprehensive discussion on the application of relaxation in deuterium NMR.

2.1 The Zeeman interaction

Nuclei with non zero spin intrinsically possess spin angular momentum (*I*) which is related to the magnetic moment (μ) of the nucleus. Nuclei with spin quantum number (*I*) possess the energy levels (2*I*+1) with magnetic quantum numbers (*m*) ranging from +*I* to –*I*. In quantum mechanics, quantum states are degenerate and the application of a magnetic field breaks the degeneracy and cause each of (2*I*+1) sublevels to have slightly different energies. This effect is called the Zeeman interaction and the energy of separation between the sublevels is called Zeeman splitting.[1,5,6] The Zeeman interaction is the strongest known interaction to be experienced by nuclei and is described by the Zeeman Hamiltonian $\widehat{H}_Z$. A schematic diagram of the Zeeman interaction is drawn below in Figure 2.1.

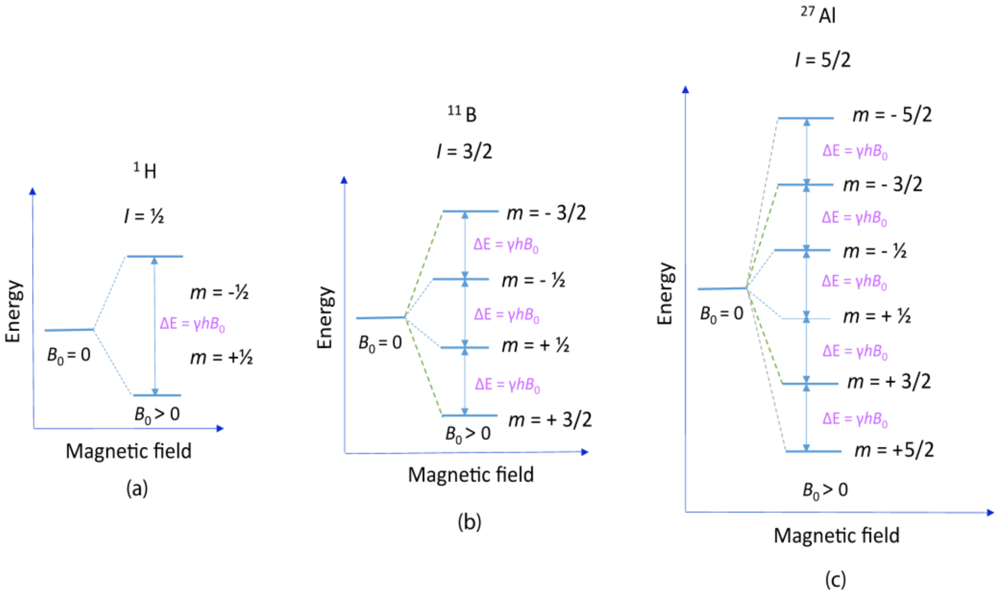

Figure 2.1. Zeeman splitting for nuclei in the presence of an external magnetic field B_0.

The Zeeman interaction energy is denoted by the Hamiltonian operator as following:

$$\hat{H}z = -\gamma B_0 \hat{I}_z \qquad \text{Eq 2.1.1}$$

In the above expression, B_0 is the applied magnetic field strength, γ is the magnetogyric ratio of the nuclei and $\hat{I}_z$ is the operator representing z-component of the nuclear spin angular momentum. The size of splitting between Zeeman energy states is related to the Larmor frequency(ν_0).[1,7] The Larmor frequency is expressed in Hz (Hertz) and is given by the following expression:

$$\nu_0 = \frac{-\gamma B_0}{2\pi} \qquad \text{Eq. 2.1.2}$$

The energy of a spin state is proportional to the Larmor frequency (ν_0).

$$E_m = mh\nu_0 \qquad \text{Eq. 2.1.3}$$

Where E_m is energy of spin state *m*, *m* is the magnetic quantum number, *h* is Planck's constant (6.62607×10^{-34} J.s). Hence, the NMR resonance frequency is directly associated with magnetic field and is larger at the higher external field strengths. Thus, NMR involves the detection of signals which arise due to the transition of spins between energy states created by Zeeman splitting and are associated with the radio frequency region of the electromagnetic spectrum. Higher magnetic field strength also helps to enhance the sensitivity of NMR as the nuclei with a lower magnetogyric ratio (low γ nuclei) by enhancing the signal-to-noise ratio.

2.2 Polarization

Nuclei that have a spin possess a magnetic moment and magnetic moment (μ) is proportional to the spin angular momentum (I), as $\mu=\gamma I$, where γ is the magnetogyric ratio which is different for different nuclear isotopes. A positive value of γ indicates that the magnetic moment of nuclei is parallel to the spin angular momentum whereas a negative γ indicates that the magnetic moment and spin angular momentum are opposite in direction. The spin angular momentum can be considered as a vector and the direction of vector or the direction of spin angular momentum is called spin polarization. When a nucleus is placed in an external magnetic field (B_0), there is an interaction between the nuclear magnetic moment ($\boldsymbol{\mu}$) and the applied field causing spins to precess at the Larmor frequency ($\omega_0 = -\gamma B_0$) as depicted in Figure 2.2 below:[8]

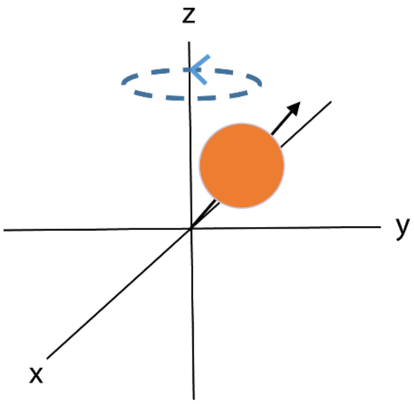

Figure 2.2. Precession of nuclei with magnetogyric ratio γ at Larmor frequency (ω_0) in the external field B_0.

The fluctuations in the local field arise due to factors such as nearby electrons, neighboring nuclei, and molecular motion of the nucleus. These fluctuations perturb nuclear precession. The precession frequency is directly proportional to the strength of the local magnetic field, any changes in the local field will affect the precession frequency of the nucleus. When the samples are first placed in the magnetic field there is no bulk magnetization along the z-axis; instead it takes a finite time to build up the magnetization. After a finite time magnetization reaches a steady value called the equilibrium magnetization. Over time, the fluctuations in the local field ensure that the lower energy populations are preferred as shown in Eq. 2.1.1 which leads to the growth of the net magnetization along z-axis (along the external magnetic field B_0) until it reaches equilibrium magnetization as stated. The process by which the spins come to equilibrium is called relaxation and the rate at which the magnetization attains equilibrium is described by the T_1 relaxation time constant. One possible alignment of spin populations is parallel to B_0 ($\theta = 0$), in which case the energy of interaction between the nuclear magnetic moment and the applied field is lowest or we can say that when the product of magnetic moment (μ) and the magnetic spin quantum number (m) of the nuclei is positive. Another possible alignment of spins is perpendicular to B_0 ($\theta = \pi/2$ radians) in which case the energy of interaction between the nuclear magnetic moment and the applied field is highest or when the product of magnetic moment (μ) and the magnetic spin quantum number (m) of the nuclei is negative.

For spin ½ nuclei in an external applied magnetic field, there are two spin states with magnetic spin quantum numbers (m) +1/2 and -1/2. The populations of these states are denoted as N_α and N_β, and at equilibrium, their ratio is governed by the Boltzmann distribution:[1,8,9]

$$\frac{N_\beta}{N_\alpha} = e^{-\Delta E/kT} = e^{-\gamma h B_0/2\pi kT} \qquad \text{Eq. 2.1.1}$$

where k is the Boltzmann constant (1.380649 x 10^{-23} J/K) and T is the temperature in K. The minute excess of nuclei in the lower energy state leads to bulk magnetization (M_0) aligned with B_0 which is detectable in NMR. A Boltzmann distribution is established after a finite time by the spins. The redistribution of spin population occurs from a nonradiative interaction of the nuclei with their surrounding lattice, which states the connection between spin system and surroundings with temperature T. This is the first order rate process with a lifetime of T_1 called the spin-lattice relaxation time. To detect an NMR signal or *free induction decay* a small coil of wire is positioned near the sample, with the axis of the coil aligned in the *xy*-plane as shown in Figure 2.3. The intensity of the NMR signal (oscillating current in the coil) oscillates depending on the delay time, pulse length and relaxation time. Delay time (D1) affects the NMR signal intensity (signal-to-noise ratio), T_2 relaxation time influences the linewidth, pulse length affects the transverse magnetization, coherence of spins, excitation profile across the sample, thus affecting the signal intensity and phase coherence, and overall quality of NMR spectra.

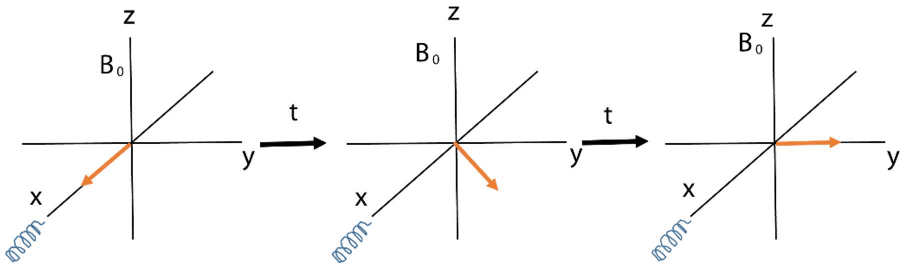

Figure 2.3. Detection of the free induction decay in the *xy*-plane.

The equilibrium magnetization is fixed in size and direction, where the magnetization is along the z-axis. In a pulse NMR experiment, the precession of magnetization vector is what we detect. The coil used to detect the bulk magnetization can also be utilized to generate an oscillating field by supplying some RF power. This results in an oscillating current, which in turn creates an oscillating magnetic field along the x-direction, called *radiofrequency* or *RF* field (B_1). If the magnetization is disturbed from its equilibrium by an on-resonance pulse (the transmitter frequency matches the Larmor frequency, ω_0), the magnetization undergoes precession in the transverse plane. The precession seems to disappear if the frame of reference is moved to the oscillating *RF* field, which is called the rotating frame.

2.3 The basic NMR experiment

A basic way of obtaining an NMR signal is by the pulse-acquire technique. After placing the sample in the probe and then probe in the magnet, an RF pulse is applied to acquire the FID. A simple pulse sequence for the pulse-acquire experiment[8] is shown in Figure 2.4:

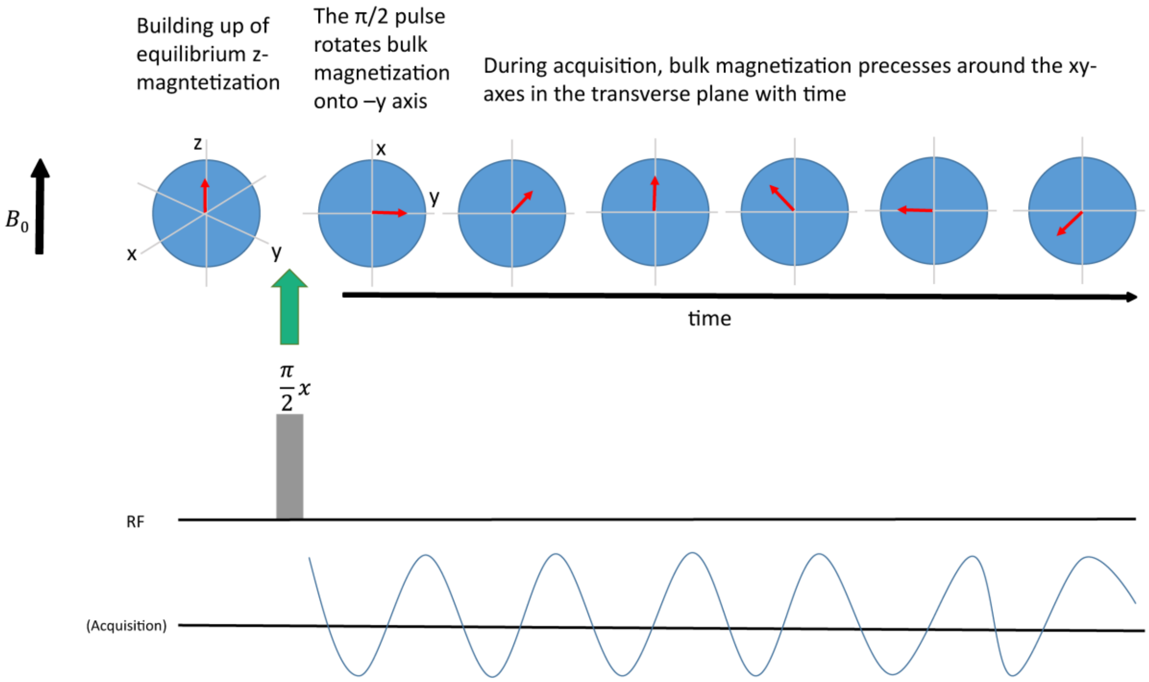

Figure 2.4. Pulse sequence for the pulse-acquire NMR experiment and evolution of the bulk magnetization M_0 during the acquisition time

Using a transverse coil, a π/2 pulse is applied which rotates the bulk magnetization from +*z* to the -*y* direction. After this, the bulk magnetization undergoes precession about the main magnetic field generating an oscillating magnetic field which induces an oscillating current in the transverse coil of the NMR probe. This oscillating current (NMR signal) in the time domain is then digitized and Fourier transformed to the frequency domain spectrum.

2.4 The Echo pulse sequences

In solid samples, line broadening is very common due to the short length of the FID, especially in the static spectrum (without spinning the sample at magic angle 54.74˚). The short FID in solids is due to the lack of molecular motion (which is commonly seen in solution) which causes the nuclear spins to experience a wide range of local magnetic environments, leading to difference in precession of frequency of spins, causing the dephasing of transverse magnetization which results in line broadening. Since T_2 relaxation (discussed in section 2.6.2) describes the decay of *xy*-magnetization over time (FID), a short FID results from faster relaxing spins or a rapid loss of phase coherence, leading to broadening of NMR spectra. The length of the FID acquired after the RF pulse during an NMR experiment is inversely proportional to the line width of the NMR signal in the NMR spectrum. A short FID (wideline) in ssNMR implies that there's a limited time window for the signal acquisition before the signal decays significantly, therefore dead time, (a time between the end of a pulse and the time when the receiver is on to collect data) becomes an issue when data points are lost during FID. Additionally in solid echo sequences, the dead time interval must be coordinated with the timing of refocusing pulses to maximize the echo formation and signal enhancement which otherwise adversely affect the quality of echo signal and hence the signal-to-noise ratio. Hence, it is necessary to acquire the data at the beginning of FID. To circumvent the problem of dephasing caused by chemical shift anisotropy, dipolar coupling, quadrupolar coupling, and magnetic field inhomogeneity, a Hahn echo is used.[10] The pulse sequence can be described as ($\pi/2$-τ-π- τ) followed by acquisition of the FID. This pulse sequence is related to the spin echo used in solution NMR to measure T_2. The depiction of the spin-echo pulse sequence[10,11] is shown Figure 2.5 below:

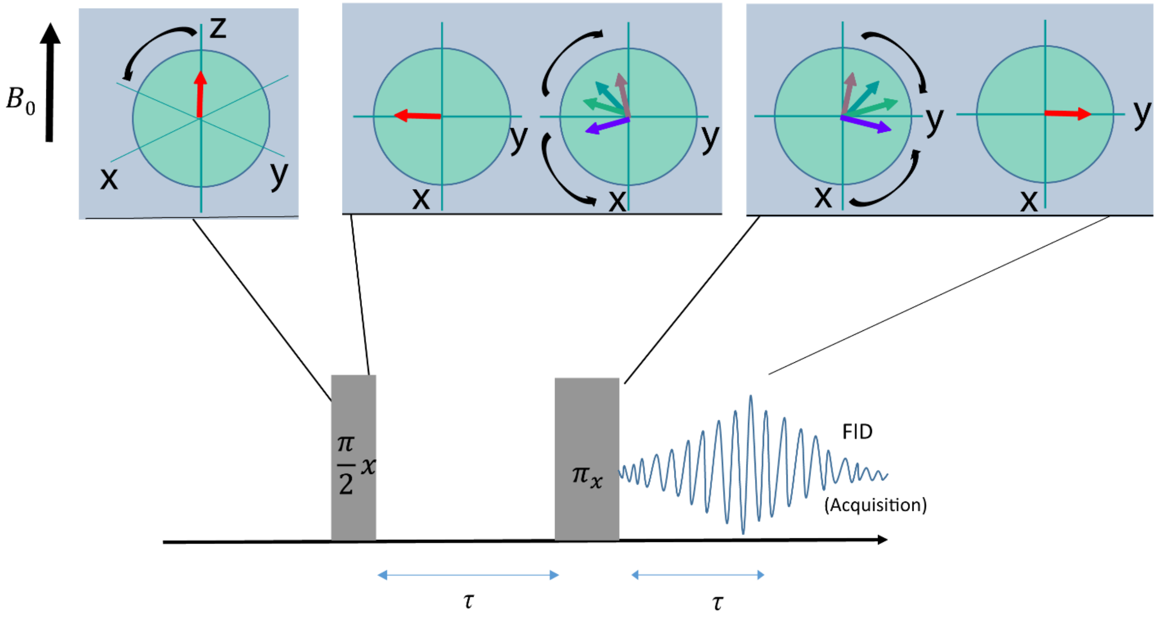

Figure 2.5. Schematic representation of vector diagram (top) and pulse sequence for the Hahn echo.

As shown in Figure 2.5, the initial π/2 excitation pulse brings the magnetization into the transverse plane, *xy*. After the first delay period τ, the magnetization precesses with different rates causing the signal to dephase. The π refocusing pulse inverts all the components of the magnetization, which maintains their initial frequencies, and thus lead to refocusing of all these components along x after the second interphase delay time τ. This removes the dephasing effect, and the FID is collected. Though Hahn echo gives the maximum signal or a strong echo signal (by effectively refocusing the dephased magnetization), it may come with line distortions (artifacts) if an imperfect refocusing pulse is used and if there are any variations in the magnetic field strength.

A quadrupolar spin-echo (designed especially for quadrupolar nuclei) is used for solid-state deuterium NMR experiments, which consists of two π/2 pulses with a time delay of τ. The second π/2 phase shifted pulse has the effect of refocusing the magnetizations at time 2τ to produce an echo. A quadrupolar-echo[12–14] results in reduction in the signal intensity obtained from a Hahn-echo (refocusing pulse in Hahn-echo cancels out the homonuclear dipolar interaction leading to effective echo signal) due to the influence of quadrupolar interactions which are not compensated fully in quadecho. But this comes with a better line shape as in quadecho the delays and pulses are calibrated to get the orientation of quadupolar nuclei, minimizing the coherence; hence the use of a quad-echo is a reasonable compromise when analyzing the solids line shape experiments. A better line shape is obtained with a quad echo because the pulse sequence avoids the loss of first critical data points in the dead time and pulse-breakthrough is avoided, which dramatically improves the spectral line shape. Such undistorted line shapes can be obtained up to a linewidth of 200 kHz.[15,16] The quadrupolar-spin echo approach is extremely useful in ^{2}H solid-state NMR experiments because of the smaller quadrupolar coupling constant and the local axially symmetric interaction associated with ^{2}H nuclei in a symmetric environment.

2.5 NMR interactions

The Zeeman interaction is the strongest interaction found in NMR and is dependent on the external magnetic field. The internal NMR interactions such as magnetic shielding, quadrupolar interactions, dipolar couplings, and scalar coupling affect the Zeeman energy levels and hence it is possible to gain the structural information from the NMR spectrum.[17] Below, the NMR interactions discussed briefly.

2.5.1 Magnetic Shielding (σ) and Chemical Shift Anisotropy (CSA)

An external magnetic field applied to a polyatomic molecule produces an additional magnetic field at the nucleus via the motion of the electrons. This new field arising at the nucleus gives rise to a slight difference in net resultant field at the nucleus which leads to frequency shifts in NMR spectra. This effect is called the magnetic shielding interaction and is denoted by σ. The frequency shift that this interaction causes in an NMR spectrum is called the chemical shift, denoted as δ. According to Ramsey's theory,[18] the shielding mechanism contains diamagnetic and paramagnetic contributions. Diamagnetic shielding arises due to the circulation of electrons under the external magnetic field, which in turn produces the secondary field opposing the applied field at the centre of motion. Consequently, this field tends to shield the nucleus. Paramagnetic shielding involves the distortion of electron distribution by the external magnetic field described as the mixing of excited electronic states into the original ground state. This generates a field, which supports the applied field at the nucleus and deshields the nucleus. The Hamiltonian for the Zeeman interaction and magnetic shielding interaction is expressed using the following equation:[19,20]

$$\widehat{H}_{z+\sigma} = \frac{\gamma}{2\pi} . \hat{I} . (1-\sigma) . B_0 \qquad \text{Eq. 2.5.1.1}$$

Where B_0 is the applied field, σ is a second-rank Cartesian tensor, γ is the magnetogyric ratio of the nucleus involved. The Zeeman shielding Hamiltonian in Eq. 2.5.1.1 can be re-written as follows:

$$\widehat{H}_{z+\sigma} = \frac{\gamma}{2\pi} \left(\widehat{I_x}, \widehat{I_y}, \widehat{I_z}\right) \begin{pmatrix} 1-\sigma_{xx} & \sigma_{xy} & \sigma_{xz} \\ \sigma_{yx} & 1-\sigma_{yy} & \sigma_{yz} \\ \sigma_{zx} & \sigma_{zy} & 1-\sigma_{zz} \end{pmatrix} \begin{pmatrix} 0 \\ 0 \\ B_0 \end{pmatrix} \qquad \text{Eq. 2.5.1.2}$$

Where x, y, z axes refer to the laboratory-fixed axis system, where z-axis is along the direction of applied magnetic field B_0.

Under the secular approximation[21] or the first order perturbation, the Zeeman shielding Hamiltonian is the following:

$$\widehat{H}_{z+\sigma} = \frac{\gamma B_0}{2\pi} \widehat{I_z} . (1-\sigma_{zz}) \qquad \text{Eq. 2.5.1.3}$$

σ_{zz} is the magnetic shielding along the z-direction of the magnetic field and is different for chemically different nuclei in the sample. It can take negative or positive values. The magnetic field at the nucleus varies depending on the chemical environment considered. σ_{zz} is calculated using the following expression:[20–22]

$$\sigma_{zz} = \sigma_{11} sin^2\theta cos^2\phi + \sigma_{22} sin^2\theta sin^2\phi + \sigma_{33} cos^2\phi \qquad \text{Eq. 2.5.1.4}$$

σ_{ii} are the principal components of the magnetic shielding tensor and ordered as $\sigma_{33} \geq \sigma_{22} \geq \sigma_{11}$. θ, ϕ are polar angles in the Cartesian coordinate system defining the orientation of the magnetic shielding tensor.

The NMR frequency thus depends both on the magnetogyric ratio and on the effective magnetic field seen by the nucleus due to the shielding effect discussed above. Magnetic shielding (σ) cannot be measured directly in an NMR experiment. Rather, chemical shifts, δ, are measured. As the frequency of absorption depends on field strength, NMR frequencies (v) are reported as chemical shifts with respect to a reference compound frequency and is expressed as following:[7,20,23]

$$\delta_{ii} = \frac{v - v_{ref}}{v_{ref}} = \frac{\sigma_{ref} - \sigma_{ii}}{1 - \sigma_{ref}} \qquad \text{Eq. 2.5.1.4}$$

Where v is the spectral frequency in Hz of the signal corresponding to the spin of interest in its given chemical site, v_{ref} is the resonance frequency of the reference compound corresponding to the same spin. The corresponding chemical shift tensors are, σ_{ref} the shielding constant of a reference compound, and δ_{ii} is the tensor component corresponding to magnetic shielding tensor component σ_{ii}. The unit used for chemical shift is ppm (parts per million) and is represented as follows:

$$\delta_{ppm} = \frac{\nu - \nu_{ref}}{\nu_{ref}} \times 10^6 \qquad \text{Eq. 2.5.1.5}$$

The chemical shift is very sensitive to local chemical environment and changes accordingly.

In solution, due to molecular tumbling, the anisotropy of the chemical shift arising due to different orientations of the molecules is averaged[23] and thus only the isotropic chemical shift (δ_{iso}) is measured. The dynamic environment averages out the variation in the local magnetic field experienced by nucleus in solution and faster T_2 relaxation causes narrower linewidth and hence sharp signals. The expression for isotropic chemical shift δ_{iso} as follows:

$$\delta_{iso} = \frac{\delta_{11} + \delta_{22} + \delta_{33}}{3} \qquad \text{Eq. 2.5.1.6}$$

Where δ_{11}, δ_{22}, δ_{33} are the principal values of the chemical shift tensor, and are arranged by convention, $\delta_{11} \geq \delta_{22} \geq \delta_{33}$.

However, in the solid state, molecular motion is restricted and anisotropic interactions are not typically averaged out. This results in broad solid-state NMR spectra, which contain a wealth of information. CSA (chemical shielding anisotropy) is defined as ($\sigma_{\perp} - \sigma_{\parallel}$), where $\sigma_{\perp}$ and $\sigma_{\parallel}$ are the two independent components in the case of axial symmetry.[24] CSA line shapes may be described using the Herzfeld-Berger convention.[25,26] In addition to the isotropic chemical shift; two additional parameters are used to describe the line shape: Ω and κ. The span (Ω) is used to quantify the breadth of the powder pattern (defined as different molecular orientations corresponding to a different orientation of principal axis frame with respect to the applied magnetic field B_0 and thus having a different chemical shift associated with it) and the skew (κ) defines the asymmetry of the chemical shift tensor.

$$\Omega = \sigma_{33} - \sigma_{11} \approx \delta_{11} - \delta_{33} \qquad \text{Eq. 2.5.1.7}$$

$$\kappa = \frac{3(\sigma_{iso}-\sigma_{22})}{\Omega} \approx \frac{3(\delta_{22}-\delta_{iso})}{\Omega} \qquad \text{Eq. 2.5.1.8}$$

The value of κ in the Eq. 2.2.1.8 varies between -1 and +1 ($-1 \leq \kappa \leq +1$), and the value $\kappa = \pm 1$ denotes an axially symmetric chemical tensor.

In the laboratory Cartesian coordinates, B_0 is normally taken along the z axis, and the shielding (σ_{zz}) alters the resonance frequency. Within the secular approximation, σ_{zz} that contributes to shielding and thereby the resonance frequency can be related to the three principal components via their direction cosines relative to the magnetic field B_0:[24]

$$\sigma_{zz} = \sigma_1 cos^2\theta_1 + \sigma_2 cos^2\theta_2 + \sigma_3 cos^2\theta_3 \qquad \text{Eq. 2.5.1.9}$$

And, the isotropic shielding value is written as, $\sigma_{iso} = \frac{1}{3}(\sigma_{11} + \sigma_{22} + \sigma_{33})$. Now Eq. 2.5.1.9 maybe written as follows:

$$\sigma_{zz} = \sigma_{iso} + \frac{1}{3}\sum_{i=1}^{3}(3cos^2\theta_i - 1)\sigma_i \qquad \text{Eq. 2.5.1.10}$$

For axially symmetric cases, where $\sigma_1 = \sigma_2 = \sigma_\perp$ and $\sigma_3 = \sigma_\parallel$, we get:

$$cos^2\theta_1 + cos^2\theta_2 + cos^2\theta_3 = 1 \qquad \text{Eq. 2.5.1.11}$$

Now the Eq. 2.5.1.9 can be written as,

$$\sigma_{zz} = \sigma_{iso} + {}^1/_3\,(3cos^2\theta_\parallel - 1)(\sigma_\parallel - \sigma_\perp) \qquad \text{Eq. 2.5.1.12}$$

The Eq. 2.5.1.12 shows that the orientation dependent ($3\cos^2\theta$-1) term directly related to the chemical shielding anisotropy leads to a variation in the resonance frequency and thus produces

SSNMR powder patterns shown in the figure below. Individual powder patterns carry a wealth of information but their overlap may render the spectrum hard to interpret. To make this simpler, a commonly used sample rotation technique for removing CSA effects to get narrower linewidths in solids, is magic angle spinning or MAS. MAS is defined as spinning of a sample at an angle θ = 54.74° with respect to the applied magnetic field, such that the molecular dependence of the nuclear spin interaction, $3\cos^2\theta - 1 = 0$, indicating θ is averaged rapidly compared with the anisotropy of the interaction, in turn averaging out the interaction anisotropy to zero. The static powder pattern is illustrated with three possible κ values below in Figure 2.6.

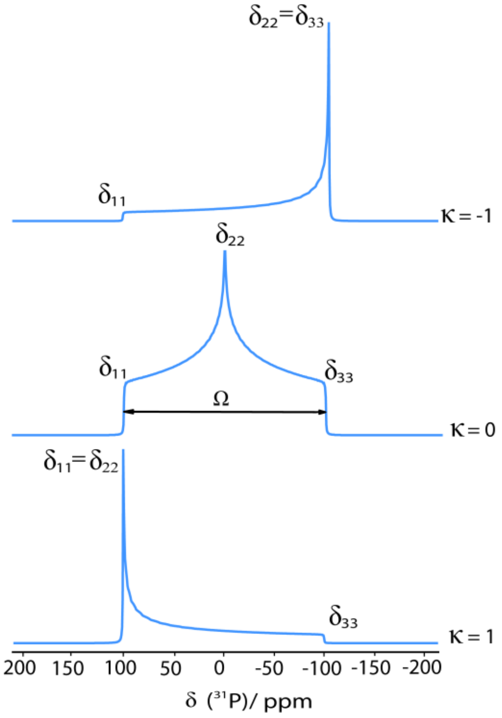

Figure 2.6. Simulated ^{31}P solid-state NMR spectra of a stationary powder (without spinning at magic angle 54.74°) at 9.4 T magnetic field strength. The powder pattern is broadened due to chemical shift anisotropy. The principal values of the chemical shift tensor are illustrated along with the asymmetry parameter (skew, κ) values.

2.5.2 Nuclear Quadrupolar Interaction

Quadrupolar nuclei[27] possess a nuclear spin, I >1/2 constituting approximately 75% of the NMR active nuclei. Unlike spin ½ nuclei which have a spherical charge distribution, quadrupolar nuclei have an asymmetric charge distribution and hence a nuclear electric quadrupole moment, eQ[28,29], where e is proton charge. A few examples of quadrupolar nuclei include ^{2}H (I = 1), ^{7}Li, (I = 3/2) ^{11}B (I = 3/2), ^{14}N (I = 1), ^{17}O (I = 5/2), ^{79}Br (I = 3/2), etc.

The term eQ, quadrupole moment,[30,31] as mentioned arises the non-spherically symmetric nuclear charge distribution. The distribution of the electric point charges may be described as a sum of the multipole moments such as monopole, dipole, quadrupole, etc. The monopole term is affected by electric potential, a dipole is affected by electric field or potential gradient and a quadrupole is affected by the inhomogeneous electric field or electric field gradient i.e. d^2V/dz^2. Q is a constant and is specific to each nuclear isotope, which might take either a positive or negative sign depending on the distribution of nuclear charge. If the nuclear charge is elongated along the nuclear spin direction, then it takes on a positive value for Q and if compressed then Q becomes negative.[7,31] A pictorial representation of prolate (positive Q) and oblate (negative Q) shapes of the nuclear charge distribution is shown in Figure 2.7.

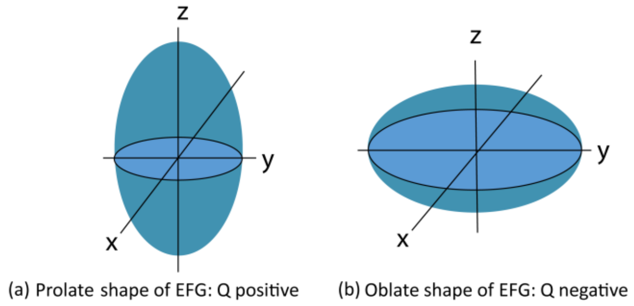

(a) Prolate shape of EFG: Q positive (b) Oblate shape of EFG: Q negative

Figure 2.7. Illustration of quadrupolar nuclei based on distribution of electric field gradient (EFG) around the nucleus. (a) prolate shape ellipsoid (b) oblate shape ellipsoid.

What is important in NMR of quadrupolar nuclei is the interaction between the nuclear electric quadrupole moment and the surrounding electric field gradient (EFG) **V** which depends on the orientation of the nuclear spin, in turn affecting the nuclear spin energy levels. The quadrupole interaction strength in NMR is largely dependent on the magnitudes of Q and the EFG tensor, **V**. The components of **V**, which describes the magnitude, and orientation of the EFG in a coordinate system, are very important factors determining NMR line shapes. The magnitude of the EFG at the nucleus is given bythe 2nd rank tensor below:

$$\mathrm{V} = \begin{pmatrix} V_{xx} & V_{xy} & V_{xz} \\ V_{yx} & V_{yy} & V_{yz} \\ V_{zx} & V_{zy} & V_{zz} \end{pmatrix} = \begin{pmatrix} V_{11} & 00 & 00 \\ 00 & V_{22} & 00 \\ 00 & 00 & V_{33} \end{pmatrix} \qquad \text{Eq. 2.5.2.1}$$

The principal axis system is shown on the right in Eq. 2.5.2.1, where the 2nd rank tensor is converted to diagonal form where V_{11}, V_{22}, V_{33} are principal components of the electric field gradient tensor at the nuclear site and describe the size and shape of the field gradient. By convention $|V_{33}| \geq |V_{22}| \geq |V_{11}|$ and the largest component is V_{33}. In solution, the interaction reduces to one third of trace as expressed below:

$$V_{\mathrm{iso}} = 1/3\ (\mathrm{Tr}(V)) = 1/3\ (V_{11} + V_{22} + V_{33}) \qquad \text{Eq. 2.5.2.2}$$

where ($V_{11} + V_{22} + V_{33} = 0$) as the tensor is traceless indicating that the quadrupole interactions[7,24] average to zero in solution NMR and as a result does not affect NMR spectra of rapid tumbling or in molecules undergoing rapid motions. The EFG tensor can be represented as an ellipsoid surrounding the nucleus with 3 principal components along the three major axes as illustrated below in Figure 2.8:

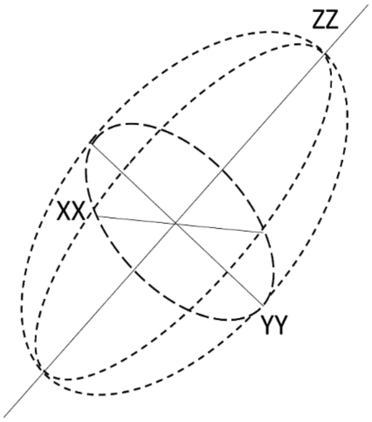

Figure 2.8. EFG tensor view as an ellipsoid surrounding a nucleus with 3 principal components along 3 major axes.

The parameters that characterize the magnitude of EFG tensor are the quadrupolar coupling constant, C_Q and asymmetry parameter (η). C_Q may vary up to megahertz in magnitude and hence, quadrupolar broadening becomes dominant in the solid state. The following is the equation for C_Q:[32]

$$C_Q = \frac{e^2QV_{33}}{h} \qquad \text{Eq. 2.5.2.1}$$

Where e is the Coulombic charge, Q is the nuclear quadrupole moment, V_{33} is the largest principal component of the tensor, and h is Planck's constant. C_Q is expressed in frequency units. The asymmetry parameter is dimensionless which ranges from 0 to 1 and is expressed as follows:[29,33]

$$\eta = \frac{V_{22}-V_{11}}{V_{33}} \qquad \text{Eq. 2.5.2.2}$$

If the EFG is symmetric about the PAS (an axis frame chosen such that an interaction tensor is diagonal with respect to the axis system and the orientation of PAS is determined by the local environment of the nucleus to which the interaction pertains) where interaction, V_{33} becomes unique with $V_{11} = V_{22}$, and η equals zero. The interaction is called "axially symmetric" about the largest EFG component.[33] The magnitude of the EFG depends on the arrangement of the chemical bonds. This is particularly true in case of ^{2}H NMR where deuterium makes a single bond with a neighbouring atom and this bond is identical to the direction V_{33}. To a good approximation, $\eta = 0$ and V_{33} is in the direction of the bond in case where deuterium makes a single bond with carbon where the Zeeman interactions is larger compared to quadrupole interaction. The simulated line shape for ^{2}H NMR in the solid state at 4.7 T magnetic field with Larmor frequency of 30.7 MHz is given below in Figure 2.9 with different asymmetry parameters:

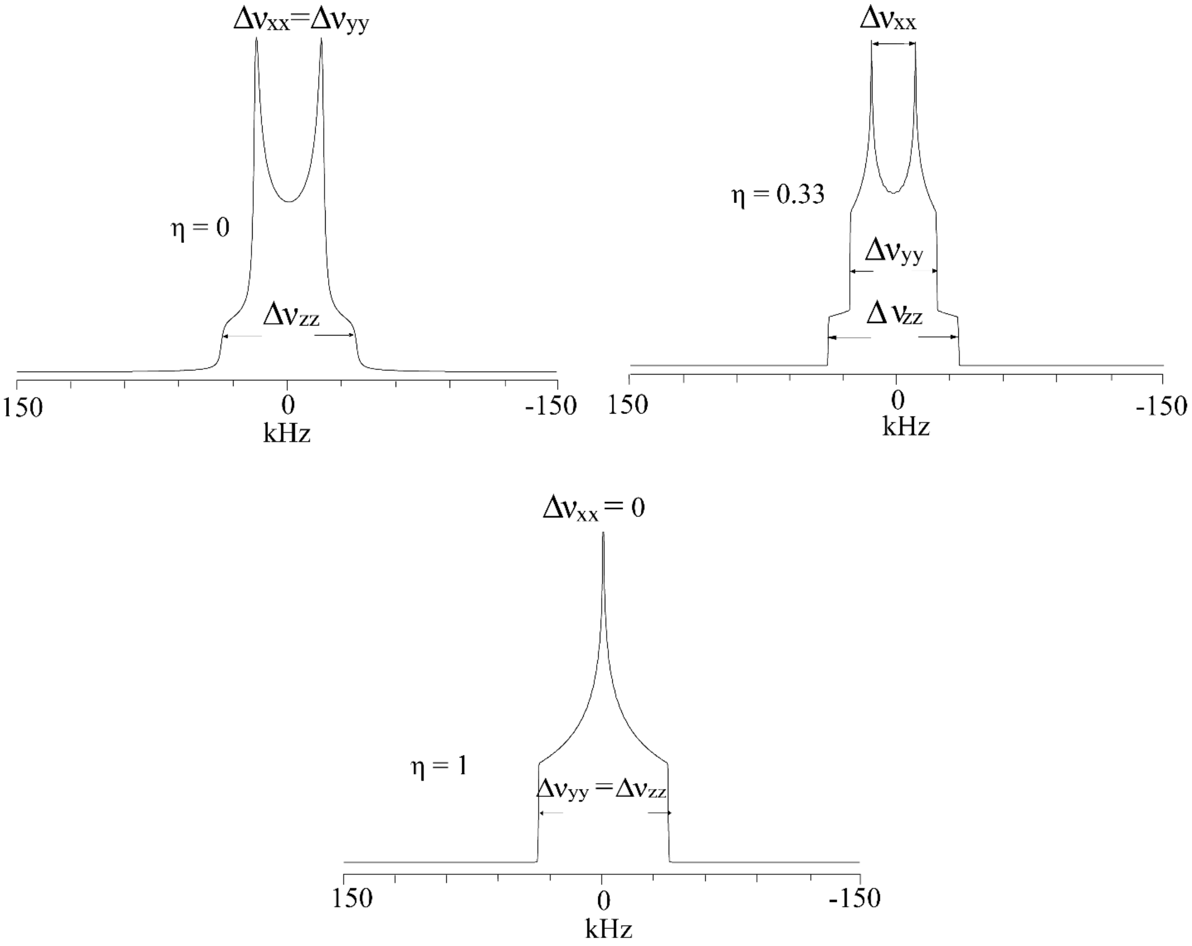

Figure 2.9. Simulated ^{2}H line shape illustration when $\eta = 0$, $\eta = 0.33$, $\eta = 1$.

The quadrupolar Hamiltonian that describes the interaction between the nuclear quadrupole moment (*eQ*) and electric field gradient (EFG) **V** is described below in Eq. 2.5.2.3:[34]

$$\widehat{H_Q} = \frac{eQ}{2I(2I-1)\hbar}\hat{I}.V.\hat{I} = \frac{eQ}{2I(2I-1)\hbar}(\widehat{I_x},\widehat{I_y},\widehat{I_z})\begin{pmatrix} V_{xx} & V_{xy} & V_{xz} \\ V_{yx} & V_{yy} & V_{yz} \\ V_{zx} & V_{zy} & V_{zz} \end{pmatrix}\begin{pmatrix} I_x \\ I_y \\ I_z \end{pmatrix} \qquad \text{Eq. 2.5.2.3}$$

Where **V** is the EFG tensor, $\hat{I}$ is the nuclear spin vector for a spin I, and $\hbar$ is the reduced Planck constant.

In the principal axis system (PAS) frame, the quadrupolar Hamiltonian can be written as follows:

$$\widehat{H_Q} = \frac{eQ}{6I(2I-1)\hbar}\left[V_{11}\left(3\hat{I}_x^2 - \hat{I}\right) + V_{22}\left(3\hat{I}_y^2 - \hat{I}\right) + V_{33}\left(3\hat{I}_z^2 - \hat{I}\right)\right] \qquad \text{Eq. 2.5.2.4}$$

Eq. 2.5.2.4 can be also described as follows:

$$\widehat{H_Q} = \frac{eQ}{4I(2I-1)\hbar}V_{33}\left[\left(3\hat{I}_z^2 - \hat{I}\right) + \eta_Q\left(\hat{I}_x^2 - \hat{I}_y^2\right)\right] \qquad \text{Eq. 2.5.2.5}$$

In a strong external field, the Zeeman term is still dominant, so quadrupolar coupling mixes the spin states established by the Zeeman interaction.[21] The quadrupolar interaction is treated as a perturbation to Zeeman states at high field and the first order quadrupolar interaction from Eq. 2.5.2.6 is given as follows:[7,35,36]

$$\widehat{H}_Q^{(1)} = \frac{C_Q}{8I(2I-1)}[3m^2 - I(I+1)]\frac{1}{2}[(3cos^2\theta - 1) + \eta\ cos2\phi\ sin^2\theta] \qquad \text{Eq. 2.5.2.7}$$

Where C_Q is the quadrupolar coupling constant with units of Hz and is denoted as $e^2qQ/\hbar$, and θ and ϕ are polar angles describing the magnetic field ($\mathbf{B}_0$) in the principal axis system (PAS) of the electric field gradient (EFG) tensor.

For the transitions from m to m-1, the first-order quadrupolar contribution to the resonance frequency is given by following expression when the asymmetry is zero ($\eta = 0$):[21,28]

$$\nu_Q{}^{(1)} = \frac{3(2m-1)}{8I(2I-1)}(1 - 3cos^2\theta)C_Q \qquad \text{Eq. 2.5.2.8}$$

When the asymmetry is non zero ($\eta \neq 0$), the transition frequency of EFG is expressed as follows:[21,37]

$$\nu_Q{}^{(1)} = \frac{3(2m-1)}{8I(2I-1)}(1 - 3cos^2\theta - \eta cos2\phi sin^2\theta)C_Q \qquad \text{Eq. 2.5.2.9}$$

As mentioned earlier, quadrupolar nuclei have spin $I \geq$ ½. The spin may take on an integer value so that I = 1, 2, 3, etc. and may also take up values of odd multiples of ½, i.e., I = 3/2, 5/2, 7/2, etc. Nuclei with integer spin do not have a central transition and their spectra are generally spread over a large range of frequencies. The nuclides with spin number equal to odd multiples of ½ possess relatively sharp central transitions (i.e., +1/2↔-1/2, CT) since the first-order quadrupolar effects on these two levels become equal as it depends on the value of spin quantum number m, which is squared (see Eq. 2.5.2.7). This makes the first-order quadrupolar contribution to the central transition zero. This explains why the central transition (CT) is independent of orientation up to first order. However, another type of transition called satellite transitions (ST) are strongly dependent on θ, and the intensity is spread over wide range of frequencies in a powder sample.[21] This is depicted in the Figure 2.10 which shows the schematic representation of (2I+1) energy levels for I = 3/2 nucleus, showing the effect of Zeeman (light green shaded), first-order (light pink shaded) and second-order quadrupolar interaction (yellow color shaded).

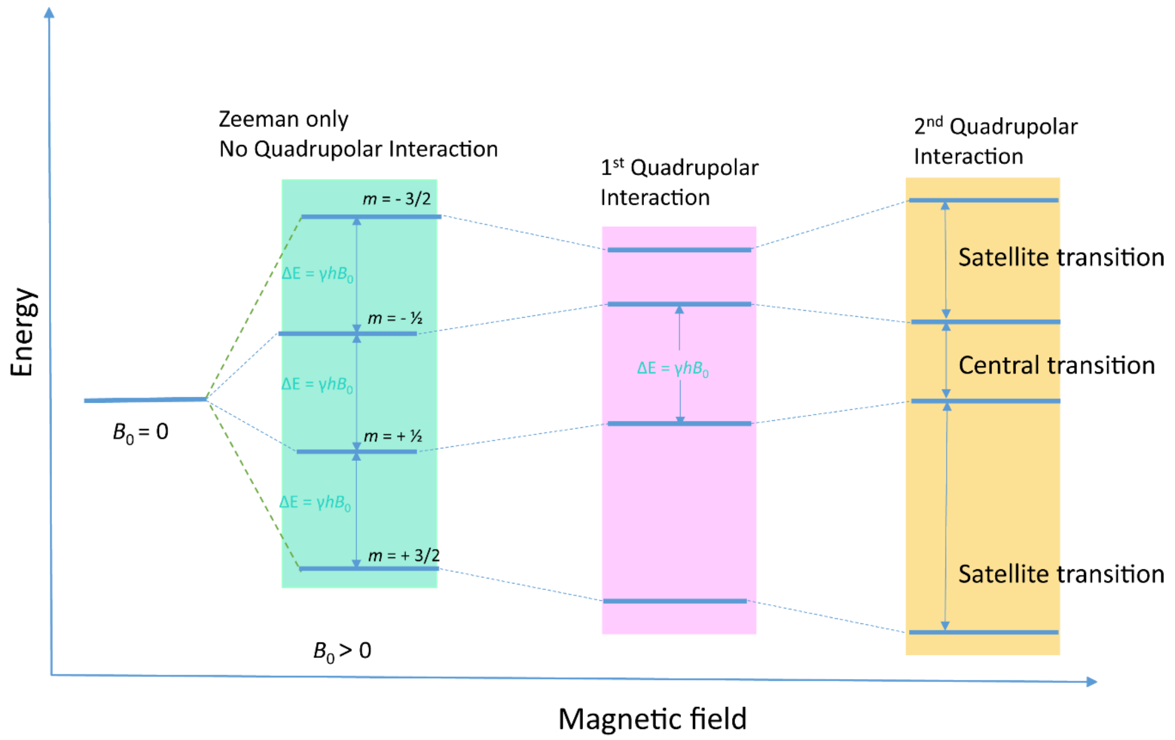

Figure 2.10. Depiction the effect of 1st and 2nd order quadrupolar effects on the Zeeman energy levels in spin 3/2 quadrupolar nuclei.

First-order quadrupolar interaction tends to be quite strong, rendering the first-order approximation insufficient for nuclei with larger quadrupolar coupling constant. Consequently, second-order perturbation is typically required. Experimental demonstrations have shown the necessity of considering higher-order perturbations to accurately replicate the NMR spectra of certain quadrupolar nuclei.[38,39] The second-order quadrupolar interaction affects all the transitions of quadrupolar nuclei including the central transition and the satellite transitions which is described as follows:[20,21,28]

$$\nu_Q{}^{(2)} = -\frac{{C_Q}^2}{\nu_0}\left[\frac{2I+3}{(16I^2)(2I-1)}\right]\left[\frac{3}{10} + \frac{6}{7}P_2(\cos\theta) - \frac{81}{70}P_4(\cos\theta)\right] \qquad \text{Eq. 2.5.2.10}$$

Where ${\nu_Q}^{(2)}$ is the second-order resonance frequency for the central transitions for an axially symmetric case, θ is the angle between V_{33} and B_0, ν_0 is the Larmor frequency, $P_2(\cos\theta) = 1/2(3\cos^2\theta\text{-}1)$ and $P_4(\cos\theta) = 1/8(35\cos^4\theta\text{-}30\cos^2\theta+3)$.

Second-order quadrupolar energy levels for central transitions change differently, meaning they are affected equally but to opposite extents. CT is shifted away from ν_0 as the effect is dependent on the orientation (θ) of the EFG.[40] Second-order effects decrease with increasing B_0 (see Eq. 2.5.2.10) and cannot be eliminated with magic angle spinning (MAS) as they are not solely dependent on the term ($3\cos^2\theta$-1). Rather, an additional term ($35\cos^4\theta - 30\cos^2\theta + 3$) is involved as well. The second-order interaction ranges from several kHz to MHz.

2.5.2.1 Deuterium

Deuterium (^{2}H) is a spin $I = 1$ nucleus with a natural abundance of 0.015%. It can substitute ^{1}H to study organic and inorganic molecules, polymers, and biomolecules by SSNMR and has mainly proven to be useful in the study of molecular dynamics in solids. Considering dominant quadrupolar interaction of ^{2}H, its weak dipolar and chemical shift interactions can be neglected, which simplifies the theoretical analysis of lineshape and relaxation data.

For ^{2}H and ^{6}Li, which possess small Q, the 2nd order corrections are very small and can be usually ignored. The energy level diagram for a spin 1 nucleus with combined Zeeman and quadrupole interactions is given in the Figure 2.11 below:

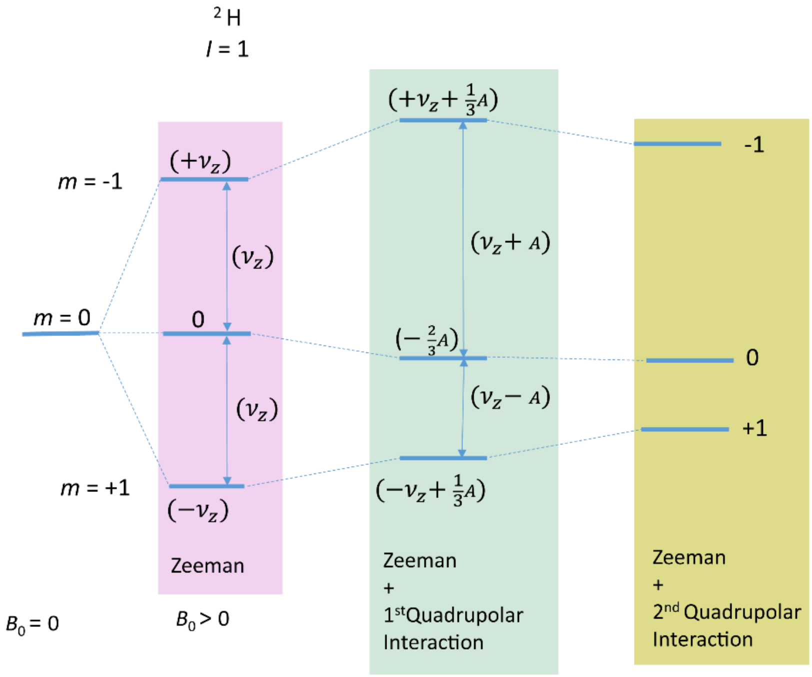

Figure 2.11. Energy levels for an I = 1 nucleus.

For I = 1 nuclei, there are 3 energy levels as (2I+1) = 3, associated with m values of -1, 0, +1. In an axially symmetric case, it is important to note that the transitions m = ± 1 levels are affected in the opposite direction to m = 0 (shown in Eq. 2.5.2.7) level by the quadrupolar interactions. Therefore, one of the $\Delta m = \pm 1$ transitions increases in frequency (as shown in Figure 2.11), while the other one decreases.[21] There can be no central transition. The spectrum for I =1 nucleus interacting with an axially symmetric field gradient gives rise to a doublet with the peak separations given by the following expression:

$$\Delta\nu = \frac{3}{4}\left(\frac{e^2qQ}{h}\right)(3\cos^2\theta - 1) \qquad \text{Eq. 2.5.2.1.1}$$

Where Δv is the separation of peaks in frequency units, θ is the angle between the principal component of the electric field gradient tensor and magnetic field vector. The 3 energy levels as mentioned above is expressed as follows:[41]

$E_{-1} = h\nu_z + {}^{A}/_{3}$ when m = -1

$E_0 = 0 - {}^{2A}/_{3}$ when m = 0

$E_{+1} = -h\nu_z + {}^{A}/_{3}$ when m = +1

Similarly, frequency for allowed transitions are expressed as follows:

$\nu_{0,-1} = h\nu_z + A$ when (m = -1) ↔ (m = 0)

$\nu_{+1,0} = h\nu_z - A$ when (m = +1) ↔ (m = 0)

where $A = \left(\frac{h\nu_Q}{4}\right)[3\cos^2\theta - 1 - \eta cos2\phi \sin^2\theta]$

$[3\cos^2\theta - 1 - \eta cos2\phi \sin^2\theta]$ is the angular term where θ, ϕ relates EFG to B_0 direction.

Quadrupole frequency, $\nu_Q = \frac{3e^2qQ}{2h} = \frac{3}{2}C_Q$

Quadrupole coupling constant, $C_Q = \frac{e^2qQ}{h}$

For deuterons bonded to carbon the value of the quadrupole coupling constant varies from 150 to 200 kHz with the principal axis being along the vector of the bond (C-D). The modulation of the EFG tensor along C-D bonds as methyl groups rotate is studied, which gives an average powder line shape in static ^{2}H NMR experiments, as EFG tensors are oriented at different θ values during the methyl rotation. For other nuclei such as ^{35}Cl, C_Q ranges up to 80 MHz and in ^{14}N it ranges up to 5 MHz making them difficult to study as compared to nuclei with small Q values. Hence, ^{2}H NMR investigation becomes the easiest approach because of the spectral width associated with it.

In the case of a polycrystalline powder sample, Eq. 2.5.2.8 is averaged over all possible crystallite orientations, which yields a Pake doublet spectrum as below:

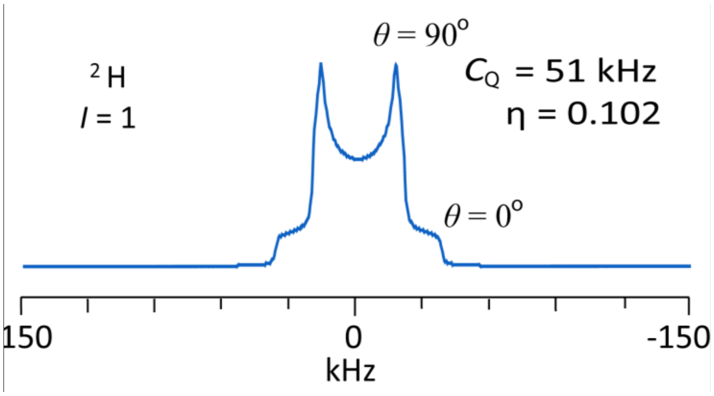

Figure 2.12. ^{2}H line shape showing a powder averaged Pake doublet with $\Delta V_{XX} = \Delta V_{YY}$. The doublet pattern is due to the allowed spin transitions.

The steps of the Pake doublet correspond to $\theta = 0°$, the central peaks corresponds to $\theta = 90°$, and the mid point to the orientation is $\theta = 54.74°$ to the magnetic field, where the quadrupolar splitting and interactions vanish. The total spectrum is the summation of two axially symmetric distributions corresponding to two lines as shown in the above Figure 2.12. The separation of the lines of the central doublet is indicated in Eq. 2.5.2.1.2 and the outermost separation is shown in Eq. 2.5.2.1.3.

$$\Delta\nu_1 = \frac{3}{4}\left(\frac{e^2qQ}{h}\right) \qquad \text{Eq. 2.5.2.1.2}$$

$$\Delta\nu_2 = \frac{3}{2}\left(\frac{e^2qQ}{h}\right) \qquad \text{Eq. 2.5.2.1.3}$$

The ^{2}H powder line shapes (illustrated in Figure 2.12) show characteristic features such as edges, shoulders, peaks separated by frequencies and the expression for $\Delta\nu_{ii}$ are given below in terms of η, asymmetry parameter and ν_Q quadrupole coupling frequency:[42]

$$\Delta\nu_{33} = \nu_Q \qquad \text{Eq. 2.5.2.1.4}$$

$$\Delta\nu_{22} = \frac{\nu_Q}{2}(1+\eta) \qquad \text{Eq. 2.5.2.1.5}$$

$$\Delta\nu_{11} = \frac{\nu_Q}{2}(1-\eta) \qquad \text{Eq. 2.5.2.1.6}$$

The NMR spectrum of a single ^2H in a single crystal sample is a doublet or 2 lines equally spaced on either side of the Zeeman frequency and the peak separation reflects the angle of orientation of the C-D vector to the magnetic field vector. There are several studies reported on single crystal systems using ^2H NMR. D_2O has been explored using ^2H NMR in inorganic salts. Two pairs of ^2H resonance lines were reported in the study of ^2H single crystal study[43] of $Li.SO_4.D_2O$ at room temperature, each corresponding to a single EFG value with quadrupole coupling constant being 123 ± 3 kHz and asymmetry parameter,[44] $\eta = 0.80 \pm 0.02$ with the maximum principal component lying perpendicular to the minimum component in the plane bisecting the D-O-D angle. The same data collected at lower temperature of about -125 °C showed the four pairs of lines with quadrupole coupling constant of 237 ± 10 kHz and asymmetry parameter of about 0.14 ± 0.04 with maximum component of EFG tensor along the O-D bonds in the unit cell. This shows the isolation of two tensors for each of the two ^2H atoms in a D_2O molecule where exchange between the two states can be restricted at lower temperatures.

2.5.3 Direct Dipolar Coupling

Nuclear spins possess magnetic moments and they generate a magnetic field in the direction of the spin magnetic moment. The magnetic field generated is experienced by the nearby spins and is mutual. The interactions between the nuclei propagate through the intervening space and hence are called through-space dipole-dipole couplings or direct dipolar couplings.[1,45] Dipolar coupling depends on the inverse cube of the interatomic distance between the spins and by measuring the dipolar coupling, it is possible to get distance information indirectly.[46,47]

The dipolar coupling constant[31] (R_{DD}) for two coupled spins (j and k) with internuclear distance r_{jk} is given by following equation:

$$R_{DD} = \gamma_j \gamma_k \left(\frac{h}{4\pi^2}\right)\left(\frac{\mu_0}{4\pi}\right) r^{-3}{}_{jk} \qquad \text{Eq. 2.5.3.1}$$

where R_{DD} is the direct dipolar coupling constant, $\gamma_j \gamma_k$, are the magnetogyric ratios of nuclei j and k, and μ_0 is the permeability constant. For a heteronuclear spin pair (J and K) the dipolar splitting given by the following expression:[7,31]

$$\nu_{DD} = -R_{DD} J_z K_z (3cos^2\theta - 1) \qquad \text{Eq. 2.5.3.2}$$

Where θ is the angle between magnetic field and internuclear vector, The dependence of the resonance frequency on the term $(3cos^2\theta - 1)$ in Eq. 2.5.3.2 shows that it is orientation dependent, hence by using higher MAS speed, the dipolar broadening can be reduced along with the use of heteronuclear decoupling techniques while collecting the spectra.[47,48] Whereas in solution NMR dipolar coupling may cause nuclear spin relaxation, due to the fact that isotropic component of the dipolar coupling tensor is zero a splitting effect is not seen on the resonance frequency in solutions.[21]

2.5.4 Indirect Nuclear Spin-Spin Coupling

Indirect nuclear spin-spin coupling, also sometimes called scalar (J) coupling, is the through bond coupling due to an internuclear interaction mediated by bonding electrons. This type of nucleus-nucleus coupling is indirect, indicating that there is assistance of electrons in the coupling mechanism.[1] The involvement of electrons affects the orientation dependence of the interaction, and the isotropic part observed in solutions is non-zero. There are five different mechanisms which contribute to *J* coupling.[49] They are diamagnetic spin-orbital coupling (DSO), paramagnetic spin-orbital coupling (PSO), Fermi-contact coupling (FC), spin-dipolar coupling (SD), and FC-SD cross coupling. DSO and PSO involve the diamagnetic and paramagnetic orbital coupling, which occurs due to the coupling of nuclei through the orbital angular momentum of electrons. SD is the direct dipolar interaction of a nucleus with an electron. The FC mechanism, which is often the largest contributor,[49] involves the interaction between nuclear and electronic spins when the electron is located at the nucleus. Orbitals with significant *s*-character can contribute via the Fermi contact mechanism as these orbitals have a non-zero probability of locating electrons at the nucleus.[50]

J coupling is an experimental measure of the nature of different chemical bonds.[1] As mentioned earlier, *J* coupling is measurable in solution NMR, as the isotropic component is not zero and the *J* coupling tensor is not traceless. This is why we often observe multiplets in solution NMR. In solid-state NMR, *J* coupling may often be smaller in magnitude than the inhomogeneous broadening arising from anisotropic interactions, transverse relaxation, etc. Hence, 1D SSNMR is often not sufficient to directly observe *J* splittings and instead *J*-resolved 2D NMR experiments can be acquired,[51,52] including REDOR[46,52,53] and TEDOR[54] and PRESTO.[55]

The isotropic component of the *J* coupling is expressed as:

$$J_{iso} = \frac{(J_{11}+J_{22}+J_{33})}{3} \qquad \text{Eq. 2.5.4.1}$$

where J_{ii} are the principal components of the tensor. The magnitude of the three components are ordered as: $|J_{33} - J_{iso}| \geq |J_{11} - J_{iso}| \geq |J_{22} - J_{iso}|$.

The anisotropy (ΔJ) and asymmetry parameters of J coupling are noted below:

$$\Delta J = J_{33} - \left(\frac{J_{22} - J_{11}}{2}\right) \qquad \text{Eq. 2.5.4.2}$$

$$\eta_J = \frac{(J_{22} - J_{11})}{(J_{33} - J_{iso})} \qquad \text{Eq. 2.5.4.3}$$

J couplings may be measured using spin-echo experiments where the echo delay periods are multiples of the rotation period. By setting the rotor angle accurately to 54.74˚, anisotropic interactions are refocused over the rotation cycle which leaves only the spin echo signals determined by J couplings that are not refocussed. This occurs due to the presence of isotropic parameter and a time dependent anisotropic term; the ratio of these two parameters result in either single isotropic peak or a static powder pattern or the rotational echoes with spinning sidebands positioned at multiple of MAS speed from the centreband. The refocusing of magnetization occurs each time a rotor completes a cycle and the crystallites returns to their initial positions, producing the rotational echoes. The main concerns in measuring J coupling involve the short T_2 relaxation times. This is partially addressed by high MAS rates (which reduces the time averaged dipolar interactions resulting in longer coherence time, leading slower decay of transverse magnetization), homonuclear decoupling techniques (help in better resolution of peaks and hence narrower linewidth which indirectly helps in increasing T_2 relaxation time) and by prolonging the T_2 relaxation times using high-power and multiple-pulse proton decoupling techniques which involves adjusting parameters such as power and duration of RF pulses to minimize the relaxation induced signal loss.[56]

2.6 General Introduction to Relaxation in SSNMR

As discussed in section 2.2, to reach a Boltzmann distribution spins undergo redistribution or relaxation to equilibrium by first order processes characterized by two relaxation times: T_1, the spin–lattice, or longitudinal, relaxation time; and T_2, the spin-spin, or transverse, relaxation time. The net magnetization of spins whenever perturbed tends to return to an equilibrium state through the interaction of the spin system with the thermal molecular environment.[1] This is considered as the origin of relaxation in NMR. The process may be understood by considering the population difference between the lower energy α-state and upper energy β-state [Let ($n = n_\alpha - n_\beta$) population difference]; let ($n_0 = n_\alpha + n_\beta$) be total population of energy states; let P_+ be the probability for a spin to undergo transition from lower to upper energy state as a result of an interaction with the environment and P_- be the probability for upper to lower energy state. Reaching equilibrium involves changing spin populations between two energy states; hence, longitudinal (T_1) relaxation is defined to arise from the transition between two energy states. Since upward and downward transitions of spin states are equal at equilibrium, we can express the relationship between spin population and probability of spin states as following:[24]

$$P_+ \, n_\alpha = P_- \, n_\beta \qquad \text{Eq. 2.6.1}$$

From Eqs. 2.1.1 and 2.6.1,

$$\frac{P_+}{P_-} = \left(\frac{n_\alpha}{n_\beta}\right)_{eq} = e^{-\gamma h B_0 / 2\pi k T} \qquad \text{Eq. 2.6.2}$$

Since the energy levels are separated only by very few millicalories in NMR, the exponential term gets smaller except at low temperature. Hence using the "high temperature" approximation as $-\gamma h B_0 / 2\pi k T << 1$ for Eq. 2 and defining P as the average of P_+ and P_-, we can write

$$\frac{P_+}{P} = \frac{(n_\beta)_{eq}}{{n_0}/{2}} = 1 - \frac{\gamma h B_0}{2\pi k T}$$ Eq. 2.6.3a

$$\frac{P_-}{P} = \frac{(n_\alpha)_{eq}}{{n_0}/{2}} = 1 - \frac{\gamma h B_0}{2\pi k T}$$ Eq. 2.6.3b

The total change of population n is

$$\frac{dn}{dt} = \frac{dn_\alpha}{dt} - \frac{dn_\beta}{dt} = 2\frac{dn_\alpha}{dt}$$ Eq. 2.6.4

But by definition of P_+ and P_-,

$$\frac{dn}{dt} = n_\beta P_- - n_\alpha P_+$$ Eq. 2.6.5

Hence, we can write,

$$\frac{dn}{dt} = -2P\left(n - n_0\frac{\gamma h B_0}{2\pi k T}\right)$$ Eq. 2.6.6

The Eq. 2.6.6 describes a first-order decay process with rate constant being *2P*, which maybe described as R_1 or $1/T_1$. The term ($n_0\gamma h B_0/2\pi kT$) is the value of equilibrium population n_{eq}. Eq. 2.6.6 can be re-written as,

$$\frac{dn}{dt} = -R_1(n - n_{eq})$$ Eq. 2.6.7

Thus longitudinal relaxation rate (R_1) or time constant (T_1) is a measure with which spin system relax back to equilibrium.

Though there are different types of relaxation processes, solid-state NMR is mainly concerned with following three types: 1) spin-lattice relaxation or longitudinal relaxation, 2) spin-spin relaxation or transverse relaxation, 3) spin-lattice relaxation in the rotating frame. We will discuss here the first two processes in brief.

2.6.1 Spin-lattice relaxation or longitudinal relaxation (T_1)

Longitudinal relaxation is an exponential process for a homogeneous solid sample and is described by the Bloch equation below (re-written from Eq. 2.6.7):[57]

$$\frac{dM_z}{dt} = -\frac{[M_z(t) - M_z^0]}{T_1} \qquad \text{Eq. 2.6.1.1}$$

This Eq. 2.6.1.1 can also be written as follows:

$$\frac{dM_z}{dt} = -R_z\,[M_z(t) - M_z^0] \qquad \text{Eq. 2.6.1.2}$$

Integration of Eq. 2.6.1.2 gives

$$\ln[M_z(t) - M_z^0] = -R_z + const \qquad \text{Eq. 2.6.1.3}$$

At $t = 0$, the magnetization is $M_z(0)$, So Eq. 2.6.1.3 becomes,

$$\ln[M_z(0) - M_z^0] = const.$$

Plugging this value in Eq. 2.6.1.3 we get,

$$\ln[M_z(t) - M_z^0] = -R_z + \ln[M_z(0) - M_z^0] \qquad \text{Eq. 2.6.1.4}$$

Simplifying Eq. 2.6.1.4 by applying exponentials and rearranging gives,

$$M_z(t) = [M_z(0) - M_z^0]e^{(-R_z t)} + M_z^0 \qquad \text{Eq. 2.6.1.5}$$

Eq. 2.6.1.5 shows that the time taken for magnetization to reach equilibrium values becomes shorter as the rate constant R_z becomes larger.

2.6.1.1 Inversion Recovery Experiments: T_1 measurement

To have an estimate for the rate constant R_z for longitudinal relaxation which was discussed earlier or to measure the time constant T_1, the method used in my work is the inversion-recovery experiment. Eq. 2.6.1.5 is useful in providing a framework for an estimate of T_1. The pulse sequence for the inversion-recovery experiment is illustrated below:

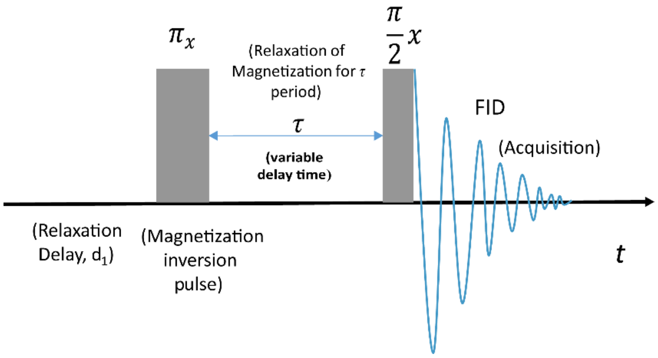

Figure 2.13. Pulse sequence for the inversion recovery experiment to measure the longitudinal relaxation time constant, T_1.

As depicted in Figure 2.13 above, the pulse sequence of *inversion-recovery* experiments[1,8,35] consists of two RF pulses separated by an interval time τ. This experiment is done in an arrayed fashion meaning a series of separate experiments is conducted with the delay time τ taking a set of different values as indicated in the Figure 2.13 as the “variable delay time” between the two pulses. The relaxation delay or recycle delay, d_1, comes at the beginning of the pulse sequence and plays a crucial role in ensuring accurate signal integration by allowing enough time for the spins to relax to their equilibrium value before the pulse is applied. A π pulse inverts the magnetization so that

$M_z(0)$ becomes $-M_z^0$. The inverted magnetization is allowed for a τ time to relax. Using Eq. 2.6.1.5 and considering $t = \tau$ and $M_z(0) = -M_0$, we can write the equation for z-magnetization as follows:

$$M_z(\tau) = -[2M_z^0]e^{(-R_z t)} + M_z^0 \qquad \text{Eq. 2.6.1.1.1}$$

$$M_z(\tau) = M_z^0\left[1 - 2e^{(-R_z t)}\right] \qquad \text{Eq. 2.6.1.1.2}$$

After the time interval τ, a π/2 pulse is applied to bring the magnetization into the *xy*-plane where an FID is observed and then Fourier transformed to give the spectrum.

The pulse sequence and the acquisition are repeated for a range of τ values. The recycle delay or wait time, d_1 mentioned previously is required magnetizations return to the thermal equilibrium. To attain thermal equilibrium, d_1 should be several times grater the T_1 time constant. A rough estimate of T_1 can be achieved by finding the τ value in the inversion-recovery pulse sequence, where signal goes through a null. Under these conditions;

$$0 = M_z^0\left[1 - 2e^{(-R_z t)}\right] \qquad \text{Eq. 2.6.1.1.3}$$

Rearranging the above equation gives, $e^{(-R_z t)} = 1/2$

Hence, $R_z = {-ln\frac{1}{2}}/{\tau_{null}}$ or $R_z = \frac{1}{T_1} = {ln2}/{\tau_{null}}$ Eq. 2.6.1.1.4

Hence, by estimating the τ_{null} value from the experiment we will be able to calculate an estimate for the T_1 value by using the relationship in Eq. 2.6.1.1.4.

If we assume that there is no z-magnetization at the end of pulse so that $M_z(0)$ becomes zero, $M_z(d_1) = nM_0$ where n is the fraction of equilibrium magnetization and after the d_1 delay $\tau = d_1$, from Eq. 2.6.1.4 we get the following expression:

$$nM_z(d_1) - M_z^0 = [0 - M_z^0]e^{(-R_z t)}$$ Eq. 2.6.1.1.5

This is simplified to,

$$d_1 = -T_1 \ln(1 - n)$$ Eq. 2.6.1.1.6

If we assume that there is no z-magnetization at the end of pulse, $M_z(0)$ becomes zero, we can work out the relaxation delay, d_1, This implies that it takes an infinite amount of time for the magnetization to return to equilibrium completely, i.e., to become $n = 1$. However, to return to 99% ($n = 0.99$), $d_1 = 4.6T_1$. Therefore, in practice d_1 is typically set to five times T_1 is used. If there are different nuclei with different T_1 values in the same sample then the longest T_1 is selected to set the d_1 value.

2.6.2 Spin-Spin Relaxation or Transverse Relaxation (T_2)

Transverse relaxation, denoted by T_2, is a quantification of rate of decay of the magnetization in the *xy*-plane. M_{xy} is orthogonal to M_z, and hence relaxation may be different compared to longitudinal relaxation, although the mechanisms of relaxation may be the same. In the case of T_2 relaxation, after the pulse, spins align themselves in the xy-plane due to phase coherence and gradually the coherence is lost due to field inhomogeneity or/and direct interactions between the spins without any energy transfer to surrounding lattice. T_2 relaxation time constants in solids are very short, often on the order of microseconds to milliseconds. To be more precise, T_2 specifically denotes intrinsic dephasing, that would occur in a perfectly homogenous magnetic field. In a real magnetic field, which inevitably possesses some degree of inhomogeneity, the transverse relaxation time is represented by T_2^* and is directly related to the linewidth or line shape of the resonances.[21]

$$T_2^* = {}^{1}\!/_{\Delta\nu_{\frac{1}{2}}} \qquad \text{Eq. 2.6.2.1}$$

where $\Delta\nu_{\frac{1}{2}}$ is the half-height of the NMR signal. $T_2 \leq T_1$, since an increase in z-magnetization will decrease xy magnetization. In solution T_2 is often equal to T_1 while in solids $T_2 << T_1$.

2.6.3 Relaxation and Rotational Dynamics

Solid state NMR is an excellent method to study dynamics as nuclear spin interactions are anisotropic, meaning they depend on the molecular orientation within the applied magnetic field of the NMR experiments.[7] A transverse magnetic field oscillating at the Larmor frequency is needed to rotate the magnetization from the xy plane to to the z-axis and this may be done manually using an appropriate RF pulse but this also occurs naturally within the sample due to the nuclear relaxation. These interactions involve electric fields for quadrupolar nuclei; fields generated by dipoles for spin ½ nuclei, and/or due to the anisotropy of the electron distribution. The RF pulse affects all the spins same way whereas the field generated by a spin is highly localized and it varies in magnitude and orientation as the molecules experience the motion. If this motion results in the transverse component of the field oscillating near the Larmor frequency, then field experienced by the magnetic moment of the spin is rotated to the new direction in the same way as it would be by an rf pulse. The oscillating fields that may arise from molecular motions in solids are incoherent and such motions may involve a rotation or ring flipping motions in solids for which there maybe a range of frequencies involved; here we consider the spectral density function[58] to describe the range of frequencies which is broad and continuous. In NMR among the range of frequencies, the contribution at the Larmor frequency governs the strength of the oscillating field that can cause the relaxation.

Molecular motions can be described by a function $f(t)$ which is the time dependent position or orientation of a molecule in the sample; its position after a time τ is $f(t+\tau)$, and the autocorrelation function $G(\tau)$ for many such molecules which is a measure of proportion of molecules in the sample having the same position at time $(t + \tau)$ as they did at t is defined by

$$G(\tau) = \overline{f(t)f(t+\tau)} \qquad \text{Eq. 2.6.3.1}$$

Where the bar indicates the average over entire ensemble of molecules. $G(\tau)$ is related to the initial position in an exponential manner, i.e., the two positions are different after a long time τ. Hence $G(\tau)$ can be expressed as follows:

$$G(\tau) = e^{\left(\frac{-\tau}{\tau_c}\right)} \qquad \text{Eq. 2.6.3.2}$$

Where τ_c is the (rotational) correlation time for the molecular motion which is defined as the average time it takes for a molecule to complete a rotation of 1 radian from the starting position.[8] Fourier transform of correlation function $G(\tau)$ is called $J(\omega)$, a spectral density function:

$$J(\omega) = \overline{B_{loc}^2}\frac{2\tau_c}{1+\omega^2\tau_c^2} \qquad \text{Eq. 2.6.3.4}$$

Where the term $\overline{B_{loc}^2}$ is the local field associated with the NMR interactions.

The motion at the Larmor frequency can be quantified by evaluating $J(\omega)$ at $\omega = \omega_0$. The reciprocal of the Larmor frequency ω_0 is comparable to τ_c values, and either very short or long τ_c values of $J(\omega)$ at ω_0 is relatively small. $J(\omega)$ reaches its maximum value when $\tau_c\omega_0 = 1$, i.e., when the frequency of average rotational motion is equal to the nuclear precession frequency. Under such a condition, energy transfer between the precessing nuclei and rotational motion of molecules is most efficient, the relaxation rate is maximum, and T_1 is a minimum. For fast motion with short

τ_c, $\tau_c\omega_0 << 1$, resulting in longer T_1. In this 'extreme narrowing' regime, T_1 is inversely proportional to τ_c. In the slow motion regime, $\tau_c\omega_0 >> 1$, faster relaxation occurs due to increased motion and T_1 is directly proportional to τ_c. For solids, $R_1 = CB^2/2\omega_0$ and relaxation efficiency decreases with an increase in resonance frequency and B^2 is independent of the field.

There are mechanisms of relaxation[1,8,21,59,60] such as shielding/chemical shift anisotropy (CSA), dipolar coupling, quadrupolar coupling,[61] relaxation by paramagnetic species[62] which induces the fluctuating local field depending on nucleus of the study.

2.7 Mechanisms of Relaxation

A particular source of a fluctuating local magnetic field experienced by the nuclei is called a relaxation mechanism.[8] The dipolar mechanism and chemical shift anisotropy mechanism are the two dominant relaxation mechanisms seen for spin ½ nuclei. For spin ½ nuclei the usual order of importance of relaxation mechanisms follows the trend shown below:

dipole-dipole > chemical shift anisotropy

For nuclei with spin > ½ the order of importance of the relaxation mechanisms is shown as follows:[1,63]

quadrupole >> dipole-dipole > CSA

The electric quadrupole relaxation mechanism dominates the relaxation of spins > ½ and its effects are seen clearly in NMR spectra. We will briefly discuss the dipolar mechanism and chemical shift anisotropy mechanism in spin ½ nuclei to start with and then the quadrupole relaxation mechanism as this thesis focusses on the spin-1 quadrupolar nucleus, ^{2}H.

2.7.1 The Dipolar Mechanism of Relaxation

Fluctuating magnetic fields arise due to the magnetic moment or magnetic dipole involving two nuclear sites. This results in dipole-dipole coupling between the two nuclear spins where the magnitude and direction of the magnetic field exerted by one spin on the other changes, leading to relaxation. The local field exerted by the nuclear spins depends on the distance (*r*) between the spins, and the dipolar interaction is related to *r* as $1/r^3$ indicating that as the distance between nuclear site increases, the dipolar interaction weakens.[45] The higher the magnetogyric ratio, the larger is the magnetic moment causing the local field between the nuclear spins; and hence a stronger dipolar interaction. The local fields can be caused by more than one spin; hence relaxation is caused by either a single or multiple spins in close proximity.

For homonuclear spin pair, relaxation rate is given by

$$R_1 = \left(\frac{\mu_0}{4\pi}\right)^2 \gamma_{1,2}^4 h^2 \frac{\tau_c}{r_{1,2}^6} \qquad \text{Eq. 2.7.1.1}$$

For heteronuclear spin pair 1 and 2, relaxation rate is expresses as follows:

$$R_1 = \left(\frac{\mu_0}{4\pi}\right)^2 \gamma_1^2 \gamma_2^2 h^2 \frac{\tau_c}{r_{1,2}^6} \qquad \text{Eq. 2.7.1.2}$$

Where *r* is the separation between the spin pair.

The local field fluctuates in magnitude and direction with the motion, and thus generates an oscillating field with frequencies of oscillation dependent on τ_c. The field can interact with molecular magnetic component at the Larmor precession frequency, which provides a time-dependent perturbation. As discussed in section 2.6.3 the effectiveness of the fluctuating local field bringing about relaxation depends on the Larmor frequency as well the square of the interaction energy (Eq. 2.6.3.4).

Additionally, the dipolar interaction between two spins may lead to relaxation via four energy levels[8,24], namely αα, ββ (where spin 1 and spin 2 are in the same energy state) and αβ, βα (where spin 1 and spin 2 are in the different energy states). The single quantum transitions with change in total magnetic quantum number (Δm) associated with the transition equal to 1 which involves one of the spins flipping at a time. The double quantum transition involves $\Delta m = 2$ both the spins flip between energy states (αα) and (ββ); zero quantum transition is denoted by $\Delta m = 0$ where transition is between the energy states (αβ) and (βα) where both the spins flip simultaneously. The single quantum relaxation rates that are induced my molecular motions depend on the spectral density at Larmor frequency of either spin 1 or 2. Double quantum relaxation rate depends on the sum of the Larmor frequencies of spin 1 and 2; while zero quantum relaxation rate depends on the spectral density at the difference of the two Larmor frequencies of spin 1 and 2.

2.7.2 Chemical Shift Anisotropy

CSA strongly depends on the bonding environment. The local field generated is proportional to the applied field and its interaction with the nucleus depends on the magnetogyric ratio of the nucleus. The anisotropy in chemical shielding leads to a dispersion of resonance frequencies for molecules in solids as discussed in section 2.5.1. The general rules discussed in section 2.6.3, anisotropy in chemical shielding due to distribution of electrons leads to relaxation.

From Eqs. 2.5.1.3 and 2.5.1.12, we can write the following relaxation expression for CSA (R_1) for an axially symmetric shielding tensor:[64]

$$R_1^{CSA} = \frac{2}{15}\gamma^2 B_0^2(\sigma_{\parallel} - \sigma_{\perp})^2\tau_c \qquad \text{Eq. 2.7.2.1}$$

Hence, R_1^{CSA} quadratically increases with B_0, and becomes significant at higher field, and is dependent on the chemical environment of the nucleus [shielding anisotropy term $(\sigma_{\parallel} - \sigma_{\perp})$] and correlation time of motion involved.

2.7.3 Electric Quadrupole Relaxation

For nuclei with spin > ½, the interaction between the nuclear electric quadrupole moment and the electric field gradient caused by the surrounding electrons and ions becomes very crucial in the case of solids. It usually dominates dipolar and chemical shift relaxation mechanisms discussed above.

The theory of quadrupolar relaxation is complex in general, but it can be simplified in terms of molecular rotation and by assuming axial symmetry of the molecular electric field.[28] The interaction energy between the nucleus and the electric field gradient from the Eq. 2.5.2.7 quadratically given by the following rate equation for a spin-1 nucleus:[65,66]

$$R_1^{Q} = \frac{1}{T_1^{Q}} = \frac{3}{10}\pi^2\frac{2I+3}{I^2(2I-1)}C_Q^2\left(1+\frac{\eta^2}{3}\right)\times\{J(\omega_0)+4J(2\omega_0)\} \qquad \text{Eq. 2.7.3.1}$$

where C_Q is the quadrupolar coupling constant, η is the asymmetry parameter, I is the spin quantum number, R_1 is the relaxation rate and T_1 is the longitudinal time constant. $J(\omega_0)$ is the spectral density function at ω_0.

The quadrupolar coupling constant, C_Q could be zero for a highly symmetric system[67] such as $^{35/37}Cl^-$ ion and tetrahedral $^{14}NH_4^+$, but can be very large in other cases such as ^{93}Nb in $NaNbO_3$ which is about 19.5 MHz.[68] For ^2H, C_Q is generally 100-200 kHz with relaxation times of several milliseconds in solids and for ^{14}N, C_Q is typically a few MHz leading to T_1 and T_2 of 10-20 ms. For bromine ($^{79/81}$Br) and chlorine ($^{35/37}$Cl) in lower symmetry environments, C_Q is ~100 MHz with T_1 on the order of microseconds. Since quadrupolar nuclei have spin > ½, there are many energy levels to consider, and the transition relaxation probability between different energy levels may differ too. For example,[69] in the case of ^{23}Na with $I = 3/2$, there are distinct relaxation rates for the $m = -1/2$ to $+1/2$ transition and the $\pm 1/2$ to $\pm 3/2$ transitions. The relaxation rates and linewidths of quadrupolar nuclei in solution also depend on correlation time τ_c, spin quantum number I, quadrupolar moment eQ, and electric field gradient V_{zz}.[70]

Quadrupolar linewidths depend on the Q values of different nuclei. The smaller Q values give rise to relatively sharp lines or less broad lines for nuclei such as ^{2}H and ^{133}Cs. In case of nuclei with larger Q values, the linewidth is broader, such as for ^{79}Br and ^{35}Cl. In the case of ^{127}I it Q is so large that it becomes too difficult to study by NMR. The linewidth factor L can be given by following equation where I and Q are characteristic of a given nucleus:[70]

$$L = \frac{Q^2(2I+3)}{I^2(2I-1)} \qquad \text{Eq. 2.7.3.3}$$

Eq. 2.7.3.3 becomes important when an element has more than one quadrupolar isotope in the same samples such as ^{63}Cu/^{65}Cu or ^{95}Mo/^{97}Mo. The direct relationship between L and Q^2 shows that ratio of linewidths can be used to find the ratios of quadrupole moments.

Symmetrical sites such as spherical, tetrahedral or cubic sites result in zero field gradient and hence sharp lines. Yet there maybe long-range order in those samples that would give rise to quadrupolar relaxation and line broadening effects. In the case of ^{35}Cl the linewidth of aqueous NaCl is around 10 Hz and in case of CCl_4 it is found to be 10 kHz[70,71] which reflects the lower local symmetry; hence electrical symmetry can cause smaller linewidths than expected from simple molecular symmetry considerations.

2.8 Effects of dynamics on ^{2}H line shapes and applications

Deuterium NMR is a powerful tool to study molecular motions. As deuterium has a low natural abundance, it becomes important to isotopically label the samples to observe deuterium solid-state NMR spectra. Deuterium being a quadrupolar nucleus, its lineshape depends on the quadrupolar interaction[21,41] with the electric field gradient at deuterium nucleus. The quadrupolar mechanism dominates its relaxation processes making the deuterium NMR spectrum sensitive to local motions. The powder spectrum or "Pake doublet" named after the physicist George E. Pake, is weighted sum over all orientations of θ, given by Eq. 2.5.2.1.1. Furthermore, the EFG tensor is approximately axially symmetric ($\eta = 0$) in case of ^{2}H spectra depending on the functional groups attached and frequency of separation in crystalline material with simple doublet reflects the C-D bond orientation to the magnetic field vector. This also facilitates the line shape calculation in the case of ^{2}H NMR.

As discussed in section 2.5.2.1, since ^{2}H has two allowed transitions and a single crystal with C-D bonds in a single orientation will give rise to two equally separated lines depending on the orientation of C-D bond magnetic field vector. By alternating the position of the single crystal with respect to external magnetic field, the positions of the peaks will change. If there was any kind of motion in the single crystal, this could average out the positions of these lines. Therefore, the amplitude of motions in the solids can be studied by investigating the line shapes of ^{2}H NMR spectra. However, the majority of samples studied are not crystalline but rather powders and the powder averaged Pake pattern results as shown in Figure 2.12.

If the C-D bond is involved in two-site hops between the two positions with bisector of the hop angle being 54.7° then the component of the electric field gradient tensor perpendicular to the hop axis is being unaffected by this motion. In case of C-D bond as a part of deuterated methyl group, methyl group rotation causes the ^{2}H static line shape to averages by a factor of $\frac{1}{2}(3cos^2\phi-1)$ where ϕ is the angle that C-D bond makes with the rotation axis. For methyl groups with 3-fold rotation it comes out to be 109.5° and the quadrupolar coupling constant averages by 1/3.

The rate of molecular motion is considered to be on the intermediate deuterium timescale is represented by correlation time τ_c, which ranges between 10^{-7} s to 10^{-3} s in solids.[72] Static line shapes generally occur when exchange rates less than 10^{-3} s while the fast motion limit exceeds 10^{-7} s. Hence, line shape simulations can be used to find the rate constant for exchange. If the rate constants are acquired for a range of temperatures then they can be plotted against inverse temperature to obtain the energy barrier for this dynamic process. H. W. Spiess et al. in in 1980 studied the ^{2}H SSNMR on of hexamethylenetetramine (HMT)[73] over a range of temperatures. They obtained the correlation time τ_c at each temperature from line shape analysis, which they confirmed followed the Arrhenius equation to allow the calculation of activation energy for reorientation of HMT.

As per Eq. 2.5.2.1.1, Δv is the doublet separation in frequency units and θ is the angle between principal axis of the EFG tensor which is considered to lie along the C-^{2}H bond vector and axis of rotation. Barnes et al.[74] have studied the separation of spectral width in perdeuterobenzene which decreased from 180.7 ± 1.5 kHz at 77 K to 69.10 ± 1.0 kHz at 200K showing that the in-plane reorientation of the molecule is restricted at lower temperatures. Further T_1 relaxation measurements on perdeuterated benzene have shown that the energy barrier to reorientation 19.0 ± 0.1 kJ/mol with an exponential function describing the activation energy.

Boden et al. calculated the quadrupolar coupling constants for –CD_2- and –CD_3 groups to be 168.0 ± 1.3 kHz and 49.9 ± 1.33 kHz in the polycrystalline n-nonadecane-d_{40} at the temperature of 165 K.[75] At 165K, the spectrum exhibits a narrow central doublet splitting as a result of rotation of two terminal CD_3 groups around the methyl axis that reduces the quadrupolar coupling constant, while the outer lines arise from the rigid backbone deuterons of –CD_2- groups. Hence –CD_2- groups have longer spin lattice relaxation (T_1) constants compared to the rotating –CD_3 groups. These characteristics can be used to differentiate these groups by recording the spectrum with a very short interscan delay so that only the fast relaxing –CD_3 groups will be detected.

In summary, the thesis explores the energy barriers of deuterated methyl groups in halogen bonded cocrystals via ^2H lineshape analysis and T_1 relaxation measurements. Understanding the details of NMR interactions is essential for interpreting our findings. We discussed here in brief all the NMR interactions and their mechanism in brief, focussing on Quadrupolar nucleus ^2H, it's relaxation mechanism, pulse program used in the chapter 4.

2.9 References

(1) Spin Dynamics: *Basics of Nuclear Magnetic Resonance*, 2nd Edition | Wiley, **2008.**

(2) Abragam, A. *Principles of Nuclear Magnetism;* International Series of Monographs on Physics; Oxford University Press: Oxford, New York, **1983.**

(3) Ernst, R. R.; Bodenhausen, G.; Wokaun, A. *Principles of Nuclear Magnetic Resonance in One and Two Dimensions*; International Series of Monographs on Chemistry; Oxford University Press: Oxford, New York, **1990.**

(4) Ashbrook, S. E.; Hodgkinson, P. *J. Chem. Phys.* **2018,** *149* (4), 040901.

(5) Zeeman, P. London, *Edinburgh, and Dublin Philos. Mag. J. Sc.***1897**, *43* (262), 226–239.

(6) Zeeman, P. *London, Edinburgh, and Dublin Philos. Mag. J. Sc.* **1897**, *44* (266), 55-60.

(7) Duer, M. J. *Introduction to Solid-state NMR spectroscopy,* Blackwell Publishing Ltd: Oxford, **2004**.

(8) Keeler, J. *Understanding NMR Spectroscopy*, 2nd ed.; John Wiley and Sons: Chichester, U.K, **2010**.

(9) Blanchard, J. W.; Sushkov, A. O.; Wickenbrock, A. Magnetic Resonance Searches. In The Springer International Publishing: Cham, **2023**; pp 173–200.

(10) Hahn, E. L. *Phys. Rev.*, *80* (4), 580, **1950**.

(11) Bodart, P. R.; Amoureux, J. P.; Dumazy, Y.; Lefort, R. *Mol. Phys.* **2000,** *98* (19), 1545-1551.

(12) Solomon, I. *Phys. Rev.* **1958**, *110* (1), 61.

(13) Weisman, I. D.; Bennett, L. H. *Physical Review* **1969**, *181* (3), 1341.

(14) Butterworth, J. *Proc. Phys. Soc.* **1965**, *86* (2), 297.

(15) Boden, N.; Hanlon, S. M.; Levine, Y. K.; Mortimer, M. *Mol. Phys.* **1978**, *36* (2), 519-540.

(16) Bloom, M.; Davis, J. H.; Valic, M. I. *Can. J. Phys.* **1980**, *58* (10), 1510-1517.

(17) Proctor, W. G.; Yu, F. C. *Phys. Rev.* **1950**, *77* (5), 717–717.

(18) Ramsey, N. F. *Phys. Rev.* **1950**, *78* (6), 699–703.

(19) Gorter, C. J. *Physica* **1936**, *3* (9), 995–998.

(20) Duer, M. J. *Ann. R. NMR. Spec.* **2006**, *59*, 41-116.

(21) Apperley, D. C.; Harris, R. K.; Hodgkinson, P. *Solid-State NMR: Basic Principles and Practice*; Momentum Press, **2012**.

(22) Duncan, T. M. *J. Phys. Chem. Ref. Data* **1987**, *16* (1), 125–151.

(23) Woessner, D. E. *Concept. Magnetic Res.* **1996**, *8* (6), 397–421.

(24) Becker, E. D. *High Resolution NMR: Theory and Chemical Applications*, 3rd ed.; Academic Press, **2000**.

(25) Herzfeld, J.; Berger, A. E. J. *Chem. Phys.* **2008**, *73* (12), 6021–6030

(26) Grutzner J.B. in Encyclopedia of Analytical Science (Second Edition), **2005.**

(27) Wasylishen, R. E.; Ashbrook, S. E.; Wimperis, S. *NMR of quadrupolar nuclei in solid materials*, John Wiley & Sons. **2012**, Vol. 3.

(28) Bryce, D. L.; Wasylishen, R. E. *Quadrupolar nuclei in solids*: Influence of different interactions on spectra, John Wiley & Sons Ltd.: Chichester, **2012**.

(29) Bryant, R. G. *Annu. Rev. Phys. Chem*. **1978**, *29* (1), 167–188.

(30) Harris, R. K.; Wasylishen, R. E.; Duer, M. J. *NMR crystallography*, John **2009**, Vol. 4.

(31) Purcell, E. M.; Torrey, H. C.; Pound, R. V. *Phys. Rev.* **1946**, *69* (1-2), 37.

(32) Autschbach, J.; Zheng, S.; Schurko, R. W. *Concepts Magn. Reson. Part A* **2010**, *36* (2), 84 126.

(33) Man, P. P. *Quadrupolar Interactions*, in Encyclopedia of Nuclear Magnetic Resonance; Harris, R.K., Wasylishen, R. E., Eds. eMagRe*s*, John Wiley & Sons, **2009**.

(34) Cohen, M. H.; Reif, F. *Quadrupole effects in nuclear magnetic resonance studies of solids.* In Solid state physics, Academic Press, *5*, 321-438, **1957**.

(35) Farrar, T. C.; Becker*,* E. D. Pulse and Fourier Transform NMR*. Introduction to Theory and Method*; Academic Press, New York, **1971**.

(36) Vega, A. J. *in Encyclopedia of Magnetic Resonance*, eds D. M. Grant and R. K. Harris, Wiley: Chichester, **1996**.

(37) Widdifield, C. M.; Bryce, D. L. *J. Phys. Chem. A* **2010**, *114* (40), 10810–10823.

(38) Widdifield, C. M.; Bain, A. D.; Bryce, D. L. *Phys. Chem. Chem. Phys.* **2011**, *13* (27), 12413-12420.

(39) Bryce, D. L.; Bernard, G. M.; Gee, M.; Lumsden, M. D.; Eichele, K.; Wasylishen, R. E. *Can. J. Anal. Sci. Spect*. **2001**, *46* (2), 46-81.

(40) Nehls, I. *Solid State NMR for Chemists.* Von COLIN A. FYFE. *Acta Polym.* **1987**, *38* (4), 251–251.

(41) Buchanan, G. W.; Moghimi, A.; Ratcliffe, C. I. *Can. J. Chem.* **1996**, *74* (8), 1437–1446.

(42) Ketudat, S.; Pound, R. V. *J. Chem. Phys.* **1957**, *26* (3), 708–709.

(43) Pound, R. V. *Phys. Rev.* **1950,** *79* (4), 685–702.

(44) Chiba, T. *J. Chem. Phys.* **1963**, *39* (4), 947-953.

(45) Jaroniec, C. P., Filip, C., Griffin, R. G. *J. Am. Chem. Soc.* **2002**, *124* (36), 10728–10742.

(46) Schaefer, J. "Development of REDOR rotational-echo double-resonance NMR" by *J. Magn. Reson*. **1989,** *81* 196–200]. *J. Magn. Reson*. **2011**, *213* (2), 421-422.

(47) Lee, Y. K.; Kurur, N. D.; Helmle, M.; Johannessen, O. G.; Nielsen, N. C.; Levitt, M. H. *Chem. Phys. Lett.* **1995**, *242* (3), 304–309.

(48) Ramsey, N. F. *Phys. Rev.* **1953**, *91* (2), 303–307.

(49) Cremer, D.; Gräfenstein, J. *Phys. Chem. Chem. Phys.* **2007**, *9* (22), 2791–2816.

(50) Hu, B.; Trébosc, J.; Amoureux, J. P. *J. Magn. Res.* **2008**, *192* (1), 112–122.

(51) Trebosc, J.; Hu, B.; Amoureux, J. P.; Gan, Z. *J. Magn. Res.* **2007**, *186* (2), 220–227.

(52) Gullion, T.; Schaefer, J. *J. Magn. Res.* **1989**, *81* (1), 196–200.

(53) Goetz, J. M.; Schaefer, J. *J. Magn. Res.* **1997**, *127* (2), 147–154.

(54) Fyfe, C. A.; Mueller, K. T.; Grondey, H.; Wong-Moon, K. C. *Chem. Phys. letters* **1992**, *199* (1-2), 198-204.

(55) Zhao, X.; Hoffbauer, W.; auf der Günne J. S.; Levitt, M. H. *Solid state Nucl. Mag.* **2004**, *26* (2), 57-64.

(56) Gan, Z. *J. Am. Chem. Soc*. **2006**, *128* (18), 6040–6041.

(57) Bloch, F. *Phys. Rev.* **1946**, *70* (7–8), 460–474.

(58) Bloembergen, N.; Purcell, E.M.; Pound, R.V. *Phys. Rev.* **1948**, *73* (7), 679.

(59) Becker, E. D.; Fisk, C. L. *An Introduction to NMR Relaxation Mechanisms*. In NMR in Living Dordrecht, **1986**, pp 39–52.

(60) Reif, B.; Ashbrook, S. E.; Emsley, L.; Hong, M. *Nat. Rev. Methods Primers* **2021**, *1*, 2.

(61) Chubak, I.; Alon, L.; Silletta, E. V.; Madelin, G.; Jerschow, A.; Rotenberg, B. *Nat. Commun*. **2023**, *14* (1), 84.

(62) Swartjes, A.; White, P. B.; Bruekers, J. P. J.; Elemans, J. A. A. W.; Nolte, R. J. M. *Nat. Commun.* **2022**, *13* (1), 1846.

(63) Steigel, A.; Spiess, H. W. *Dynamic NMR Spectroscopy*; Springer Science & Business Media, **2012**, Vol. 15.

(64) Becker, E. D. Chapter 8 - *Relaxation.* In High Resolution NMR, 3rd ed, Academic Press: San Diego, **2000**, pp 205–225.

(65) Abragam, A. The Principles of Nuclear Magnetism; Clarendon Press, **1961**.

(66) Gill, D.; Pathania, V. Chapter Ten - The Chemistry of Monovalent Copper in Solutions of Pure and Mixed Nonaqueous Solvents. In Advances in Inorganic Chemistry; van Eldik, R.; Hubbard, C. D., Eds.; Insights from Imaging in Bioinorganic Chemistry; Academic Press, **2016**; Vol. 68, pp 441–481.

(67) Reimarsson, P.; Wennerstrom, H.; Engstrom, S.; Lindman, B. *J. Phys. Chem.* **1977**, *81* (8), 789–792.

(68) Meadows, M. D.; Smith, K. A.; Kinsey, R. A.; Rothgeb, T. M.; Skarjune, R. P.; Oldfield, E. *P. Natl. A. Sci.* **1982**, *79* (4), 1351-1355.

(69) Venkatachalam, C. M.; Urry, D. W. *J. Magn. Reson*. **1980**, *41* (2), 313–335.

(70) Harris, R. K.; Lynden-Bell, R. M. *Nuclear Magnetic Resonance Spectroscopy: A Physicochemical View*; Pitman: Marshfield, Mass, **1983**.

(71) Gerothanassis, I. P.; Tsanaktsidis, C. G. *Concepts Magn. Res*. **1996**, *8* (1), 63–74.

(72) Jelinski, L. W. *Annu. Rev. Mater. Sci.* **1985**, *15* (1), 359–377.

(73) Pschorn, O.; Spiess, H. W. *J. Magn. Reson*. **1980**, *39* (2), 217–228.

(74) Barnes, R. G.; Bloom, J. W. *J. Chem. Phys.* **1972**, *57* (8), 3082–3086.

(75) Boden, N.; Clark, L. D., Hanlon, S. M.; Mortimer, M. *Faraday Symp. Chem. Soc.* **1978**, *13* (0), 109–123.

Chapter 3 X-Ray Crystallography

3.1 Background on X-ray diffraction and its importance

Understanding high resolution crystal structures of molecules is crucial. Presently, the gold standard for solving structures is via diffraction studies either by X-rays or neutrons. X-rays are scattered by electrons of atoms which occurs due to the oscillations of electrons from in the electric field of the incoming X-ray beam and such scattering by electrons is called Thomson scattering.[1] This results in a diffraction pattern, the measurement of which gives information on the arrangements of atoms within the crystal of being studied. In 1895, Wilhelm Conrad Roentgen discovered X-rays[2] and in 1912 Max von Laue showed that these X-rays could be diffracted by crystals.[3] In 1913, William Laurence Bragg used X-ray diffraction for the first time to establish the three-dimensional arrangement within an NaCl crystal where he found that each sodium ion is surrounded by six equidistant chloride ions and each chloride by six equidistant sodium ions. From this Bragg hypothesized that the crystal consisted of sodium and chloride ions rather than uncharged individual atoms as there was no discrete molecule of NaCl found.[4,5] This was predicted earlier in 1907 by William Barlow and William Jackson Pope,[6] but was experimentally demonstrated by Bragg in 1913.[4,5,7]

In this thesis, X-ray diffraction studies have been employed to determine the single crystal structures of halogen bonded cocrystals and powder X-ray studies are used as preliminary methods to distinguish the new structures. X-ray diffraction acts here as a complementary technique in determining the structures of samples which were then used in SSNMR studies. Single crystals were grown, screened, and structures solved to be able to understand the features of novel structures designed for the thesis. These studies were helpful in understanding the various aspects of molecular arrangement leading to observed differences in energy barriers to methyl group rotations in halogen-bonded cocrystals discussed in the Chapter 4.

3.2 Growing crystals: Methods in brief

There are various methods[8] used to grow single crystals. The better the quality of a crystal, the more precise the resulting crystal structure. Crystals are grown from solution as a commonly practiced method; however, other methods like cooling molten material, sublimation, and vapour diffusion methods are also useful. Growing crystals from solution involves dissolving the sample in a solvent of choice and/or a combination of solvents until the saturation point. The solvent is then removed or evaporated to slowly increase the concentration. The resulting saturated or supersaturated solution may yield crystals. During this crystal growth process, solute molecules interact with each other forming aggregates, a process referred to as nucleation. Crystal growth continues until the sample concentration drops down to the saturation point. The crystallization process relies on having an appropriate nucleation site. If crystallization conditions are reached quickly, the resulting crystal size is smaller than those obtained via a longer crystallization process, as the faster approach produces many nucleation sites. Crystals will not grow if there are very few nucleation sites as crystal growth may have to compete with other processes like precipitation or aggregation, which may dominate.

Key factors affecting the growth of crystals include the choice of solvent, generation of enough nucleation sites, the rate of crystal growth and maintaining an undisturbed crystallization system.[9] There is advanced equipment available for crystal growth, especially for macromolecules where robotics can be used to test a wide variety of crystallization conditions.[10] The preparation of crystals can be difficult for some samples or sample may be unstable under normal laboratory conditions. Such samples require extra care since may lose solvent and become polycrystalline powder or absorb water from the atmosphere and dissolve. Biomolecular crystals need optimal humidity and they are fragile due to the high proportion of water they possess. These difficulties make it necessary to use special techniques such as sealing the crystal in a capillary tube in suitable atmospheric conditions, cooling the crystals or growing them in a very low temperature. Some unstable organometallic crystals are grown in inert atmospheres to avoid unwanted side reactions. A twinned crystal may be formed when there is intergrowth of two different crystals in the same sample. This complicates a diffraction studies; however, the treatment of twin crystals while data processing and refinement is a standard practice. The size of a crystal for single crystal diffraction studies ranges from 0.2 to 0.4 mm or less and they weigh less than a small fraction of a milligram. However, some samples do not yield single crystals and thus powder X ray diffraction studies are used to obtain structural information. Mechanochemical techniques such as ball milling, grinding of samples by mortar and pestle, resonant acoustic mixing (RAM) yield novel cocrystals and are being explored these days.[11]

3.3 Basics of X-ray crystallography

3.3.1 Crystals and polycrystalline or powder samples

A crystal is a solid that contains a high degree of long-range three-dimensional internal order of the atoms, ions or molecules. The term “crystallography” was termed by the Swiss physician and naturalist Moritz Anton Cappellar in his work published in Lucerne in 1723.[12,13] By contrast, in non crystalline or powdered samples there is no evident geometric order beyond the immediate neighbouring environment of the fundamental structural unit. X-ray diffraction patterns of powders indicate that there is no geometric order in space in any possible direction that could define a period. They are termed as “amorphous”. The only regularities seen in the diffraction pattern (symmetrically spherical) of amorphous materials are due to the recurring bond distances. Not all solid materials can be assumed to be perfect crystals e.g. glass, calcite are not crystalline. Though crystalline material is known to have perfectly arranged components in three dimensions, a real crystal at non-zero temperature can have a variety of imperfections including defects, twinning, disorder, dislocations, and impurities. The internal regularity of crystal was used as diffraction grating in 1912 to demonstrate the wavelike property of X-rays[5] and also led to a useful technique to study molecular structure. The internal regularity is what defines the crystal more than the external appearance and the diffraction pattern obtained with X-rays shows the extent of crystallinity.

3.3.2 The unit cell and faces of a crystal

A crystal is built up by the continuing three-dimensional translational repetition of a basic structural unit, which may include one or more atoms, molecules, or ions or a complex assembly of the same. The simplest component of this three-dimensional pattern is called the "unit cell".[14] The word "translational" implies that the repetition of an arrangement of atoms in a specific direction at regular intervals. The unit cell hence contains a translationally repeating pattern defined by crystal axes namely **a, b** and **c,** with magnitudes a, b and c. The angles between these axes are named for convenience, α between **b** and **c**, β between **b** and **c,** and γ between **a** and **b**. The three lengths and the three angles are called *lattice parameters* or *unit cell parameters.* The atomic positions along each of the unit cell directions are measured as fractions of x, y and z of repeat lengths a, b and c. The crystal planes are characterized by the three integers and is known as "indexing", namely h, k, and l. The ratio of the lengths of the unit cell and hence the shape of the unit cell is obtained after the cell indexing which has the information of crystal faces and the angles between them measured.

3.3.3 Crystal lattice, symmetry, space groups

If the repeating unit cell in a crystal is replaced by a point, a crystal lattice is generated and is an infinite network of points arranged in three-dimensional space. A crystal lattice consists of an ordered array of imaginary points whereas a crystal structure consists of an ordered array of components such as atoms/ions/molecules as defined earlier. Crystal lattice points are positioned uniformly in every repetitive unit cell and as a result every crystal lattice point in the unit cell has the same environment in the entire crystal structure. Unit cells and crystal lattices are classified based on their rotational symmetry.[14,15] Physically, symmetry elements can be visualized as a point, line or plane in any object or molecule around which symmetry operations are applied. Such symmetry operations may include an inversion through a point, a rotation about a line or a reflection in a plane resulting in the identical appearance of the molecule afterwards. Each symmetry element thus has characteristic number of symmetry operations that can be performed; for example, the presence of an *n*-fold rotation axis implies that when the unit cell is rotated (360/*n*)° about this axis, the crystal lattice obtained afterwards is indistinguishable from the original before the rotation (*n* can be any integer). The Figure 3.1 shows the symmetry operations of rotation, inversion and reflection and the resultant images.

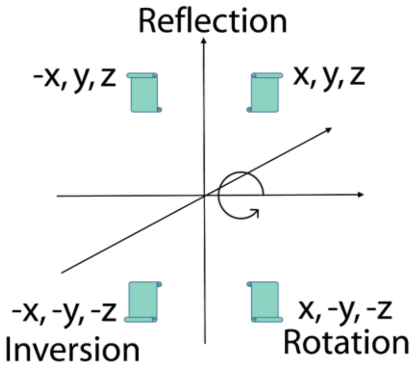

Figure 3.1. Illustration of basic symmetry operations.

Different types of possible rotational symmetry including two-fold, three-fold, and six-fold rotational axes result in seven types of crystal systems namely triclinic, monoclinic, orthorhombic, tetragonal, trigonal/rhombohedral, hexagonal and cubic. Any crystal lattice may always be described as primitive with only one crystal point or non-primitive with more than one crystal point. By considering the fact that the non-primitive cell has more than one crystal point and necessity being that the crystal lattice point must have the identical surrounding, there are 14 types of crystal lattices that were deduced by Moritz Ludwig Frankenheim and Auguste Bravais. These 14 crystal lattice types are named after Bravais in 1850 which were obtained by the combination of 7 crystal systems mentioned before Figure 3.2 with the four crystal lattice types based on arrangement of atoms in crystal lattice (*P*-primitive*, A* or *B* or *C*-simple cubic, *F*-face centered, and *I*-body centered).

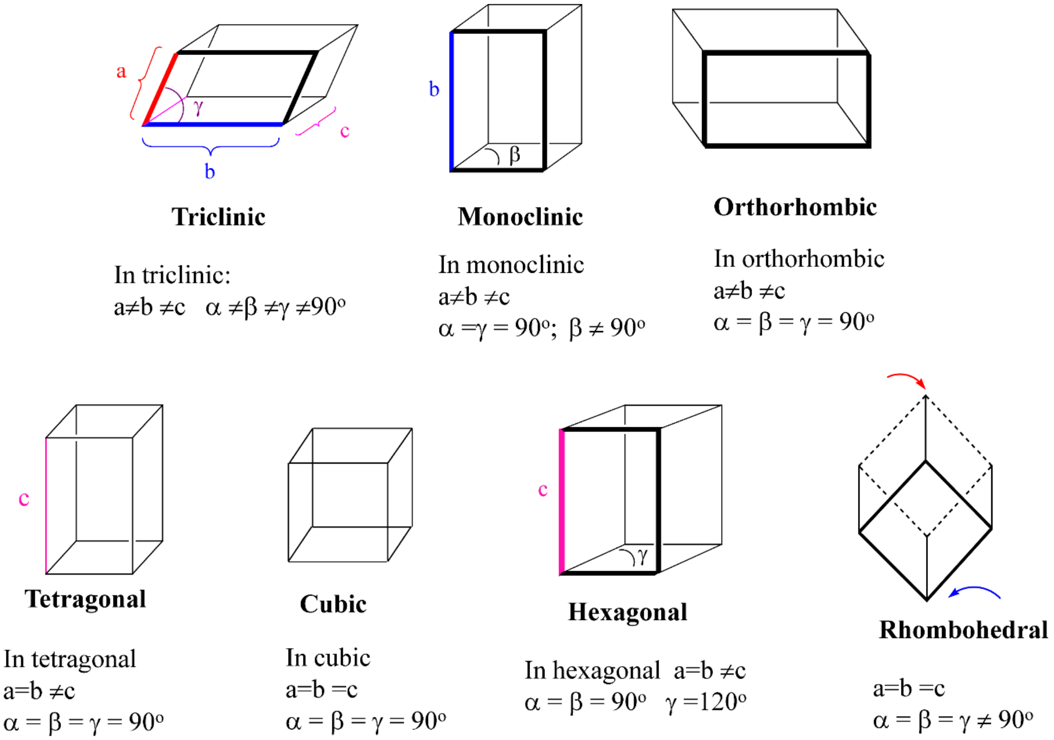

Triclinic

In triclinic:
a≠b ≠c α ≠β ≠γ ≠90°

Monoclinic

In monoclinic
a≠b ≠c
α =γ = 90°; β ≠ 90°

Orthorhombic

In orthorhombic
a≠b ≠c
α = β = γ = 90°

Tetragonal

In tetragonal
a=b ≠c
α = β = γ = 90°

Cubic

In cubic
a=b =c
α = β = γ = 90°

Hexagonal

In hexagonal a=b ≠c
α = β = 90° γ =120°

Rhombohedral

a=b =c
α = β = γ ≠ 90°

Figure 3.2. Depiction of 7 types of crystal systems with corresponding cell parameters to distinguish them.

The collection of all the symmetry operations for a molecule is called its *point group* and each point group has its own characteristics. There are a total of 32 point groups. The number of molecules in each unit cell is denoted as *Z*. The smallest part of a crystal structure from which the complete crystal structure can be obtained by symmetry operations using appropriate space groups is called the *asymmetric unit*. The number of molecules in the asymmetric unit is denoted by *Z'*. The combination of symmetry elements consistent with 14 Bravais lattices can be arranged in such way that there will be 230 distinct combinations possible for three dimensional crystals called crystallographic space groups. They are listed in the *International Tables for Crystallography, Volume A*.

3.3.4 Diffraction and Bragg's equation

Von Laue with Friedrich and Knipping discovered the diffraction of X rays by crystals in 1912.[3] In 1913, William Lawrence Bragg with his father William Henry Bragg, explained that the diffracted X-ray beams were reflected from planes passing through points of the crystal lattice.[4,5] Bragg's diffraction condition is shown in the Figure 3.3 below:

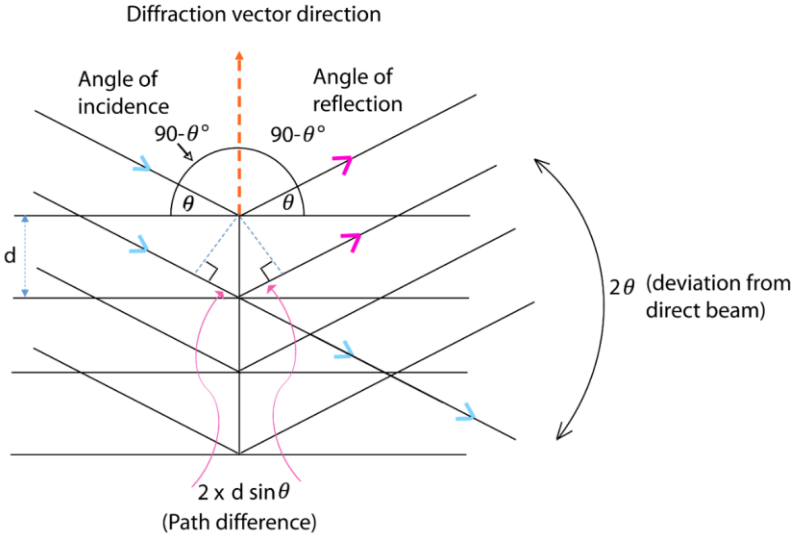

Figure 3.3. Illustration of Bragg's law: Diffraction of X-rays from the lattice plane.

Bragg's law states that difference in the paths traveled by the scattered waves from adjacent crystal lattice plane will be an integral multiple of the wavelength, $n\lambda$. Below is Bragg's equation:

$$n\lambda = 2d \sin\theta \qquad \text{Eq. 5.3.4.1}$$

Where λ is the wavelength of radiation used, n is an integer, $n\lambda$ is the path difference, d is the perpendicular spacing between the lattice planes in the crystal, θ is the complement (90°-θ) of the angle of incidence of X-ray beam.

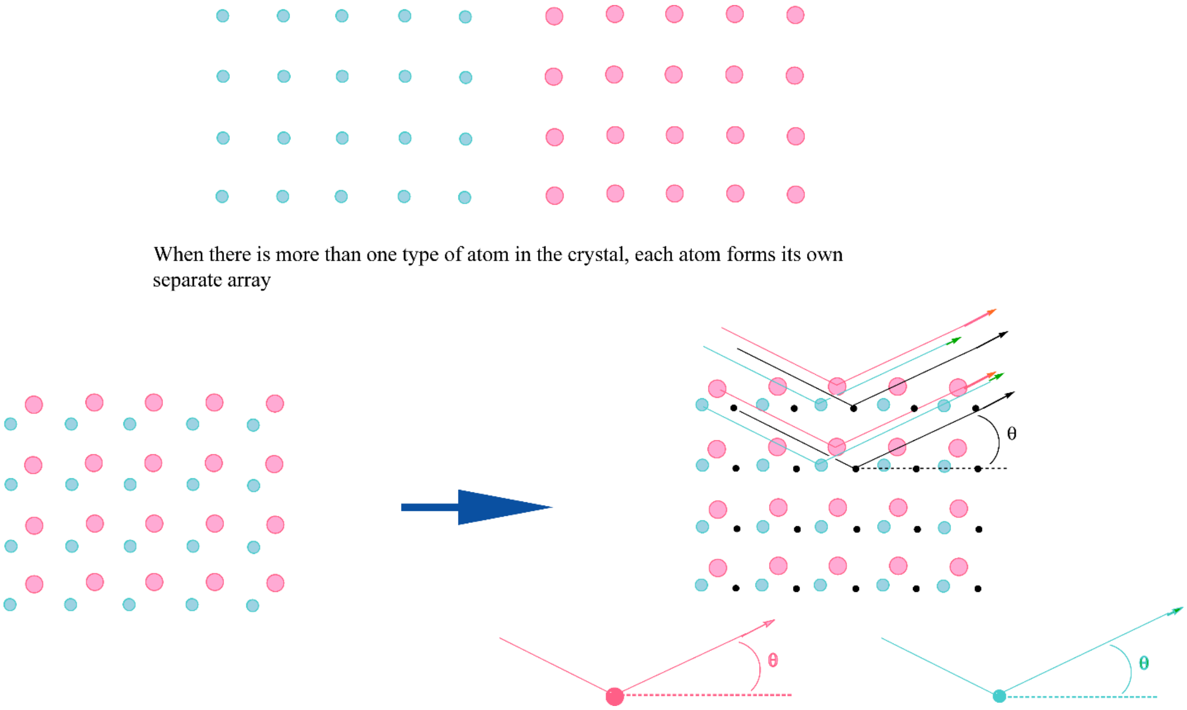

Figure 3.4. Depiction of array of two type of atoms in a crystal and each array separately satisfies the Bragg equation. The amplitude of the diffracted wave depends on the number of electrons in the two atoms here and the angle, $\boldsymbol{\theta}$. This produces different intensities of diffraction spots for the two atoms in consideration.

3.4 Single crystal X-ray diffraction

The conditions of data collection can be decided by a crystallographer, which include the radiation source, temperature, and pressure.[16] The radiation source could be copper ($\lambda = 1.54184$ Å) or molybdenum ($\lambda = 0.71073$ Å). Copper radiation is particularly useful for weakly diffracting crystals which are smaller in size and contains lower atomic number elements (smaller path difference with respect to wavelength used) whereas molybdenum radiation allows collection of higher resolution data. The analysis of a crystal structure by single crystal X-ray diffraction as performed for this thesis consists of three stages:

Screening of crystal involves the selection of a crystal from multiple crystals; indexing the diffraction spots gives the unit cell parameters and evaluate the quality of crystal based on their intensity of spots indexed.

Data collection involves experimental measurement of the directions of scatter of the diffracted beams and measuring the unit cell dimensions. The Bragg reflection (where the wavelength, λ of X-ray comparable to the lattice spacing d in lattice; each crystal plane acts as weakly reflecting plane; the radiation is called Bragg reflected and the reflections produced if satisfy the Bragg equation they add constructively to produce nearly 100% reflections) with different intensities based on the type of atoms present in the sample and their relative positions of atoms in the unit cell is recorded.

Finding a possible structure is the deduction by direct methods which are based on statistical and probabilistic calculations which use the experimental structure factor modulus for each reflection and inverse Fourier transform of structure factors (contains information of x, y, z values for each atom; h, k, l Bragg reflections) provides electron density map whose maxima corresponding to the atomic positions.[15] This is embedded in the software program used to solve the data. In the current work atomic coordinates that are measured with respect to unit cell are located based on electron density map using the software *WingX*.[17,18]

Refinement of the trial structure involves modifications made to obtain agreement between calculated and experimentally measured intensities within the limits of any errors. The discrepancy index, R is a useful measure of reliability of a crystal structure. R is called as reliability index and or conventional residual or residual index; it is defined as following:[19]

$$R = \frac{\Sigma|(|F_0|-|F_c|)|}{\Sigma|(F_0)|} \qquad \text{Eq. 3.4.1}$$

R is a measure of how closely the experimentally observed structure factor amplitudes are matched by the calculated values for a possible structure model proposed. F_0 is the observed structure factor amplitudes and F_c is the calculated structure factor amplitudes. In general, the lower the R value, the better the structure determination.

Mercury[20] is software which provides comprehensive tools to visualize crystal structures after solving them. *WingX*[17,18] and *ShelXle*[21] software programs are used for solving the crystal structures described in this thesis. Crystal structures in this thesis were prepared using this program and then novel structures were deposited in the CCDC.[22]

3.5 Powder X-ray diffraction

Powder X-ray diffraction was used in this thesis to check the purity of the novel cocrystals along with characterizing the products formed in the crystallization process. Around 1917, Johannes Christian Michael Brentano worked on the Bragg-Brentano geometry[23] used in powder X-ray diffraction instruments. Sample preparation for X-ray powder diffraction measurements becomes important to avoid any impurity or phase changes.[24] The samples must be finely grinded to achieve a good signal-to-noise ratio and to minimize the preferred orientation of crystallites, also making enough particles to participate in the diffraction process. For phases quantification of samples, its recommended that the particle size be in the range of 1 – 5 μm.[25,26] For routine qualitative evaluation, samples are ground to pass through a 325-mesh sieve, resulting in particles about 45 μm in size. Powdered sample is prepared by mechanochemical methods such as mortar and pestle, ball milling and resonant acoustic mixing. The scattering angle, θ is measured for every family of planes by rotating the sample and measuring the angle of diffracted rays with respect to the angle of incidence. Alternatively, the detector could be moved while keeping the angle between sample and the X-ray source fixed. Since the wavelength of the X-ray source is known, *d*-spacings or the spacing between the planes can be calculated by Bragg's Law. The powder X-ray data collected for the starting materials and products are compared using X'Pert HighScore Plus software to get a fingerprint pattern. The software can be used to convert the raw files into desired file format for interpretation of diffraction data; it helps with background subtraction, peak fitting to determine the positions, intensities and width of diffraction peak, profile fitting, semi-quantitative phase analysis. This helps in the initial screening of samples by comparing the powder patterns obtained by simulation of single crystal data and experimental powder pattern in our studies to identify the phase purity and carry forward for subsequent SSNMR experiments.

3.6 Applications of X-ray diffraction data

X-ray diffraction remains a powerful technique that has a long history of solid-state structure characterization. There are a wide range applications of X-ray diffraction studies in identifying phases, crystal size and structure, residual strain,[27] phase transformation,[28,29] studying non-covalent interactions,[30,31] structural information of protein-ligand complexes, supramolecular chemistry, structure based drug discovery,[32] and many more.

The earliest days of crystallography involved the study of small molecules. One such example includes the structure of resorcinol reported by Robertson in 1936,[27] which was termed as α-form. Shortly thereafter in 1938, it was found that the α–form underwent a transformation to the β-form when heated to 74 °C.[25] Though both forms were in the *P*na space group, the new form was denser and the structure was completely different from the α-form. Each form is characterized by different type of hydrogen bond motif.

The qualitative use of powder X-ray diffraction provides a fingerprint of powder samples. Quantitative analysis of complex powder sample mixtures is done using a profile refinement method developed by Rietveld, which involves in simple terms to input the cell parameter (a, b, c and symmetry unrestricted angle, example being β angle in monoclinic system) of known phase for the refinement in such a way that it matches best with the experimental powder pattern.[33] This approach has been useful for detecting as little as 1% of analyte concentration in a mixture. Since each component in a mixture contributes to the overall scattering in a manner that is proportional to its weight fraction the powder pattern of a mixture will contain one or more peaks whose scattering angle is unique to that analyte. For example, powder X-ray diffraction of ranitidine hydrochloride that crystallizes in two polymorphic forms[34,35] showed the presence of 0.50% w/w of Form I in a bulk Form II sample.

Over the years, CCDC[22] has had millions of crystal structures deposited into its database. Crystal engineering[35–38] defined as the building of crystal structures of organic, metal organic species, using the knowledge of intermolecular interactions, as the base for supramolecular structures required to generate macromolecular crystals. Engineered crystals have potential to be used to make functional materials, catalysts, molecular rotors, drug-delivery complexes, etc. To engineer a crystal, a molecule is chosen so that there are appropriate donors and acceptors of hydrogen bonds or halogen bonds. While hydrogen bonds are more directional and ubiquitous in nature, the halogen bonds have gained interest since they can play a similar as hydrogen bonds a discussed in Chapter 1 of the thesis. The location and position of bonding groups are chosen to 3-dimensional bonding network. For example, Colin-Molina et al.[39] synthesized and studied the dynamics of a supramolecular rotor composed of a cocrystal components comprised of two carbazoles and a DABCO molecule acting as a stator and a rotator respectively, held together by N-H···N bonds. ^{1}H T_1 spin-lattice measurements were carried out using saturation recovery in solid-state cocrystals as a function of temperature, to measure the activation energy of this rotation, which was to be 2.6 kcal/mol, comparable with ultrafast supramolecular rotors. As is shown in the results of Chapter 6 in this, halogen bonded novel cocrystals are studied by both SSNMR and X-ray diffraction to characterize the intermolecular interactions and their influence on dynamics.

In summary, thesis deals with designing novel cocrystals using the knowledge of halogen bonding interactions and crystal engineering principles. Newly prepared cocrystals were semi-quantitavely analyzed using powder diffraction studies to identify new peaks when compared and overlaid with the powder diffractogram of starting materials using X'Pert HighScore Plus software. The structure of new cocrystals were confirmed by solving single crystal X-ray diffraction data and then comparing them with powder difractograms obtained experimentally. Mercury software was used to study the intermolecular interactions, crystal packing, void volume, geometry and unit cell parameters to analyse the results obtained with respect to barrier energy measured using variable temperature ^{2}H SSNMR experiments.

3.7 References

(1) Waseda, Y.; Matsubara, E.; Shinoda, K. Scattering and Diffraction. In *X-Ray Diffraction Crystallography: Introduction, Examples and Solved Problems*; Waseda, Y., Matsubara, E., Shinoda, K., Eds.; Springer: Berlin, Heidelberg, **2011**; pp 67–106.

(2) Roentgen, W. C. Ueber Eine Neue Art von Strahlen. *Sitzungsberichte der Physikalisch-medizinischen Gesellschaft zu Wuerzburg* **1895**, *29*.

(3) Friedrich, W.; Laue, M. Interferenz-Erscheinungen bei Röntgenstrahlen.

(4) Bragg, W. H.; Bragg, W. L. *Proceedings of the Royal Society of London. Series A, Containing Papers of a Mathematical and Physical Character* **1913**, *88* (605), 428–438.

(5) Bragg, W. H.; Bragg, W. L. *Proceedings of the Royal Society of London. Series A, Containing Papers of a Mathematical and Physical Character* **1913**, *89* (610), 277–291.

(6) Barlow, W.; Pope, W. J. *J. Chem. Soc., Trans.* **1907**, *91* (0), 1150–1214.

(7) Bragg, W. L. *Nature* **1912**, *90* (2250), 410–410.

(8) McPherson, A. *Preparation and Analysis of Protein Crystals*; Wiley: New York, **1982**.

(9) Chayen, N. E. *Prog. Biophys. Mol. Biol.* **2005**, *88* (3), 329–337.

(10) Snook, C. F.; Purdy, M. D.; Wiener, M. C. *J. Appl. Cryst.* **2000**, *33* (2), 344–349.

(11) Tan, D.; Friščić, T. *Eur. J. Org. Chem.* **2018**, *2018* (1), 18–33.

(12) Moritz Anton Cappeller. *Prodromus Crystallographiae De Crystallis Improprie Sic Dictis Commentarium,* **1723,** (Digitized on July 21, 2023)

(13) Jean-Claude Boulliard, Delphine Cabaret, Paola Giura, René-Just Haüy and the birth of crystallography, *IUCr Newsletter*, Vol. 30, Number 4, **2022**.

(14) Ladd, M. F. C., Palmer, R. A., & Palmer, R. A. Structure determination by X-ray crystallography **1977**, (Vol. 233). New York: Plenum Press.

(15) Giacovazzo, C.; Monaco, H. L.; Artioli, G.; Viterbo, D.; Milanesio, M.; Gilli, G.; Gilli, P.; Zanotti, G.; Ferraris, G.; Catti, M. *Fundamentals of Crystallography*, Oxford University Press, **2011**.

(16) Moggach, S. A.; Allan, D. R.; Clark, S. J.; Gutmann, M. J.; Parsons, S.; Pulham, C. R.; Sawyer, L. *Acta. Cryst. B* **2006**, *62* (2), 296–309.

(17) Farrugia, L. J. *J. Appl. Cryst.* **1999**, *32* (4), 837–838.

(18) Farrugia, L. J. *J. Appl. Cryst.* **2012**, *45* (4), 849–854.

(19) McREE, D. E. Computational Techniques. In *Practical Protein Crystallography (Second Edition)*; Academic Press: San Diego, **1999**.

(20) Macrae, C. F.; Sovago, I.; Cottrell, S. J.; Galek, P. T. A.; McCabe, P.; Pidcock, E.; Platings, M.; Shields, G. P.; Stevens, J. S.; Towler, M.; Wood, P. A. *J. Appl. Crystallogr.* **2020**, *53* (Pt 1), 226–235.

(21) Hübschle, C. B.; Sheldrick, G. M.; Dittrich, B. *J. Appl. Cryst.* **2011**, *44* (6), 1281–1284.

(22) Groom, C. R.; Bruno, I. J.; Lightfoot, M. P.; Ward, S. C. *Acta. Crystallogr. B Struct. Sci. Cryst. Eng. Mater.* **2016**, *72* (2), 171–179.

(23) Etter, M.; Dinnebier, R. E. *Zeitschrift für anorganische und allgemeine Chemie* **2014**, *640* (15), 3015–3028.

(24) Buhrke, V. E.; Jenkins, R.; Smith, D. K. A Practical Guide for the Preparation of Specimens for X-Ray Fluorescence and X-Ray Diffraction Analysis, Wiley, **1997**.

(25) Cullity, B. D. Elements of X-Ray Diffraction; Addison-Wesley Publishing, **1956**.

(26) Klug, H. P.; Alexander, L. E. *X-Ray Diffraction Procedures: For Polycrystalline and Amorphous Materials*; **1974**, p 992.

(27) Robertson, J. M. *Proceedings of the Royal Society of London. Series A-Mathematical and Physical Sciences* **1936**, *157* (890), 79–99.

(28) Li, B.; Li, S.; Gong, J.; Wu, X.; Li, Z.; Gao, D.; Zhao, D.; Zhang, C.; Wang, Y.; Zhu, Z. *Chem* **2024**, 10 (1), 35–47.

(29) Scheidel, S.; Östreicher, L.; Mark, I.; Pöppler, A.-C. *Magnetic Resonance in Chemistry* **2022**, 60 (6), 572–582.

(30) Scilabra, P.; Terraneo, G.; Daolio, A.; Baggioli, A.; Famulari, A.; Leroy, C.; Bryce, D. L.; Resnati, G. *Crystal Growth & Design* **2020**, *20* (2), 916–922.

(31) Leroy, C.; Johannson, R.; Bryce, D. L. *J. Phys. Chem. A* **2019**, 123 (5), 1030–1043.

(32) Wranik, M.; Weinert, T.; Slavov, C.; Masini, T.; Furrer, A.; Gaillard, N.; Gioia, D.; Ferrarotti, M.; James, D.; Glover, H. *Nat. Commun.* **2023**, *14* (1), 903.

(33) Rietveld, H. M. A. *J. appl. Crystallogr.* **1969**, *2* (2), 65–71.

(34) Brittain, H. G. *Profiles of Drug Substances, Excipients and Related Methodology* **2003**, *30*, 271–319.

(35) Desiraju, G. R. *J. Chem. Sci.* **2010**, *122* (5), 667–675.

(36) Desiraju, G. R. *J. Am. Chem. Soc.* **2013**, *135* (27), 9952–9967.

(37) Simanek, E. E.; Mammen, M.; Gordon, D. M.; Chin, D. N.; Mathias, J. P.; Seto, C. T.; Whitesides, G. M. *Tetrahedron* **1995**, *51*, 607–619.

(38) Aakeröy, C. B. *Acta Crystallogra. Section B* **1997**, *53* (4), 569–586.

(39) Colin-Molina, A.; Karothu, D. P.; Jellen, M. J.; Toscano, R. A.; Garcia-Garibay, M. A.; Naumov, P.; Rodríguez-Molina, B. *Matter* **2019**, *1* (4), 1033–1046.

Part 2: Modulation of Dynamics

Chapter 4 Modulation of Rotational Dynamics in Halogen-Bonded Cocrystalline Solids

Permission: Chapter 4 is from Shubha S. Gunaga and David L. Bryce, J. Am. Chem. Soc. 2023, 145, 34, 19005–19017 (DOI:10.1021/jacs.3c06343). Reproduced with permission of American Chemical Society.

4.1 Abstract

Dynamic processes are responsible for the functionality of a range of materials, biomolecules, and catalysts. We report a detailed systematic study of the modulation of methyl rotational dynamics via the direct and indirect influence of non-covalent halogen bonds. For this purpose, a novel series of cocrystalline architectures featuring halogen bonds (XB) to tetramethylpyrazine (TMP) is designed and prepared using gas-phase, solution, and solid-state mechanochemical methods. Single-crystal X-ray diffraction reveals the capacity of molecular bromine as well as weak chloro-XB donors to act as robust directional structure-directing elements. Methyl rotational barriers (E_a) measured using variable-temperature deuterium solid-state NMR range from 3.75 ± 0.04 kJ mol^{-1} in 1,3,5-trichloro-2,4,6-trifluorobenzene·TMP to 7.08 ± 0.15 kJ mol^{-1} in 1,4-dichlorotetrafluorobenzene·TMP. E_a data for a larger series of TMP cocrystals featuring chloro-, bromo-, and iodo-XB donors are shown to be governed by a combination of steric and electronic factors. The average number of carbon-carbon close contacts to the methyl group is found to be a key steric metric capable of rationalizing the observed trends within each of the Cl, Br, and I series. Differences between each series are accounted for by considering the strength of the σ-hole on the XB donor. One possible route to modulating dynamics is therefore via designer cocrystals of variable stoichiometry, maintaining the core chemical features of interest between a given donor and acceptor, while simultaneously modifying the number of carbon close contacts affecting dynamics. These principles may provide design opportunities to modulate more complex geared or cascade dynamics involving larger functional groups.

4.2 Introduction

Molecular dynamics are crucial to the functionality of biomolecules,[1] chemical catalysts,[2,3] and supramolecular systems.[4] The intelligent and deliberate engineering of molecular structure and dynamics also holds the key to improving the properties of designer proteins,[5] advanced functional materials,[6] and molecular machines.[7,8] While atomic-level structure resolution has long been a goal of chemical and biochemical crystallography, be it via diffraction methods, complementary approaches such as NMR crystallography,[9,10] or purely computational crystal structure prediction (CSP) methods,[11] it has become more evident in recent years that static structures only provide part of the story, and that dynamical features are of comparable importance in many cases.[12,13]

For example, in the realm of structural biology, AlphaFold2[14] has found great success in generating structural models which are consistent with those established experimentally via diffraction or NMR approaches.[15] However, it is clear that NMR spectroscopy provides invaluable insights into dynamic processes,[16] including the interconversion between states,[17,18,19] slow motions in proteins,[20] and hierarchical protein dynamics across a range of timescales[21,22] which are not available from a static structural model. Low methyl rotational barriers have recently been identified in proposed drugs against the SARS-CoV-2 virus.[23]

From the perspective of materials and crystal engineering, great strides have been made in designing metal-organic frameworks and other porous systems which feature molecular rotors.[24,25,26,27,28,29,30,31,32] The characterization of the dynamic features of these rotors is often carried out with solid-state NMR spectroscopy, typically via the analysis of deuterium NMR line shapes and spin-lattice relaxation time constants (T_1) measured as a function of temperature. Analysis of these data can provide activation energies (E_a) corresponding to the rotational energy barrier, among other parameters. For example, Schurko and Loeb have explored mechanically interlocked linkers and pillars in MOFs, and the role of sterics and phase changes in controlling their dynamics.[28,29,30] Comotti, Sozzani, and coworkers have recently described a number of fascinating examples which demonstrate how molecular rotors offer a platform to realize controlled dynamics and modulate the functions of solids. In one case, a so-called ‘hypermobile’ rotor within the bicyclopentane–dicarboxylate struts of a zinc-based metal–organic framework was found to have an energy barrier of just 6.2 cal mol^{-1}.[24] Garcia-Garibay and coworkers have invested significant effort into designing and understanding the dynamics of supramolecular and ultrafast rotors, with some focus on systems constructed via halogen bonds.[33,34,35,36,37,38,38,39] Their work has also explored the role of intrinsic rotational barriers as well as crystal fluidity in determining dynamics in molecular rotors and machines.[40,41]

Although non-covalent interactions, typically hydrogen bonds and sometimes halogen bonds, are often used as the anchor points of supramolecular rotors in, e.g., MOFs and other porous systems,[42] the possible indirect or unanticipated steric and electronic effects of these non-covalent bonds on rotational energy barriers are less understood. The factors which may influence rotational energy barriers have been often discussed,[43,44,45,46] and while there are certain classes of systems whose rotational energy barriers may be well described by e.g., a steric model, the role of non-covalent interactions as tools to expressly modulate rotational energy barriers is an open question. In a series of papers, Baudry[47,48,49] showed computationally that the rotational barriers of methyl groups may either increase or, somewhat counterintuitively, decrease depending on the microenvironment. Skrynnikov and coworkers[50] reached similar conclusions via side-chain ^{2}H and backbone ^{15}N NMR relaxation data recorded for the SH3 domain from α-spectrin; that is, the methyl rotational activation energies outside the fluid hydrophobic protein core were either elevated or decreased from the core reference value of 2.8 ± 0.9 kcal/mol. However, an assessment of activation energies compared with various structural parameters on a per-residue basis yielded no correlation.

A recent communication from our laboratory described the ability of halogen bonds[42] to catalyze supramolecular dynamics in cocrystalline solids.[51] This work demonstrated that a counterintuitive reduction in the methyl rotational barrier of 2,3,5,6-tetramethylpyrazine (TMP) could be achieved by preparing cocrystalline materials featuring hydrogen bonds or halogen bonds to the pyrazyl nitrogen atom. Interestingly, this decrease was greater when strong prototypical halogen bond donors (1,4-diiodotetrafluorobenzene, 1,3,5-trifluoro-2,4,6-triiodobenzene, and molecular iodine) were used compared to hydrogen bond donors, despite the greater steric bulk of the former. Furthermore, the reduction in this barrier was absent in control experiments where an iodide salt was cocrystallized with TMP. These observations, coupled with calculations of the magnitude of the σ-hole[52] molecular electrostatic potential maximum on iodine, suggested that a combination of electronic and steric factors is at play in determining the overall rotational barrier.

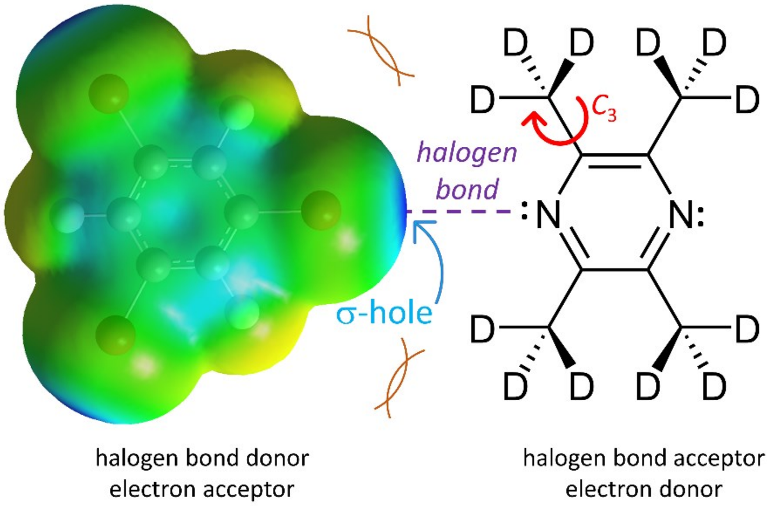

Figure 4.1. Key concepts explored in this work. Left: Molecular electrostatic potential surface of one of the halogen bond donors used herein, 1,3,5-tribromo-2,4,6-trifluorobenzene, with the σ-hole on bromine indicated (blue). Right: 2,3,5,6-tetramethylpyrazine, the halogen bond acceptor. The halogen bond is indicated in purple. The possible role of steric clashes (brown), both with the halogen bond donor and with atoms in the extended crystal lattice, in determining the barrier to pseudo-C3 rotation (red) of the deuterated methyl groups, is depicted.

In the context of the foregoing discussion, we sought to provide new insight into how molecular dynamics in solids may be tailored for certain applications. In the present contribution, we establish some general principles of modulation of methyl rotational energy barriers via cocrystal engineering of halogen-bonded frameworks (Figure 4.1). A series of novel halogen-bonded cocrystals is designed and synthesized using mechanochemical and cosublimation techniques, and their static structures are solved via single-crystal X-ray diffraction (Figure 4.2). Deuterium spin-lattice relaxation time constants are measured as a function of temperature for the cocrystalline powders in order to determine the methyl rotational activation energy barriers. These data are carefully interpreted in the context of the single-crystal X-ray structures to deconvolute the influence of steric and electronic factors, thereby providing a pathway towards the control of molecular and supramolecular dynamics in related systems.

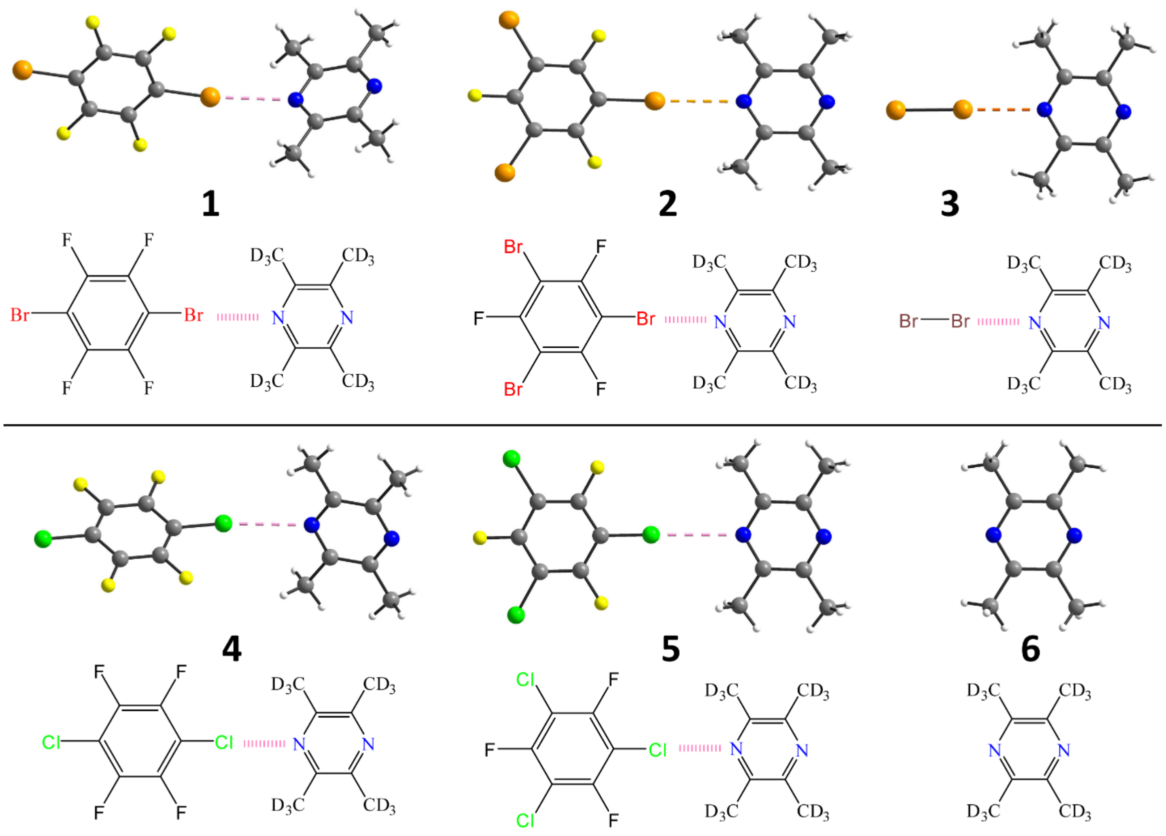

Figure 4.2. Depiction of halogen bonds in the single crystal structures (this work) and molecular structures of five halogen-bonded cocrystals. Pure TMP (6) is also shown. The dashed light pink lines represent halogen bonds. Carbon: grey; fluorine: yellow; chlorine: green; nitrogen: blue; hydrogen/deuterium: white; bromine: orange.

4.3 Experimental

4.3.1 (i) Sample preparation

2,3,5,6-tetramethylpyrazine (98%), 1,4-dibromotetrafluorobenzene (≥ 99%), and Br_2 (≥ 99.99%) were purchased from Sigma Aldrich. 1,3,5-tribromo-2,4,6-trifluorobenzene (95%) was purchased from abcr GmbH, 1,4-dichlorotetrafluorobenzene was purchased from Synquest Laboratories, and 1,3,5-trichloro-2,4,6-trifluorobenzene (95%) was purchased from AmBeed.

These chemicals were used without further purification. Deuterium oxide, D_2O, was purchased from Sigma Aldrich (99.9 atom % D) and other solvents were purchased from Macron Fine Chemicals and from Alfa Aesar.

2,3,5,6-Tetramethylpyrazine was deuterated following a modified procedure from the literature.[51,53] In a 100 mL glass pressure tube, 50 mL of 0.6 M NaOH solution in D_2O was prepared in an ice bath, to which 3 g of 2,3,5,6-tetramethylpyrazine was added carefully. The sealed glass tube was then placed in an oven at 92 ºC and left for 7 days. The glass tube was taken out and allowed to cool to room temperature, resulting in crystallization of deuterated 2,3,5,6-tetramethylpyrazine. The solution was filtered to isolate crystalline flakes of the product, which was further rinsed with water and sublimed to get the pure product with a yield of 65%. This procedure afforded a deuterium enrichment factor of approximately 73% as assessed by NMR spectroscopy and mass spectrometry.

The cocrystals **1**, **2**, **3**, **4**, and **5** (Figure 4.2) were prepared using slow evaporation and cosublimation techniques with deuterated 2,3,5,6-tetramethylpyrazine as the halogen bond acceptor. Cocrystal **3** was prepared using a cosublimation apparatus[54] by using liquid Br_2 and solid deuterated 2,3,5,6-tetramethylpyrazine; orange crystals were produced over 48 h (see SI for further details). Cocrystals **1**, **4**, and **5** were produced using a 1:1 molar ratio of donor and acceptor molecules with slow evaporation from dichloromethane. **2** was produced using a 1:1 molar ratio of donor and acceptor molecules with slow evaporation from anhydrous acetonitrile (99.8+%) initially at room temperature and subsequently at 5 ºC in the refrigerator over 7 to 10 days.

4.3.2 (ii) Single crystal X-ray diffraction

Single crystals were mounted on glass fibres or transparent MiTeGen Micromounts^{TM} precision tools and cooled to 200 ± 2 K before data collection using an FTS AirJet compressed air refrigerator (SP Scientific) liquid nitrogen cryogenic system. The X-ray diffraction data were collected on Bruker Kappa Apex and Bruker Smart Apex diffractometers equipped with APEX II CCD detectors using MoKα radiation (wavelength $\lambda = 0.7103$ Å). The distance from crystal to detector was between 43 mm and 45 mm as needed, and the scan width ($\Delta\omega$) was 0.5° per frame. The data collection strategy was chosen in such a way to get 100% completeness. The data collection, cell refinement, integration, and reduction were carried out using the APEX III software package. Structures of cocrystals were solved using WinGX software packages with the direct method and refined based on the spherical atom approximation based on F2 using SHELXL 97.[55] Crystal packing diagrams and the crystal structure images were generated using Mercury 2020.1 and POV-Ray.[56] Analysis of intermolecular interactions was done with PLATON.[57] The non hydrogen atoms were refined anisotropically and hydrogen atoms were refined using difference Fourier maps or positioned geometrically. Crystallographic information files have been deposited in the Cambridge Structural Database, entries 2215842 – 2215846. It is noted that after work on this project commenced, Pennington and coworkers reported the X-ray diffraction structure of **1**, which is in agreement with our findings.[58]

4.3.3 (iii) Mechanochemistry and powder X-ray diffraction

The cocrystals were also synthesized mechanochemically using a Retsch MM400 ball mill and by placing deuterated 2,3,5,6-tetramethylpyrazine and halogen bond donors (except Br_2) in a 1:1 molar ratio in 10 mL stainless steel ball mill jars. The mixtures were ground for 45 min at 18 Hz frequency with two stainless steel milling balls. The produced cocrystalline powders were individually placed in zero diffraction plate sample holders and diffraction data were collected on a Rigaku UltimaIV powder diffractometer at 293 ± 2 K (Cu Kα_1 radiation with a wavelength of λ = 1.54056 Å). The measurements were carried out in focussed beam geometry with a step scan technique, with 2θ ranging from 5 to 60°. Data were acquired by a scintillation counter detector in continuous scanning mode with a step size of 0.02°. Experimental and simulated PXRD patterns were then compared to assess morphology and phase purity.

4.3.4 (iv) ^{2}H solid-state NMR spectroscopy

^{2}H solid-state NMR experiments were performed on a 200 MHz (B_0 = 4.7 T) spectrometer using a Bruker Avance III console and a single-channel wideline probe fitted with a 5 mm solenoid coil. Static ^{2}H NMR spectra were acquired using a quadrupolar echo[59,60] $(\frac{\pi}{2} - \tau - \frac{\pi}{2} - \tau)$ pulse sequence using a 4 μs π/2 pulse length and a 20 μs τ delay. The T_1 relaxation experiments were performed using a quadrupolar echo coupled with an inversion recovery sequence at temperatures ranging from approximately 140 K to 320 K at roughly 10 to 20 K intervals. A high-pressure liquid nitrogen cylinder was connected to the VT inlet of the probe via a wide mouth insulated glass Dewar which was continuously maintained at liquid N_2 temperature. The sample temperature was measured with a thermocouple connected to a multimeter.

(v) Density functional theory calculations

DFT calculations (LDA/VWN functional) were carried out using the Amsterdam Modelling Suite (2020). 61,62 Models consisting of a halogen donor and acceptor molecule were built based on the single X-ray crystal structures. A series of linear transit calculations were performed using the TZ2P basis set by optimizing the Cartesian coordinates and varying the H-C-C-C dihedral angle from -180° to +180° for the methyl group of TMP nearest to the halogen bond. After each geometry optimization cycle, the energy was calculated at every point of methyl group rotation of interest. The activation energy is then estimated by subtracting the energy minimum from the energy maximum.

4.4 Results and Discussion

4.4.1 (i) Synthesis, X-ray diffraction, and description of crystal structures

Five halogen-bonded cocrystals were prepared as described in the Experimental section: 1,4-dibromotetrafluorobenzene·2,3,5,6-tetramethylpyrazine (**1**); 1,3,5-tribromo-2,4,6-trifluorobenzene·2,3,5,6-tetramethylpyrazine (**2**); Br_2·2,3,5,6-tetramethylpyrazine (**3**); 1,4-dichlorotetrafluorobenzene·2,3,5,6-tetramethylpyrazine (**4**); 1,3,5-trichloro-2,4,6-trifluorobenzene·2,3,5,6-tetramethylpyrazine (**5**) (see Figure 4.2). Initial cocrystallization tests employed protiated halogen bond acceptor 2,3,5,6-tetramethylpyrazine (TMP; **6**). Further preparations of these five cocrystals employed deuterated **6**, prepared as described in the Experimental section.

Single cocrystals of samples **1** to **5** were grown and their structures solved using single-crystal X-ray diffraction. Crystallographic information on these samples is summarized in Table 4.1 and complete details are provided in the Supporting Information (SI). Shown in Figure 4.3 are the packing motifs obtained from the single-crystal X-ray diffraction models for each cocrystal as well as for pure TMP. These images serve to highlight the halogen bonds in these structures as well as the overall nature of the packing of molecules in each system. Key features of the structures and solid-state packing of each compound will be discussed briefly in turn in the following paragraphs. Weaker interactions which may influence methyl rotational barriers will be discussed in a subsequent section in the context of deuterium spin-lattice relaxation data (*vide infra*).

Cocrystal **1** packs in the $P2_1/n$ space group and features one crystallographically distinct molecule of 1,4-dibromotetrafluorobenzene and two crystallographically distinct molecules of 2,3,5,6-tetramethylpyrazine. One of the TMP molecules is halogen-bonded ($r_{\mathrm{N}\cdots\mathrm{Br}} = 2.919(3)$ Å), via each of its two nitrogen atoms, to the bromine atoms in two molecules of 1,4-dibromotetrafluorobenzene, with a halogen bond angle of 171.37(8)°. The corresponding reduced distance parameter ($R_{\mathrm{XB}} = r_{\mathrm{N}\cdots\mathrm{Br}} / \Sigma r_{\mathrm{vdW}}$, where $r_{\mathrm{N}\cdots\mathrm{Br}}$ is the halogen bond distance and the denominator is the sum of the van der Waals' radii of the halogen and nitrogen) of 0.86 suggests a moderately strong halogen bond. The other TMP molecule in **1** does not engage in halogen bonding. The constituent molecules in cocrystal **1** are seen to stack in a T-shape (Figure 4.3) whereby the planes of the donor and acceptor molecules involved in the halogen bonds are nearly orthogonal to each other, rather than nearly coplanar. The structure of **1** was also reported recently at a lower temperature of 100 K.[58]

Cocrystal **2** packs in the $P2_1/n$ space group. The asymmetric unit is comprised of one molecule of 1,3,5-tribromo-2,4,6-trifluorobenzene and one molecule of 2,3,5,6-tetramethylpyrazine. In contrast to cocrystal **1**, the donor and acceptor molecules of **2** are nearly coplanar (Figure 4.3). There are two crystallographically distinct bromine-nitrogen halogen bonds with distances of 3.028(3) Å and 2.958(3) Å and angles of 177.3(1)° and 178.2(1)°, respectively. The reduced distance parameters of 0.88 and 0.86, respectively, are again indicative of moderately strong halogen bonds. The third bromine atom of the ring has a close contact with one of the fluorine atoms of an adjacent 1,3,5-tribromo-2,4,6-trifluorobenzene molecule.

Cocrystal **3** packs in the $P\overline{1}$ space group and features half a molecule of 2,3,5,6-tetramethylpyrazine and half a molecule of Br_2 in the asymmetric unit. Each bromine molecule engages in two crystallographically identical and nearly perfectly linear (178.26(7)°) halogen bonds with two TMP molecules (Figure 4.3). The bromine-nitrogen halogen bonds are 2.87(1) Å long, corresponding to the smallest reduced distance parameter of 0.84 among the novel cocrystals prepared in this work. The crystal structure is thus comprised of offset planar sheets of halogen bonded $–(\mathrm{TMP{\cdot}Br_2})_n–$ moieties, with a spacing of 3.103 Å between sheets. This structure provides a particularly clearcut demonstration of the ability of molecular bromine to engage in structure-directing halogen bonding, in analogy with the ability of molecular iodine,[51] the stronger halogen bond donor.

Cocrystal **4** packs in the $P2_1/n$ space group. There are two crystallographically distinct molecules of 2,3,5,6-tetramethylpyrazine and one crystallographically distinct molecule of 1,4-dichlorotetrafluorobenzene. As with cocrystal **1**, in cocrystal **4** there is one TMP molecule which does not participate in any halogen bonds. The second TMP molecule has two crystallographically identical halogen bonds to chlorine at each of its two nitrogen atoms (Figure 4.3). These halogen bonds are 2.979(2) Å long and have a $\mathrm{C\text{-}Cl\cdots N}$ angle of 170.62(7)°. They are relatively weak, with a reduced distance parameter of 0.90, and also deviate furthest from linearity among those studied presently. The planes of the halogen bond donor and acceptor molecules are twisted by approximately 72° relative to one another, resulting in another example of the "T-shape" conformation as seen in cocrystal **1**.

Cocrystal **5** packs in the $P2_1/n$ space group and has one molecule each of 1,3,5-trichloro-2,4,6-trifluorobenzene and of 2,3,5,6-tetramethylpyrazine in the asymmetric unit. Similarly to cocrystal **2**, the rings of donor and acceptor molecules are approximately coplanar, resulting in extended rippled and stacked halogen-bonded sheets (Figure 4.3). These sheets are ~3.57 Å apart. Analogously to cocrystal **2**, each of the two crystallographically distinct nitrogen atoms in each

TMP molecule forms a halogen bond to an adjacent 1,3,5-trichloro-2,4,6-trifluorobenzene molecule via chlorine. Similarly, two of the three crystallographically distinct chlorine atoms are engaged in halogen bonds with these nitrogen atoms, while the third chlorine atom has a close contact with fluorine on an adjacent 1,3,5-trichloro-2,4,6-trifluorobenzene molecule. The two halogen bonds have distances of 3.010(2) and 3.128(2) Å, with halogen bond angles of 177.88(8) and 174.02(8)°, respectively. These are the longest and weakest halogen bonds in the present study, with reduced distance parameters of 0.92 and 0.96, respectively. In fact, given the relatively weak capacity of chlorine to form halogen bonds, compared to the larger and more polarizable Br and I, the preparation of stable cocrystals **4** and **5** in and of itself is somewhat remarkable.

Taken together, the preparation of cocrystals **1** through **5** via cosublimation, slow evaporation, and mechanochemical methods provides evidence for the strong structure-directing capabilities of even weaker halogen bonds in the gas phase, in solution, and in the solid state.

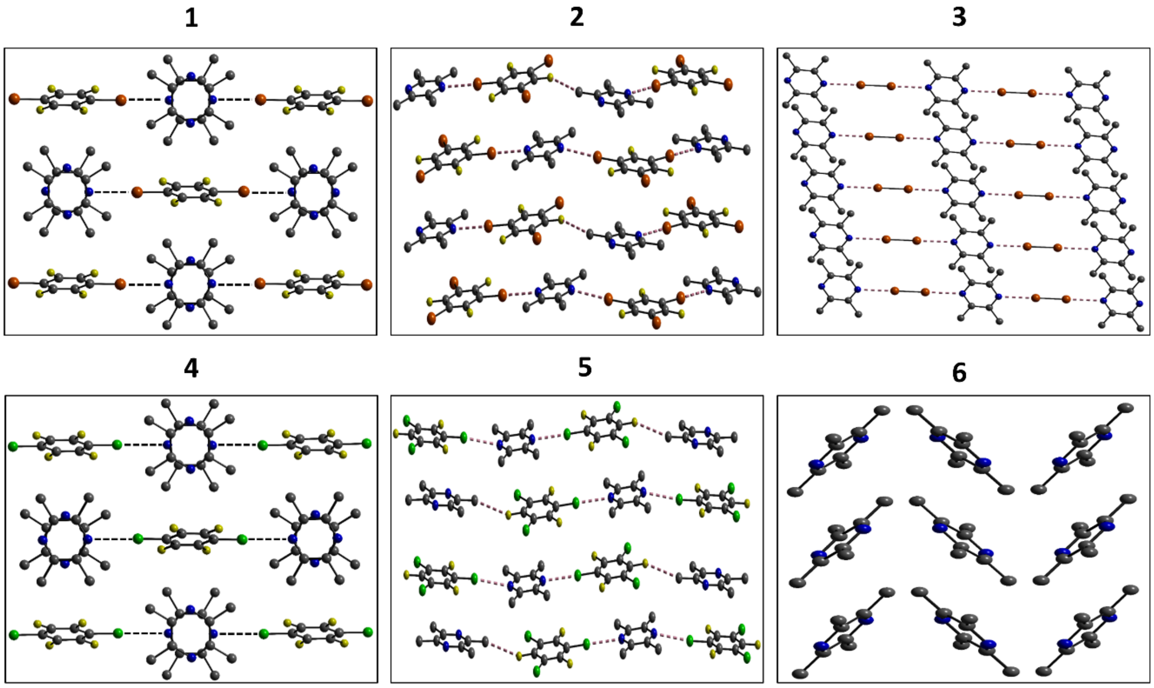

Figure 4.3. Packing motifs obtained from single-crystal X-ray diffraction studies of cocrystals 1, 2, 3, 4, 5, and pure TMP (6). Halogen bonds are depicted with dashed lines. Carbon: grey; hydrogen/deuterium: white; nitrogen: blue; bromine: orange; yellow: fluorine; green: chlorine.

Table 4.1. Selected crystallographic and halogen bond geometrical parameters for the compounds studied herein.

entry	space group	R_{XB}	X···N / Å	Y-X···N / °	CCDC entry
1	$P2_1/n$	0.86	2.919(3)	171.37(8)	2215842
2	$P2_1/n$	0.88	3.028(3)	177.3(1)	2215844
		0.86	2.958(3)	178.2(1)	
3	$P\bar{1}$	0.84	2.87(1)	178.26(7)	2215846
4	$P2_1/n$	0.90	2.979(2)	170.62(7)	2215843
5	$P2_1/n$	0.92	3.010(2)	177.88(8)	2215845
		0.96	3.128(2)	174.02(8)	
6	*Pbca*	n/a	n/a	n/a	1214276

The cocrystals were also prepared as powders and powder X-ray diffractograms were recorded for each sample. A representative example of the agreement between the diffractogram obtained from a powdered sample of **1** and the simulated diffractogram generated from the single-crystal X-ray structure is shown in Figure 4.4. Analogous comparisons for the remaining cocrystals are provided in the Supporting Information. These data show that the powdered samples studied by ^{2}H solid-state NMR spectroscopy (*vide infra*) have the same structure as single-crystalline samples, which is essential to interpreting the NMR data in the context of the crystal structures. These data also again demonstrate the robust ability of the halogen bonds in these systems, some of which are relatively weak, to predictably direct the cocrystallization pathway regardless of whether this is carried out in the gas phase, in solution, or directly in the solid state.

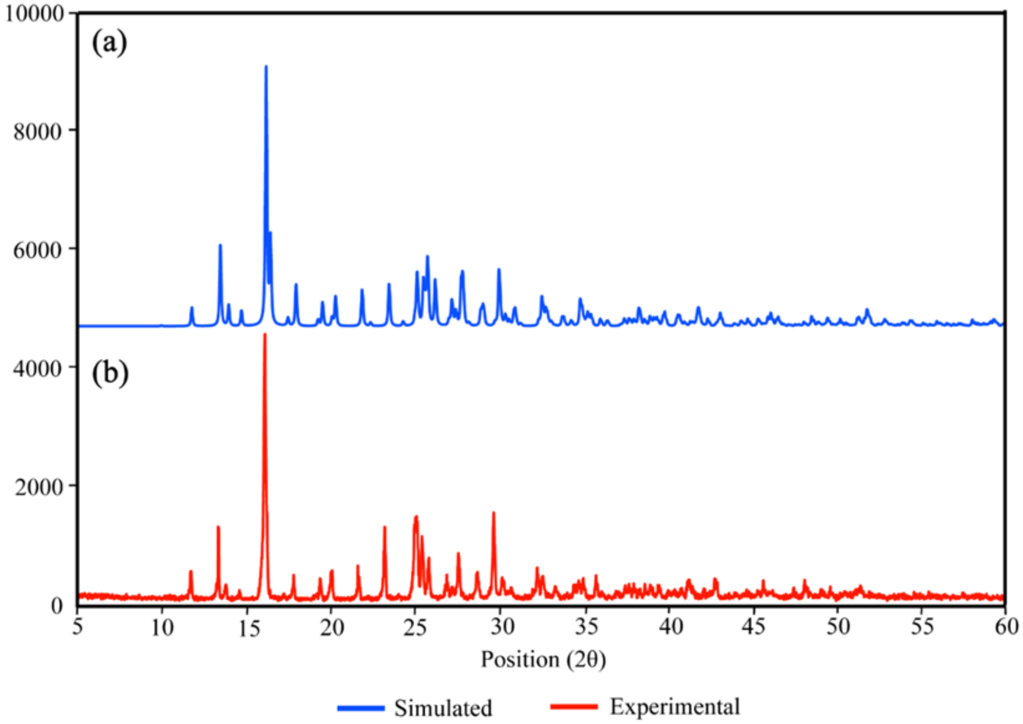

Figure 4.4. Experimental (bottom) and simulated (top) powder X-ray diffractograms of the 1,4-dibromotetrafluorobenzene·TMP cocrystal (cocrystal 1). A partially resolved peak splitting near 2θ = 16° in the simulated diffractogram appears as an unresolved asymmetric broadening in the experimental pattern.

4.4.2 (ii) Measurement of methyl rotational activation energies via ^{2}H NMR spectroscopy

As mentioned in the Introduction, deuterium NMR spectroscopy is a very valuable probe of dynamics in solids. In this section, the results of variable-temperature ^{2}H solid-state NMR experiments carried out on samples **1** to **6** are described and discussed. In addition to recording one-dimensional spectra, a large series of inversion-recovery experiments over a range of temperatures are analyzed to extract information on the methyl rotational barriers in these samples (see SI).

Shown in Figure 4.5 are some representative Pake patterns obtained with a one-dimensional ^{2}H quadrupolar echo pulse sequence for stationary powdered samples of **1** to **6**. These spectra have been simulated in order to extract the effective quadrupolar coupling constant (C_Q) and asymmetry parameter (η) for deuterium. As methyl groups are known to rotate over a wide range of temperatures (well-modelled by methyl hopping about the local pseudo-C_3 axis down to about 80 K)[43], the observed patterns shown at room temperature (~296 K) and low temperature (~147 K) reflect a motionally-averaged electric field gradient tensor. Rotation about the local methyl C_3 axis results in a scaling of this tensor by $3cos^2\theta$-1, where θ is the angle between the C-D bond vector and the local rotation axis (i.e., $\theta \approx 109.47°$). For methyl groups, the powder patterns and effective ^{2}H quadrupolar coupling constants are thus scaled by -1/3. The effective deuterium quadrupolar coupling constants obtained from the simulations are roughly constant across all samples and across the temperature range studied, i.e., about 51 to 53 kHz. These data therefore correspond to standard $C_Q(^2H)$ values for static methyl deuterons of approximately 156 kHz. The effective asymmetry of the EFG tensor, representative of librational motions, shows slight variations (see Figure 4.5 and SI), particularly at lower temperatures. It is noted that the above-mentioned scaling and derived values of the static quadrupolar coupling constants are consistent with an absence of any other significant dynamic processes (e.g., ring flips) on the time scale of these NMR experiments.

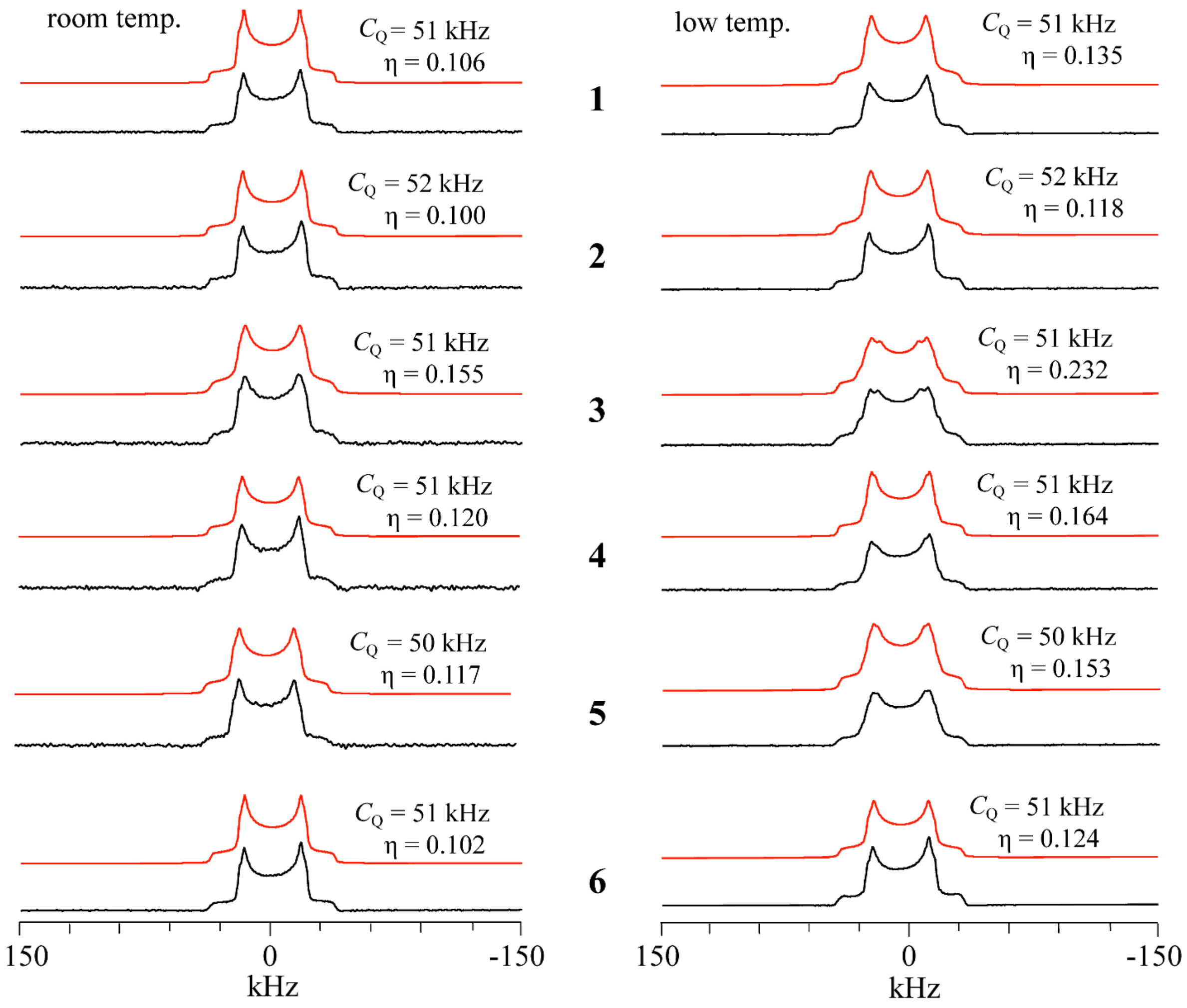

Figure 4.5. Experimental and simulated deuterium quadrupolar echo line shapes for compounds 1 to 6 at room temperature (296 ± 3 K; left) and low temperature (147 ± 3 K; right). These errors represent the small range in temperatures over which the data were acquired for different samples rather than the uncertainty in the temperature measurement.

Deuterium spin-lattice relaxation time constants were recorded as a function of temperature (~140 K to ~320 K) using a quadrupolar echo inversion-recovery NMR pulse sequence. The integrated Pake pattern areas were plotted as a function of time and fit to an exponential function to determine T_1 for each compound at each temperature. A representative example of these data is shown in Figure 4.6 for cocrystal **3** at 296.1 K, and all other data are provided as Supporting

Information. T_1 values range from 0.129 s at 144.6 K to 2.013 s at 323.5 K for **1**, 1.269 s at 149.3 K to 5.905 s at 321.1 K for **2**, 0.036 s at 132.5 K to 1.472 s to 316.3 K for **3**, 0.868 s at 146.3 K to 4.447 s at 311.3 K for **4**, and 0.446 s at 144.9 K to 5.202 s at 313.4 K for **5**.

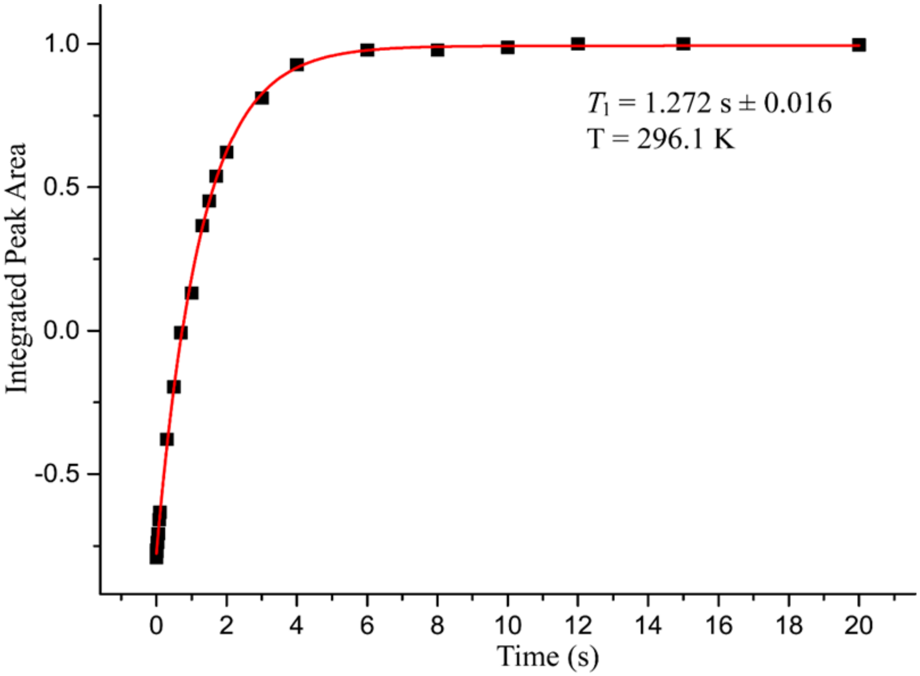

Figure 4.6. Inversion-recovery ^{2}H NMR measurement of $T_1(^2H)$ for cocrystal 3 at 296.1 K. Experimental data are shown in black and the best fit is shown in red. Data were fit to $I[t]=I[\infty](1-2A\exp(-t/T_1))$.

Arrhenius plots of $\ln(T_1)$ as a function of inverse temperature furnish the activation energies associated with the methyl rotation in each of the compounds studied (Figure 4.7). This analysis assumes that methyl deuteron relaxation is dominated by modulation of its nuclear quadrupolar interaction induced by its three-fold rotation. The activation energies determined thusly are summarized in Table 4.2. These range from a high of 7.31 ± 0.17 kJ mol^{-1}, as reported previously,[51] for TMP, to a low of 3.75 ± 0.04 kJ mol^{-1} for cocrystal **5**. Importantly, even for cocrystals **1** and **4**, which include additional TMP molecules in the crystal lattice which are not engaged in halogen bonds, the relaxation data fit well to a single exponential function, implying that a single T_1 value is sufficient to describe the effective relaxation in these systems. Maus et al. have commented that possible exchange between different methyl sites can result in an effective decrease of the T_1 of a slower-relaxing site.[63] The quality of the fits of the data obtained, together with the relatively small spread in derived activation energies, further justifies the use of a single T_1 value; however, these values are best considered effective or averaged values across all methyl groups in a given system. Also included for comparison in Table 4.2 are data[51] for some iodinated analogues of the chloro- and bromo- cocrystals studied presently. Among all of these halogen-bonded systems, the lowest activation energy of 2.84 ± 0.14 kJ mol^{-1} is seen for 1,4-diiodotetrafluorobenzene·TMP. DFT calculations of the rotational activation energies using small cluster models comprised of donor and acceptor molecules only roughly reproduce the experimental trend (Figure S14 and S15, SI) with a correlation coefficient (R^2) of just 0.6024. This result suggests that longer range contacts from the crystal lattice play determinative roles in the values of E_a (*vide infra*). It is also noted that the measurement and interpretation of quadrupolar order relaxation time constants (T_{1Q}) could provide additional insights for future work, as they probe different spectral densities than do T_1 values.[64]

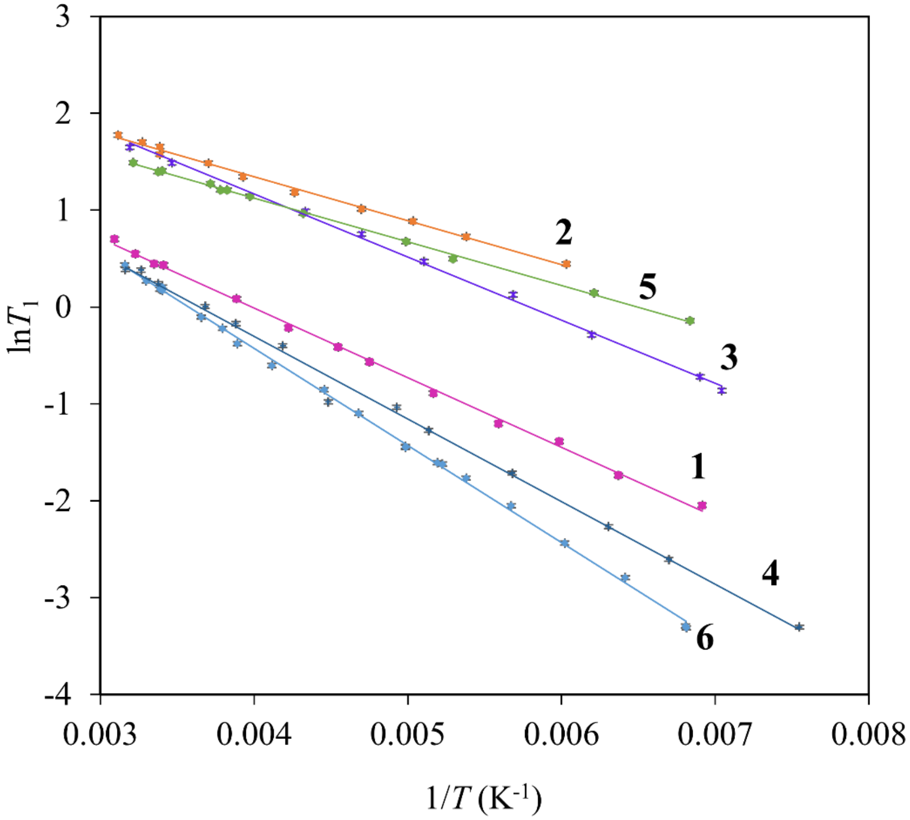

Figure 4.7. Arrhenius plot of lnT_1(^{2}H) vs 1/T for compounds 1 to 6.

Table 4.2. Experimental activation energies for methyl rotation, and computed molecular electrostatic potential maxima, in a series of halogen-bonded cocrystals of 2,3,5,6-tetramethylpyrazine (TMP)

Compound	E_a / kJ mol^{-1}	packing motif	MEP on σ-hole / kJ mol^{-1}
1,4-dibromotetrafluorobenzene·TMP (**1**)	5.98 ± 0.07	T-shape	132
1,3,5-tribromo-2,4,6-trifluorobenzene·TMP (**2**)	3.77 ± 0.08	coplanar	128
Br_2·TMP (**3**)	5.41 ± 0.09	linear	127
1,4-dichlorotetrafluorobenzene·TMP (**4**)	7.08 ± 0.15	T-shape	81
1,3,5-trichloro-2,4,6-trifluorobenzene·TMP (**5**)	3.75 ± 0.04	coplanar	82
TMP (**6**)	7.31± 0.17[a]	zig-zag	n/a
1,4-diiodotetrafluorobenzene·TMP[a]	2.84 ± 0.14[a]	coplanar	168
1,3,5-trifluoro-2,4,6-triiodobenzene·TMP[a]	3.24 ± 0.13[a]	coplanar	162
I_2·TMP[a]	3.62 ± 0.13[a]	linear	155

[a]. Data from reference 51.

These activation energies may be compared with data available for other organic systems not featuring halogen bonds. Typical barriers for methyl rotation in aliphatic systems range from 8 to 12 kJ mol^{-1}.[63] Wang et al. reported values ranging from 1.7 to 13.4 kJ mol^{-1} for a series of methyl-substituted phenanthrenes and naphthalenes.[46] All of the values described in the present work (Table 4.2) fall within this range. The average value in the fluid hydrophobic core of SH3 domain from α-spectrin was found to be 11.7 ± 3.8 kJ mol^{-1},[50] while a particularly high barrier of 26.8 ± 1.7 kJ mol^{-1} for the axial methyl group of trigonal-bipyramidal $[W(\eta^5\text{-}C_5Me_5)Me_4]^+$ has been reported.[63] In this context it is important to note that different classes of systems are likely to be subject to a different weighting of factors which may determine the activation energies associated with methyl rotation. For instance, substitution on an aromatic core may result in correlations not only with steric effects, but also with the local π-bond order of the aromatic rings.[46] Maus et al.[63] commented on the impossibility of interpreting the barrier of 26.8 ± 1.7 kJ mol^{-1} in the above-mentioned tungsten complex due to the unknown influence of the charge of the system, local symmetry, and the nature of other nearby ligands. In the following section, we therefore aim to interpret the activation energies determined for halogen bonded systems of TMP within a self-consistent context that is able to rationalize and account for the experimental observations.

4.4.3 (iii) Factors influencing methyl dynamics

To understand the underlying origins of the experimentally observed methyl rotational barriers, several hypotheses were considered. As it has been demonstrated previously that there is a significant electronic component which influences the activation energy in related iodinated systems, we first sought to simply correlate the rotational barriers with the strength of the σ-hole. Szell et al.[51] have demonstrated that the trend in experimental activation energies in three iodinated cocrystals of TMP follow the trend in computed σ-hole electrostatic potentials (Table 4.2). This work also established computationally the importance of the strength of the halogen bond donor in determining the methyl rotational barriers, thereby proving that simple steric considerations were not sufficient to explain the observed trends.[51] However, for the broader range of systems studied presently, which have a range of crystal morphologies and which cover chloro, bromo, and iodinated halogen bond donors, it is clear that that the MEP maximum does not correlate universally with the observed activation energies (see Figure S17, SI).

Although the MEP maximum at the σ-hole does not correlate universally with the experimental activation energies, it is constructive to examine subsets of the data shown in Table 4.2. Consider the pair of isomorphic ($P2_1/n$) cocrystals **1** and **4** which feature 'T-shaped' arrangements and additional TMP molecules in the unit cell. The activation energies for these two cocrystals (5.98 and 7.08 kJ mol^{-1}) correlate inversely with the MEP maximum of the halogen donor (132 and 81 kJ mol^{-1}), correlate directly with the length of the halogen bond (2.919 and 2.979 Å), and correlate directly with the reduced distance parameter (0.86 and 0.90, respectively). The MEP maxima of the halogen bond donor atoms in Br_2.TMP and I_2.TMP (127 and 155 kJ mol^{-1}) similarly correlate inversely with the methyl rotational barriers (5.41 and 3.62 kJ mol^{-1}). However, the isomorphous cocrystals **2** and **5** have the same activation energy within experimental error, while their MEP maxima are very different (128 and 82 kJ mol^{-1}). These isolated comparisons among pairs of analogous cocrystalline systems further establish that while electronic considerations play a key role in determining the rotational energy barriers, there are other factors which must be uncovered.

As a further electronic consideration, a representation of π-order of the N-C/C-C bonds of the TMP rings was computed as the difference between the N-$\underline{C}$ and $\underline{C}$-C bond lengths where the underlined carbon atom represents the anchor point on the pyrazine ring for each methyl group. The results were analyzed for the various cocrystals. Wang et al. have described for a series of phenanthrenes and naphthalenes how orbital overlap between the methyl groups and adjacent aromatic rings can stabilize certain conformations of the methyl group.[46] Their work showed that some changes in activation energy could be explained by differences in the π-bond order of the adjacent C-C aromatic rings, but there were exceptions to this due to steric effects. We find similar results here, where the π-bond orders computed for the TMP nitrogen-carbon bonds adjacent to the methyl groups do not show any general correlation with the experimental methyl rotation activation energies (see SI).

A simple consideration of local steric hindrance of the methyl rotation was considered. One hypothesis was that shorter contacts between the methyl deuterons and the halogen bond donor molecule would result in more hindered rotation. However, no general correlations with the length of the halogen bond nor with the reduced distance parameter are noted (see SI). Furthermore, such an argument goes completely counter to all experimental observations to date for halogen bonded systems, where it is seen that forming a halogen bond to the nitrogen of TMP, directly adjacent to the methyl groups, actually reduces the rotational barrier, rather than increasing it.

Table 4.3. Void volumes.

compound	unit cell volume /Å^3	void volume / Å^3	void volume / %
1	1158.8	138.79	12.0
2	1655.25	218.89	13.2
3	274.4	56.92	20.7
4	1147.6	141.42	12.3
5	1610.4	269.46	16.7
6	788.005	103.55	13.1

a. Probe radius = 0.4 Å; grid spacing = 0.4 Å.

The next consideration was that of total available void volume in the unit cell for each of the cocrystals (Table 4.3). The hypothesis in this case was that a brute-force assessment of total free volume could be correlated with the ease of methyl rotation. Void volumes, defined as empty spaces in crystal unit cells that are big enough to hold a spherical "probe" of a given radius, were computed using Mercury software and the available crystallographic information files for each cocrystal and for TMP. Although different probe radii and grid setting are known to influence the specific results obtained in void volume calculations,[65] the main finding here, that this void volume percentage does not correlate with the changes in methyl rotational barriers, is consistent across a range of settings used (see Table 4.3 and SI). The lack of any correlation clearly runs counter to simplistic notion that more empty space in the unit cell will translate directly to freer methyl rotation.

More specific consideration was given to short intermolecular contacts to the methyl groups, and possible steric effects which could influence their rotational energy barriers. All contacts to the methyl carbons and to the methyl hydrogens/deuterons were assessed and tabulated. It quickly became apparent that there are many such contacts within the van der Waals' radii + 0.5 Å in some of the cocrystals and that discerning any possible influencing factors required some informed filtering of the contacts. The approach of Baudry[49] was explored, whereby satellites of the methyl groups at specific angular positions within a certain distance were considered. However, this did not lead to any meaningful results for the present systems.

To understand which contacts to the methyl groups are the most influential in determining the rotational activation energies, attention was paid to the two limiting cases, namely the TMP molecule which has the highest methyl rotational barrier among those compounds studied herein, and 1,4-diiodotetrafluorobenzene·TMP, which has the lowest (Table 4.2). Careful inspection of the close contacts (sum of vdW radii + 0.5 Å) to the methyl groups in these structures revealed that in TMP, the average number of close contacts to the methyl carbons was 3.00, while in 1,4-

diiodotetrafluorobenzene·TMP, the average is 1.50 (Figure 4.8). Assessment of the halogen-bonded system with the highest activation energy, **4**, showed that the average number of close contacts to the methyl carbons was large, 3.75 (Figure 4.8b). These findings led to further consideration of the number of close contacts to nearby carbon atoms (*N*) in the remaining cocrystals. This approach yielded very interesting strong correlations with the experimental activation energies.

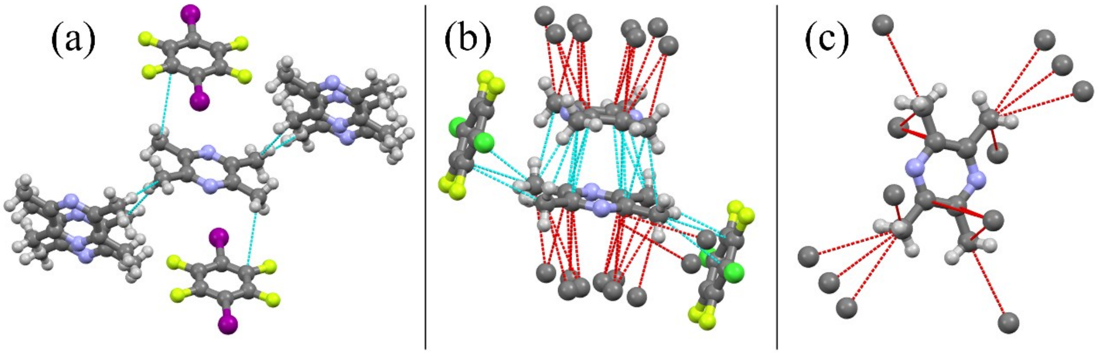

Figure 4.8. (a) The 1,4-diiodotetrafluorobenzene·TMP cocrystal (which has the lowest methyl rotational barrier among the compounds discussed in this work) has an average of 1.5 close contacts between the methyl carbons and any other carbons in the crystal structure. (b) The largest number of methyl-carbon contacts (marked with dashed red and turquoise lines) are noted for 1,4-dichlorotetrafluorobenzene·TMP (4), with an average of 3.75 contacts per methyl group. (c) The pure TMP molecule has an average of 3.00 contacts per methyl group. Contacts are defined here as carbon-carbon distances within the sum of the van der Waals' radii + 0.5 Å.

As shown in Figure 4.9A, a weak direct correlation between the experimental activation energies and the average number of carbon close contacts exists ($E_a = 1.0208N + 2.5376$; $R^2 = 0.6588$). The average number arises from the fact that there are typically two crystallographically distinct methyl carbons in each cocrystal, and four in the cases of cocrystals

1 and **4**. The use of an average value (Table 4.4) is an approximation, but nevertheless provides an empirical point of reference for exploring correlations with activation energy. Further inspection of the data, as well as consideration of the electronic effects of the halogen bond discussed above, led us to plot the data separately on the basis of the nature of the halogen involved in the halogen bond. Shown in Figure 4.9B are three data sets, one for chloro-, bromo-, and iodinated systems. Remarkably, near-perfectly linear correlations ($R^2 \geq 0.96$) between the experimental activation energies and the average number of close contacts to carbon are obtained. While the two-point correlation for the chloro compounds is not meaningful in isolation, and there are a limited number of datapoints overall, consideration of all three datasets provides a convincing basis for understanding the experimental trends. The correlations for each halogen are characterized by different slopes, largest for chlorine and smallest for iodine, which is consistent with the notion that the electronic effect of the stronger iodine-based halogen bonds is more difficult to disrupt via steric effects, whereas the influence of the quite weak chlorine-based halogen bonds is much easier to disrupt. The intercepts of the three lines of best fit lie between 0.839 and 2.935 kJ mol^{-1}, suggesting that in absence of any steric hindrance due to nearby carbon atoms, methyl rotational energy barriers as low as this could potentially be achieved in an isolated TMP molecule. These values remain much higher than the 26 J mol^{-1} reported for bicyclopentane-dicarboxyate struts in a zinc organic framework,[24] reflecting at least in part the intrinsic rotational barrier within an isolated 2,3,5,6-tetramethylpyrazine molecule which has close intramolecular steric contacts between the methyl group and both the pyrazine ring and the adjacent methyl group on this ring.

Table 4.4. Average number of carbon-carbon contacts to methyl groups[a]

compound	Average number of C-C contacts
1	3.50
2	1.00
3	3.00
4	3.75
5	1.75
6	3.00
1,4-diiodotetrafluorobenzene·TMP	3.00
1,3,5-trifluoro-2,4,6-triiodobenzene·TMP	1.50
I_2·TMP	2.00

a. Sum of van der Waals' radii + 0.5 Å.

The offsets seen for the three datasets shown in Figure 4.9B are rationalized in the context of the electronic factors (σ-hole MEP) discussed above. For example, although Br_2·TMP and I_2·TMP have the same number of average contacts to carbon ($N = 3$), the latter has a deeper σ-hole on the halogen with a MEP maximum of 155 kJ mol^{-1} compared to the former which has a MEP maximum of only 127 kJ mol^{-1}. Thus, their difference in experimental methyl rotational barriers may be attributed largely to differences in electronic effects rather than steric ones. The mechanism of this effect was elucidated by Szell et al., who showed via DFT calculations that within the typical range of reduced distances observed here, a halogen bond donor with a stronger σ-hole (iodotrifluoromethane) results in a decreased activation energy compared to an analogous donor (iodomethane) with a weaker σ-hole.[51]

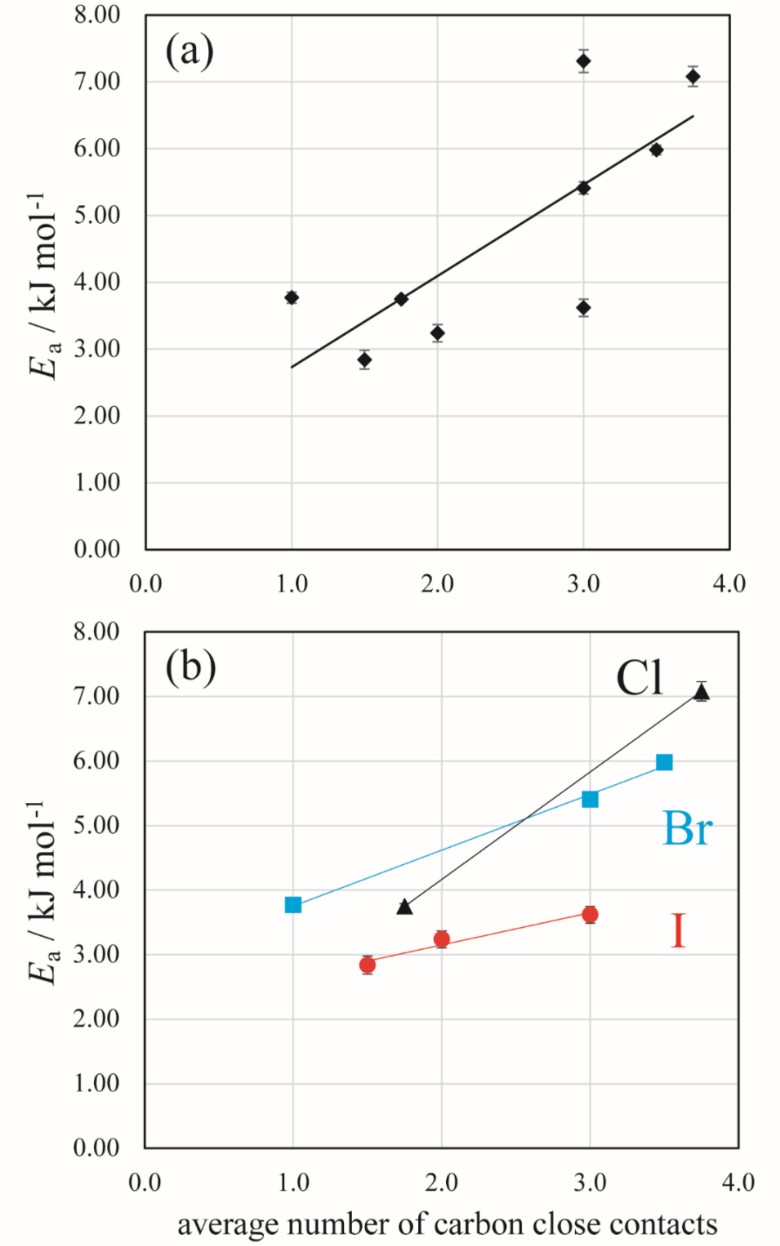

Figure 4.9. Plots of experimental methyl rotational barriers vs the average number of carbon close contacts. (a) Data for all cocrystals discussed in this work, plus TMP. $E_a = 1.3658N + 1.3634$; $R^2 = 0.5958$. (b) Data separated by the nature of the halogen bond donor: iodinated (red circles; E_a

= $0.5000N + 2.150$; $R^2 = 0.9586$); brominated (blue squares; $E_a = 0.8657N + 2.889$; $R^2 = 0.9963$); chlorinated (black triangles; $E_a = 1.665N + 0.8386$; $R^2 = 1$).

The role of carbon-carbon contacts in governing the observed trends in activation energy may be due to their uniqueness when carbon is compared to the other elements in these systems. There are numerous contacts beyond the sum of the van der Waals' radii in the systems studied herein, not just those between carbon atoms. Aside from hydrogen, which is small and also in constant motion in these systems, every other element (N, F, Cl, Br) has lone pairs of electrons and/or a large polarizable electron cloud. These elements may act as transient electron donors to engage in weak hydrogen bonds or close contacts with the methyl hydrogens, neither reducing nor increasing the overall rotational barrier. Carbon, on the other hand, cannot provide the same sort of interaction and would therefore appear to act only as a steric barrier, resulting in increased activation energies as described above.

Finally, it is noted that the average number of carbon-carbon contacts may also be proxied by the qualitative nature of the crystal packing shown in Figure 4.3 and described in Table 4.2. For instance, the "T-shaped" brominated and chlorinated cocrystals (**1** and **4**) have a larger number of carbon contacts and larger E_a values when compared to their "coplanar" analogues (**2** and **5**). The fact that **1** and **4** have additional TMP molecules not engaged in halogen bonds suggests that in future work, tuning cocrystal stoichiometry 66,67 could provide a systematic route to modulating rotational dynamics in novel systems.

On the basis of the above findings, the application of halogen bonds and other σ-hole interactions to modulate rotational dynamics in more complex systems including molecular machines and biological systems may be considered. For example, the role of halogen bonds in governing structural, enthalpic, and entropic factors in proteins, enzymes and nucleic acids has been discussed by Ho and coworkers.[68,69,70,71] The engineering of biomolecules to feature halogen bonding moieties and other non-covalent interactions at specific backbone sites so as to influence dynamics and function may now be considered on the basis of the principles discussed herein, namely via a judicious balance of steric and electronic effects. Halogen bonds may possibly be a valuable new tool for engineering not only protein and enzyme structure, but also dynamics and functionality.

4.5 Conclusions

A series of new halogen-bonded cocrystals has been designed and prepared via gas-phase cosublimation, solution-phase slow evaporation methods, and solid-state mechanochemical ball milling. Within these systems, even weak halogen bonds involving chlorine proved effective in consistently generating cocrystalline architectures whose structural features are governed by these bonds. A rare example of molecular bromine as a halogen bond donor has been established. A detailed X-ray diffraction and solid-state ^{2}H NMR study has shown that methyl dynamics in the crystalline state are modulated via halogen bonds. More precisely, the activation energy associated with these rotational dynamics is controlled by a combination of electronic and steric factors. Somewhat counterintuitively, the introduction of a halogen bond donor molecule in relatively close steric contact with rotating methyl groups consistently results in a decrease of the rotational energy barrier. This finding is explained via a close examination of the electronic, structural, and crystallographic features of the cocrystalline systems.

The average number of carbon-carbon close contacts to the methyl group is found to be a key steric metric capable of rationalizing the observed trends in rotational energy barrier when the compounds are grouped by the identity of the halogen bond donor atom (Cl, Br, or I). Differences between each of these groups are accounted for by considering the strength of the σ-hole, as measured via computed molecular electrostatic potential maxima. The correlations for each halogen group are characterized by different slopes, demonstrating that the electronic impact of the σ-hole of the stronger iodine-based halogen bonds is more difficult to disrupt via steric effects, whereas the influence of the weaker chlorine-based halogen bonds on methyl rotation is easier to disrupt via steric effects. This work has also suggested that one possible route to modulating these dynamics is to design and engineer novel cocrystals of variable stoichiometry, thereby maintaining the core chemical features of interest between a given donor and acceptor molecule, while simultaneously modifying the number of carbon close contacts affecting methyl rotation.

To conclude, it is noted that methyl rotation is just one example of the type of dynamical process which could in principle be modulated via the direct and indirect impact of halogen bonds. More complex geared or cascade dynamics, and dynamics of larger functional groups, are also amenable to the types of modulation described here. Finally, one may envisage the application of entire additional classes of non-covalent interactions toward the direct and indirect modulation of dynamics in cocrystalline architectures, supramolecular systems, and porous materials, including chalcogen bonds, pnictogen bonds, tetrel bonds, and other tuneable and directional element-based σ-hole interactions.

4.6 Acknowledgements

We are grateful to the solid-state NMR group at the University of Ottawa for helpful feedback and discussions. We thank Dr. Jeffrey Ovens, Dr. Patrick Szell, Dr. Glenn Facey, Dr. Peter Pallister, and Mr. Vincent Morin for technical support. Prof. Natalie Goto and Prof. Javier Giorgi are thanked for valuable advice. D. L. B. thanks the Natural Sciences and Engineering Research Council of Canada for funding. This research was enabled in part by support provided by Compute Ontario (computeontario.ca) and the Digital Research Alliance of Canada (alliancecan.ca).

4.7 References

(1) Karplus, M.; Kuriyan, J. Molecular dynamics and protein function. *Proc. Natl. Acad. Sci. USA* **2005**, *102*, 6679-6685.

(2) Crawford, J. M.; Sigman, M. S. Conformational dynamics in asymmetric catalysis: is catalyst flexibility a design element? *Synthesis* **2019**, *51*, 1021-1036.

(3) Zhang, S. B. X. Y.; Pessemesse, Q.; Lätsch, L.; Engel, K. M.; Stark, W. J.; van Bavel, A. P.; Horton, A. D.; Payard, P.-A.; Copéret, C. Role and dynamics of transition metal carbides in methane coupling. *Chem. Sci.* **2023**, *14*, 5899-5905.

(4) Panja, S.; Adams, D. J. Stimuli responsive dynamic transformations in supramolecular gels. *Chem. Soc. Rev.* **2021**, *50*, 5165-5200.

(5) Davey, J. A.; Damry, A. M.; Goto, N. K.; Chica, R. A. Rational design of proteins that exchange on functional timescales. *Nature Chem. Biol.* **2017**, *13*, 1280-1285.

(6) Castet, F.; Tonnelé, C.; Muccioli, L.; Champagne, B. Predicting the Second-Order Nonlinear Optical Responses of Organic Materials: The Role of Dynamics. *Acc. Chem. Res.* **2022**, *55*, 3716-3726.

(7) Aprahamian, I. The future of molecular machines. *ACS Cent. Sci.* **2020**, *6*, 347-358.

(8) Lubbe, A. S.; van Leeuwen, T.; Wezenberg, S. J.; Feringa, B. L. Designing dynamic functional molecular systems. *Tetrahedron* **2017**, *73*, 4837-4848.

(9) Harris, R. K.; Wasylishen, R. E.; Duer, M. J., Eds. *NMR Crystallography*, Wiley, 2012.

(10) Bryce, D. L. NMR crystallography: structure and properties of materials from solid-state nuclear magnetic resonance observables. *IUCrJ* **2017**, *4*, 350-359.

(11) Oganov, A. R.; Pickard, C. J.; Zhu, Q.; Needs, R. J. Structure prediction drives materials discovery. *Nature Rev. Mater.* **2019**, *4*, 331-348.

(12) Friščić, T.; Day, G. M. Dynamic behaviour in the solid state. *CrystEngComm* **2011**, *13*, 4303.

(13) Hughes, A. R.; Liu, M.; Paul, S.; Cooper, A. I.; Blanc, F. Dynamics in flexible pillar[n]arenes probed by solid-state NMR. *J. Phys. Chem. C* **2021**, *125*, 13370-13381.

(14) Jumper, J.; Evans, R.; Pritzel, A.; Green, T.; Figurnov, M.; Ronneberger, O.; Tunyasuvunakool, K.; Bates, R. et al. Highly accurate protein structure prediction with AlphaFold. *Nature* **2021**, *596*, 583-589.

(15) Robertson, A. J.; Courtney, J. M.; Shen, Y.; Ying, J.; Bax, A. Concordance of X-ray and AlphaFold2 models of SARS-CoV-2 main protease with residual dipolar couplings measured in solution. *J. Am. Chem. Soc.* **2021**, *143*, 19306-19310.

(16) Mandala, V. S.; Williams, J. K.; Hong, M. Structure and dynamics of membrane proteins from solid-state NMR. *Annu. Rev. Biophys.* **2018**, *47*, 201-222.

(17) Alderson, T. R.; Kay, L. E. NMR spectroscopy captures the essential role of dynamics in regulating biomolecular function. *Cell* **2021**, *184*, 577-595.

(18) Toyama, Y.; Kay, L. E. Probing allosteric interactions in homo-oligomeric molecular machines using solution NMR spectroscopy. *Proc. Natl. Acad. Sci. USA.* **2021**, *118*, e2166325118.

(19) Bax, A.; Clore, G. M. Protein NMR : boundless opportunities. *J. Magn. Reson.* **2019**, *306*, 187-191.

(20) Vugmeyster, L. Recent developments in deuterium solid-state NMR for the detection of slow motions in proteins. *Solid State Nucl. Magn. Reson.* **2021**, *111*, 101710.

(21) Lewandowski, J. R.; Halse, M. E.; Blackledge, M.; Emsley, L. Direct observation of hierarchical protein dynamics. *Science* **2015**, *348*, 578-581.

(22) Shcherbakov, A. A.; Brousseau, M.; Henzler-Wildman. K. A.; Hong, M. Microsecond motion of the bacterial transporter EmrE in lipid bilayers. *J. Am. Chem. Soc.* **2023**, *145*, 10104-10115.

(23) Mamontov, E.; Cheng, Y.; Daemen, L. L.; Kolesnikov, A. I.; Ramirez-Cuesta, A. J.; Ryder, M. R.; Stone, M. B. Low rotational barriers for the most dynamically active methyl groups in the proposed antiviral drugs for treatment of SARS-CoV-2, apilimod and tetrandrine. *Chem. Phys. Lett.* **2021**, *777*, 138727.

(24) Perego, J.; Bracco, S.; Negroni, M.; Bezuidenh, C. X.; Prando, G.; Carretta, P.; Comotti, A.; Sozzani, P. Fast motion of molecular rotors in metal–organic framework struts at very low temperatures. *Nat. Chem.* **2020**, *12*, 845-851.

(25) Perego, J.; Bezuidenhout, C. X.; Bracco, S.; Piva, S.; Prando, G.; Aloisi, C.; Carretta, P.; Kaleta, J.; Phuong Le, T.; Sozzani, P.; Daolio, A.; Comotti, A. Benchmark dynamics of dipolar molecular rotors in fluorinated metal-organic frameworks. *Angew. Chem. Int. Ed.* **2023**, *62*, e202215893.

(26) Gonzalez-Nelson, A.; Mula, S.; Šimenas, M.; Balčiūnas, S.; Altenhof, A. R.; Vojvodin, C. S.; Canossa, S.; Banys, J.; Schurko, R. W.; Coudert, F.-X.; van der Veen, M. A. Emergence of coupled rotor dynamics in metal–organic frameworks via tuned steric interactions. *J. Am. Chem. Soc.* **2021**, *143*, 12053-12062.

(27) Baggi, G.; Wilson, B. H.; Dhara, A.; O'Keefe, C. A.; Schurko, R. W.; Loeb, S. J. Dynamics of a [2]rotaxane wheel in a crystalline molecular solid. *Chem. Commun.* **2021**, *57*, 8210-8213.

(28) Martinez-Bulit, P.; O'Keefe, C. A.; Zhu, K.; Schurko, R. W.; Loeb, S. J. Solvent and steric influences on rotational dynamics in porphyrinic metal–organic frameworks with mechanically interlocked pillars. *Cryst. Growth Des.* **2019**, *19*, 5679-5685.

(29) Vukotic, V. N.; O'Keefe, C. A.; Zhu, K.; Harris, K. J.; To, C.; Schurko, R. W.; Loeb, S. J. Mechanically interlocked linkers inside metal–organic frameworks: effect of ring size on rotational dynamics. *J. Am. Chem. Soc.* **2015**, *137*, 9643-9651.

(30) Zhu, K.; Vukotic, V. N.; O'Keefe, C. A.; Schurko, R. W.; Loeb, S. J. Metal–organic frameworks with mechanically interlocked pillars: controlling ring dynamics in the solid-state via a reversible phase change. *J. Am. Chem. Soc.* **2014**, *136*, 7403-7409.

(31) De Nicola, A.; Correa, A.; Bracco, S.; Perego, J.; Sozzani, P.; Comotti, A.; Milano, G. Collective dynamics of molecular rotors in periodic mesoporous organosilica: a combined solid-state ^{2}H-NMR and molecular dynamics simulation study. *Phys. Chem. Chem. Phys.* **2022**, *24*, 666-673.

(32) Perego, J.; Bezuidenhout, C. X.; Bracco, S.; Prando, G.; Marchiò, L.; Negroni, M.; Carretta, P.; Sozzani, P.; Comotti, A. Cascade dynamics of multiple molecular rotors in a MOF: benchmark

mobility at a few kelvins and dynamics control by CO_2. *J. Am. Chem. Soc.* **2021**, *143*, 13082-13090.

(33) Lemouchi, C.; Vogelsberg, C. S.; Zorina, L.; Simonov, S.; Batail, P.; Brown, S.; Garcia-Garibay, M. A. Ultra-fast rotors for molecular machines and functional materials via halogen bonding: crystals of 1,4-bis(iodoethynyl)bicyclo[2.2.2]octane with distinct gigahertz rotation at two sites. *J. Am. Chem. Soc.* **2011**, *133*, 6371-6379.

(34) Catalano, L.; Pérez-Estrada, S.; Terraneo, G.; Pilati, T.; Resnati, G.; Metrangolo, P.; Garcia-Garibay, M. A. Dynamic characterization of crystalline supramolecular rotors assembled through halogen bonding. *J. Am. Chem. Soc.* **2015**, *137*, 15386-15389.

(35) Liepuoniute, I.; Jellen, M. J.; Garcia-Garibay, M. A. Correlated motion and mechanical gearing in amphidynamic crystalline molecular machines. *Chem. Sci.* **2020**, *11*, 12994-13007.

(36) Jin, M.; Ando, R.; Jellen, M. J.; Garcia-Garibay, M. A.; Ito, H. Encapsulating N-heterocyclic carbene binuclear transition-metal complexes as a new platform for molecular rotation in crystalline solid-state. *J. Am. Chem. Soc.* **2021**, *143*, 1144-1153.

(37) Catalano, L.; Perez-Estrada, S.; Wang, H.-H.; Ayitou, A. J.-L.; Khan, S. I.; Terraneo, G.; Metrangolo, P.; Brown, S.; Garcia-Garibay, M. A. Rotational dynamics of diazabicyclo[2.2.2]octane in isomorphous halogen-bonded co-crystals: entropic and enthalpic effects. *J. Am. Chem. Soc.* **2017**, *139*¸843-848.

(38) Pérez-Estrada, S.; Rodriguez-Molina, B.; Maverick, E. F.; Khan, S. I.; Garcia-Garibay, M. A. Throwing in a monkey wrench to test and determine geared motion in the dynamics of a crystalline one-dimensional (1D) columnar rotor array. *J. Am. Chem. Soc.* **2019**, *141*, 2413-2420.

(39) Jiang, X.; Duan, H.-B.; Jellen, M. J.; Chen, Y.; Chung, T. S.; Liang, Y.; Garcia-Garibay, M. A. Thermally activated transient dipoles and rotational dynamics of hydrogen-bonded and charge-transferred diazabicyclo [2.2.2]octane molecular rotors. *J. Am. Chem. Soc.* **2019**, *141*, 16802-16809.

(40) Jiang, X.; O'Brien, Z. J.; Yang, S.; Lai, L. H.; Buenaflor, J.; Tan, C.; Khan, S.; Houk, K. N.; Garcia-Garibay, M. A. Crystal fluidity reflected by fast rotational motion at the core, branches, and peripheral aromatic groups of a dendrimeric molecular rotor. *J. Am. Chem. Soc.* **2016**, *138*, 4650-4656.

(41) Howe, M. E.; Garcia-Garibay, M. A. The roles of intrinsic barriers and crystal fluidity in determining the dynamics of crystalline molecular rotors and molecular machines. *J. Org. Chem.* **2019**, *84*, 9835-9849.

(42) Cavallo, G.; Metrangolo, P.; Milani, R.; Pilati, T.; Priimagi, A.; Resnati, G.; Terraneo, G. The halogen bond. *Chem. Rev.* **2016**, *116*, 2478-2601.

(43) Beckmann, P. A.; Conn, K. G.; Mallory, C. W.; Mallory, F. B.; Rheingold, A. L.; Rotkina, L.; Wang, X. Distributions of methyl group rotational barriers in polycrystalline organic solids. *J. Chem. Phys.* **2013**, *139*, 204501.

(44) Beckmann, P. A.; Mallory, C. W.; Mallory, F. B.; Rheingold, A. L.; Wang, X. Methoxy and methyl group rotation: solid-state NMR ^{1}H spin-lattice relaxation, electronic structure calculations, X-ray diffractometry, and scanning electron microscopy. *ChemPhysChem* **2015**, *16*, 1509-1519.

(45) Beckmann, P. A.; Rablen, P. R.; Schmink, J.; Szewczyk, S. T.; Rheingold, A. L. Concomitant polymorphism in an organic solid: molecular and crystal structure and intra- and intermolecular

potential contributions to tert-butyl and methyl group rotation. *ChemPhysChem* **2019**, *20*, 2887-2894.

(46) Wang, X.; Beckmann, P. A.; Mallory, C. W.; Rheingold, A. L.; DiPasquale, A. G.; Carroll, P. J.; Mallory, F. B. Intramolecular and intermolecular contributions to the barriers for rotation of methyl groups in crystalline solids: electronic structure calculations and solid-state NMR relaxation measurements. *J. Org. Chem.* **2011**, *76*, 5170-5176.

(47) Baudry, J.; Smith, J. C. Can Proteins and crystals self-catalyze methyl rotations? *J. Phys. Chem. B* **2005**, *109*, 20572-20578.

(48) Baudry, J. van der Waals interactions and decrease of the rotational barrier of methyl-sized rotators: a theoretical study. *J. Am. Chem. Soc.* **2006**, *128*, 11088-11093.

(49) Hembree, W.I.; Baudry, J. Three-dimensional mapping of microenvironmental control of methyl rotational barriers. *J. Phys. Chem. B* **2011**, *115*, 8575-8580.

(50) Xue, Y.; Pavlova, M. S. Ryabov, Y. E.; Reif, B. Skrynnikov, N. R. Methyl rotation barriers in proteins from ^{2}H relaxation data. Implications for protein structure. *J. Am. Chem. Soc.* **2007**, *129*, 6827-6838.

(51) Szell, P. M. J.; Zablotny, S.; Bryce, D. L. Halogen bonding as a supramolecular dynamics catalyst. *Nat. Commun*. **2019**, *10*, 916.

(52) Politzer, P.; Murray, J. S.; Clark, T.; Resnati, G. The □-hole revisited. *Phys. Chem. Chem. Phys.* **2017**, *19*, 32166-32178.

(53) Vincent, J. S. Paramagnetic resonance of the triplet state of tetramethylpyrazine. *J. Chem. Phys.* **1967**, *47*, 1830–1833.

(54) Szell, P. M. J.; Gabriel, S. A.; Caron-Poulin, E.; Jeannin, O.; Fourmigué, M.; Bryce, D. L. *Cryst. Growth Des.* **2018**, *18*, 6227-6238.

(55) (b) Sheldrick, G. M. A short history of SHELX. *Acta Crystallogr. Sect. A* **2008**, *64*, 112-122. (b) Farrugia, L. J. WinGX and ORTEP for Windows: an update. *J. Appl. Crystallogr.* **2012**, *45*, 849-854.

(56) Macrae, C. F.; Bruno, I. J.; Chisholm, J. A.; Edgington, P. R.; McCabe, P. Pidcock, E.; Rodriguez-Monge, L.; Taylor, R.; van de Streek, J.; Wood, P. A. Mercury CSD 2.0 - new features for the visualization and investigation of crystal structures. *J. Appl. Cryst.* **2008**, *41*, 466-470.

(57) Spek, A. L. Structure validation in chemical crystallography. *Acta Crystallogr. Sect. D* **2009**, *65*, 148-155.

(58) Peloquin, A. J.; McMillen, C. D.; Pennington, W. T. One dimensional halogen bond design: Br···N versus I···N with fluoroarenes. *CrystEngComm* **2021**, *23*, 6098-6106.

(59) Solomon, I. Multiple echoes in solids. *Phys. Rev.* **1958**, *110*, 61-65.

(60) Davis, J. H.; Jeffrey, K. R.; Bloom, M.; Valic, M. I.; Higgs, T. P. Quadrupolar echo deuteron magnetic resonance spectroscopy in ordered hydrocarbon chains. *Chem. Phys. Lett.* **1976**, *42*, 390–394.

(61) Baerends, E. J; Ziegler, T; Atkins, A. J.; Autschbach, J.; Baseggio, O.; Bashford, D.; Bérces, A.; Bickelhaupt, F.M. et al. ADF 2019.305, SCM, Theoretical Chemistry, Vrije Universiteit, Amsterdam, The Netherlands. http://www.scm.com (accessed 2023-07-31).

(62) te Velde, G.; Bickelhaupt, F.M.; Baerends, E.J.; Fonseca Guerra, C., van Gisbergen, S.J.A.; Snijders, J.G.; Ziegler, T. *Chemistry with ADF. J. Comput. Chem.* **2001**, *22*, 931-967.

(63) Maus, D. C.; Copié, V.; Sun, B.; Griffiths, J. M.; Griffin, R. G.; Luo, S.; Schrock, R. R.; Liu, A. H.; Seidel, S. W.; Davis, W. M.; Grohmann, A. A solid-state NMR study of tungsten methyl group dynamics in [W(h^5-C$_5$Me$_5$)Me$_4$][PF$_6$]. *J. Am. Chem. Soc.* **1996**, *118*, 5665-5671.

(64) Spiess, H. W. Deuteron spin alignment: A probe for studying ultraslow motions in solids and solid polymers. *J. Chem. Phys.* **1980**, *72*, 6755-6762.

(65) Barbour, L. J. Crystal porosity and the burden of proof. *Chem. Commun*. **2006**, 1163-1168.

(66) Saikia, B.; Pathak, D.; Sarma, B. Variable stoichiometry cocrystals: occurrence and significance. *CrystEngComm* **2021**, *23*, 4583-4606.

(67) Hajjar, C.; Nag, T.; Al Sayed, H.; Ovens, J. S.; Bryce, D. L. Stoichiomorphic halogen-bonded cocrystals. A case study of 1,4-diiodotetrafluorobenzene and 3-nitropyridine. *Can. J. Chem.* **2022**, *100*, 245-251.

(68) Scholfield, M. R.; Vander Zanden, C .M.; Carter, M.; Ho, P. S. Halogen bonding (X-bonding): A biological perspective. *Prot. Sci.* **2013**, *22*, 139-152.

(69) Carter, M.; Regier Voth, A.; Scholfield, M. R.; Rummel, B.; Sowers, L. C.; Ho, P. S. Enthalpy–entropy compensation in biomolecular halogen bonds measured in DNA junctions. *Biochemistry* **2013**, *52*, 4891-4903.

(70) Ho, P. S. Halogen bonding: a new mechanism for enzyme catalysis. *Biophys. J.* **2022**, *121,* 479a.

(71) Walker, M. G.; Mendez, C. G.; Ho, P. S. Non-classical Non-covalent σ-hole interactions in protein structure and function: concepts for potential protein engineering applications. *Chem. Asian J.* **2023**, *18*, e202300026.

Part 3: Cocrystal design and study

Chapter 5 Type II Halogen-Halogen Contacts in the Single-Crystal X-ray Diffraction Structure of a 1:1 Halogen-Bonded Cocrystal of 2,3,5,6-Tetramethylpyrazine and 1,3,4,5-Tetrabromo-2,6-difluorobenzene

Permission: Chapter 4 is from Shubha S. Gunaga and David L. Bryce J. Chem. Crystallogr., 2024, 54, 150-156. (https://doi.org/10.1007/s10870-024-01007-4). Reproduced with permission of Springer Nature - Journal of Chemical Crystallography.

5.1 Abstract

A cocrystal of 2,3,5,6-tetramethylpyrazine and 1,3,4,5-tetrabromo-2,6-difluorobenzene has been prepared and its crystal structure has been determined via single-crystal X-ray diffraction. Infinite chains of roughly coplanar donor and acceptor molecules are held together by two crystallographically distinct and highly linear Br···N halogen bonds. Four further crystallographically distinct Br···Br halogen bonds are also observed. Each of the two Br atoms in the 3 and 5 positions on the benzene ring acts simultaneously as a halogen bond donor and acceptor to two additional bromines on two neighbouring 1,3,4,5-tetrabromo-2,6-difluorobenzene molecules. These halogen bonds are also classified as type II halogen-halogen contacts. As a result of these contacts, a staggered herringbone arrangement of the infinite chains results. These structural features are shown to be consistent with computed molecular electrostatic potential and Hirshfeld surfaces. The insights gained through this analysis imply that additional systematic variations in the substitution motifs of aromatic halogen bond donors may lead to new structures and properties. As part of this work, a single-crystal X-ray structure of 1,3,4,5-tetrabromo-2,6-difluorobenzene of moderate quality is also reported.

5.2 Graphical Abstract

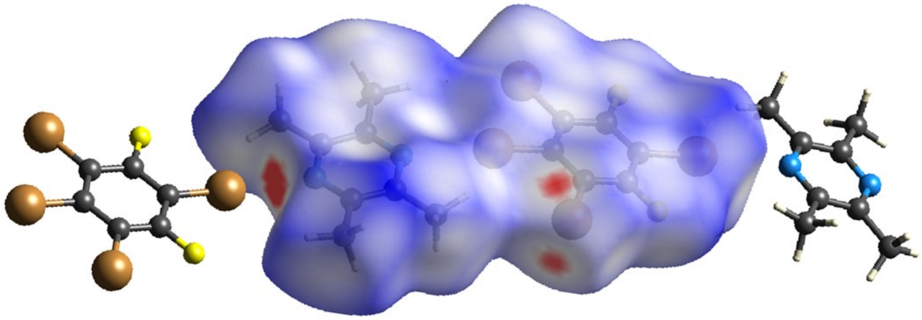

The single-crystal X-ray diffraction structure of a 1:1 cocrystal of 2,3,5,6-tetramethylpyrazine and 1,3,4,5-tetrabromo-2,6-difluorobenzene is reported. Bromine-nitrogen halogen bonds link the two types of molecules together, forming infinite chains. Bromine-bromine halogen bonds (type II contacts) between aromatic molecules stabilize a herringbone-like packing arrangement.

5.3 Introduction

Halogen bonds[1] and related non-covalent interactions including chalcogen bonds,[2] tetrel bonds,[3] and pnictogen bonds,[4] find diverse applications across a broad range of fields such as crystal engineering,[5] catalysis,[6] and biomolecular engineering.[7] These types of interactions are often interpreted in terms of the interaction of an electron donor moiety with an area of elevated electrostatic potential (σ-hole)[8] on the electron acceptor. New classes of σ-hole interactions continue to be explored via crystal structure database searches, computational chemistry, and experimental approaches. The most recent of these include, e.g., spodium bonds,[9] erythronium bonds,[10] and matere bonds.[11,12]

Our own recent work on using halogen bonds to modulate or catalyze rotational dynamics in solids has focussed on a series of cocrystals formed with 2,3,5,6-tetramethylpyrazine (TMP) as the halogen bond acceptor.[13,14] Single-crystal X-ray diffraction structures are known for cocrystals of TMP for a series of aromatic chloro-, bromo- and iodo- halogen bond donors including 1,4-dichlorotetrafluorobenzene, 1,3,5-trichloro-2,4,6-trifluorobenzene, 1,4-dibromotetrafluorobenzene, 1,3,5-tribromo-2,4,6-trifluorobenzene, 1,4-diiodotetrafluorobenzene, and 1,3,5-trifluoro-2,4,6-triiodobenzene.[13,14] We and others have also described further TMP cocrystallization efforts using other 1,4-halobenzenes,[13,15,16] 1,3,5-halobenzenes,[16,17,18] molecular iodine[19] and bromine,[14] and 3-iodoethynylbenzoic acid.[20]

In this work, we report the single-crystal X-ray diffraction structure of a cocrystal of TMP with 1,3,4,5-tetrabromo-2,6-difluorobenzene (**1**). The substitution motif of the benzene molecule differs from those discussed above (typically 1,4- and 1,3,5-halo substitution). The impact of this substitution motif on the resulting crystal packing is discussed. Along with the experimental data, calculations of the molecular electrostatic potential and Hirshfeld surfaces reveal that in addition to the anticipated bromine-nitrogen halogen bonds between the donor and acceptor molecules, bromine-bromine halogen bonds (type II contacts)[21,22] play a key role in determining the overall structure. Such contacts are not prevalent in the previously reported TMP-halobenzene structures due to the different substitution motifs.

5.4 Experimental

5.4.1 (i) Synthesis

2,3,5,6-tetramethylpyrazine (98%) and 1,3,5-tribromo-2,4,6-trifluorobenzene (≥ 99%) were purchased from Sigma Aldrich and used as received. However, as described below, it was concluded that the halogen bond donor compound received was in fact 1,3,4,5-tetrabromo-2,6-difluorobenzene. The cocrystal (**1**) was produced using a 1:1 molar ratio of donor and acceptor molecules dissolved in anhydrous acetonitrile by continuous stirring at room temperature. The solution was then kept at 4-5 ºC in the refrigerator to allow for slow evaporation of the solvent, resulting in crystal formation. The crystals were consistently of poor quality despite repeated attempts to grow better quality crystals.

5.4.2 (ii) Single crystal X-ray diffraction

Single crystals were mounted on transparent MiTeGen MicromountsTM precision tools and cooled to 203 ± 2 K before data collection using a cryogenic liquid nitrogen system. The X-ray diffraction data were collected on a Bruker Kappa Apex diffractometer equipped with APEX II CCD detectors using MoKα radiation (wavelength λ = 0.7103 Å). The data collection, cell refinement, integration, and reduction were carried out using the APEX III software package. The structure of cocrystal **1** was solved using WinGX software with the direct method and refined based on the spherical atom approximation based on F2 using SHELXL 97.[23] Analysis of intermolecular interactions was done with PLATON.[24] The non-hydrogen atoms were refined anisotropically and hydrogen atoms were positioned geometrically using a riding model. The refinement data are summarized in Table 5.1.

5.4.3 (iii) Computational details

Molecular electrostatic potential surfaces were calculated using Gaussian 03 (revision C.02)[25] at the B3LYP/6-311+G* level of theory using atomic coordinates taken directly from the experimental crystal structure. Hirshfeld surfaces and fingerprint plots[26] were generated using CrystalExplorer.[27] Structures were visualized and some images were generated using Mercury software (2021.1.0 (Build 319587)).[28]

5.5 Results and Discussion

Single cocrystals comprised of TMP and 1,3,4,5-tetrabromo-2,6-difluorobenzene (compound **1**) were grown via slow evaporation from acetonitrile. As shown in Table 5.1, the cocrystal packs in the orthorhombic $P2_12_12_1$ space group. The asymmetric unit consists of one molecule of TMP and one molecule of 1,3,4,5-tetrabromo-2,6-difluorobenzene (Figure 5.1(a)). Covalent bond lengths and angles are given in Table 5.2.

Table 5.1. Single crystal data and structure refinement for 1 (2,3,5,6-tetramethylpyrazine 1,3,4,5-tetrabromo-2,6-difluorobenzene (1:1 cocrystal))

CCDC Number	2301003
Empirical formula	C_{14} H_{12} Br4 F_2 N_2
Formula weight	565.90
Temperature/K	203 (2)
Crystal system	Orthorhombic
Space group	$P2_12_12_1$
a/Å	4.5828(12)
b/Å	12.401(3)
c/Å	30.473(8)
α/°	90
β/°	90
γ/°	90
Volume/Å^3	1731.9(8)
Z	4
ρ_{calc}g/cm^3	2.170
μ/mm^{-1}	9.310
F(000)	1072
Crystal size/mm^3	0.620 x 0.312 x 0.112
Radiation	MoKα (λ = 0.71073)
2θ range for data collection/°	1.336 to 25.529
Index ranges	-5<=h<=5, -14<=k<=12, -36<=l<=28
Reflections collected	5451
Independent reflections	3214 [R(int) = 0.0531]
Data/restraints/parameters	3214 / 0 / 203
Goodness-of-fit on F^2	0.911

Final R indexes [I>=2σ (I)]	$R_1 = 0.0549$, $wR_2 = 0.1147$
Final R indexes [all data]	$R_1 = 0.0854$, $wR_2 = 0.1254$
Largest diff. peak/hole / e Å^{-3}	1.467 and -1.035 e.Å^{-3}

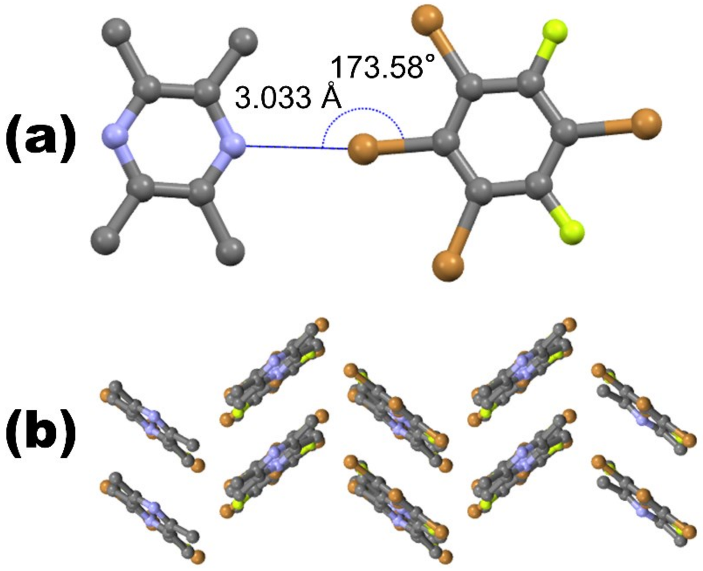

Figure 5.1. (a) Asymmetric unit of 1 showing the one of the halogen bonds between 2,3,5,6-tetramethylpyrazine 1,3,4,5-tetrabromo-2,6-difluorobenzene (Br1···N3); (b) Crystal packing of 1 shown along the *c* axis.

Within the asymmetric unit, one halogen bond between the bromine at the 4 position and one of the nitrogen atoms on TMP is noted. The Br···N distance is 3.033 Å and the C-Br···N angle is 173.58°. The other nitrogen atom of TMP forms a crystallographically distinct halogen bond with the bromine at the 1 position in a second molecule of 1,3,4,5-tetrabromo-2,6-difluorobenzene ($r_{\mathrm{Br...N}}$ = 2.974 Å; C-Br···N angle = 177.37°). These two bromine-nitrogen bonds therefore result in an overall crystal packing arrangement including infinite chains of TMP and 1,3,4,5-tetrabromo-

2,6-difluorobenzene in which the molecules are approximately coplanar. This aspect of the crystal packing is similar to that seen for related cocrystals 1,3,5-tribromo-2,4,6-trifluorobenzene·2,3,5,6-tetramethylpyrazine and 1,3,5-trichloro-2,4,6-trifluorobenzene·2,3,5,6-tetramethylpyrazine.[14]

Table 5.2. Selected distances (Å) and angles (°) in cocrystal 1.

C1—C2	1.398 (17)	C6—Br2	1.859 (13)
C1—C6	1.397 (16)	C7—N1	1.338 (16)
C1—Br1	1.900 (12)	C7—C8	1.419 (15)
C2—C3	1.365 (15)	C7—C11	1.497 (17)
C2—Br4	1.878 (12)	C8—N3	1.326 (16)
C3—F3	1.342 (14)	C8—C12	1.536 (18)
C3—C4	1.378 (17)	C9—N1	1.343 (16)
C4—C5	1.390 (18)	C9—C10	1.382 (16)
C4—Br3	1.888 (12)	C9—C13	1.497 (17)
C5—F2	1.331 (15)	C10—N3	1.373 (15)
C5—C6	1.392 (16)	C10—C14	1.479 (17)
C2—C1—C6	121.0 (11)	C5—C6—Br2	119.0 (10)
C2—C1—Br1	119.9 (9)	C1—C6—Br2	123.2 (9)
C6—C1—Br1	119.1 (9)	N1—C7—C8	119.9 (12)
C3—C2—C1	118.7 (12)	N1—C7—C11	118.5 (11)
C3—C2—Br4	118.7 (11)	C8—C7—C11	121.6 (12)
C1—C2—Br4	122.6 (9)	N3—C8—C7	121.5 (12)
F3—C3—C4	117.7 (11)	N3—C8—C12	118.0 (11)

F3—C3—C2	119.8 (12)	C7—C8—C12	120.5 (12)
C4—C3—C2	122.5 (12)	N1—C9—C10	122.0 (12)
C3—C4—C5	118.0 (12)	N1—C9—C13	116.8 (11)
C3—C4—Br3	122.3 (10)	C10—C9—C13	121.2 (13)
C5—C4—Br3	119.7 (10)	N3—C10—C9	120.1 (12)
F2—C5—C6	119.0 (12)	N3—C10—C14	116.3 (11)
F2—C5—C4	119.1 (11)	C9—C10—C14	123.6 (12)
C6—C5—C4	121.9 (12)	C9—N1—C7	118.5 (10)
C5—C6—C1	117.8 (12)	C8—N3—C10	117.9 (11)

In addition to bromine-nitrogen halogen bonds involving the bromine atoms at positions 1 and 4 of the aromatic ring, additional bromine-bromine halogen bonds are noted in the structure of **1** (Figure 5.2; Table 5.3). The bromine atom at position 3 (labelled Br4 in the cif) is involved in two type II bromine-bromine contacts with crystallographically equivalent bromine atoms on two adjacent molecules of 1,3,4,5-tetrabromo-2,6-difluorobenzene. The bromine atom at position 3 acts as an electron acceptor via its σ-hole (halogen bond donor) in one case, and simultaneously acts as an electron donor via its electron-rich equatorial region (halogen bond acceptor). In the first case, the Br···Br distance is 3.682 Å and the C-Br···Br angle (θ_1) is 155.96°. In the second case, the Br···Br distance is identical but the C-Br···Br angle (θ_2) is 102.96°. An entirely analogous pair of type II contact halogen bonds is also noted for the bromine atom at position 5 (labelled Br2 in the cif). In this case the two Br···Br distances are 3.524 Å and the relevant angles are θ_1 = 167.92° and θ_2 = 107.52°. These four distinct Br···Br halogen bonds between infinite chains of

TMP-1,3,4,5-tetrabromo-2,6-difluorobenzene result in a staggered herringbone arrangement of molecules in the crystal when viewed along the *c* axis (Figure 5.1(b)).

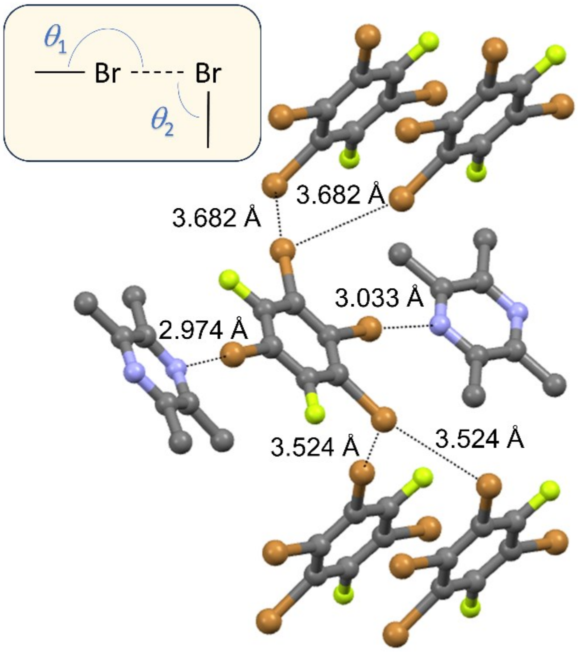

Figure 5.2. Halogen bond network in 1, with bromine-nitrogen and bromine-bromine distances indicated. Inset: geometry of the type II bromine-bromine contact.

Table 5.3. Halogen bond distances and angles in 1.

distances	
Br1···N3	3.033
Br3···N1	2.974
Br4···Br4	3.682
Br2···Br2	3.524
angles	
C1-Br1···N3	173.58

C4-Br3···N1	177.37
C2(i)-Br4(i)···Br4(ii) (θ_1)	155.96
C2(ii)-Br4(ii)···Br4(i) (θ_2)	102.96
C6(i)-Br2(i)···Br2(ii) (θ_1)	167.92
C6(ii)-Br2(ii)···Br2(i) (θ_2)	107.52

Interestingly, although 1,3,5-tribromo-2,4,6-trifluorobenzene was nominally used for the preparation of **1**,1,3,4,5-tetrabromo-2,6-difluorobenzene (with one additional bromine atom and one less fluorine atom) was consistently seen in repeated preparations of the cocrystal. This result was obtained regularly, despite sourcing three different bottles of the aromatic compound from Sigma-Aldrich. As any sort of chemical reaction under the conditions used seems highly unlikely, it is concluded that the product supplied was in fact 1,3,4,5-tetrabromo-2,6-difluorobenzene and not 1,3,5-tribromo-2,4,6-trifluorobenzene. This was confirmed by checking the microcrystalline powder as supplied by Sigma-Aldrich using both powder and single-crystal X-ray diffraction (Figure 5.3). A small crystal was selected from the bottle and it was possible to solve its single-crystal structure, albeit at a moderate quality level (CCDC deposition number 2328690; see Supporting Information). Despite the poor-quality crystal, it was possible to unequivocally demonstrate the identity of the compound as 1,3,4,5-tetrabromo-2,6-difluorobenzene (Figure 5.3(d). Furthermore, collection of PXRD data on the as-received material clearly demonstrates that 1,3,4,5-tetrabromo-2,6-difluorobenzene is the major product present, not 1,3,5-tribromo-2,4,6-trifluorobenzene (Figure 5.3(a), (b), (c)). Several characteristic peaks at $2\theta < 20°$ most clearly demonstrate this.

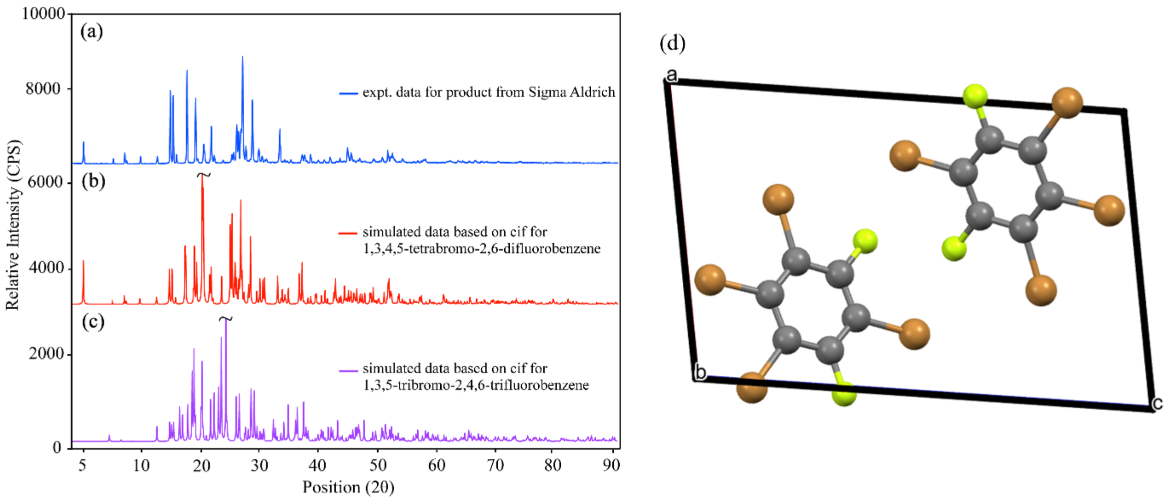

Figure 5.3. (a) Experimental powder X-ray diffractogram acquired for the as-received product from Sigma-Aldrich. (b) Simulated PXRD data based on the cif file of 1,3,4,5-tetrabromo-2,6-difluorobenzene (CCDC 2328690). (c) Simulated PXRD data based on the structure of 1,3,5-tribromo-2,4,6-trifluorobenzene.[29] (d) Unit cell viewed along the *b*-axis from the single-crystal X-ray structure of 1,3,4,5-tetrabromo-2,6-difluorobenzene (CCDC deposition number 2328690) determined in this work (see Supporting Information for further details on this structure).

The experimental structure of **1** is consistent with information gleaned from calculations of the molecular electrostatic potential (MEP) of 1,3,4,5-tetrabromo-2,6-difluorobenzene and of the Hirshfeld d_{norm} surface for **1** (Figure 5.3). As seen in Figure 5.4(a), 1,3,4,5-tetrabromo-2,6-difluorobenzene has four σ-holes (shown in blue), one on each bromine atom. Interestingly, the calculated MEP maxima are extremely similar for all four bromine atoms, i.e,. 0.027 a.u. for the bromine in the 1 position and 0.026 a.u. for the three others (B3LYP/6-311+G* plotted with a 0.0004 a.u isosurface). This suggests that all four bromine atoms may be equally likely to engage as halogen bond donors, which is fully consistent with the crystal structure obtained experimentally. The computed Hirshfeld d_{norm} surface (Figure 5.4(b)) similarly depicts all halogen bonds seen experimentally, with the two halogen bonds to the ortho bromine atoms clearly visible as red regions; one of these lies approximately in line with the covalent C-Br bond ($\theta_1 \approx 180°$) while the second is approximately orthogonal to this bond ($\theta_2 \approx 90°$).

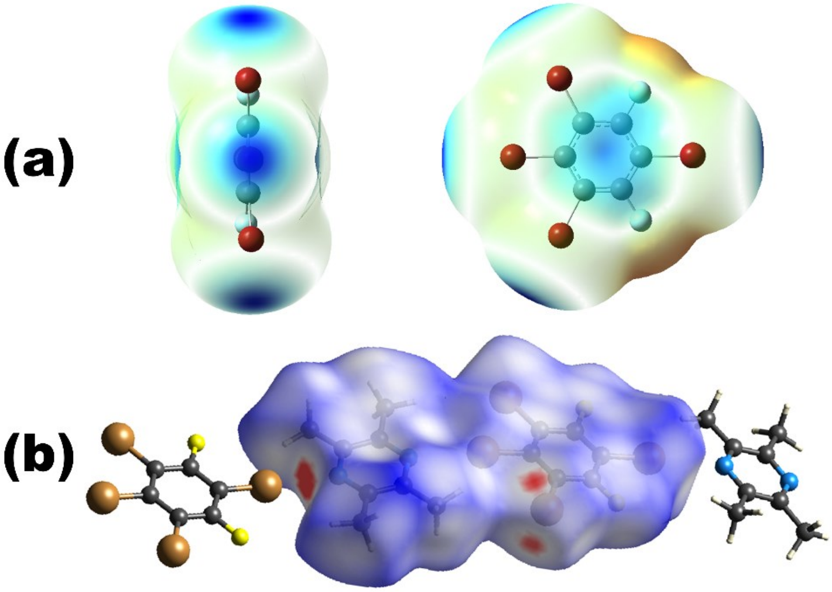

Figure 5.4. (a) Computed molecular electrostatic potential surface of 1,3,4,5-tetrabromo-2,6-difluorobenzene (B3LYP/6-311+G*; 0.0004 a.u isosurface.). Areas in blue show elevated electrostatic potential while areas in yellow-orange show areas of depleted electrostatic potential. (b) Hirshfeld d_{norm} surface of 1. Areas in red depict close contacts.

Finally, Hirshfeld fingerprint plots[26] can provide some indication of the importance and prevalence of particular contacts in the crystal packing of **1** (Figure 5.5). A Hirshfeld surface envelops a region of space where the electron distribution of a molecule exceeds that from any other molecule in the crystal. Filtered plots of d_e (the distance from the surface to the nearest atom exterior to the surface) against d_i (the distance from the surface to the nearest atom interior to the surface) highlight in color the prevalence of Br-Br (Figure 5.5(b)) and Br-N (Figure 5.5(c)) contacts. These are dominated by the shortest halogen bond contacts discussed above. The Br-Br contacts contribute 10.7% towards the total fingerprint plot while the Br-N contacts contribute only 2 %. A large number of non-specific and non-directional weak interactions involving hydrogen and fluorine also contribute to the total.

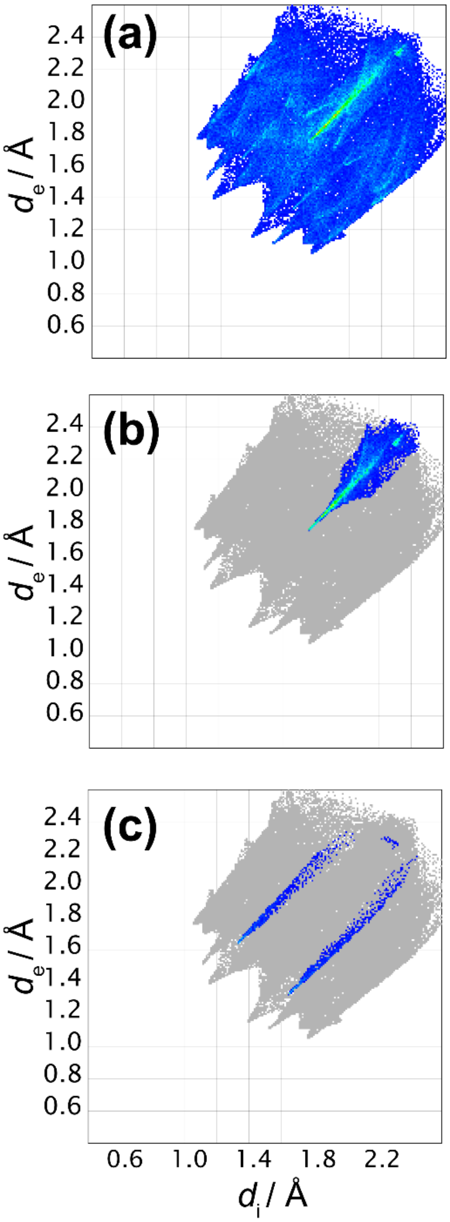

Figure 5.5. (a) Hirshfeld fingerprint plot for 1; (b) Br-Br contacts highlighted; (c) Br-N contacts highlighted.

5.6 Conclusions

A cocrystal of 2,3,5,6-tetramethylpyrazine and 1,3,4,5-tetrabromo-2,6-difluorobenzene has been prepared and its crystal structure has been determined via single-crystal X-ray diffraction. Infinite chains of approximately coplanar TMP-1,3,4,5-tetrabromo-2,6-difluorobenzene groups are held together by two crystallographically distinct bromine-nitrogen halogen bonds. In addition, four further crystallographically unique bromine-bromine halogen bonds are noted. Each of the two bromines in the 3 and 5 positions on the benzene ring acts simultaneously as a halogen bond donor and acceptor to two additional bromines on two adjacent 1,3,4,5-tetrabromo-2,6-difluorobenzene molecules. These halogen bonds are also classified as type II halogen-halogen contacts, with characteristic angles θ_1 and θ_2 approaching 180 and 90 degrees, respectively. As a result of these contacts, a staggered herringbone arrangement of the infinite chains results. These structural features are shown to be consistent with computed molecular electrostatic potential and Hirshfeld surfaces. This work suggests that further systematic variations in the substitution motifs of aromatic halogen bond donors, beyond those which are most commonly used in the literature, may lead to new structures and properties.

5.7 References

(1) (a) Desiraju GR, Ho PS, Kloo L, Legon AC, Marquardt R, Metrangolo P, Politzer P, Resnati G, Rissanen K (2013) Pure Appl Chem 85:1711. (b) Cavallo G, Metrangolo P, Milani R, Pilati T, Priimagi A, Resnati G, Terraneo G (2016) Chem Rev 116:2478.

(2) Aakeroy CB, Bryce DL, Desiraju GR, Frontera A, Legon AC, Nicotra F, Rissanen K, Scheiner S, Terraneo G, Metrangolo P, Resnati G (2019) Pure Appl Chem 91:1889.

(3) Bauzá A, Mooibroek TJ, Frontera A (2013) Angew Chem Intl Ed 52:12317.

(4) Scheiner S (2013) Acc Chem Res 46:280.

(5) Mukherjee A, Tothadi S, Desiraju GR (2014) Acc Chem Res 47:2514.

(6) Benz S, Poblador-Bahamonde AI, Low-Ders N, Matile S (2018) Angew Chem Intl Ed 57:5408.

(7) Walker MG, Mendez CG, Ho PS (2023) Chem Asian J 18:e20230026.

(8) Politzer P, Murray JS, Clark T, Resnati G (2017) Phys Chem Chem Phys 19:32166.

(9) Bauzá A, Alkorta I, Elguero J, Mooibroek TJ, Frontera A (2020) Angew Chem Intl Ed 59:17482.

(10) Calabrese M, Gomila RM, Pizzi A, Frontera A, Resnati G (2023) Chem Eur J e202303083.

(11) Daolio A, Pizzi A, Terraneo G, Frontera A, Resnati G (2021) ChemPhysChem 22:2281.

(12) Xu Y, Calabrese M, Demitri N, Pizzi A, Nag T, Hung I, Gan Z, Resnati G, Bryce DL (2023) Chem Commun, in press. https://doi.org/10.1039/D3CC04090A

(13) Szell PMJ, Zablotny S, Bryce DL (2019) Nature Chem 10:916.

(14) Gunaga SS, Bryce DL (2023) J Am Chem Soc 145:19005.

(15) Syssa-Magalé J-L, Boubekeur K, Palvadeau P, Meerschaut A, Schöllhorn B (2005) CrystEngComm 7:302.

(16) Szell PMJ, Gabriel SA, Caron-Poulin E, Jeannin O, Fourmigué M, Bryce DL (2018) Cryst Growth Des 18:6227.

(17) El-khawaldeh RK, Gunaga SS, Bryce DL (2022) Results Chem 4:100336.

(18) Szell PMJ, Gabriel SA, Gill RDD, Wan SYH, Gabidullin B, Bryce DL (2017) Acta Cryst C 73:157.

(19) Bailey RD, Buchanan ML, Pennington WT (1992) Acta Cryst C 48:2259.

(20) Morin VM, Szell PMJ, Caron-Poulin E, Gabidullin B, Bryce DL (2019) ChemistryOpen 8:1328.

(21) Mukherjee A, Desiraju GR (2014) IUCrJ 1:49.

(22) Metrangolo P, Resnati G (2014) IUCrJ 1:5.

(23) (a) Sheldrick GM (2008) Acta Crystallogr Sect A 64:112. (b) Farrugia LJ (2012) J Appl Crystallogr 45:849.

(24) Spek AL (2009) Acta Crystallogr Sect D 65:148.

(25) Gaussian 03, Revision C02. Frisch MJ et al. Gaussian, Inc., Wallingford CT, 2004.

(26) (a) McKinnon JJ, Mitchell AS, Spackman MA (1998) Chem Eur J 4:2136. (b) Spackman MA, McKinnon JJ (2002) CrystEngComm 4:378.

(27) (a) Spackman PR, Turner MJ, McKinnon JJ, Wolff SK, Grimwood DJ, Jayatilaka D, Spackman MA (2021) J Appl Crystallogr 54:1006. (b) Turner MJ, McKinnon JJ, Wolff SK, Grimwood DJ, Spackman PR, Jayatilaka D, Spackman MA (2017) CrystalExplorer17 University of Western Australia.

(28) Macrae CJ, Sovago I, Cottrell SJ, Galek PTA, McCabe P, Pidcock E, Platings M, Shields GP, Stevens JS, Towler M, Wood PA (2020) J Appl Cryst 53:2260.

(29) Liu ZF, Chen X, Wu WX, Zhang GQ, Li X, Li ZZ, Jin WJ (2020) Spectrochim Acta Part A: Mol Biomol Spectrosc 224:117428.

Part 4: Final Conclusions

Overview

The halogen bond has garnered increasing interest in over the years, primarily due to its remarkable directionality and tuneability, which are essential factors in the creation of novel supramolecular architectures.[1,2,3] Experimental observations and theoretical modelling have continuously played significant roles in advancing our understanding of the nature of the halogen bond (XB) and exploring its potential applications.[4,5] The sections of the thesis undertook a thorough examination of halogen bonds, as well as our exploration of their application through crystal engineering and preparation methods to produce novel crystals. These newly created crystal structures were then deposited in the Cambridge Structural Database (CSD) which receives thousands of new crystal structures from researchers every year.[6] Solid-state NMR relaxation measurements were performed on these novel cocrystals to elucidate the significance of the halogen bond, while simultaneously showcasing the crucial roles played by solid-state NMR and crystallography techniques in extracting the essential information from novel systems. Our discussion encompasses results obtained from both techniques underscoring their equal importance in the analysis and interpretation process.

Part 1 of this dissertation discussed the origin and fundamentals of the analytical techniques presented in the thesis. Chapter 1 focussed on the halogen bond, σ-hole interactions highlighting their significance in crystal engineering, pharmaceutical science, biological systems, materials and dynamics involved in different systems. It included well documented literature examples to provide a solid foundation for our research. Chapter 2 primarily addressed solid state NMR, providing an overview of its fundamentals and highlighting its effectiveness as spectroscopic method for obtaining NMR observables. Additionally, this chapter explores relaxation measurements in solid-state NMR, emphasizing their importance in our current study and their role in analyzing and interpreting our results, including ^{2}H quadrupolar nuclei and inversion recovery experiments, supported by relevant literature. Chapter 3 offers an overview of X-ray diffraction, covering topics such as crystal growth, diffraction basics, and their relevance to dynamics studies, accompanied by literature examples. In summary, Part 1 lays a strong foundation for understanding the subsequent chapters by providing insights into halogen bonding, solid state NMR relaxation measurements and X ray diffraction studies.

Part 2 presented the experimental evidence and results of our work, primarily focussing on dynamics. Chapter 4 represented our main experimental findings concerning the characterization of the halogen bond and relaxation experiments conducted on the novel cocrystal prepared by using solid state, mechanochemical, cosublimation, and slow evaporation techniques using deuterated 2,3,5,6-tetramethylpyrazine as halogen bond acceptor, while brominated, and chlorinated compounds acting as the halogen bond donors. A rare example of molecular bromine in halogen bonding is established despite of the difficulty it posed during preparation. Detailed ^{2}H solid-state NMR T_1 relaxation experiments and X ray diffraction studies reveal that halogen bonds modulate the methyl dynamics in solid state. Specifically, the barrier energy associated with these rotational dynamics influenced by combination of electronic and steric factors. Intriguingly, introducing halogen bonding close steric contact to the rotating methyl group consistently reduced the rotational barrier. This finding is elucidated through a thorough examination of the electronic, structural and crystallographic features involving, close contacts, void volume calculation, crystal packing analysis.

The average number of carbon-carbon close contacts to the methyl groups emerges as a crucial steric metric, rationalizing the observed trends in rotational energy barriers when compounds are grouped by the identity of the halogen bond donor atom (Cl, Br, I). Differences between these groups are attributed to the strength of the σ-hole, calculated through computed electrostatic potential maxima. Correlations for each halogen group exhibit different slopes, indicating that disrupting the electronic impact of the σ-hole of stronger iodine-based halogen bonds is more challenging via steric effects, whereas the influence of weaker chlorine-based halogen bonds on methyl rotation is more easily disrupted via steric effects.

Part 3 presents the experimental and computational X ray diffraction analysis results of a novel halogen bonded cocrystal and its importance. Chapter 5 focusses on cocrystallization of 2,3,5,6-tetramethylpyrazine as halogen bond acceptor and 1,3,4,5-tetrabromo-2,6-difluorobenzene acting halogen bond donor. This study reveals the type II halogen bonding resulted due to the ability of bromine at the 3 and 5 position of aromatic ring acting simultaneously halogen bond donor and acceptor to two additional bromine atoms on 1,3,4,5-tetrabromo-2,6-difluorobenzene. These halogen bonds are categorized as type II halogen bond, characterized by characteristic θ_1 and θ_2 angles approaching 90° and 180° respectively. Consequently, the arrangement of the infinite chains adopts a herringbone configuration. These observed characteristics are further validated by computed molecular electrostatic potential and Hirshfeld surfaces.

Challenges/limitations

Despite the successful preparation of the cocrystals using various methods listed in the thesis, challenges may arise in optimizing these methods for specific compounds and in terms of yield, reproducibility and purity. Obtaining a crystal is again not an easy task that too with desired quality[7] and moreover to get diffraction-quality crystals becomes challenging in cocrystals presented here with chlorinated and molecular bromine as halogen bond donors. For example, the novel cocrystal produced in Chapter 4 was not subject to the dynamics study here due to presence of the lower quantity of sample and the presence of unidentified peaks in powder X-ray. Mechanochemical synthesis[8] are being studied extensively these days, yet lack the understanding of molecular level understanding of such processes. Phase transformation during the synthesis and experimentation poses a threat in the analysis of systems where the different phases are close in transition energy barriers. The ^{2}H solid state NMR experiments were done in the temperature range of 140 K to 320 K. Lower than 140 K data were not possible due to technical limitations, otherwise the results at below 100 K temperature would have helped us to see if there are any hindered rotations exist. The T_1 relaxation time constants were measured for done using 2,3,5,6-tetramethylpyrazine as a halogen bond acceptor in the study; cocrystals obtained using a different set of halogen acceptor systems were not subjected to this study due the unsuccessful deuteration and lower amount of products obtained during crystallization. Those systems would have made a better understanding of findings we have made here.

Future directions

Halogen bonding, characterized by the electrophilic nature of halogen substituents presents intriguing properties and applications. Crystal engineering methodologies coupled with structure prediction tools, may be used to design novel halogen bonded systems, by manipulating substituents on both donors and acceptor molecules. Exploring the synergistic effects between halogen bonds and other non-covalent interactions such as chalcogen bonds,[9,10,11,12] pnictogen bonds,[13] and tetrel bonds,[14,15] opens up new avenues for controlling molecular dynamics and supramolecular assembly.

Furthermore, investigating the potential of these systems in molecular gyroscopes and molecular machines can expand their application to electronics, sensing and catalysis. Recent studies have demonstrated the utility of using halogen bonds in organic catalysis reactions; particularly using perfluorinated derivatives, haloimidazoles, halobenzimidazoles, and especially halotriazoles due to their easy accessibility through simple click reactions of azide with haloalkynes. Notably halotriazoles and their salts exhibit enhanced halogen bond donor abilities due to quaternization.[16] Integration of halogen bonding interactions and other noncovalent interactions into rotaxanes and catenanes, facilitate mechanical movements and functionalities,[17] offering opportunities to explore the efficacy of these interactions in molecular ring shuttling dynamics across various systems. Additionally, phase transformation studies leading to photosalient effects in halogen derivatives of azobenzene, induced by dynamically involved halogen bond interactions upon photo irradiation. These findings hold promise for the development of novel photosalient devices based on halogen bond derivatives, specifically due to the tailored dynamics.

In this study, our examination of methyl dynamics has been primarily focussed on T_1 relaxation constants. However, it is important to note that due to technical constraints, our experiments were limited to temperatures as low as 140 K. Consequently, we were only able to detect the low energy processes with methyl group rotation. To expand our understanding of the effects of halogen bonds on dynamics, future investigations may incorporate T_{1_D} measurements on non-deuterated systems. T_{1_D} measurements are indicative of relaxation in the dipolar field and are particularly sensitive to high-energy (low-frequency) motions. By conducting T_{1_D} measurements within the same temperature range, we can probe potential in-plane reorientations of the entire molecule by designing set of novel systems. This additional analysis can provide valuable insights into how halogen bonds influence high-energy molecular motions, thereby offering a more comprehensive understanding of their impact on molecular dynamics.

Temperature dependent ^{19}F chemical shift can be studied to observe motion induced changes in shielding tensor involving CF_3 groups. This would offer broader perspectives on the methyl dynamics and structural properties of halogen bonded systems, beyond the scope of the methyl group rotations alone but about hopping motions if present.

References

(1) Li, Y.; Zhao, C.; Wang, Z.; Zeng, Y. *J. Phys. Chem. A* **2024**, *128* (3), 507–527.

(2) Xu, Y.; Gabidullin, B.; Bryce, D. L. *J. Phys. Chem. A* **2019**, *123* (29), 6194–6209.

(3) Zhang, Y.; Wang, J.; Liao, Y.; Xie, X. *Chemistry – An Asian Journal* **2023**, *18* (12), e202300097.

(4) Wolters, L. P.; Schyman, P.; Pavan, M. J.; Jorgensen, W. L.; Bickelhaupt, F. M.; Kozuch, S. *WIREs Computational Molecular Science* **2014**, *4* (6), 523–540.

(5) Politzer, P.; Murray, J. S. Halogen Bonding: An Interim Discussion. *ChemPhysChem* **2013**, 14 (2), 278–294.

(6) H. Allen, F.; Taylor, R. *Chem. Soc. Rev.* **2004**, *33* (8), 463–475.

(7) L. Price, S. Chem. Soc. Rev. **2014**, 43 (7), 2098–2111.

(8) Xu, Y.; Champion, L.; Gabidullin, B.; Bryce, D. L. *Chem. Commun.* **2017**, *53* (71), 9930–9933.

(9) Pascoe, D. J.; Ling, K. B.; Cockroft, S. L. *J. Am. Chem. Soc.* **2017**, *139* (42), 15160-15167.

(10) Vogel, L.; Wonner, P.; Huber, S. M. *Angew. Chem. Int. Ed.* **2019**, *58* (7), 1880-1891.

(11) Aakeroy, C. B., Bryce, D. L., Desiraju, G. R., Frontera, A., Legon, A. C., Nicotra, F., Resnati, G. *Pure and Appl. Chem.* **2019**, *91* (11), 1889-1892.

(12) G. Resnati, D. L. Bryce, G. R. Desiraju, A. Frontera, I. Krossing, A. C. Legon, P. Metrangolo, F. Nicotra, K. Rissanen, S. Scheiner, G. Terraneo *Pure Appl. Chem*. **2024,** *96*, 135-145.

(13) Scilabra, P., Terraneo, G., Resnati, G. *J. of Fluorine Chemistry*, **2017**, *203*, 62-74.

(14) Southern, S. A.; West, M. S.; Bradshaw, M. J.; Bryce, D. L. *J. Phys. Chem. C*, **2021**, *125* (3), 2111-2123.

(15) Bauzá, A.; Mooibroek, T. J.; Frontera, A. *Angew. Chem .Int. Ed.* **2013**, *52* (47), 12317-12321.

(16) Kaasik, M.; Kaabel, S.; Kriis, K.; Järving, I.; Aav, R., Rissanen, K.; Kanger, T. *Chem. Eur J.* **2017**, *23* (30), 7337-7344.

(17) Ghosh, P.; Nandi, M., Bej, S.; Jana, T. *Chem. Comm*. **2023**.

Appendices

Appendix 1: Chapter 4 Supporting Information

1. Single Crystal X-Ray Data and Structure Refinement Tables

Table S 1. Single crystal data and structure refinement for 1,4-dibromotetrafluorobenzene·2,3,5,6-tetramethylpyrazine (1)

CCDC Number	2215842
Empirical formula	$C_{22}H_{24}Br_2F_4N_4$
Formula weight	580.25
Temperature/K	203
Crystal system	monoclinic
Space group	$P2_1/n$
a/Å	7.1235(18)
b/Å	14.926(4)
c/Å	11.157(3)
α/°	90
β/°	102.368(7)
γ/°	90
Volume/Å^3	1158.8(5)
Z	2
ρ_{calc}g/cm^3	1.663
μ/mm^{-1}	3.547
F(000)	580.0
Crystal size/mm^3	0.390 × 0.287 × 0.228
Radiation	MoKα (λ = 0.71073)
2θ range for data collection/°	2.314 to 27.824

Index ranges	$-9 \leq h \leq 9$, $-19 \leq k \leq 19$, $-14 \leq l \leq 14$
Reflections collected	56905
Independent reflections	2742 [R(int) = 0.0632]
Data/restraints/parameters	2742 / 0 / 149
Goodness-of-fit on F^2	1.134
Final R indexes [I>=2σ (I)]	$R_1 = 0.0292$, $wR_2 = 0.0704$
Final R indexes [all data]	$R_1 = 0.0389$, $wR_2 = 0.0752$
Largest diff. peak/hole / e Å^{-3}	0.561 and -0.596

Table S 2. Single crystal data and structure refinement for 1,3,5-tribromo-2,4,6-trifluorobenzene·2,3,5,6-tetramethylpyrazine (2).

CCDC Number	2215844
Empirical formula	$C_{14}H_{12}Br_3F_3N_2$
Formula weight	504.99
Temperature/K	203
Crystal system	monoclinic
Space group	$P2_1/n$
a/Å	7.4109(4)
b/Å	26.2209(16)
c/Å	9.1408(5)
α/°	90
β/°	111.270(4)
γ/°	90
Volume/Å^3	1655.25(17)
Z	4
ρ_{calc}g/cm^3	2.026
μ/mm^{-1}	7.337
F(000)	968

Crystal size/mm^3	0.277 x 0.260 x 0.232
Radiation	0.71073
2θ range for data collection/°	1.553 to 27.283
Index ranges	-9<=h<=9, -33<=k<=33, -11<=l<=11
Reflections collected	23295
Independent reflections	3712 [R(int) = 0.0376]
Data/restraints/parameters	3712 / 0 / 201
Goodness-of-fit on F^2	1.069
Final R indexes [I>=2σ (I)]	R_1 = 0.0296, wR_2 = 0.0554
Final R indexes [all data]	R1 = 0.0447, wR2 = 0.0592
Largest diff. peak/hole / e Å^{-3}	0.558 and -0.331

Table S 3. Single crystal data and structure refinement for bromine·2,3,5,6-tetramethylpyrazine (3).

CCDC Number	2215846
Empirical formula	$C_8H_{12}Br_2N_2$
Formula weight	296.02
Temperature/K	202
Crystal system	triclinic
Space group	*P* -1
a/Å	4.626(2)
b/Å	7.090(3)
c/Å	8.613(4)
α/°	93.072(8)
β/°	99.664(8)
γ/°	98.741(8)
Volume/Å^3	274.4(2)

Z	1
ρ_{calc}g/cm^3	1.792
μ/mm^{-1}	7.340
F(000)	144
Crystal size/mm^3	0.258 x 0.204 x 0.197
Radiation	0.71073
2θ range for data collection/°	2.916 to 31.284
Index ranges	-6<=h<=6, -10<=k<=10, -12<=l<=12
Reflections collected	6405
Independent reflections	1665 [R(int) = 0.0725]
Data/restraints/parameters	1665 / 0 / 57
Goodness-of-fit on F^2	0.968
Final R indexes [I>=2σ (I)]	R_1 = 0.0534, wR_2 = 0.1447
Final R indexes [all data]	R_1 = 0.0940, wR_2 = 0.1741
Largest diff. peak/hole / e Å^{-3}	1.104 and -0.993 e.Å^{-3}

Table S 4. Single crystal data and structure refinement for 1,4-dichlorotetrafluorobenzene·2,3,5,6-tetramethylpyrazine (4).

CCDC Number	2215843
Empirical formula	$C_{22}H_{24}Cl_2F_4N_4$
Formula weight	491.35
Temperature/K	203
Crystal system	monoclinic
Space group	*P*2$_1$/*n*
a/Å	7.1006(10)
b/Å	14.757(2)
c/Å	11.2091(16)

α/°	90
β/°	102.289(8)
γ/°	90
Volume/Å^3	1147.6(3)
Z	2
ρ_{calc}g/cm^3	1.422
μ/mm^{-1}	0.333
F(000)	508
Crystal size/mm^3	0.447 x 0.201 x 0.102
Radiation	0.71073
2θ range for data collection/°	2.316 to 26.779
Index ranges	-8<=h<=8, -18<=k<=18, -14<=l<=14
Reflections collected	34127
Independent reflections	2433 [R(int) = 0.0255]
Data/restraints/parameters	2433 / 0 / 149
Goodness-of-fit on F^2	1.132
Final R indexes [I>=2σ (I)]	R$_1$ = 0.0371, wR$_2$ = 0.0979
Final R indexes [all data]	R$_1$ = 0.0475, wR$_2$ = 0.1116
Largest diff. peak/hole / e Å^{-3}	0.349 and -0.208

Table S 5. Single crystal data and structure refinement for 1,3,5-trichloro-2,4,6-trifluorobenzene·2,3,5,6-tetramethylpyrazine (5).

CCDC Number	2215845
Empirical formula	$C_{14}H_{12}Cl_3F_3N_2$
Formula weight	371.61
Temperature/K	203
Crystal system	monoclinic
Space group	$P2_1/n$
a/Å	7.1243(9)
b/Å	26.058(3)
c/Å	9.1483(11)
α/°	90
β/°	108.521(2)
γ/°	90
Volume/Å^3	1610.4(3)
Z	4
ρ_{calc}g/cm^3	1.533
μ/mm^{-1}	0.595
F(000)	752
Crystal size/mm^3	0.295 x 0.276 x 0.257
Radiation	0.71073
2θ range for data collection/°	1.563 to 26.425
Index ranges	-8<=h<=8, -32<=k<=32, -11<=l<=11
Reflections collected	28532
Independent reflections	3278 [R(int) = 0.0293]
Data/restraints/parameters	3278 / 0 / 203
Goodness-of-fit on F^2	1.101
Final R indexes [I>=2σ (I)]	R_1 = 0.0413, wR_2 = 0.1031
Final R indexes [all data]	R_1 = 0.0521, wR_2 = 0.1110
Largest diff. peak/hole / e Å^{-3}	0.216 and -0.271

2. X-ray Diffraction Structures: Packing Diagrams

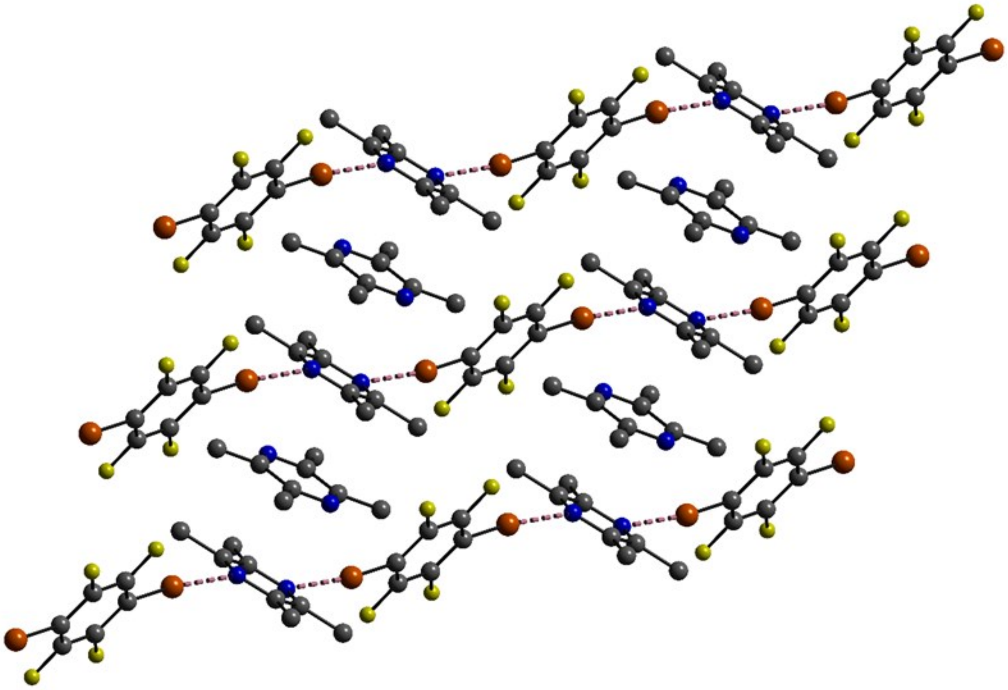

Figure S 1. Packing diagram of 1,4-dibromotetrafluorobenzene·2,3,5,6-tetramethylpyrazine (1).

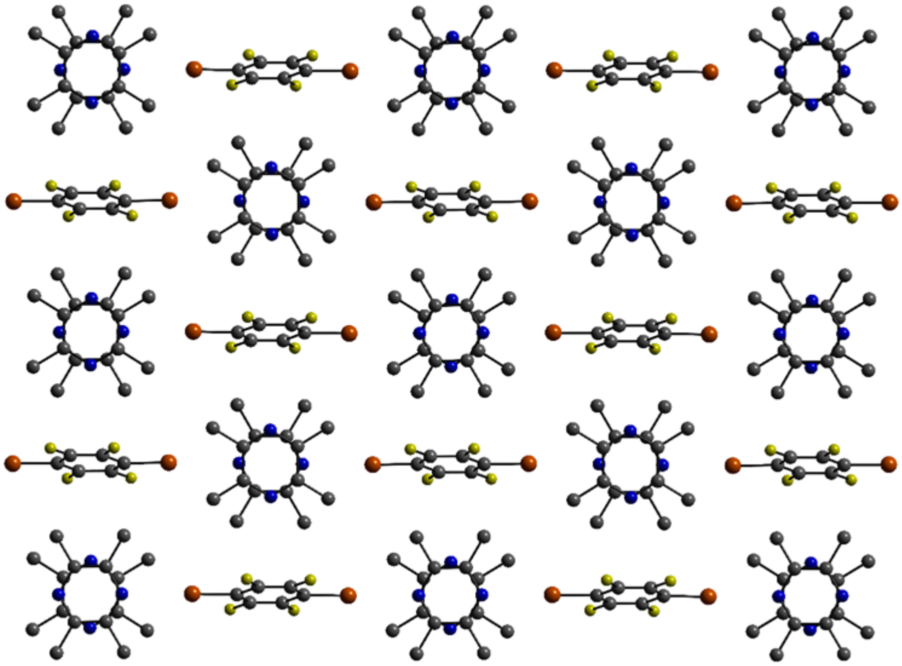

Figure S 2. Packing diagram of 1,4-dibromotetrafluorobenzene·2,3,5,6-tetramethylpyrazine (1).

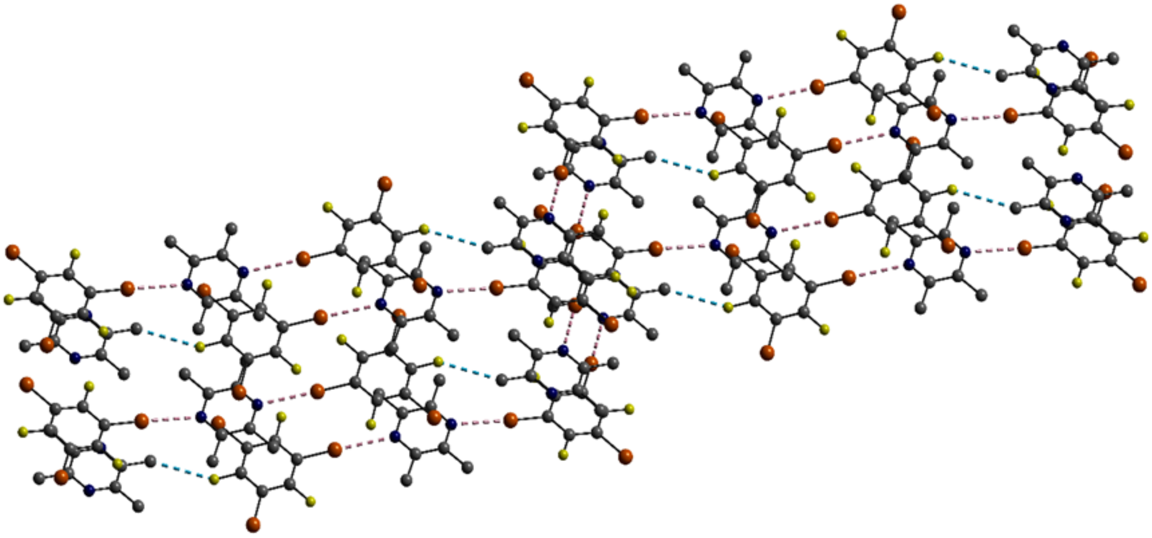

Figure S 3. Packing diagram of 1,3,5-tribromo-2,4,6-trifluorobenzene·2,3,5,6-tetramethylpyrazine

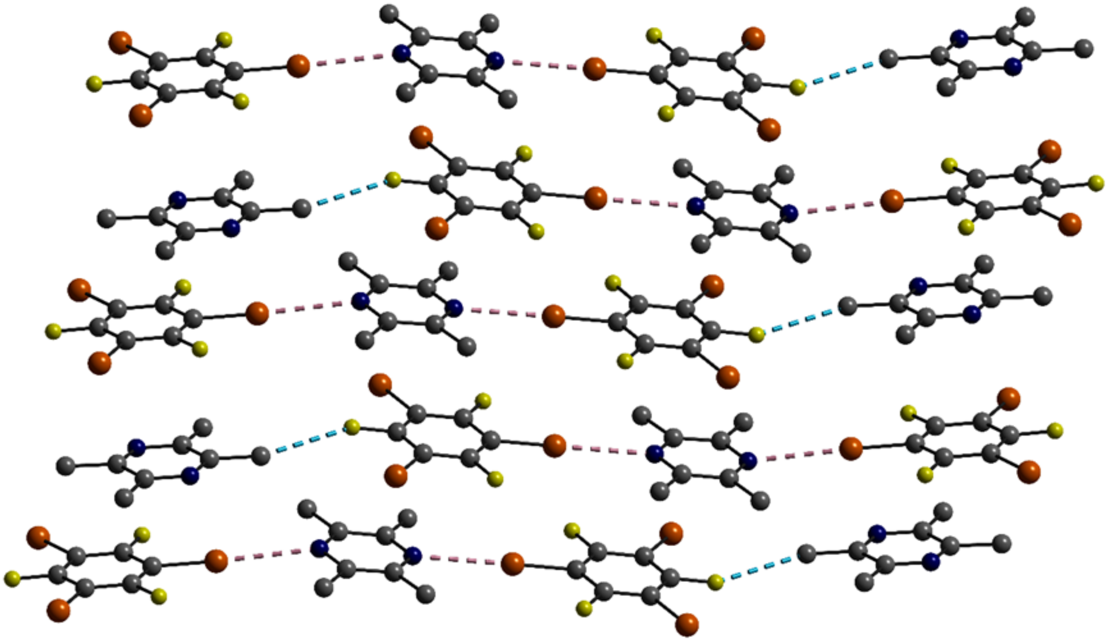

Figure S 4. Packing diagram of 1,3,5-tribromo-2,4,6-trifluorobenzene·2,3,5,6-tetramethylpyrazine (2).

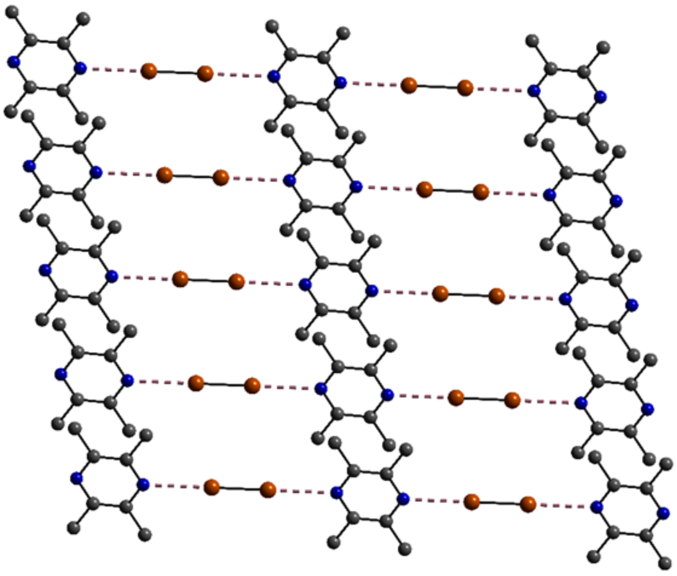

Figure S 5. Packing diagram of Br_2·2,3,5,6-tetramethylpyrazine (3)

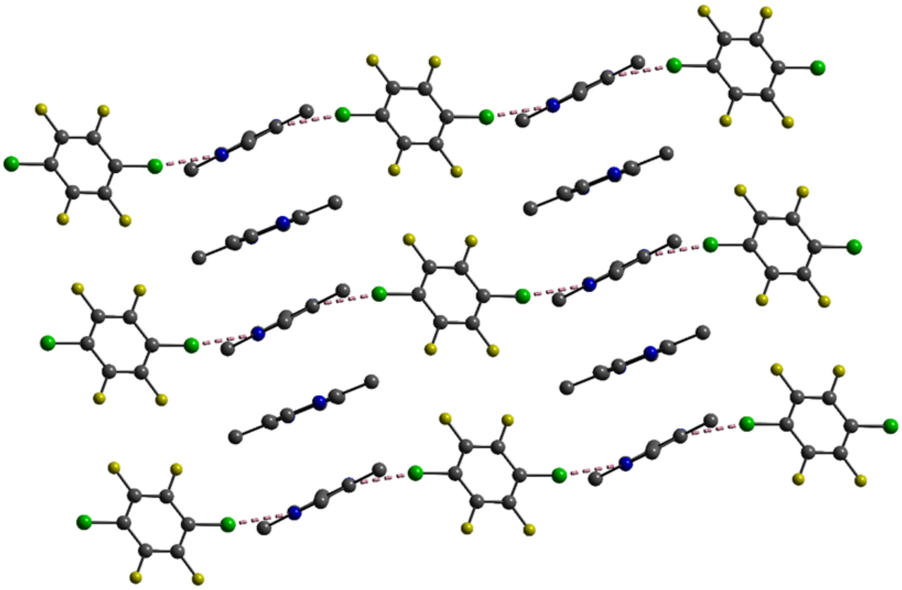

Figure S 6. Packing diagram of 1,4-dichlorotetrafluorobenzene·2,3,5,6-tetramethylpyrazine (4).

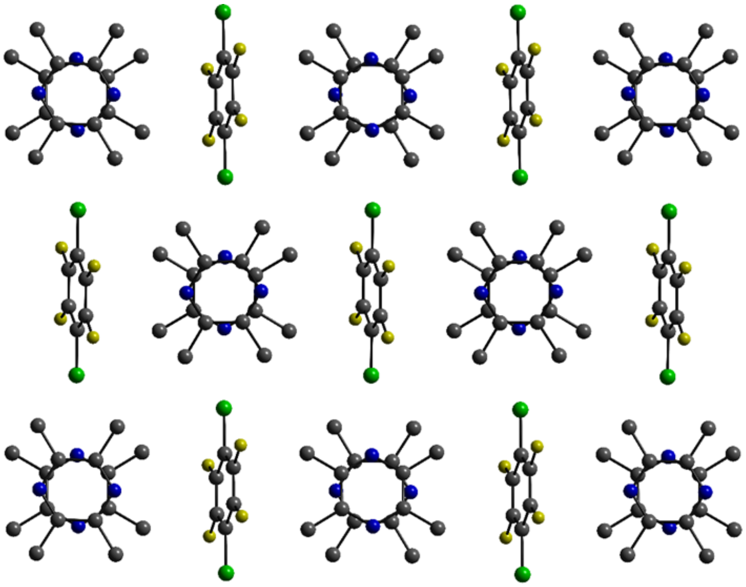

Figure S 7. Packing diagram of 1,4-dichlorotetrafluorobenzene·2,3,5,6-tetramethylpyrazine (4).

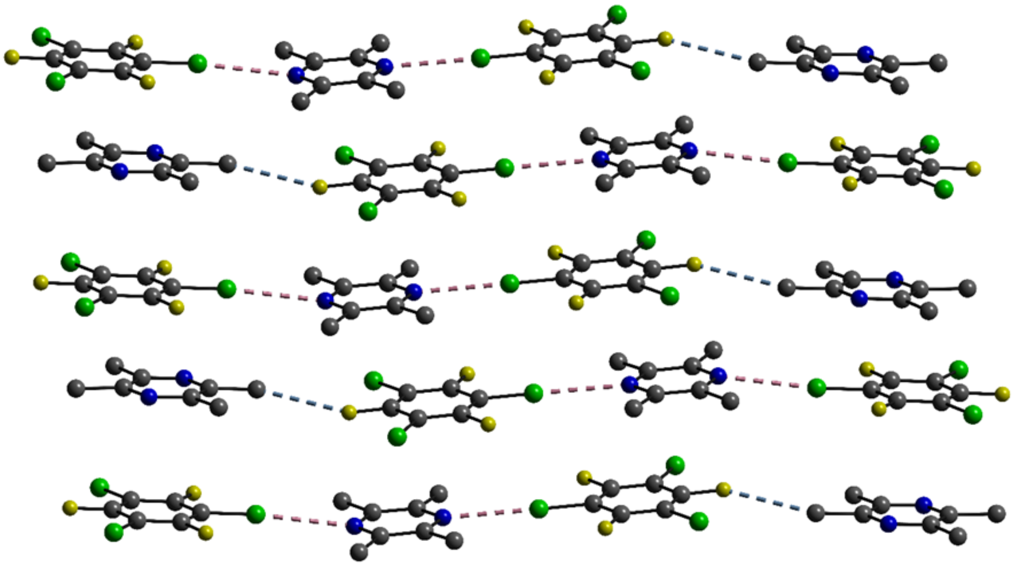

Figure S 8. Packing diagram of 1,3,5-trichloro2,4,6-trifluorobenzene·2,3,5,6-tetramethylpyrazine (5).

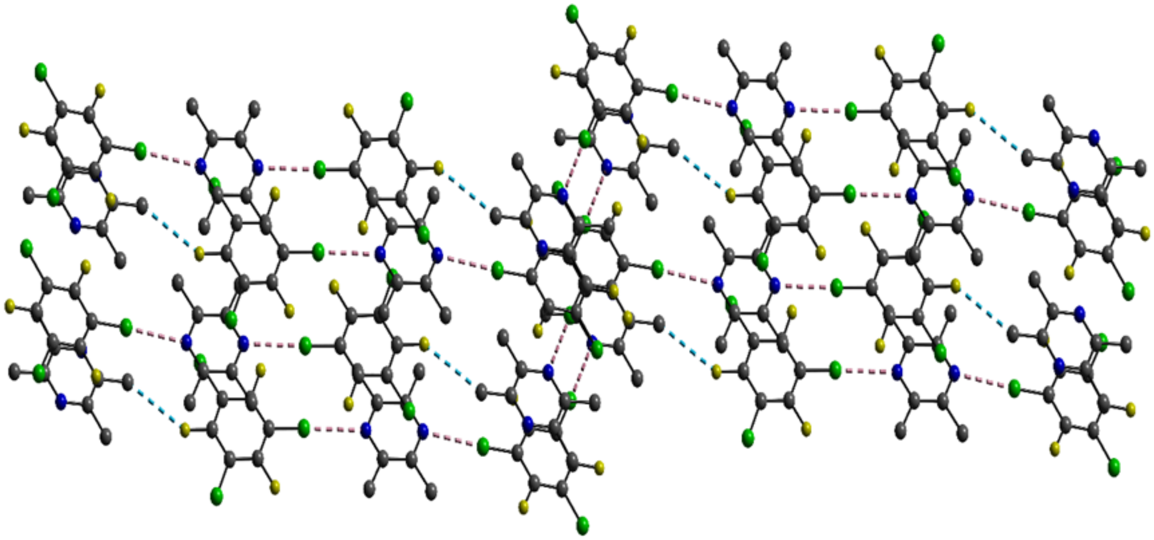

Figure S 9. Packing diagram of 1,3,5-trichloro-2,4,6-trifluorobenzene·2,3,5,6-tetramethylpyrazine (5).

3. Powder X-ray Diffractograms

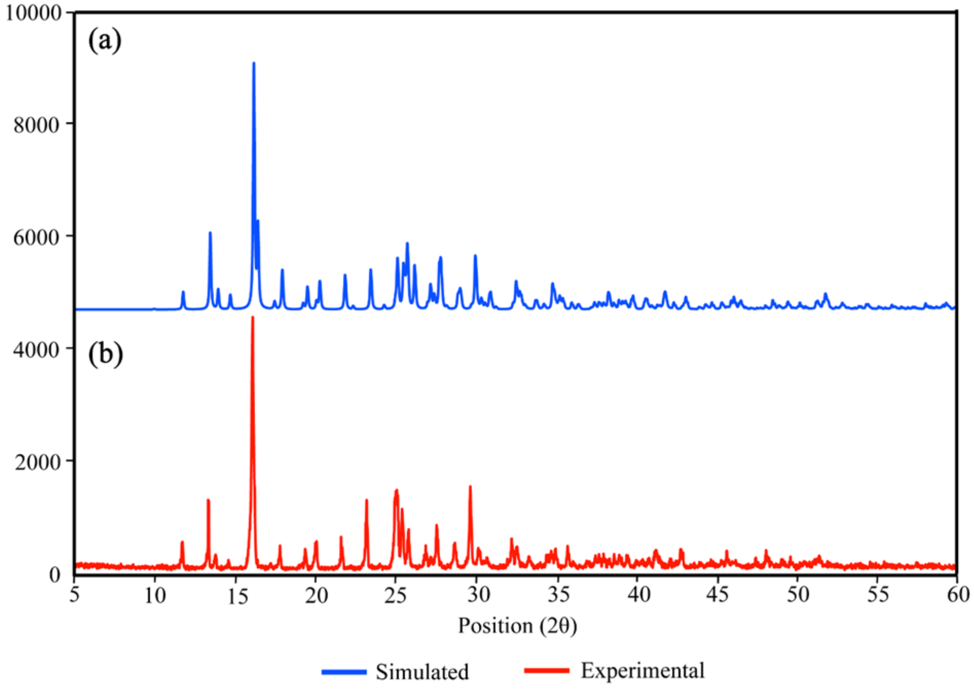

Figure S 10. PXRD for 1,4-dibromotetrafluorobenzene·2,3,5,6-tetramethylpyrazine (1).

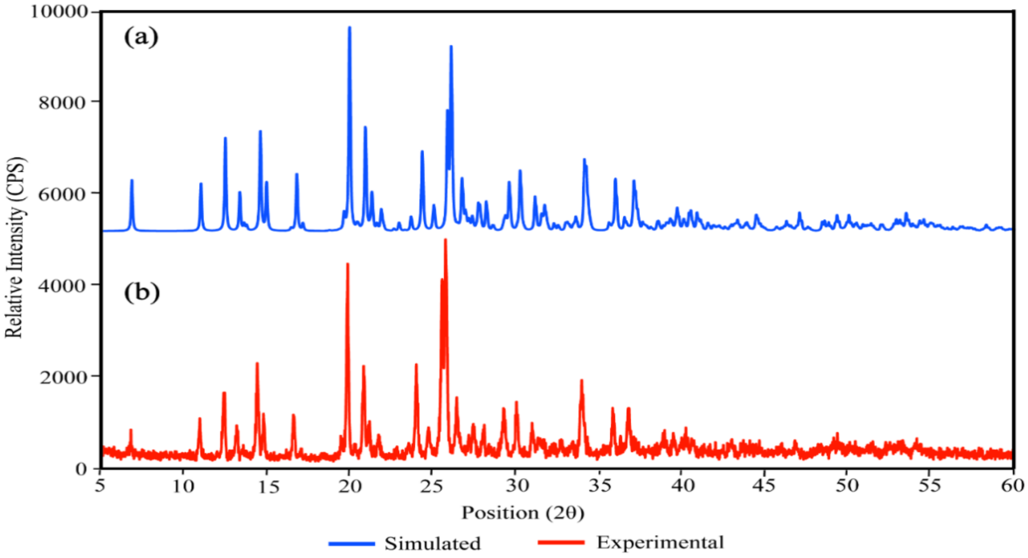

Figure S 11. PXRD of 1,3,5-tribromo-2,4,6-trifluorobenzene·2,3,5,6-tetramethylpyrazine (2).

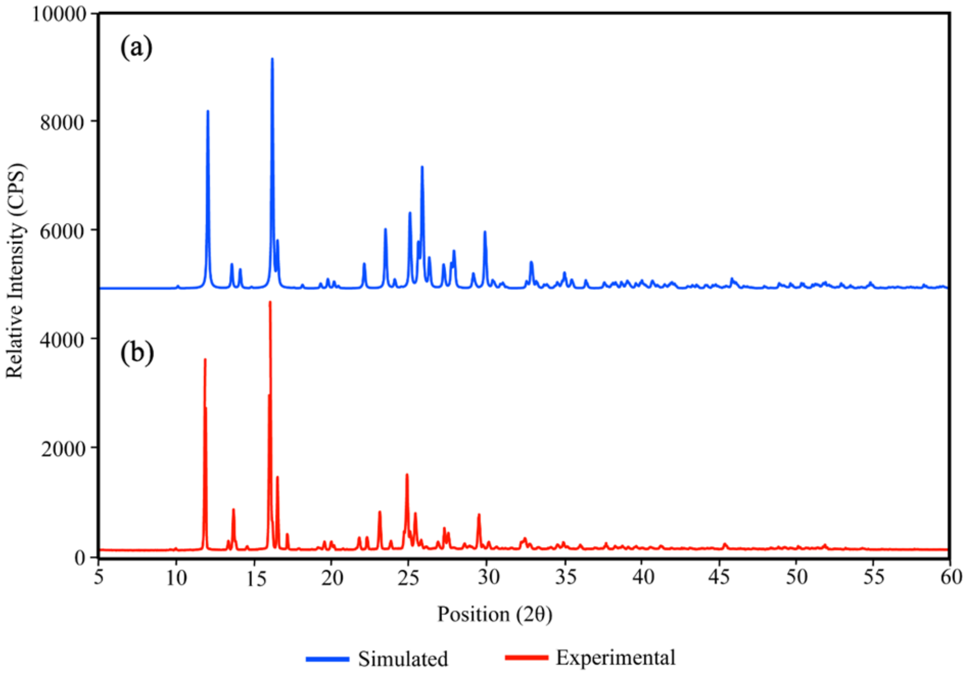

Figure S 12. PXRD of 1,4-dichlorotetrafluorobenzene·2,3,5,6-tetramethylpyrazine (4).

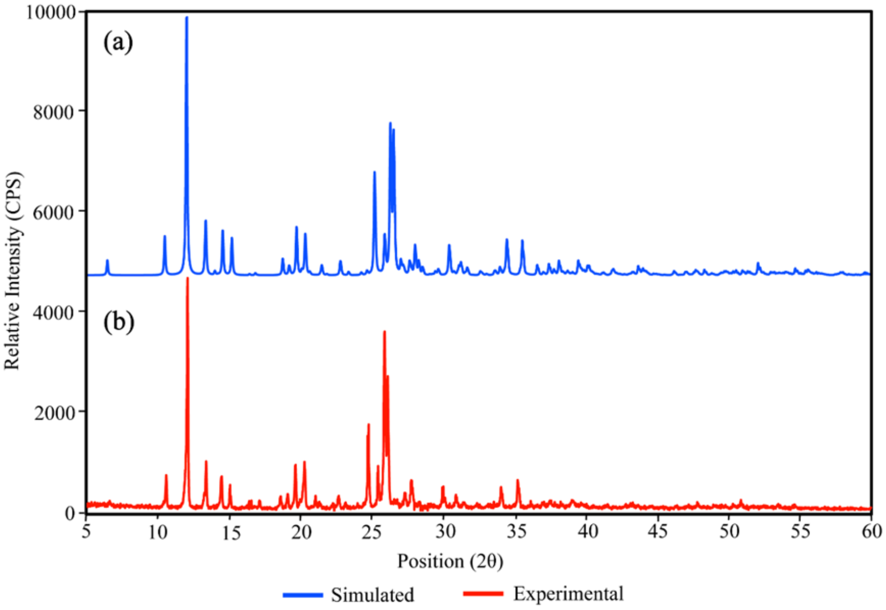

Figure S 13. PXRD of 1,3,5-trichloro-2,4,6-trifluorobenzene·2,3,5,6-tetramethylpyrazine (5).

4. T_1 Measurements via ^{2}H NMR Inversion Recovery Variable Temperature Experiments

1) *1,4-dibromotetrafluorobenzene·2,3,5,6-tetramethylpyrazine (**1**)*

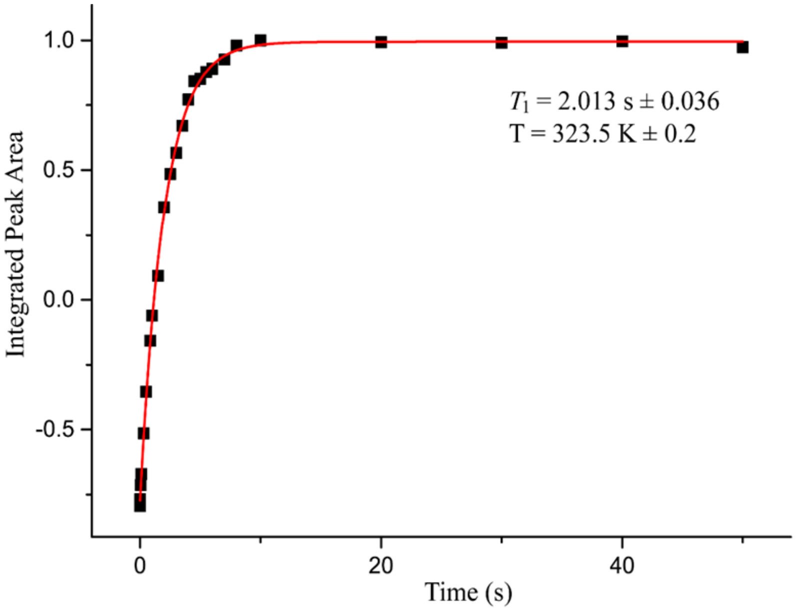

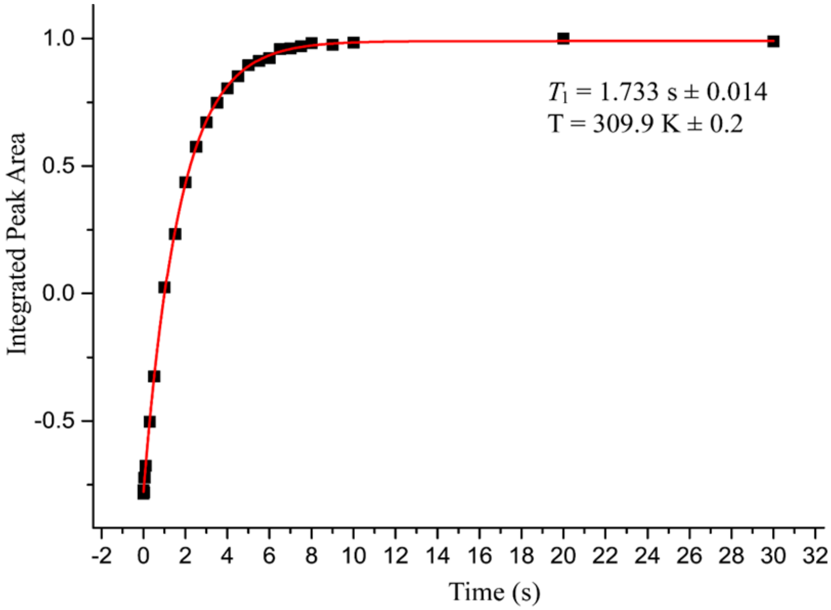

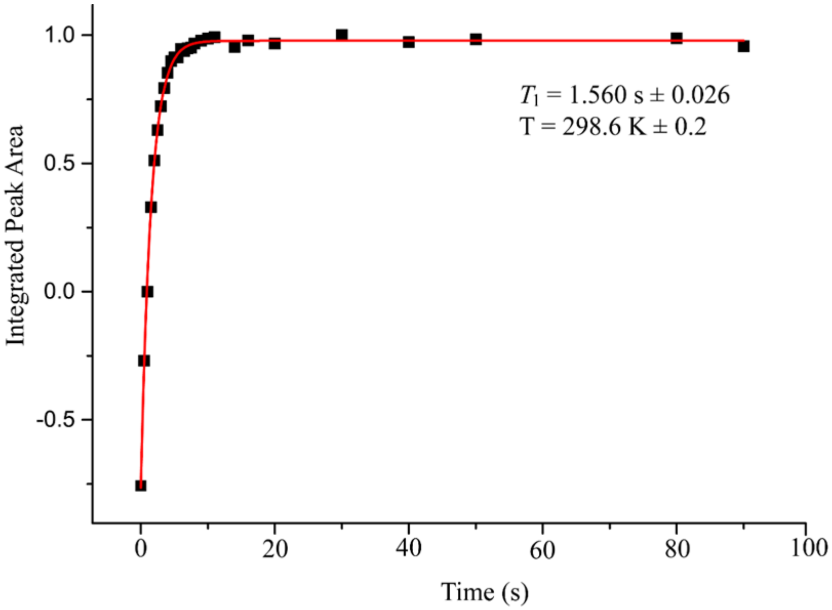
Integrated Peak Area
1.0
0.5
0.0
-0.5
0
20
40
60
80
100
Time (s)
T_1 = 1.560 s ± 0.026
T = 298.6 K ± 0.2

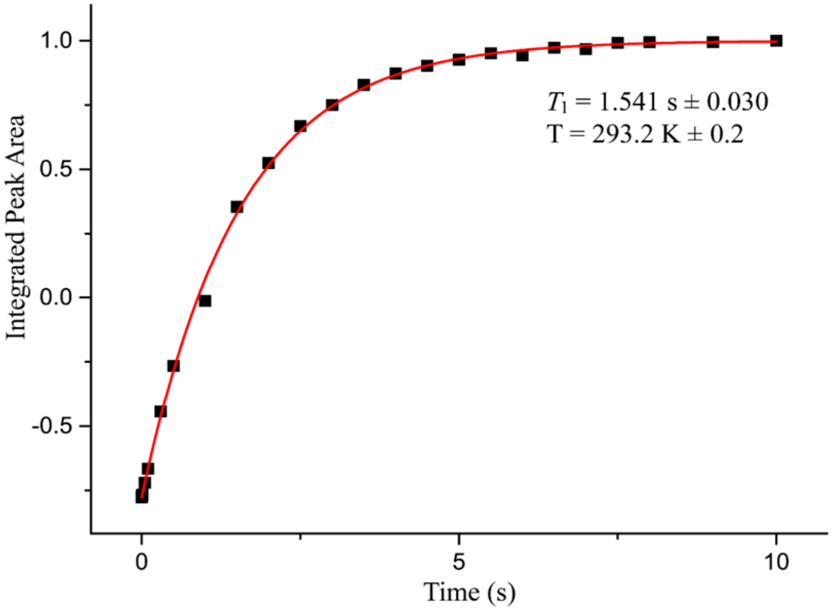
Integrated Peak Area
1.0
0.5
0.0
-0.5
0
5
10
Time (s)
T_1 = 1.541 s ± 0.030
T = 293.2 K ± 0.2

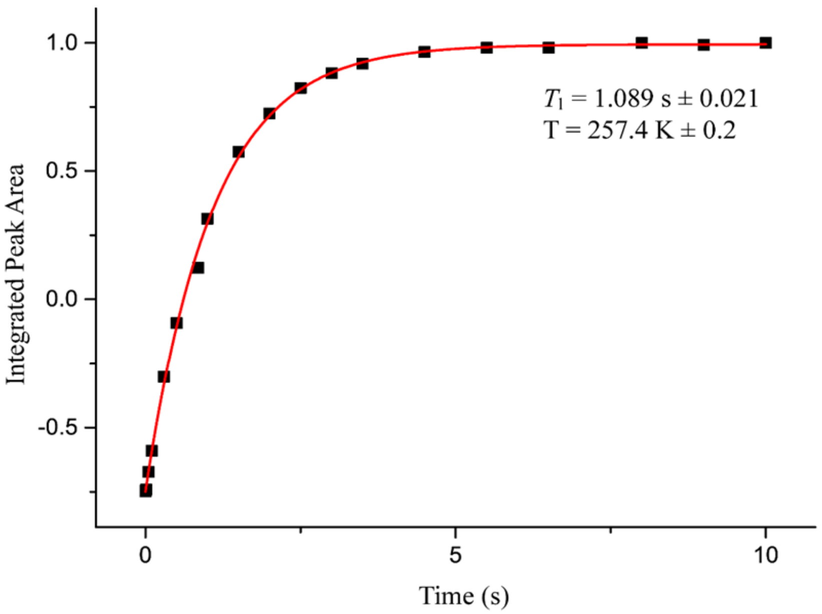
1.0
0.5
0.0
-0.5
Integrated Peak Area
0
5
10
Time (s)
T_1 = 1.089 s ± 0.021
T = 257.4 K ± 0.2

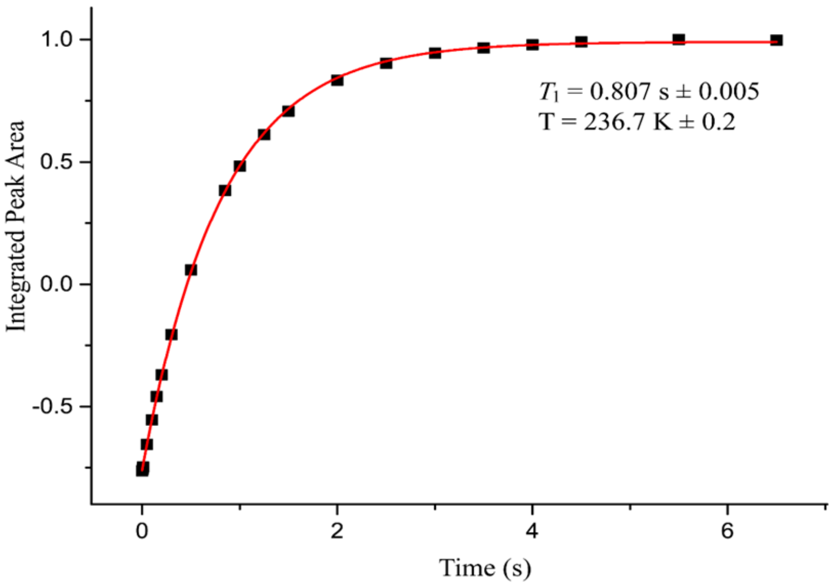
1.0
0.5
0.0
-0.5
Integrated Peak Area
0
2
4
6
Time (s)
T_1 = 0.807 s ± 0.005
T = 236.7 K ± 0.2

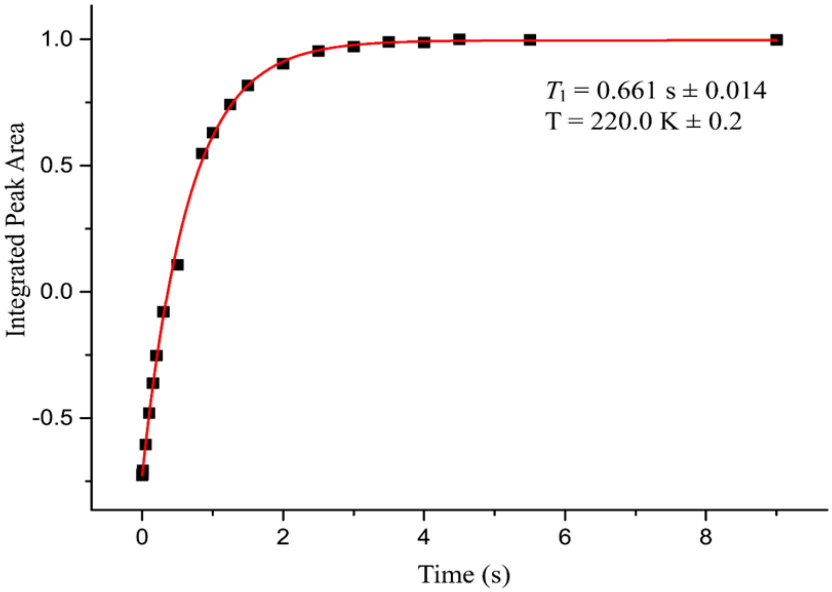
Integrated Peak Area
1.0
0.5
0.0
-0.5
0
2
4
6
8
Time (s)
T_1 = 0.661 s ± 0.014
T = 220.0 K ± 0.2

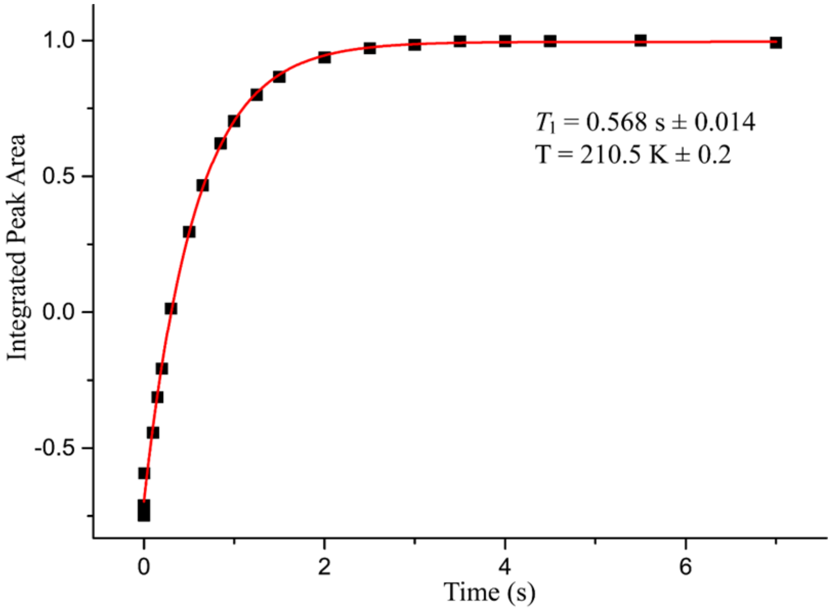
Integrated Peak Area
1.0
0.5
0.0
-0.5
0
2
4
6
Time (s)
T_1 = 0.568 s ± 0.014
T = 210.5 K ± 0.2

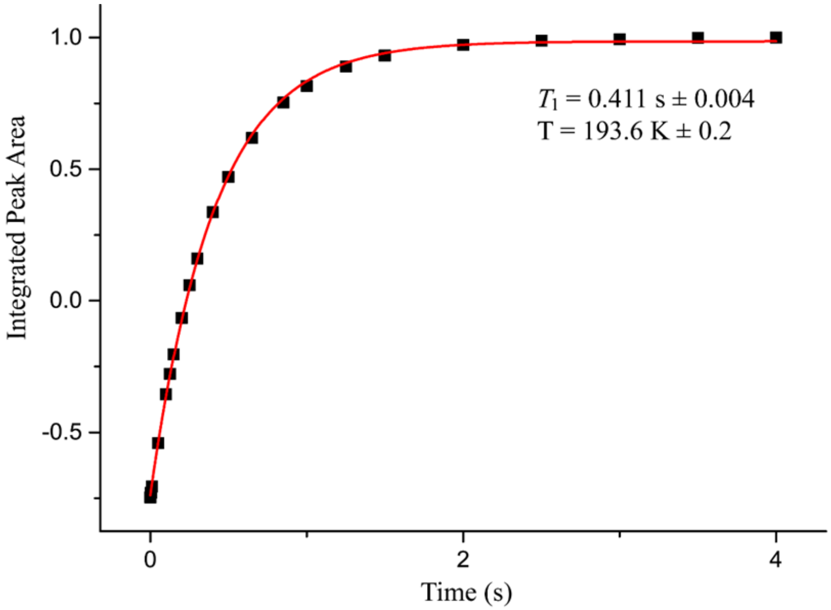

1.0
0.5
0.0
-0.5
Integrated Peak Area
0
2
4
Time (s)
T_1 = 0.411 s ± 0.004
T = 193.6 K ± 0.2

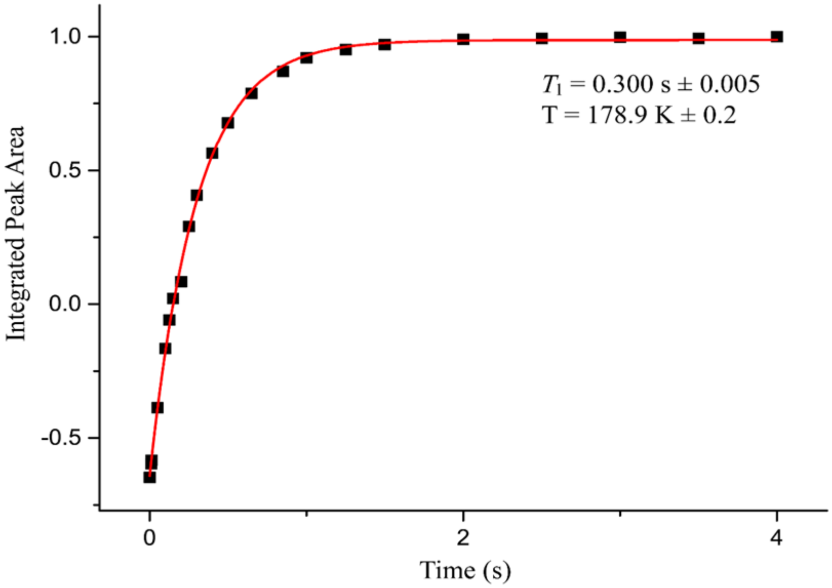

1.0
0.5
0.0
-0.5
Integrated Peak Area
0
2
4
Time (s)
T_1 = 0.300 s ± 0.005
T = 178.9 K ± 0.2

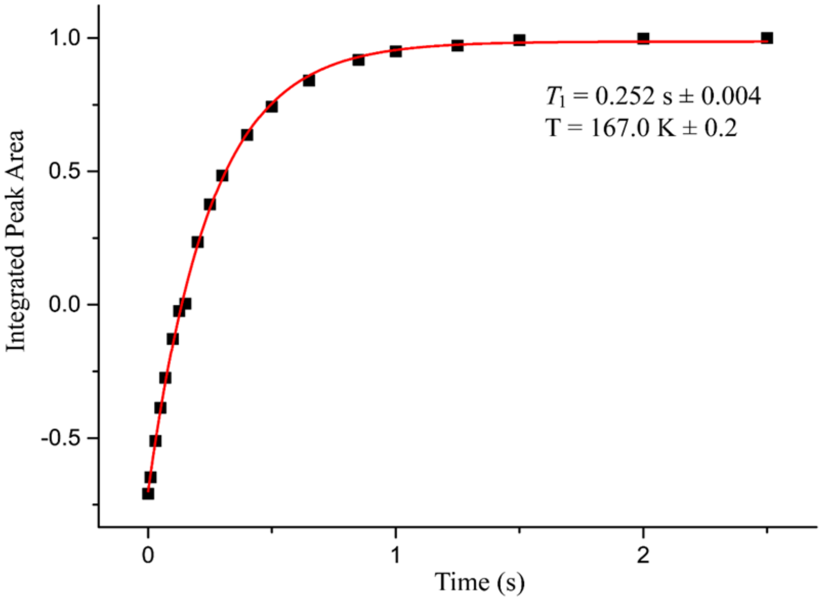
1.0
0.5
0.0
-0.5
Integrated Peak Area
0
1
2
Time (s)
T_1 = 0.252 s ± 0.004
T = 167.0 K ± 0.2

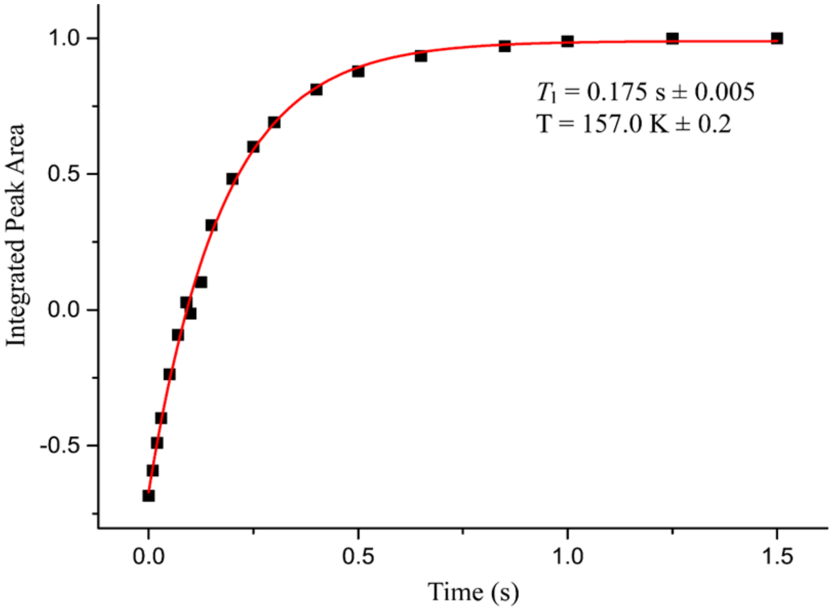
1.0
0.5
0.0
-0.5
Integrated Peak Area
0.0
0.5
1.0
1.5
Time (s)
T_1 = 0.175 s ± 0.005
T = 157.0 K ± 0.2

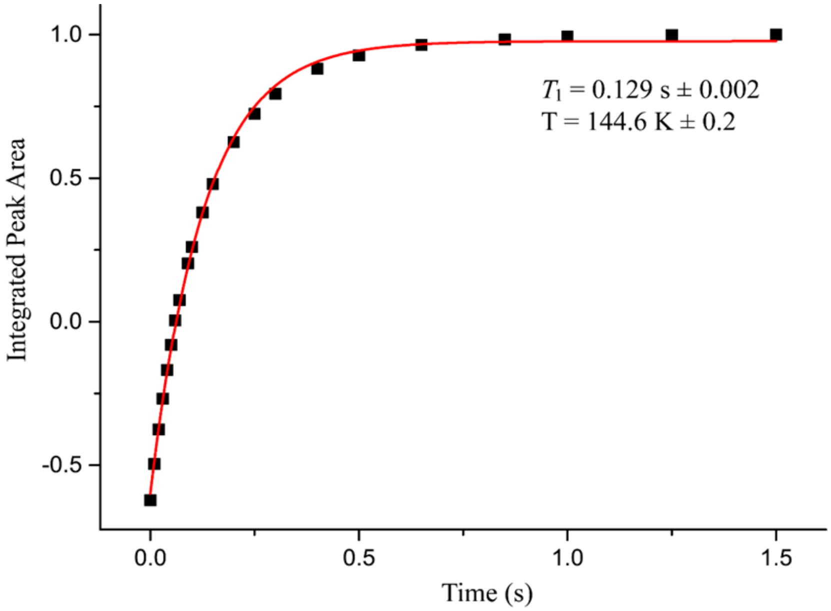

2) *1,3,5-tribromotrifluorobenzene·2,3,5,6-tetramethylpyrazine (**2**)*

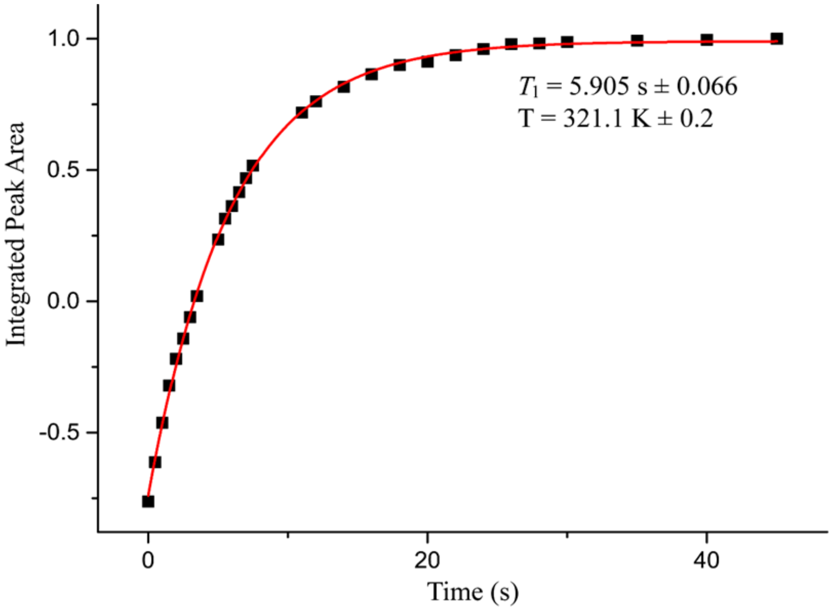

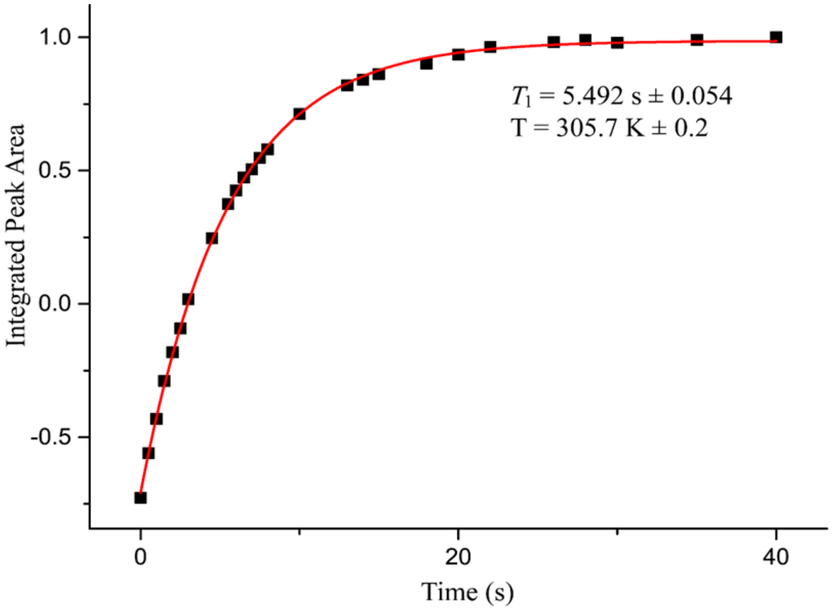
1.0
0.5
0.0
-0.5
Integrated Peak Area
0
20
40
Time (s)
T_1 = 5.492 s ± 0.054
T = 305.7 K ± 0.2

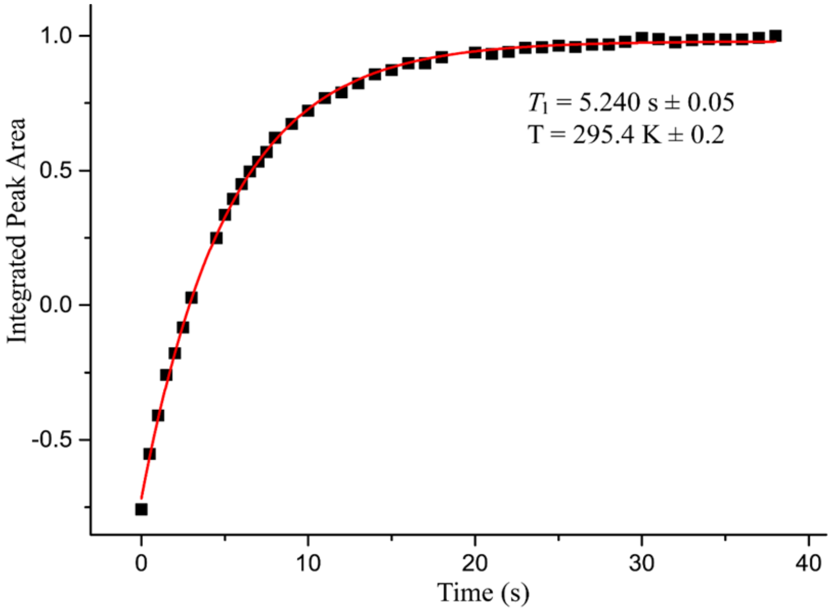
1.0
0.5
0.0
-0.5
Integrated Peak Area
0
10
20
30
40
Time (s)
T_1 = 5.240 s ± 0.05
T = 295.4 K ± 0.2

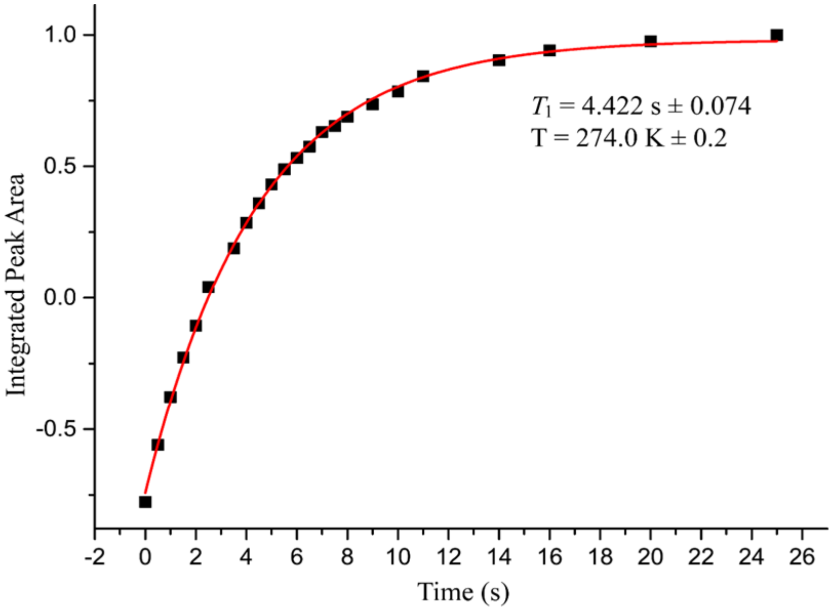
T_1 = 4.422 s ± 0.074
T = 274.0 K ± 0.2
Integrated Peak Area
Time (s)
1.0
0.5
0.0
-0.5
-2
0
2
4
6
8
10
12
14
16
18
20
22
24
26

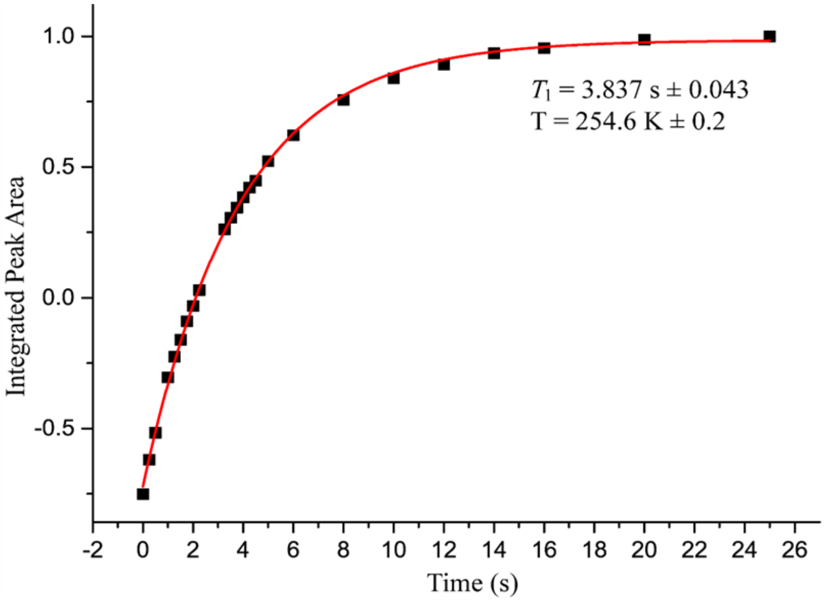
T_1 = 3.837 s ± 0.043
T = 254.6 K ± 0.2
Integrated Peak Area
Time (s)
1.0
0.5
0.0
-0.5
-2
0
2
4
6
8
10
12
14
16
18
20
22
24
26

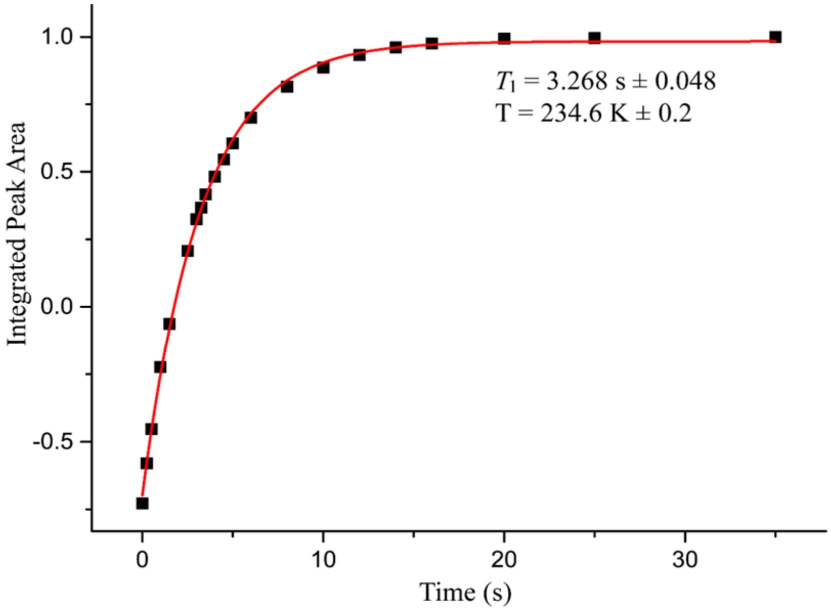
1.0
0.5
0.0
-0.5
Integrated Peak Area
0
10
20
30
Time (s)
T_1 = 3.268 s ± 0.048
T = 234.6 K ± 0.2

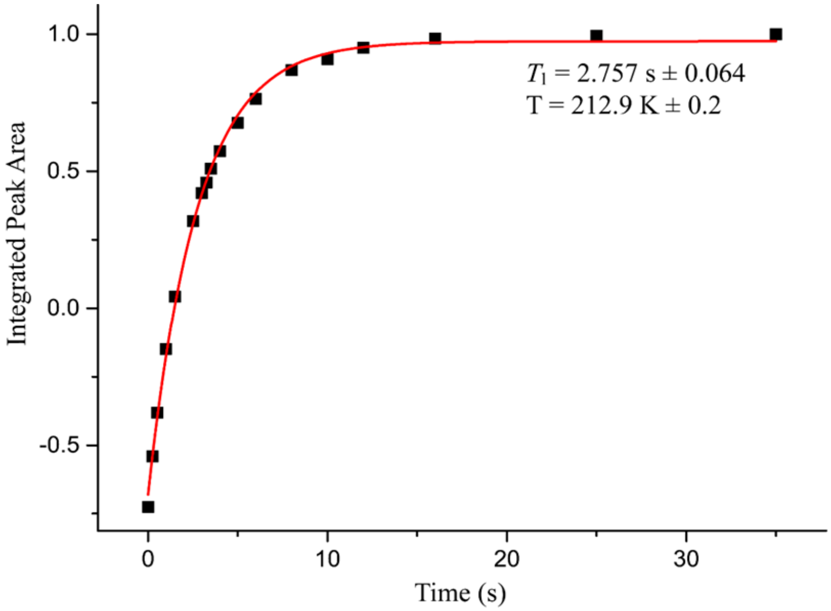
1.0
0.5
0.0
-0.5
Integrated Peak Area
0
10
20
30
Time (s)
T_1 = 2.757 s ± 0.064
T = 212.9 K ± 0.2

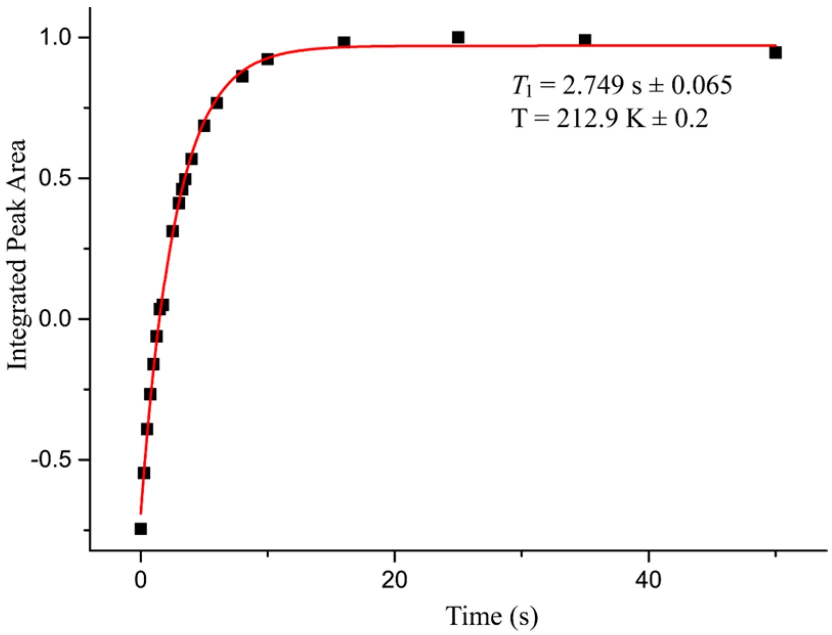

T_1 = 2.749 s ± 0.065
T = 212.9 K ± 0.2
Integrated Peak Area
1.0
0.5
0.0
-0.5
0
20
40
Time (s)

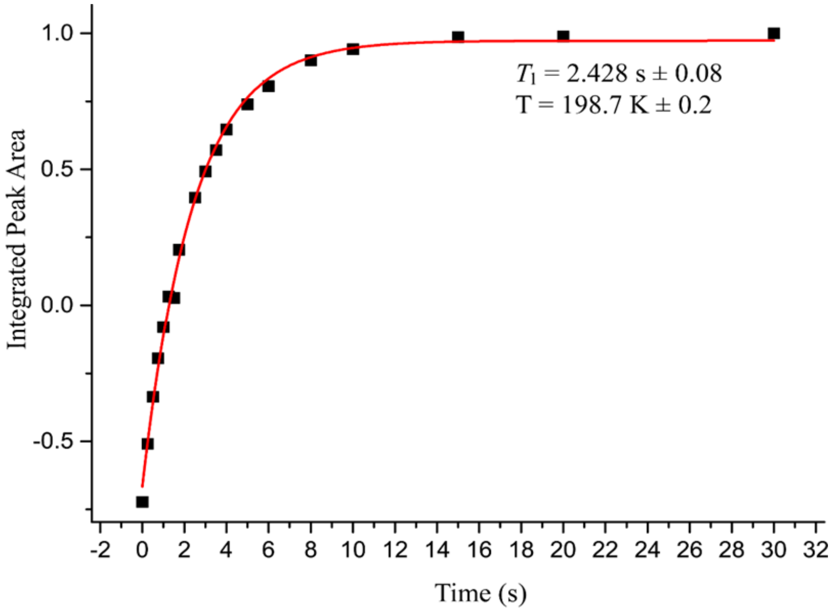

T_1 = 2.428 s ± 0.08
T = 198.7 K ± 0.2
Integrated Peak Area
1.0
0.5
0.0
-0.5
-2
0
2
4
6
8
10
12
14
16
18
20
22
24
26
28
30
32
Time (s)

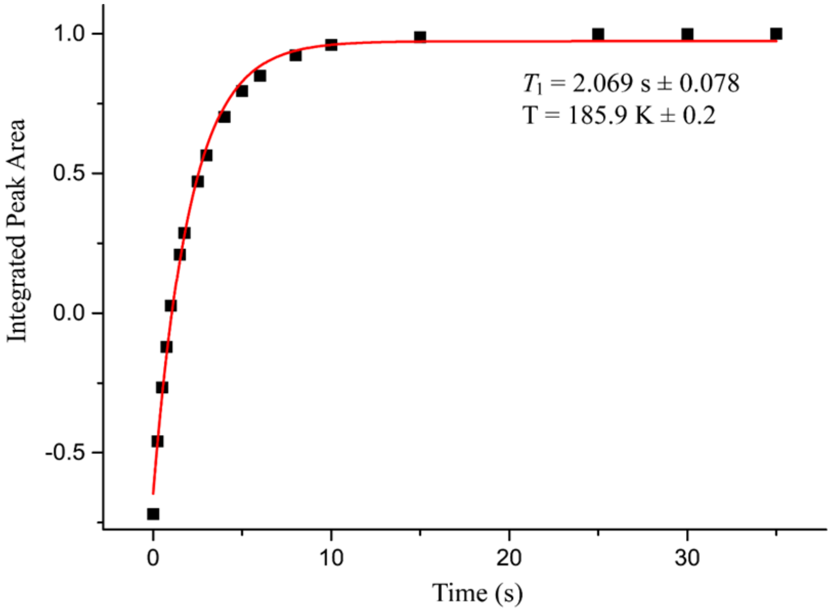
T_1 = 2.069 s ± 0.078
T = 185.9 K ± 0.2
Integrated Peak Area
Time (s)
1.0
0.5
0.0
-0.5
0
10
20
30

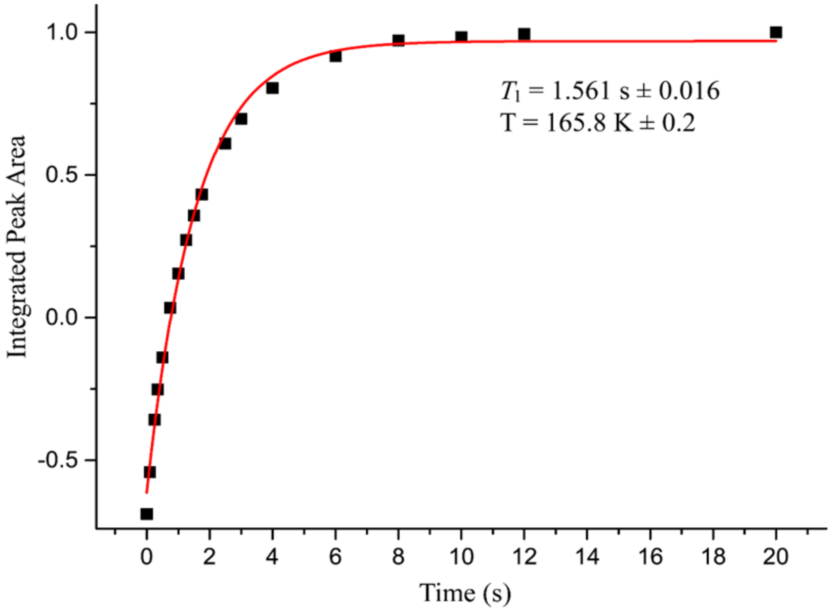
T_1 = 1.561 s ± 0.016
T = 165.8 K ± 0.2
Integrated Peak Area
Time (s)
1.0
0.5
0.0
-0.5
0
2
4
6
8
10
12
14
16
18
20

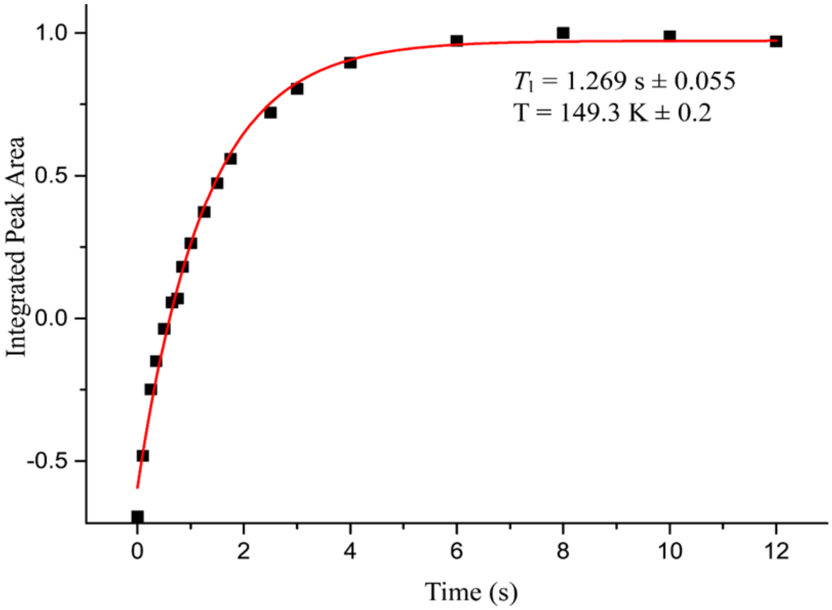

T_1 = 1.269 s ± 0.055
T = 149.3 K ± 0.2
Integrated Peak Area
1.0
0.5
0.0
-0.5
0
2
4
6
8
10
12
Time (s)

3) *Bromine·2,3,5,6-tetramethylpyrazine (**3**)*

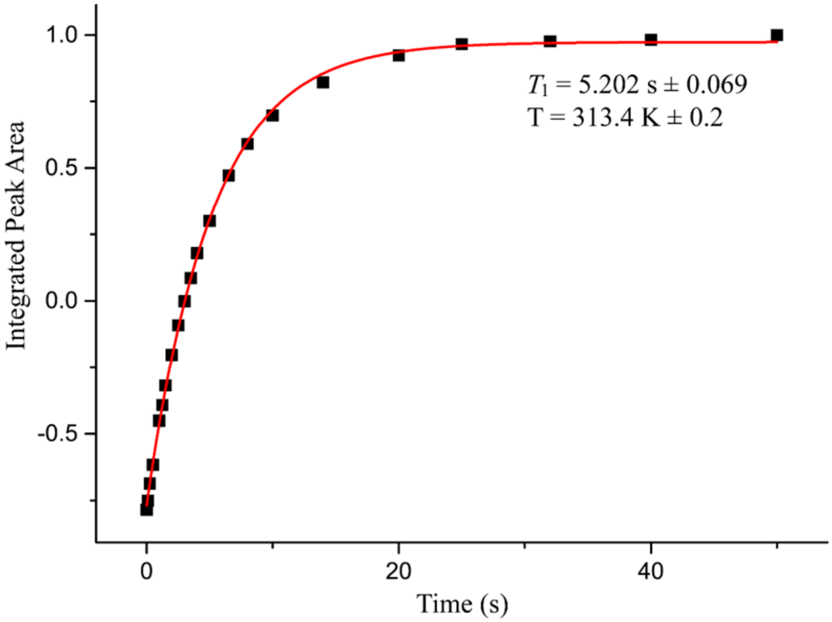

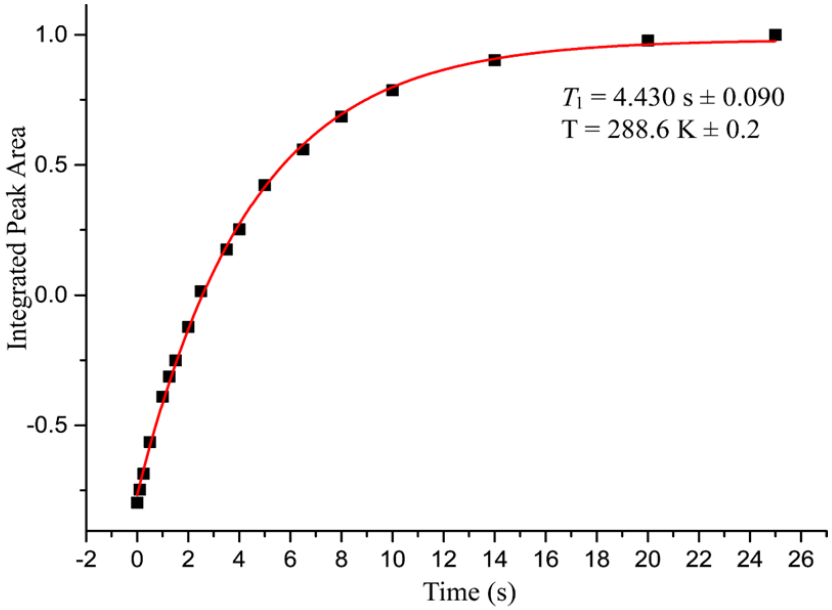

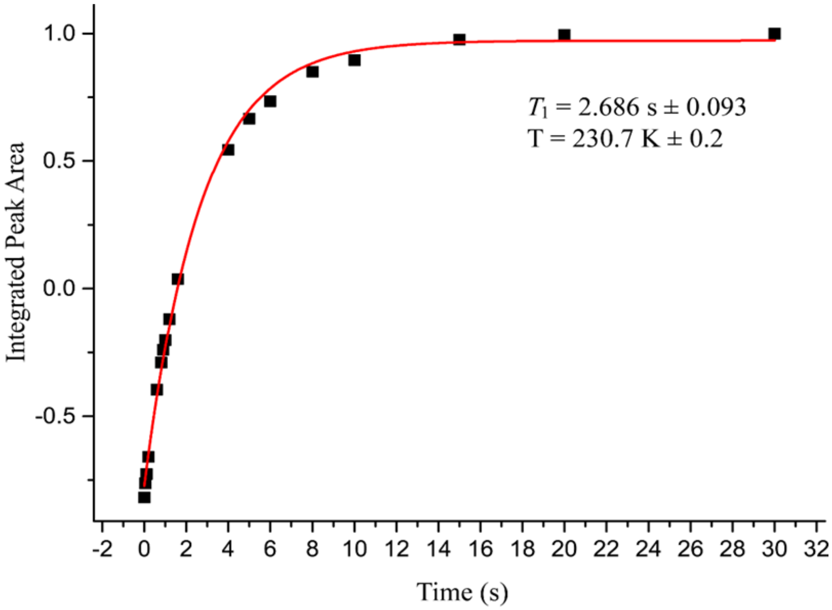
1.0
0.5
0.0
-0.5
Integrated Peak Area
-2
0
2
4
6
8
10
12
14
16
18
20
22
24
26
28
30
32
Time (s)
T_1 = 2.686 s ± 0.093
T = 230.7 K ± 0.2

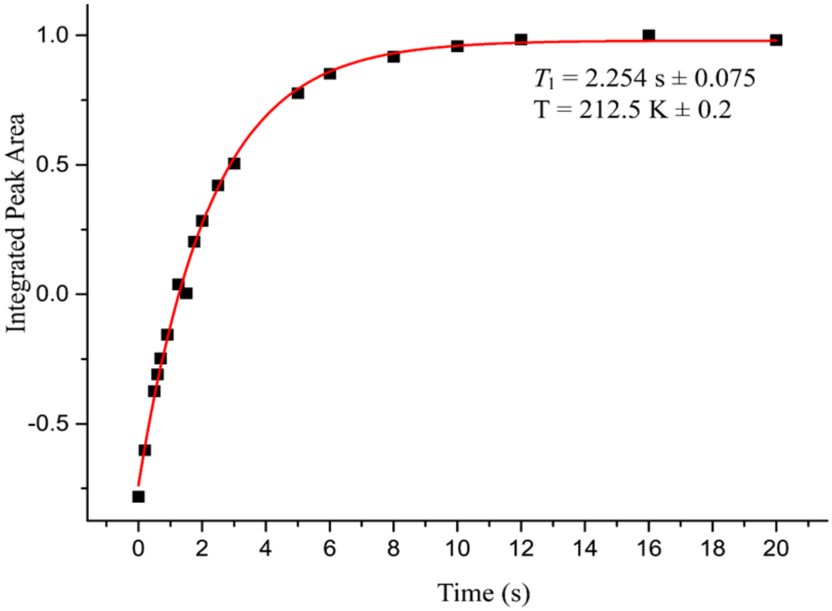
1.0
0.5
0.0
-0.5
Integrated Peak Area
0
2
4
6
8
10
12
14
16
18
20
Time (s)
T_1 = 2.254 s ± 0.075
T = 212.5 K ± 0.2

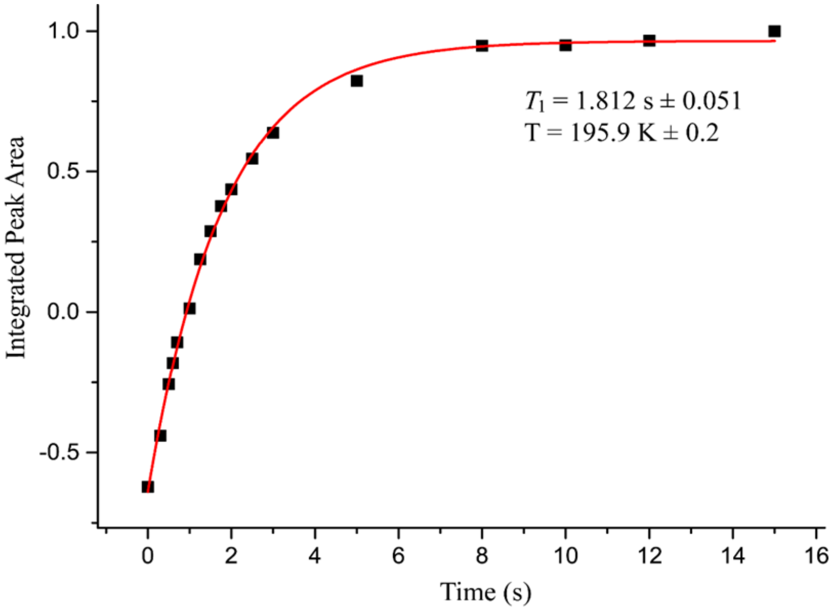
T_1 = 1.812 s ± 0.051
T = 195.9 K ± 0.2
Integrated Peak Area
1.0
0.5
0.0
-0.5
Time (s)
0
2
4
6
8
10
12
14
16

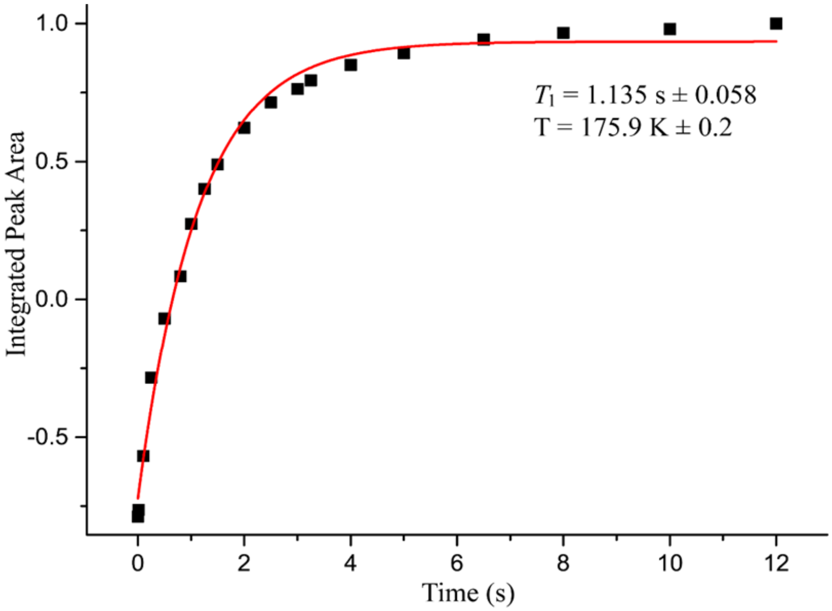
T_1 = 1.135 s ± 0.058
T = 175.9 K ± 0.2
Integrated Peak Area
1.0
0.5
0.0
-0.5
Time (s)
0
2
4
6
8
10
12

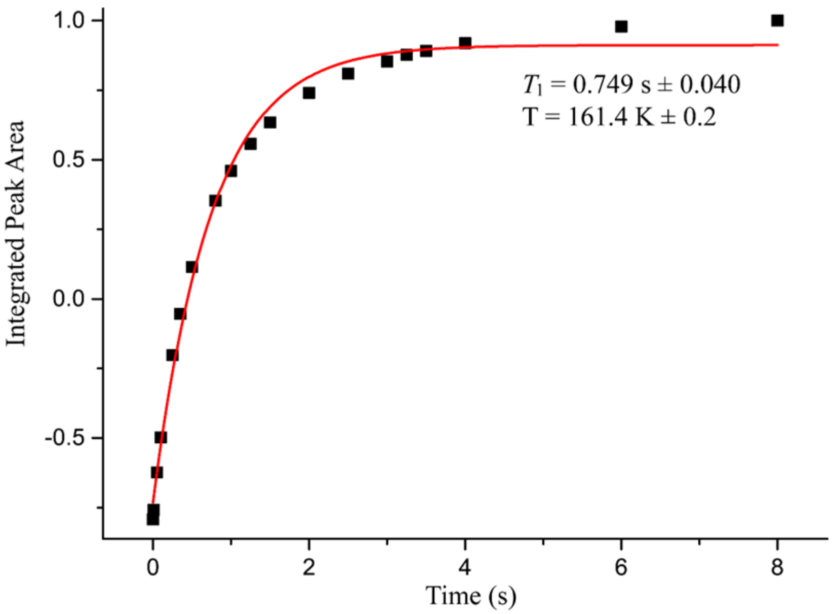
1.0
0.5
0.0
-0.5
Integrated Peak Area
0
2
4
6
8
Time (s)
T_1 = 0.749 s ± 0.040
T = 161.4 K ± 0.2

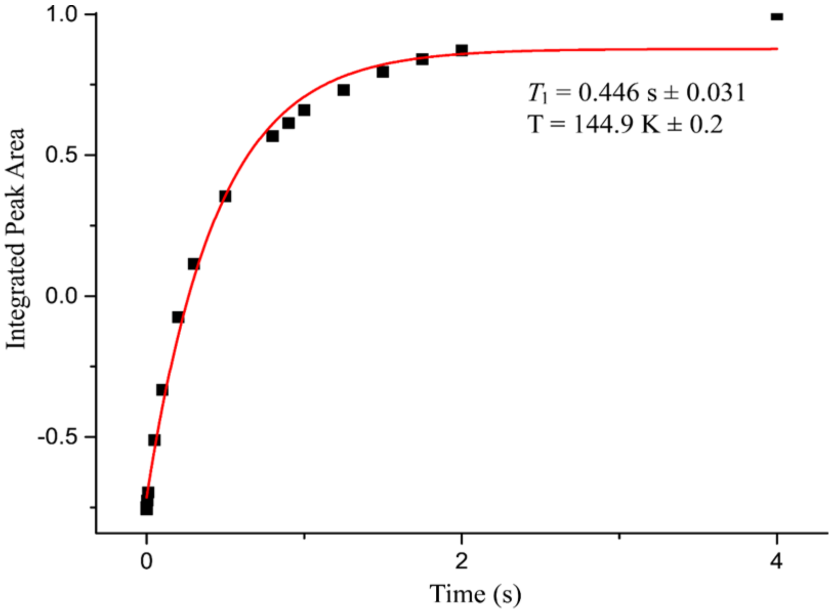
1.0
0.5
0.0
-0.5
Integrated Peak Area
0
2
4
Time (s)
T_1 = 0.446 s ± 0.031
T = 144.9 K ± 0.2

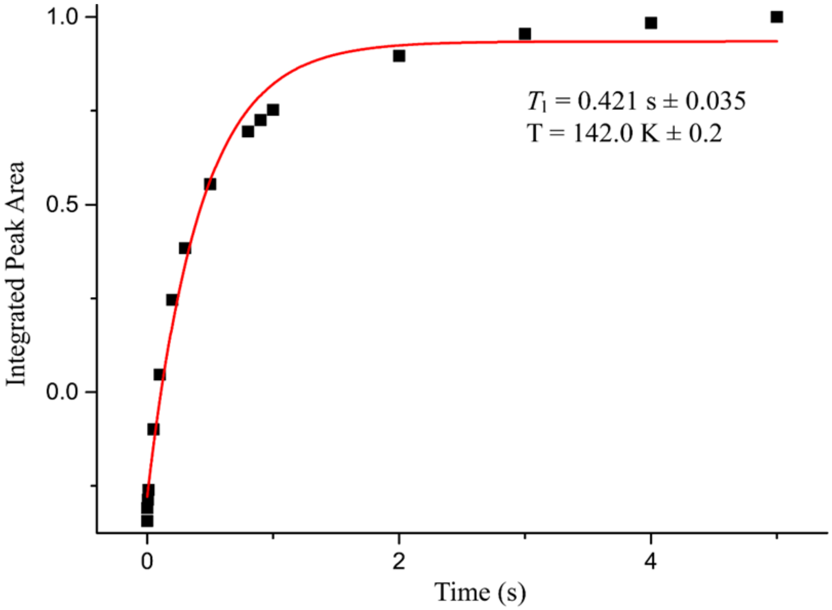

4) *1,4-dichlorotetrafluorobenzene·2,3,5,6-tetramethylpyrazine* (***4***)

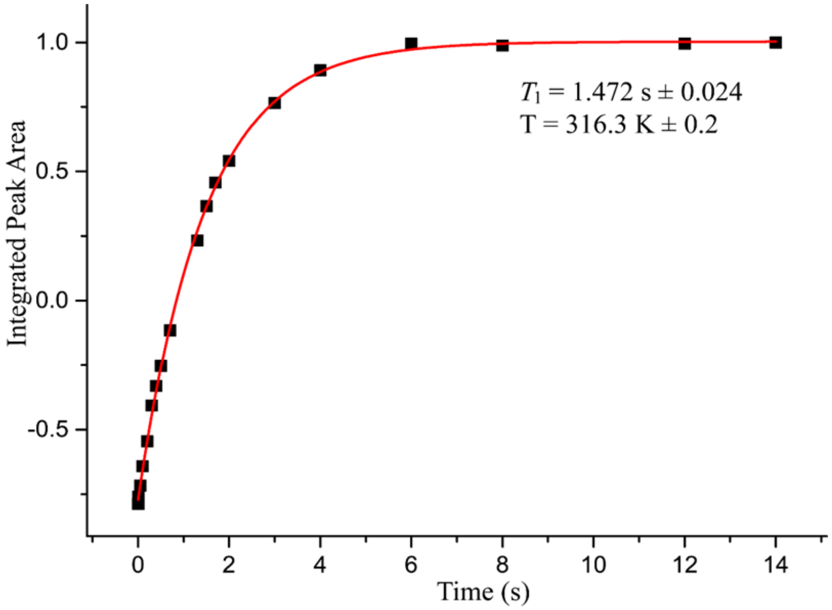

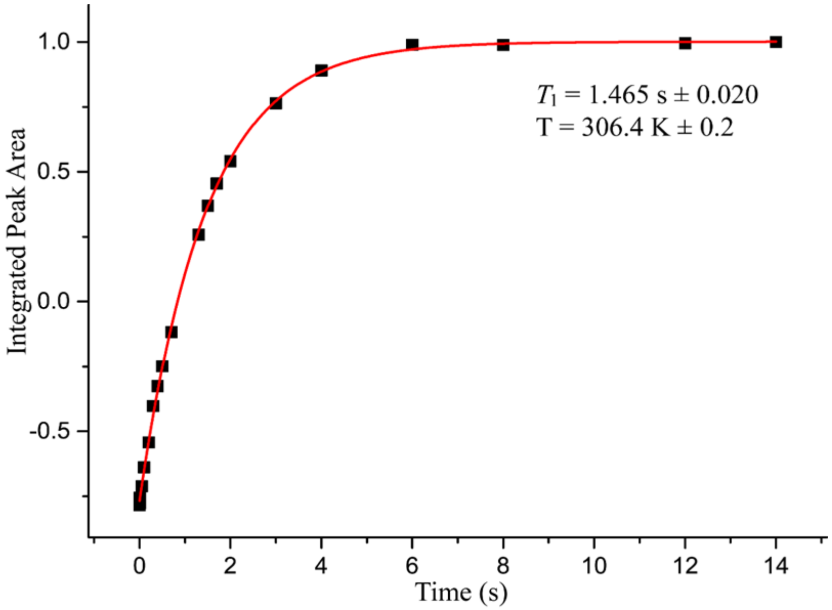
Integrated Peak Area
1.0
0.5
0.0
-0.5
0
2
4
6
8
10
12
14
Time (s)
T_1 = 1.465 s ± 0.020
T = 306.4 K ± 0.2

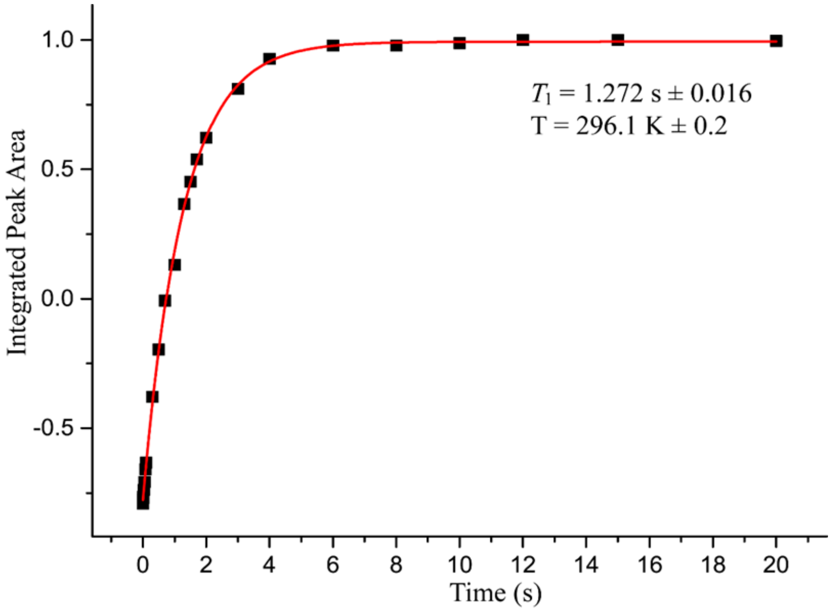
Integrated Peak Area
1.0
0.5
0.0
-0.5
0
2
4
6
8
10
12
14
16
18
20
Time (s)
T_1 = 1.272 s ± 0.016
T = 296.1 K ± 0.2

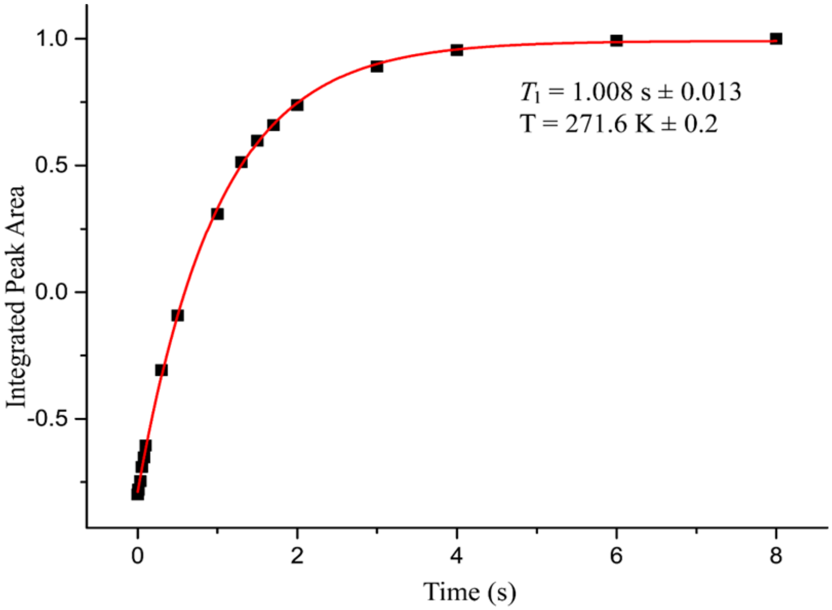

Integrated Peak Area
Time (s)
1.0
0.5
0.0
-0.5
0
2
4
6
8
T_1 = 1.008 s ± 0.013
T = 271.6 K ± 0.2

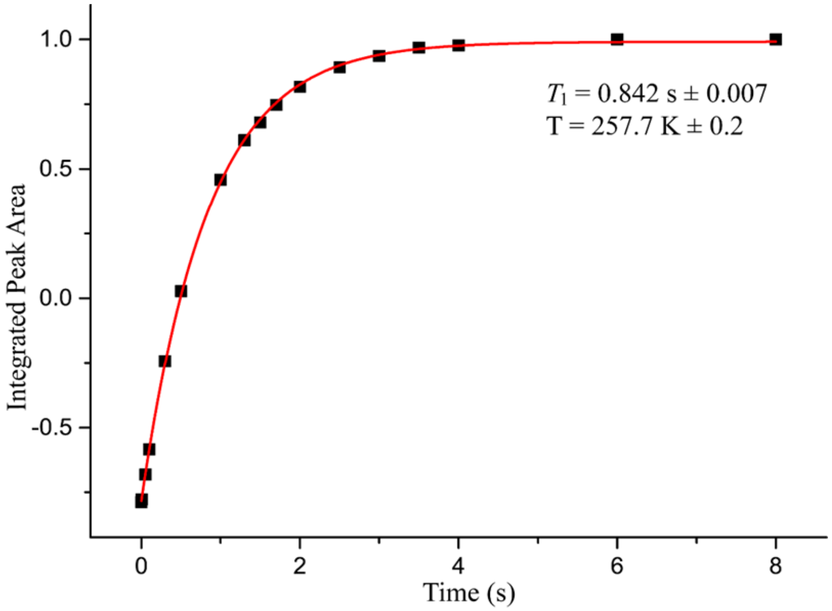

Integrated Peak Area
Time (s)
1.0
0.5
0.0
-0.5
0
2
4
6
8
T_1 = 0.842 s ± 0.007
T = 257.7 K ± 0.2

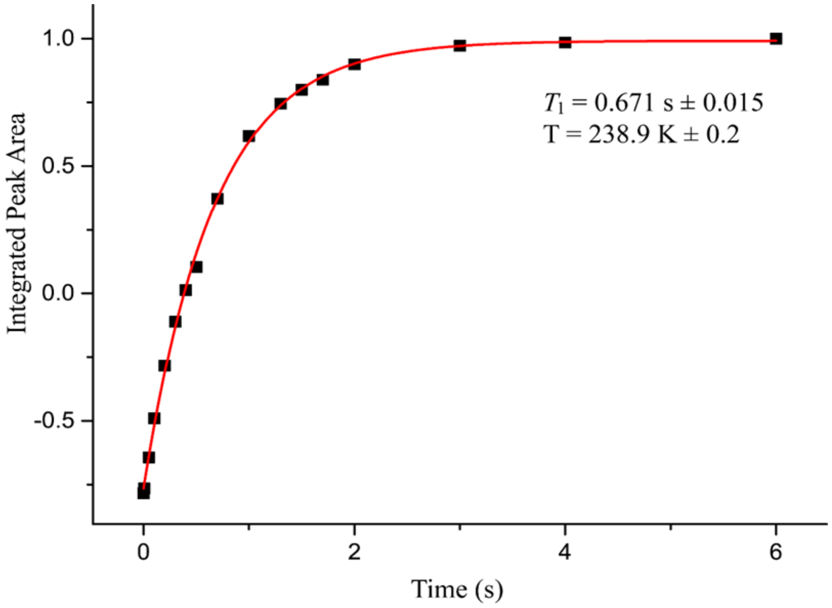
Integrated Peak Area
1.0
0.5
0.0
-0.5
0
2
4
6
Time (s)
T_1 = 0.671 s ± 0.015
T = 238.9 K ± 0.2

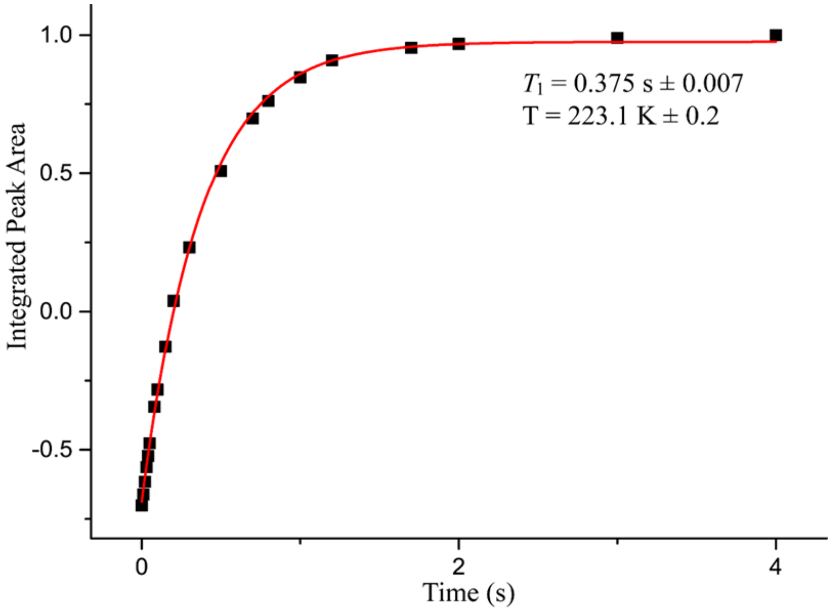
Integrated Peak Area
1.0
0.5
0.0
-0.5
0
2
4
Time (s)
T_1 = 0.375 s ± 0.007
T = 223.1 K ± 0.2

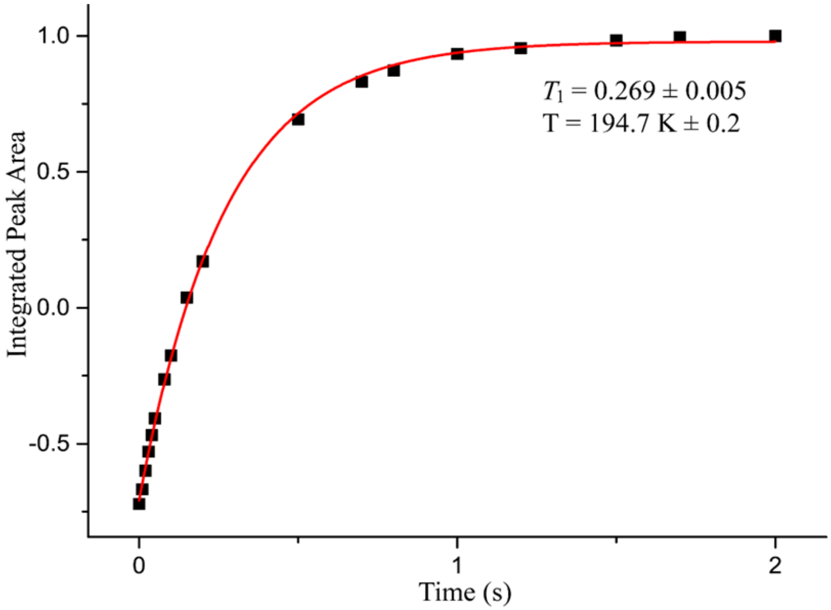
1.0
0.5
0.0
-0.5
Integrated Peak Area
0
1
2
Time (s)
T_1 = 0.269 ± 0.005
T = 194.7 K ± 0.2

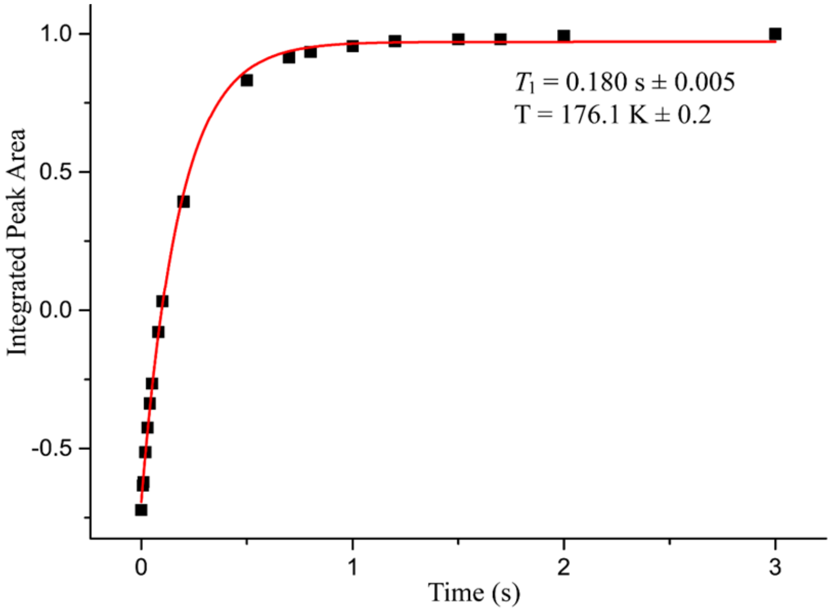
1.0
0.5
0.0
-0.5
Integrated Peak Area
0
1
2
3
Time (s)
T_1 = 0.180 s ± 0.005
T = 176.1 K ± 0.2

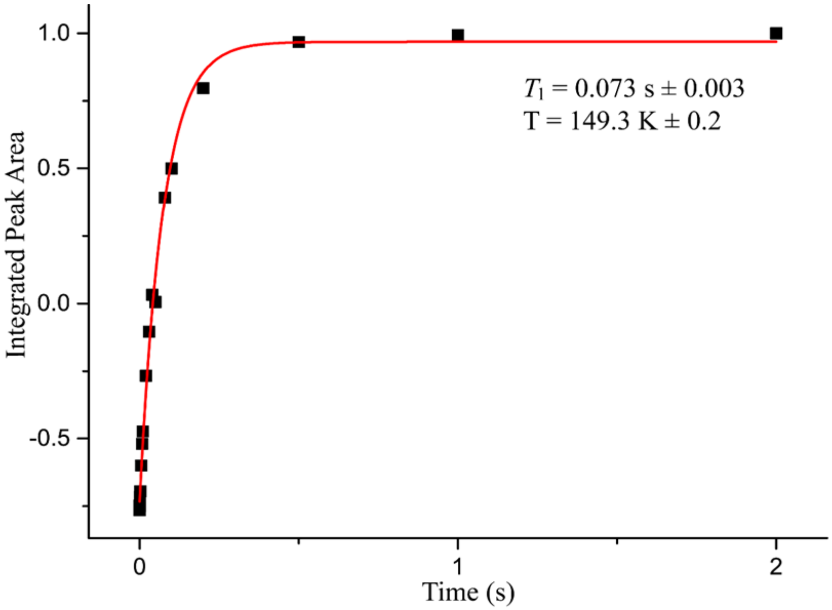
Integrated Peak Area
1.0
0.5
0.0
-0.5
0
1
2
Time (s)
T_1 = 0.073 s ± 0.003
T = 149.3 K ± 0.2

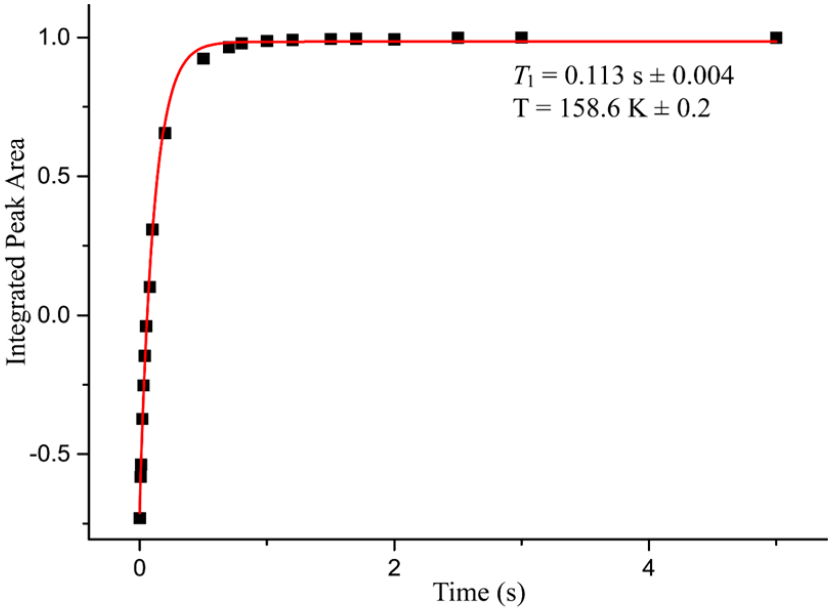
Integrated Peak Area
1.0
0.5
0.0
-0.5
0
2
4
Time (s)
T_1 = 0.113 s ± 0.004
T = 158.6 K ± 0.2

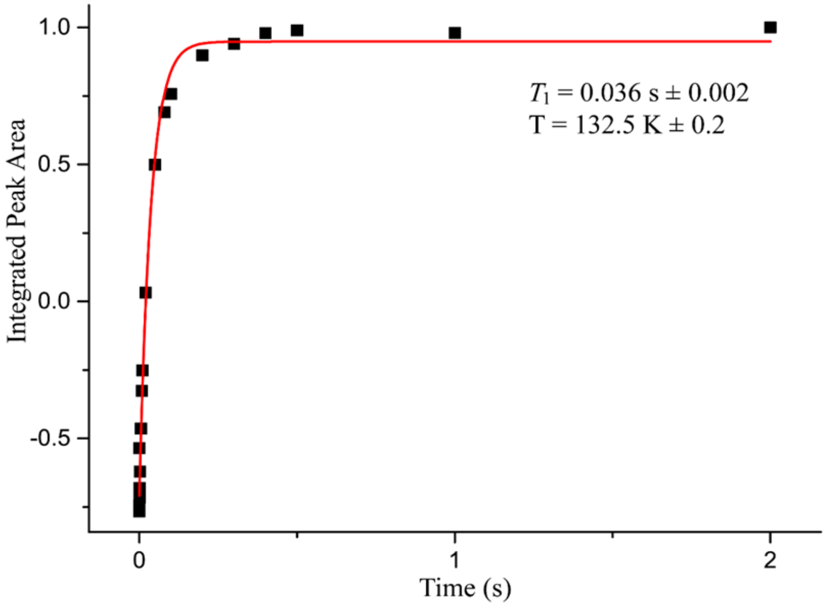

5) *1,3,5-trichloro-2,4,6-trifluorobenzene·2,3,5,6-tetramethylpyrazine (**5**)*

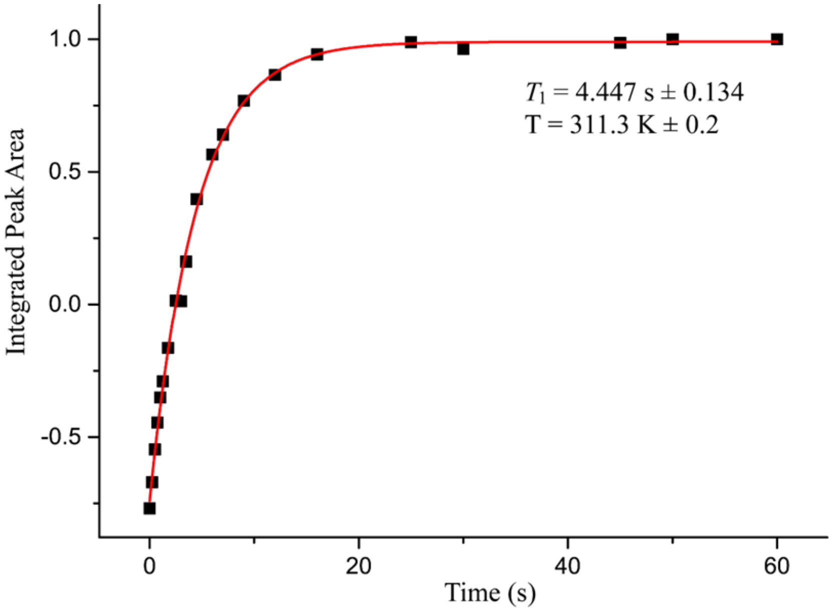

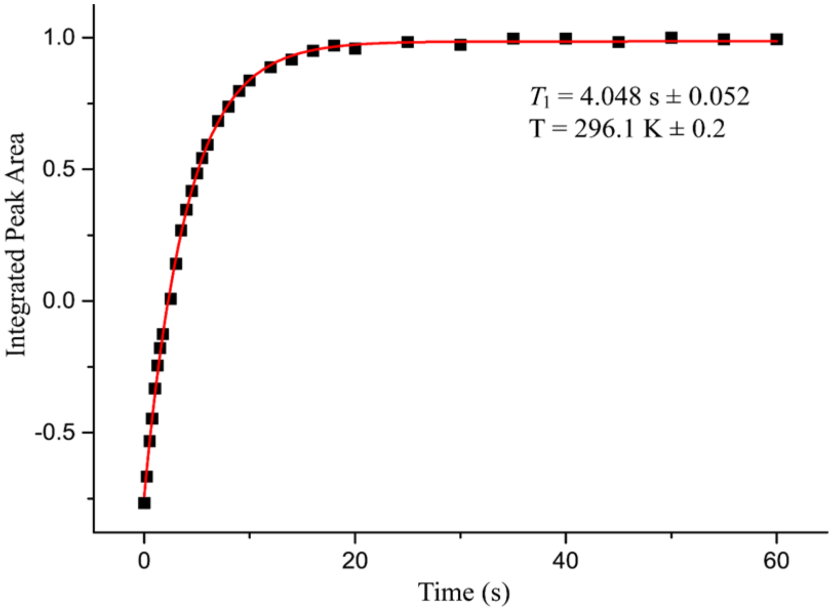
1.0
0.5
0.0
-0.5
Integrated Peak Area
0
20
40
60
Time (s)
T_1 = 4.048 s ± 0.052
T = 296.1 K ± 0.2

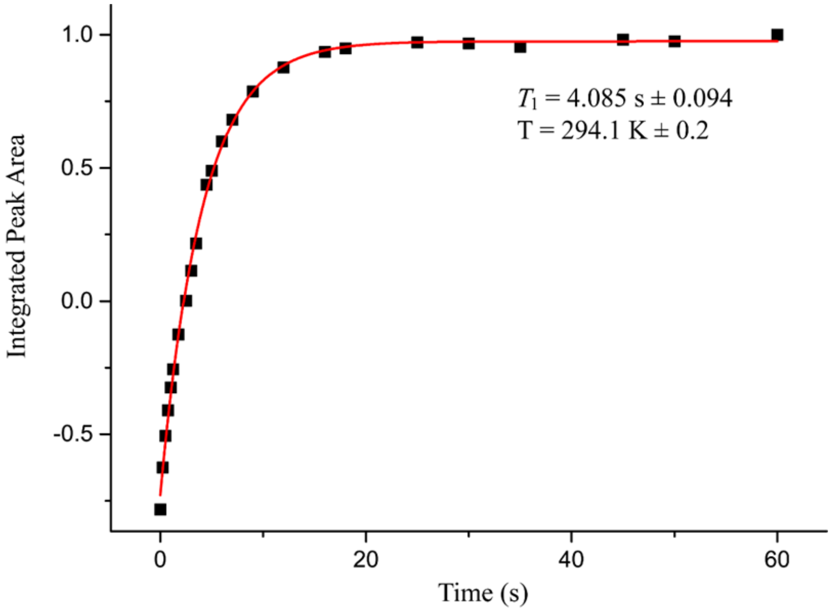
1.0
0.5
0.0
-0.5
Integrated Peak Area
0
20
40
60
Time (s)
T_1 = 4.085 s ± 0.094
T = 294.1 K ± 0.2

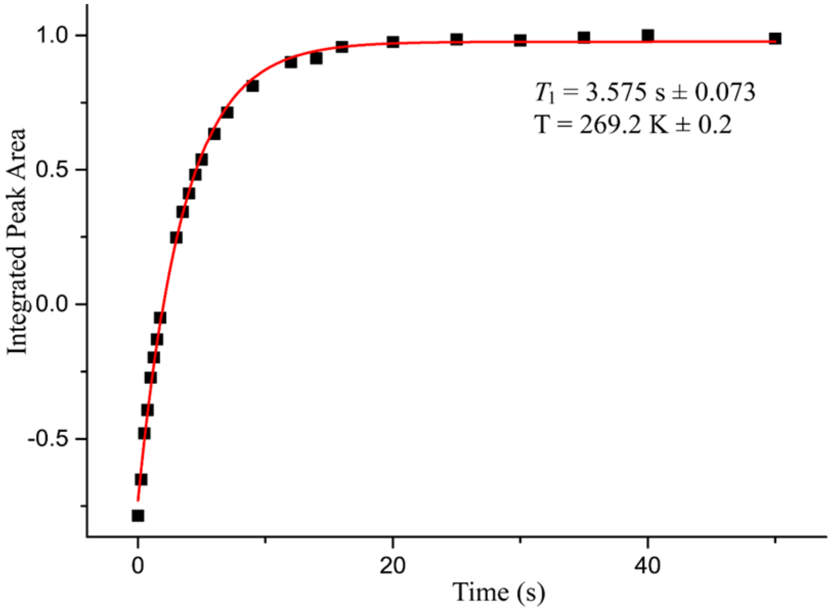
T_1 = 3.575 s ± 0.073
T = 269.2 K ± 0.2
Integrated Peak Area
1.0
0.5
0.0
-0.5
Time (s)
0
20
40

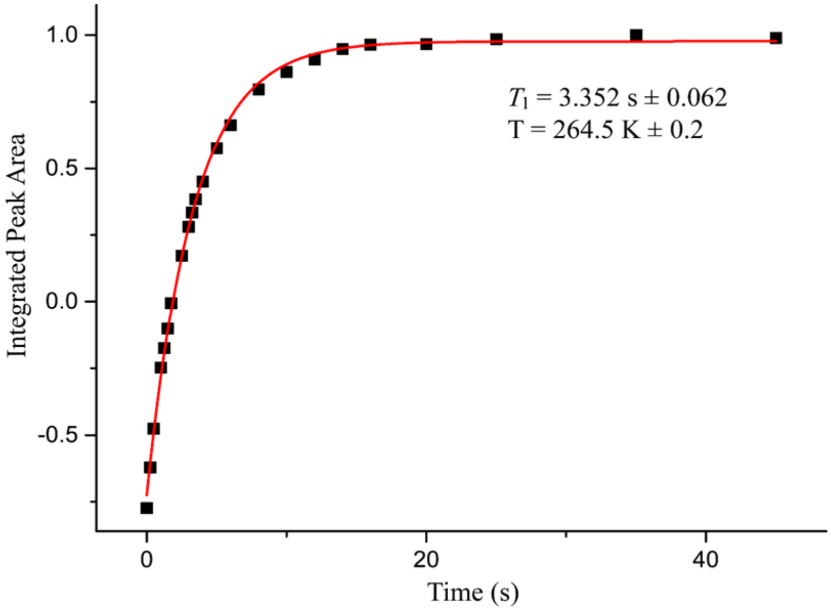
T_1 = 3.352 s ± 0.062
T = 264.5 K ± 0.2
Integrated Peak Area
1.0
0.5
0.0
-0.5
Time (s)
0
20
40

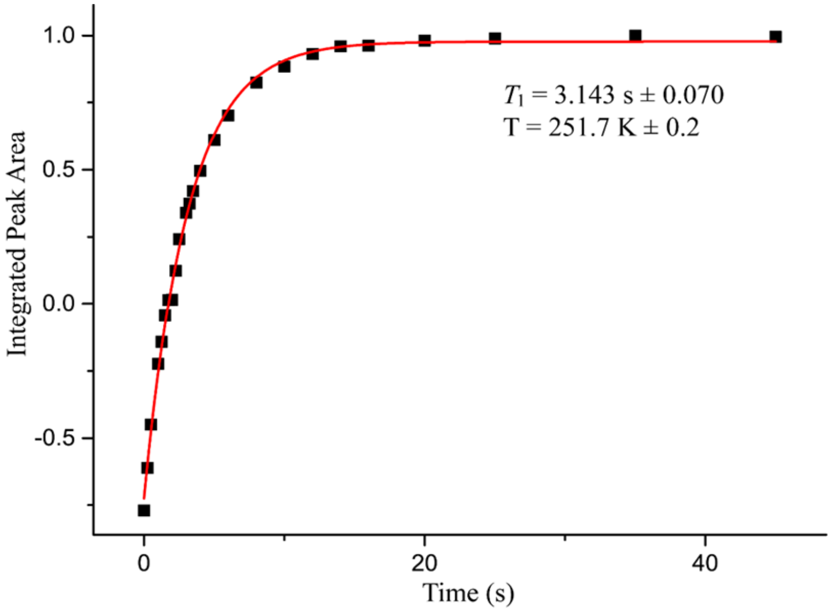
T_1 = 3.143 s ± 0.070
T = 251.7 K ± 0.2
Integrated Peak Area
Time (s)
1.0
0.5
0.0
-0.5
0
20
40

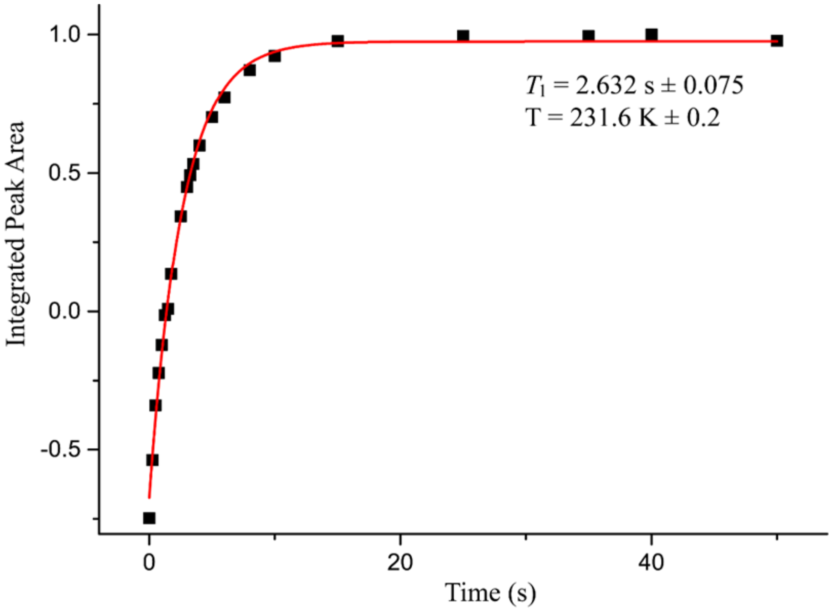
T_1 = 2.632 s ± 0.075
T = 231.6 K ± 0.2
Integrated Peak Area
Time (s)
1.0
0.5
0.0
-0.5
0
20
40

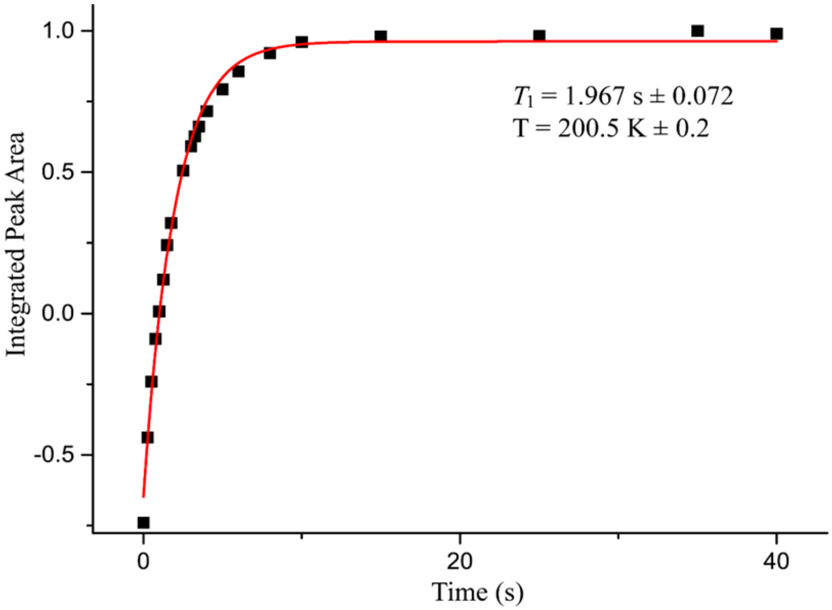
1.0
0.5
0.0
-0.5
Integrated Peak Area
0
20
40
Time (s)
T_1 = 1.967 s ± 0.072
T = 200.5 K ± 0.2

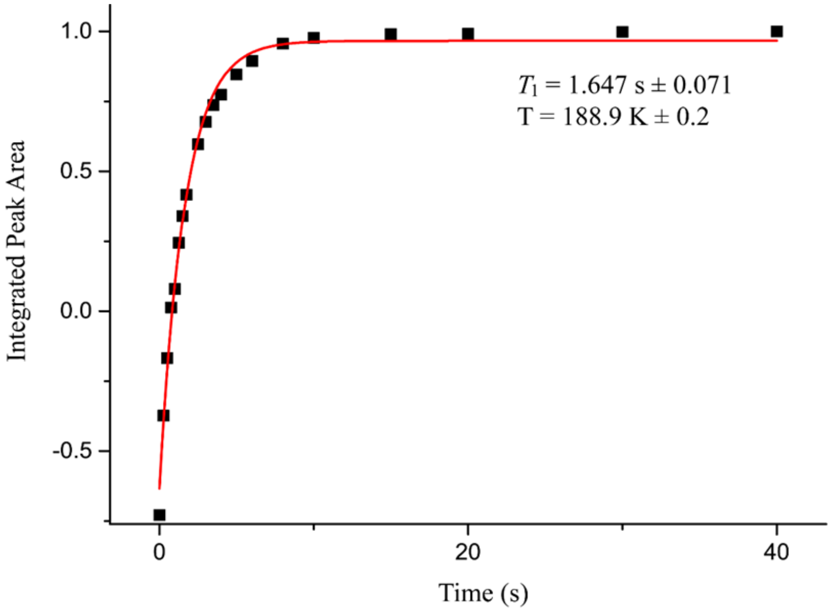
1.0
0.5
0.0
-0.5
Integrated Peak Area
0
20
40
Time (s)
T_1 = 1.647 s ± 0.071
T = 188.9 K ± 0.2

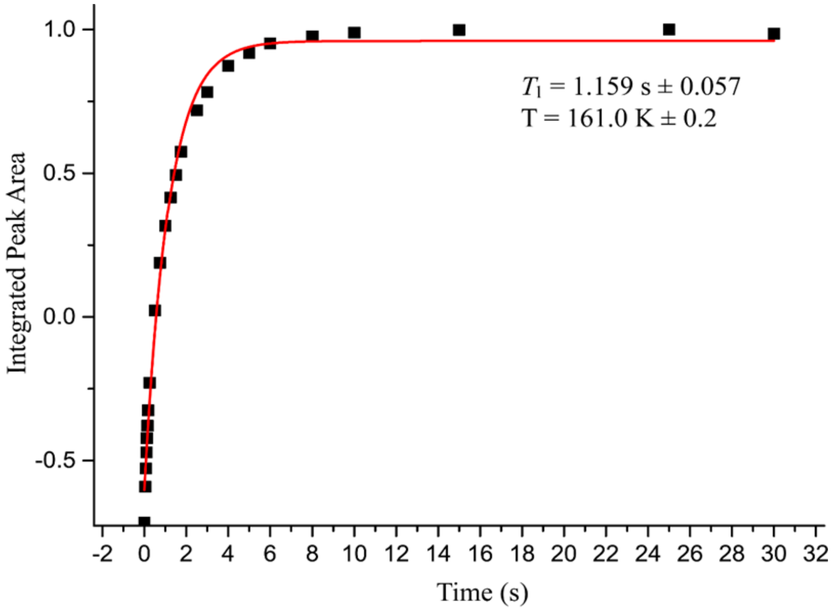

Integrated Peak Area
1.0
0.5
0.0
-0.5
-2
0
2
4
6
8
10
12
14
16
18
20
22
24
26
28
30
32
Time (s)
T_1 = 1.159 s ± 0.057
T = 161.0 K ± 0.2

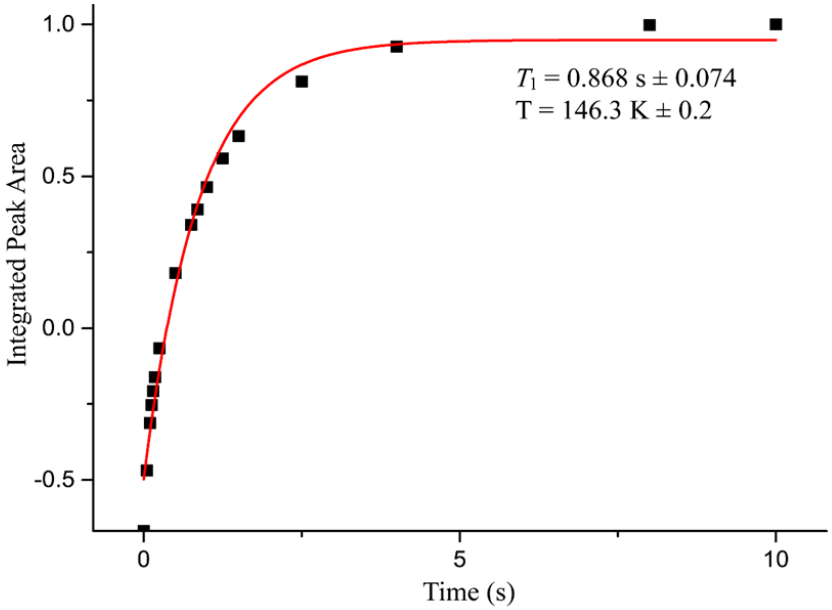

Integrated Peak Area
1.0
0.5
0.0
-0.5
0
5
10
Time (s)
T_1 = 0.868 s ± 0.074
T = 146.3 K ± 0.2

5. Tables of T_1 Data as a Function of Temperature

Table S 6. T_1 and Effective Quadrupolar Data for Cocrystal (1)

T / K ± 0.2 K	Relaxation time constant T_1 / s	C_Q / kHz ± 1 kHz	η ± 0.05
323.5	2.013 ± 0.036	51	0.127
309.9	1.733 ± 0.014	51	0.107
298.6	1.560 ± 0.026	51	0.109
293.2	1.541 ± 0.030	51	0.106
257.4	1.089 ± 0.021	51	0.127
236.7	0.807 ± 0.005	51	0.122
220.0	0.661 ± 0.014	51	0.105
210.5	0.568 ± 0.014	51	0.131
193.6	0.411 ± 0.004	51	0.134
178.9	0.300 ± 0.005	51	0.143
167.0	0.252 ± 0.004	51	0.125
157.0	0.175 ± 0.005	51	0.137
144.6	0.129 ± 0.002	51	0.135

Table S 7. T_1 and Effective Quadrupolar Data for Cocrystal (2)

T / K ± 0.2 K	Relaxation time constant T_1 / s	C_Q / kHz ± 1 kHz	η ± 0.05
321.1	5.905 ± 0.066	52	0.100
305.7	5.492 ± 0.054	52	0.107
295.4	5.240 ± 0.050	52	0.105
274.0	4.422 ± 0.074	52	0.102
254.6	3.837 ± 0.043	52	0.110
234.6	3.268 ± 0.048	52	0.117
212.9	2.757 ± 0.064	52	0.110
212.9	2.749 ± 0.065	52	0.111
198.7	2.428 ± 0.080	52	0.100
185.9	2.069 ± 0.078	52	0.120
165.8	1.561 ± 0.062	52	0.120
149.3	1.269 ± 0.055	52	0.118

Table S 8. T_1 and Effective Quadrupolar Data for Cocrystal (3)

T / K ± 0.2 K	Relaxation time constant T_1 / s	C_Q / kHz ± 1 kHz	η ± 0.05
313.4	5.202 ± 0.069	51	0.143
288.6	4.430 ± 0.090	51	0.155
230.7	2.686 ± 0.093	50	0.163
212.5	2.254 ± 0.075	51	0.165
195.9	1.812 ± 0.051	51	0.175
175.9	1.135 ± 0.058	50	0.190
161.4	0.749 ± 0.040	49	0.193
144.9	0.446 ± 0.031	51	0.232
142.0	0.421 ± 0.035	52	0.235

Table S 9. T_1 and Effective Quadrupolar Data for Cocrystal (4)

T / K ± 0.2 K	Relaxation time constant T_1 / s	C_Q / kHz ± 1 kHz	η ± 0.05
316.3	1.472 ± 0.024	51	0.125
306.4	1.465 ± 0.020	51	0.130
296.1	1.272 ± 0.016	51	0.120
271.6	1.008 ± 0.013	51	0.127
257.7	0.842 ± 0.007	51	0.118
238.9	0.671 ± 0.015	51	0.115
223.1	0.375 ± 0.007	51	0.133
194.7	0.269 ± 0.005	51	0.138
176.1	0.180 ± 0.005	50	0.136
158.6	0.113 ± 0.004	51	0.143
149.3	0.073 ± 0.003	51	0.164
132.5	0.036 ± 0.002	52	0.150

Table S 10. T_1 and Effective Quadrupolar Data for Cocrystal (5)

T / K ± 0.2 K	Relaxation time constant T_1 / s	C_Q / kHz ± 1 kHz	η ± 0.05
311.3	4.447 ± 0.134	50	0.114
296.1	4.048 ± 0.052	51	0.117
294.1	4.085 ± 0.094	51	0.119
269.2	3.575 ± 0.073	51	0.100
264.5	3.352 ± 0.062	51	0.123
251.7	3.143 ± 0.070	51	0.116
231.6	2.632 ± 0.075	51	0.132
200.5	1.967 ± 0.072	51	0.105
188.9	1.647 ± 0.071	51	0.150
161.0	1.159 ± 0.057	50	0.134
146.3	0.868 ± 0.074	50	0.153

6. Additional Data and Plots

Table S 11. Linear fits of lnT_1 vs 1/T data

cocrystal	equation	R^2
1	y = -718.96x + 2.8663	0.9983
2	y = -453.45x + 3.1573	0.9955
3	y = -651.40x + 3.7748	0.9981
4	y = -852.57x + 3.1085	0.9951
5	y = -450.93x + 2.9295	0.9988

Table S 12. Void volumes

cocrystal	unit cell vol. / Å^3	void vol.^{a} / Å^3	% void^a	void vol.^{b} / Å^3	% void^b	void vol.^{c} /Å^3	% void^c
1	1158.8	314.60	27.2	195.76	16.9	138.79	12.0
2	1655.25	446.43	27.0	302.86	18.3	218.89	13.2
3	274.4	84.32	30.7	66.04	24.1	56.92	20.7
4	1147.6	319.46	27.8	201.20	17.5	141.42	12.3
5	1610.4	473.95	29.4	340.33	21.1	269.46	16.7
6	788.005	242.44	30.8	153.76	19.5	103.55	13.1

a. Probe radius = 0.2 Å; grid spacing = 0.1 Å. b. Probe radius = 0.4 Å; grid spacing = 0.2 Å. c. Probe radius = 0.4 Å; grid spacing = 0.4 Å.

Table S 13. DFT computed activation energies from linear transit calculations

cocrystal	E_a (calc) / kJ mol^{-1}
1	4.04
2	3.16
3	3.18
4	3.88
5	3.06
6	3.62
I_2·TMP	2.17

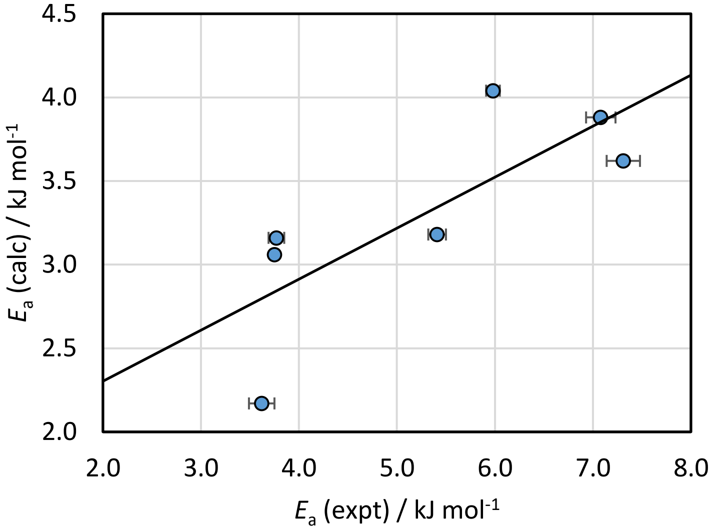

Figure S 14. Plot of DFT calculated vs experimental activation energies for methyl rotation in compounds 1 to 6 plus I_2.TMP. E_a(calc) = 0.3051 x E_a(expt) + 1.6924. R^2=0.6024.

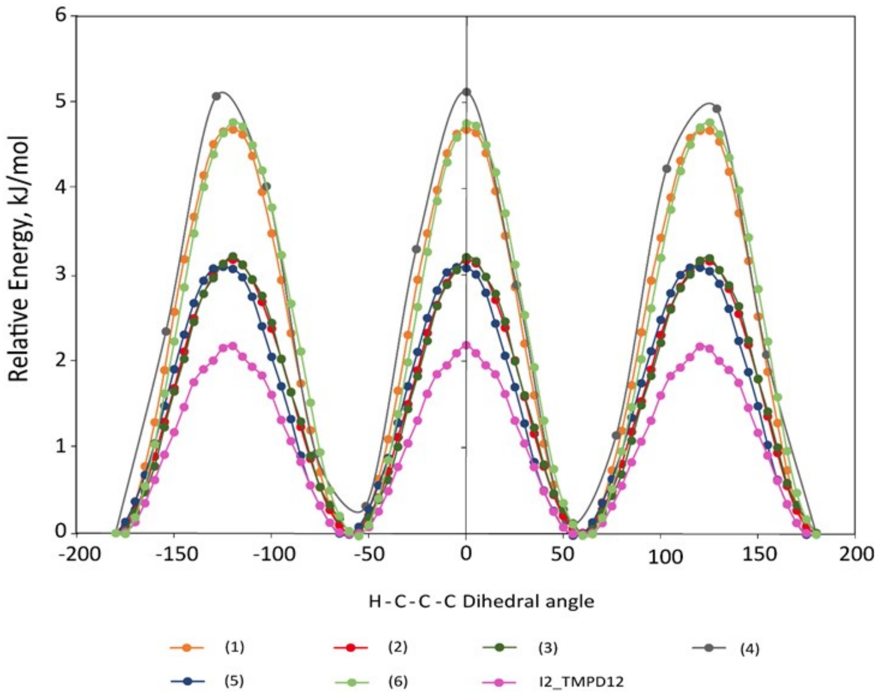

Figure S 15. DFT-computed linear transit calculations of rotational energy barriers in compounds 1-6 plus I_2·TMP.

Table S 14. Average effective π bond order[b]

cocrystal	**1**	**2**	**3**	**4**	**5**	2I[b]	3I[b]	I_2·TMP	**6**
average π bond order / Å	0.055875	0.0575	0.0316	0.0575	0.0585	0.0615	0.05375	0.0755	0.0645

a. Effective π bond order is calculated as the difference in covalent C-C and N-C ring bond lengths involving the carbon bearing the methyl group.

b. "2I" = 1,4-diiodotetrafluorobenzene·TMP; "3I" = 1,3,5-trifluoro-2,4,6-triiodobenzene·TMP

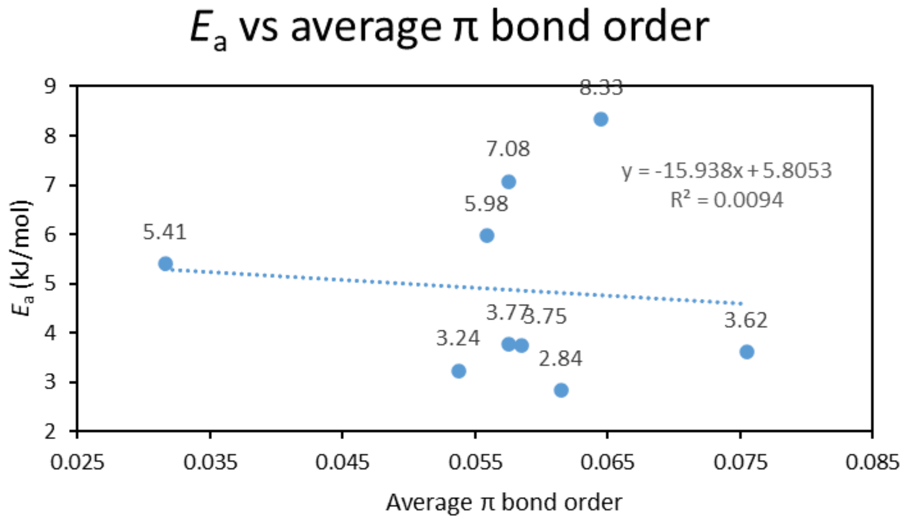

Figure S 16. Lack of correlation between experimental activation energies and π bond order.

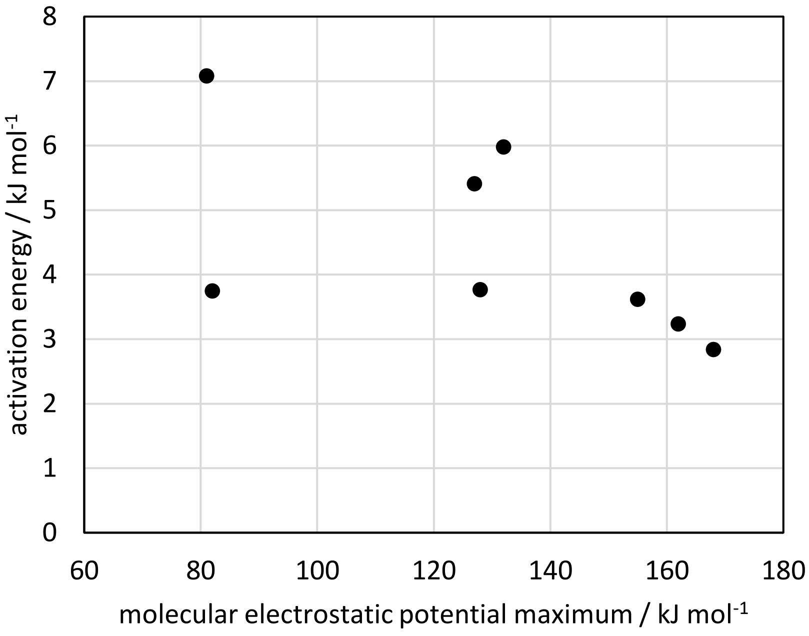

Figure S 17. Rotational activation energy does not correlate universally with the molecular electrostatic potential maximum at the σ-hole.

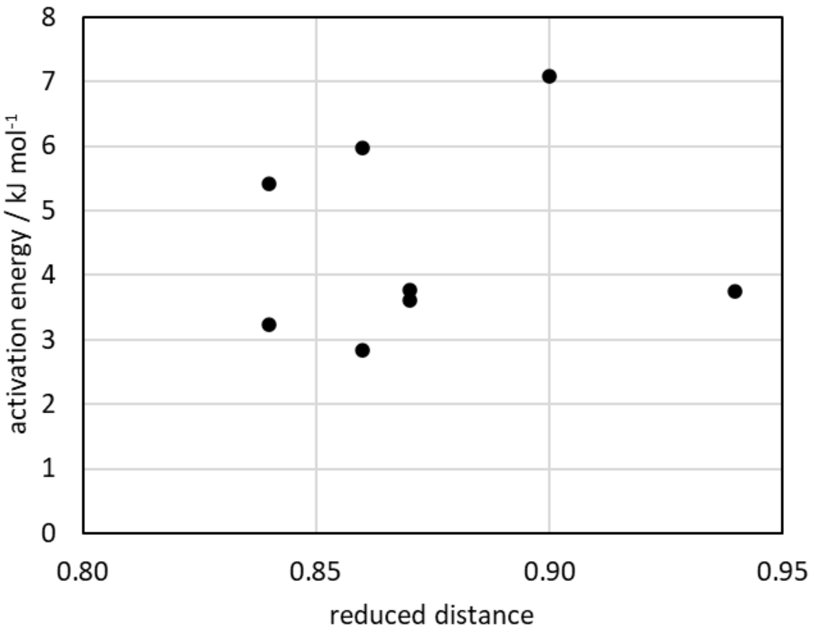

Figure S 18. Rotational activation energy does not correlate universally with the reduced distance parameter associated with the halogen bond.

7. Additional Details on the Preparation of Br_2·TMP (3)

Equimolar amounts of deuterated 2,3,5,6-tetramethylpyrazine and liquid Br_2 were placed in opposite ends of a cosublimation tube which was placed inside a furnace which is part of a homebuilt automated cosublimation apparatus.[1] The initial and final temperatures were set for both forward and backward reaction (sublimation/evaporation and desublimation process), from room temperature (RT) to 90 ˚C to RT for TMP, and RT to 40 ˚C to RT for Br_2. The reagents met in the vapor state where they were held for 2 h before returning the set-up to RT. The total process took 48 h to yield orange crystals (Figure S19) which were later confirmed by single-crystal X-ray diffraction as Br_2·TMP cocrystals.

Figure S 19. Orange Br_2·TMP cocrystals (3) obtained using a cosublimation furnace.

References

(1) Szell, P. M. J.; Gabriel, S. A.; Caron-Poulin, E.; Jeannin, O.; Fourmigué, M.; Bryce, D. L. *Cryst. Growth Des.* **2018**, *18*, 6227-6238.

Appendix 2: Chapter 5 Supporting Information

Single-crystal X-ray diffraction of 1,3,4,5-tetrabromo-2,6-difluorobenzene

A single crystal was mounted on a glass fibre and cooled to 200 ± 2 K before data collection using an FTS AirJet compressed air refrigerator (SP Scientific) liquid nitrogen cryogenic system. The X-ray diffraction data were collected on Bruker Smart Apex diffractometers equipped with APEX II CCD detectors using MoKα radiation (wavelength $\lambda = 0.7103$ Å). The distance from crystal to detector was 45 mm and the scan width ($\Delta\omega$) was 0.5° per frame. The data collection strategy was chosen in such a way to get 100% completeness; however, a few frames were of 97% completeness. The data collection, cell refinement, integration, and reduction were carried out using the APEX III software package. The structure was solved using WinGX and shelxle[1] software packages with the direct method and refined based on the spherical atom approximation based on F2 using SHELXL 97.[1,2] Analysis of intermolecular interactions was done with PLATON.[3] The fluorine atoms were refined anisotropically and carbon and bromine atoms were modeled using SIMU and DELU commands to improve the refinement. Twinning was treated with 26% BASF. A crystallographic information file has been deposited in the Cambridge Structural Database, entry 2328690.

Table S 15. Single crystal X-ray data and structure refinement details for 1,3,4,5-tetrabromo-2,6-difluorobenzene.

CCDC Number	2328690
Empirical formula	$C_6Br_4F_2$
Formula weight	429.70
Temperature/K	202(2)
Crystal system	monoclinic
Space group	$P2_1$
a/Å	8.73(2)
b/Å	4.110(9)
c/Å	13.41(3)
α/°	90
β/°	99.44(4)
γ/°	90
Volume/Å^3	474.9(18)
Z	2
ρ_{calc}g/cm^3	3.005
μ/mm^{-1}	16.920
F(000)	388
Crystal size/mm^3	0.352 x 0.246 x 0.128
Radiation	0.71073
2θ range for data collection/°	1.539 to 25.021
Index ranges	-9<=h<=10, -4<=k<=4, -15<=l<=15
Reflections collected	3153
Independent reflections	1548 [R(int) = 0.0541]
Data/restraints/parameters	1548 / 123 / 110
Goodness-of-fit on F^2	1.112
Final R indexes [I>=2σ (I)]	R_1 = 0.0780, wR_2 = 0.2128
Final R indexes [all data]	R_1 = 0.1038, wR_2 = 0.2419
Largest diff. peak/hole / e Å^{-3}	2.189 and -2.254

References

(1) Sheldrick GM (2008) Acta Crystallogr Sect A 64:112.

(20 Farrugia LJ (2012) J Appl Crystallogr 45:849.

(3) Spek AL (2009) Acta Crystallogr Sect D 65:148.

Appendix 3: Contributions by Shubha S. Gunaga and conference presentations, participation

El-khawaldeh, R. K.; **Gunaga, S.S.**; Bryce, D. L. Assessment of Halogen-Bond Induced Cocrystallization of 1,3,5-Trihalo-2,4,6-trifluorobenzenes with 2,3,5,6 Tetramethylpyrazine, Results Chem., 2022, 4, 100336.

Gunaga, S. S. and Bryce, D. L. Modulation of Rotational Dynamics in Halogen-Bonded Cocrystalline Solids, J. Am. Chem. Soc., 2023, 145, 19005-19017.

Gunaga, S. S. and Bryce, D. L. Type II Halogen-Halogen Contacts in the Single-Crystal X-ray Diffraction Structure of a 1:1 Halogen-Bonded Cocrystal of 2,3,5,6-Tetramethylpyrazine and 1,3,4,5-Tetrabromo-2,6-difluorobenzene, J. Chem. Crystallogr., 2024, 1-7.

Conference presentations, participation

Attended MOOT NMR symposium-32 during first year of PhD at uOttawa, (2019).

Presented research poster (virtual) at International School for Young Scientists in Roshchino (Russia) during first year of PhD at uOttawa (September 2020).

Attended 4th International Symposium on Halogen Bonding (ISXB-4 Virtual) event held from 2 – 5 November 2020.

Presented poster at Virtual CCCE 2021 51st IUPAC General Assembly 48th World Chemistry Congress 104th Canadian Chemistry Conference and Exhibition August 13 -20, 2021.

Gunaga, S. S. and Bryce, D. L. "Halogen Bond-Catalyzed Reduction in Potential Barrier of Methyl Group Rotations via Deuterium Solid-State NMR Relaxation Measurements" Delivered a talk at CCCE at Calgary, Alberta on 14th June, 2022.

Gunaga, S. S. and Bryce, D. L. “Study of methyl rotations in halogen bonded cocrystals via deuterium NMR using T1 time constants”, presented poster at 61st Rocky Mountain Conference on Magnetic Resonance at Copper Mountain, Colorado, July 25-29, 2022

Attended hands on training and workshop with PANACEA solid-state NMR workshop for pharmaceutical formulations held in Lausanne at EPFL from 30 August- 02 September 2022.

Gunaga, S. S., Rusli, J, Bryce, D. L. "Bicalutamide polymorphism: solid-state NMR characterization of two crystalline forms" Presented poster in an International meeting on crystallography by American Crystallographic Association in July 7-11, 2023 at Baltimore, USA and received the Delbaere Pauling poster prize for outstanding poster presentation.